Longitudinal Double Spin Asymmetry for Inclusive Jet Production in Polarized Proton-Proton Collisions at $\sqrt{s}$=200 GeV

by

Julie Marie Millane

Submitted to the Department of Physics
in partial fulfillment of the requirements for the degree of

Doctor of Philosophy in Physics

at the

MASSACHUSETTS INSTITUTE OF TECHNOLOGY

May 2008

Author . . . .
Department of Physics
May 21, 2008

Certified by . . . .
Robert P. Redwine
Professor
Thesis Supervisor

Accepted by . . . .
Thomas J. Greytak
Associate Department Head for Education

Longitudinal Double Spin Asymmetry for Inclusive Jet Production in Polarized Proton-Proton Collisions at $\sqrt{s}$=200 GeV

by

Julie Marie Millane

Submitted to the Department of Physics
on May 21, 2008, in partial fulfillment of the
requirements for the degree of
Doctor of Philosophy in Physics

Abstract

We present the Inclusive Jet Longitudinal Double-Spin Asymmetry for polarized protons at $\sqrt{s} = 200$ GeV. The data were taken on the STAR experiment at RHIC during the 2005 run period and cover a jet transverse momentum range of $5 < p_T < 30$ GeV/c. The main detector components used were the time-projection chamber (TPC), barrel-electromagnetic calorimeter (BEMC), and beam-beam counters (BBC).

Comparison of the asymmetry with theoretical calculations, which utilized deep inelastic scattering results, places constraints on the gluon contribution to the proton's spin. The asymmetry is consistent with prior measurements and further constrains the gluon's contribution over previous results. ΔG, a measure of the gluon's contribution, is restricted to less than 65% of the proton's spin at 90% confidence level.

We also present the Inclusive Jet Cross-Section for unpolarized proton-proton collisions at $\sqrt{s} = 200$ GeV. It covers a transverse momentum range of $5 < p_T < 49$ GeV/c. The cross-section is calculated for five triggers and the five triggers show good agreement among the cross-section results.

The cross-section is compared with theoretical predictions based on NLO pQCD using the CTEQ6M parton distribution functions. The cross-section agrees with theoretical predictions when the uncertainty in jet momentum is taken into account. The cross-section is within the systematic uncertainties of previous measurements. The largest systematic uncertainty for the cross-section is due to the jet energy scale. This uncertainty ranges varies from 1.5% to 38% depending on the trigger and transverse momentum range.

Thesis Supervisor: Robert P. Redwine
Title: Professor

Acknowledgments

I would like to thank Renee Fatemi for all her help. She went above and beyond, offering encouragement and advice. Special thanks go to my daughter Cecilia. She reminded me of what is most important and kept me in touch with reality. Also, to my sisters Kathy and Patty I need to say thank you. They listened to all my complaints and encouraged me through the rough patches. I would like to thank my advisor Robert Redwine. His support and guidance smoothed my path to graduation. He read many drafts of my thesis and helped shape it into its current form. Thanks go to the STAR spin group for listening to my results and offering advice. I would like to thank my thesis committee: Robert Jaffe, Richard Milner, and Robert Redwine. I need to thank the MIT RHIC Spin graduate students for their friendship and interesting lunchtime conversation. Finally, thanks to my fellow members of WPHYS. My stay at MIT was much more enjoyable thanks to you.

THIS PAGE INTENTIONALLY LEFT BLANK

Contents

List of Figures

List of Tables

THIS PAGE INTENTIONALLY LEFT BLANK

Chapter 1

Introduction

Protons are not elementary particles, but rather have an internal structure of quarks and gluons. These quarks and gluons give the proton its properties, including its spin. A simple picture of the proton's spin is

$$J_z = S_z^q + L_z^q + S_z^g + L_z^g$$

where J_z is the proton spin, S_z is the intrinsic spin of the quarks (or gluons), L_z is the orbital angular momentum of the quarks (or gluons), and q (g) stands for quarks (gluons). How the quarks and gluons contribute to the proton's spin is not currently fully understood.

1.1 The Spin Crisis

Lepton scattering has been used very successfully in the past to determine the spin structure of nucleons. Its success is due to the fact that the electroweak interaction is well understood and is weak enough to use perturbative methods. The nucleon's spin structure can be found by using polarized beams and targets.

The Quark-Parton Model can be used to model the nucleon in deep-inelastic scattering (DIS). A charged lepton (electron, muon, etc) scattering from a quark inside the proton is shown in Fig. 1-1. If the lepton and nucleon are unpolarized,

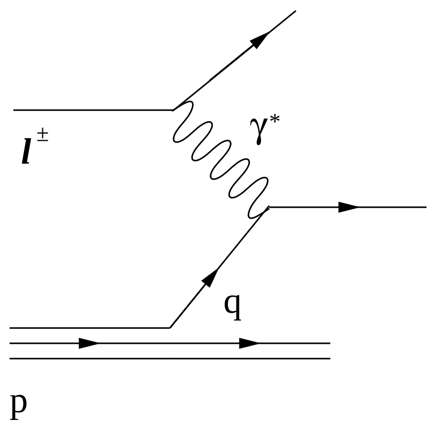

Figure 1-1: A Feynman diagram of deep inelastic scattering of a lepton off a proton

then the quark distributions (u(x), d(x), s(x), $\cdots$) can be determined.

The structure function,

$$F_1(x) = \frac{1}{2}\sum_i e_i^2 q_i(x),$$

is the sum over all quark and anti-quark flavor unpolarized distributions. The sum over polarized distributions is

$$g_1(x) = \frac{1}{2}\sum_i e_i^2 \Delta q_i(x).$$

g_1 can be found be looking at polarized beams and measuring the cross-section asymmetry[3].

Experiments probing the spin structure of the nucleon have been done at SLAC, CERN, DESY and BNL. The European Muon Collaboration (EMC) measured both the quark and gluon contributions to the proton's spin[4, 1]. Figure 1-2 shows the EMC results. The plot on the right is for $\Delta\Sigma$, the contribution to the proton's spin from all quarks.

Ellis and Jaffe used a sum-rule to estimate that the quarks contribute 60% of the proton's spin[5]. DIS experiments found that the quarks contribute approximately 30% of the proton's spin, about half of what was predicted by Ellis and Jaffe. The remaining 70% could be from sea quarks[1], gluons, or orbital angular momentum.

[1] Ellis and Jaffe assumed that strange quarks do not contribute to the proton's spin.

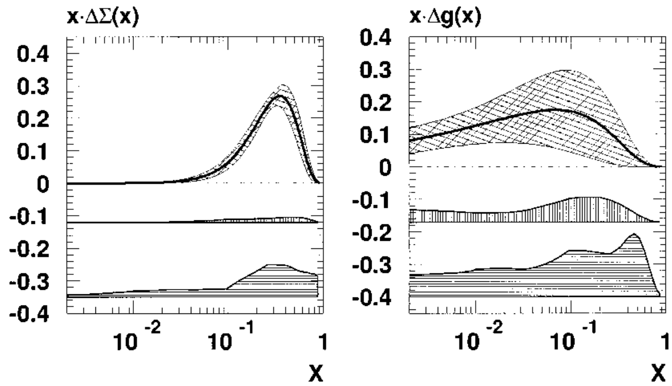

Figure 1-2: Polarized parton distribution functions from EMC[1]. The crossed hatch bands are the statistical uncertainties. The horizontally (vertically) hatched bands are the theoretical (experimental systematic) uncertainties.

In Fig. 1-2, the plot on the right is the contribution to the proton's spin from the gluons. The error band for the gluons is much larger than that for quarks because the gluons interact only at next-to-leading order with leptons. Since DIS experiments poorly constrain the gluon contribution to the proton, experiments involving polarized protons, such as at RHIC, can give a better understanding of how the gluon contributes to the proton's spin.

1.2 An Experimental Method to Determine the Proton's Gluon Contribution

The double spin asymmetry is defined as

$$A_{LL} \equiv \frac{d\Delta\sigma}{d\sigma} = \frac{\sigma^+ - \sigma^-}{\sigma^+ + \sigma^-},$$

where σ^+ (σ^-) is the cross-section for proton-proton collisions where the product of the helicities[2] is +1 (-1).

The factorization theorem says that $\Delta\sigma$, the spin-dependent cross section for jets,

[2]A particle has +1 (-1) helicity if the spin and velocity are parallel (anti-parallel).

can be written as

$$\frac{d\Delta\sigma}{dp_T d\eta} = \sum_{a,b} \Delta f_a(x_a, \mu) \bigotimes \Delta f_b(x_b, \mu) \bigotimes \frac{d\Delta\hat{\sigma}_{ab}}{dp_T d\eta}(x_a, x_b, p_T, \eta, \mu),$$

where convolutions are represented as $\bigotimes$ and the sum is over all participating partons. Δf_a and Δf_b are the two partons interacting in the collision. They could be quarks (Δq) and/or gluons (Δg). This is how Δg can be obtained from the asymmetry measurement. $d\Delta\hat{\sigma}_{ab}$ is the parton level cross section and can be expanded as follows:

$$d\Delta\hat{\sigma}_{ab} = d\Delta\hat{\sigma}_{ab}^{(0)} + \frac{\alpha_s}{\pi} d\Delta\hat{\sigma}_{ab}^{(1)} + \cdots$$

In order to extract Δg from the asymmetry measurement it is necessary that gluons take part in the collisions. In collisions of protons at the RHIC center-of-mass energy, gluon-gluon collisions dominated[6] for $p_T < 10 GeV/c$, totaling about 50% of the collisions. Their contribution steadily declined to less than 10% for $p_T > 25$ GeV/c. Quark-gluon interactions ranged from 40% to 50% for $p_T < 30$ GeV/c. Interactions that did not contain a gluon were less than 10% for low p_T ($p_T < 8$ GeV/c). However, their contribution steadily increased to around 40% at $p_T = 30$ GeV/c.

All interactions do not contribute the same amount to the asymmetry. For the p_T range covered by this data, the asymmetry for quark-quark interactions is negligible compared to the asymmetry for gluon-gluon and quark-gluon interactions[7]. So over many interactions, quark-quark interactions contribute almost nothing to the asymmetry measurement.

Theory curves of A_{LL} for various values of ΔG are given in Fig. 1-3. GRSV-std was calculated based on the best fit to polarized inclusive DIS experimental data. GRSV $\Delta g = 0$ ($\Delta g = \pm g$) was calculated assuming no (maximum/minimum) gluon polarization, $\Delta g = 0$ ($\Delta g = \pm g$). An initial scale of $Q_0^2 = 0.4 GeV^2/c^2$ was used and the expressions were evaluated at factorization and renormalization scales of$\mu_F = \mu_R = p_T$. Global analysis other than GRSV are also available, although GRSV was

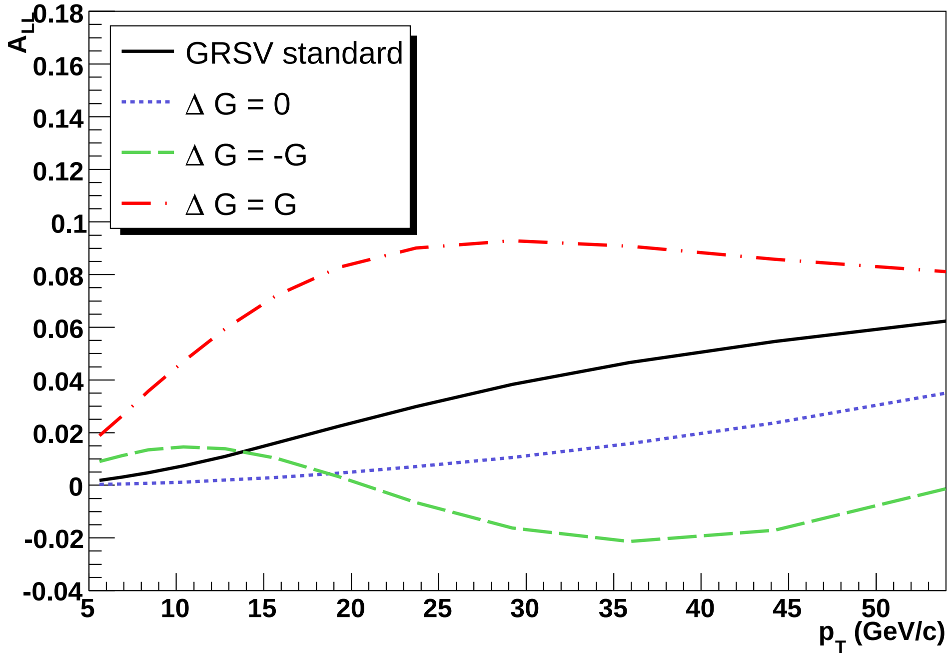

Figure 1-3: GRSV predictions for A_{LL} for various ΔG values[2]

the main global analysis considered in this thesis. One global analysis, GS-C[8], is similar to the GRSV-std curve. The main difference is that its functional form has a node at $x \sim 0.1, Q^2 = 1GeV^2/c^2$. Figure 1-3 shows that A_{LL} is dependent on ΔG and so a measurement of A_{LL} can yield a determination of ΔG.

NLO pQCD was assumed in calculating the asymmetry theory curves. So it is important that the data were following NLO pQCD predictions. A cross section measurement can confirm that the data were consistent with NLO pQCD.

THIS PAGE INTENTIONALLY LEFT BLANK

Chapter 2

Experimental Setup

2.1 Brookhaven National Laboratory

Brookhaven National Laboratory (BNL) is located in Upton, NY on Long Island. Founded in 1947, BNL is operated by Brookhaven Science Associates for the U.S. Department of Energy. About 3000 permanent researchers/staff and 4000 guest researchers use the lab annually. Research at the lab covers a broad spectrum including studying new nanostructures, high-temperature superconductors, medical imaging techniques, understanding the proton spin structure and determining how infections start in the body. Breakthroughs at BNL include the discovery of L-dopa (used to treat Parkinson's disease), detection of the Quark Gluon Plasma (QGP) and the invention of magnetically levitated trains.

2.2 The Relativistic Heavy Ion Collider

The Relativistic Heavy Ion Collider (RHIC)[9] collides both heavy ions and polarized protons at BNL. The proton's spin structure and the Quark Gluon Plasma's properties are studied at RHIC. Figure 2-1 gives a view of the RHIC facility at BNL.

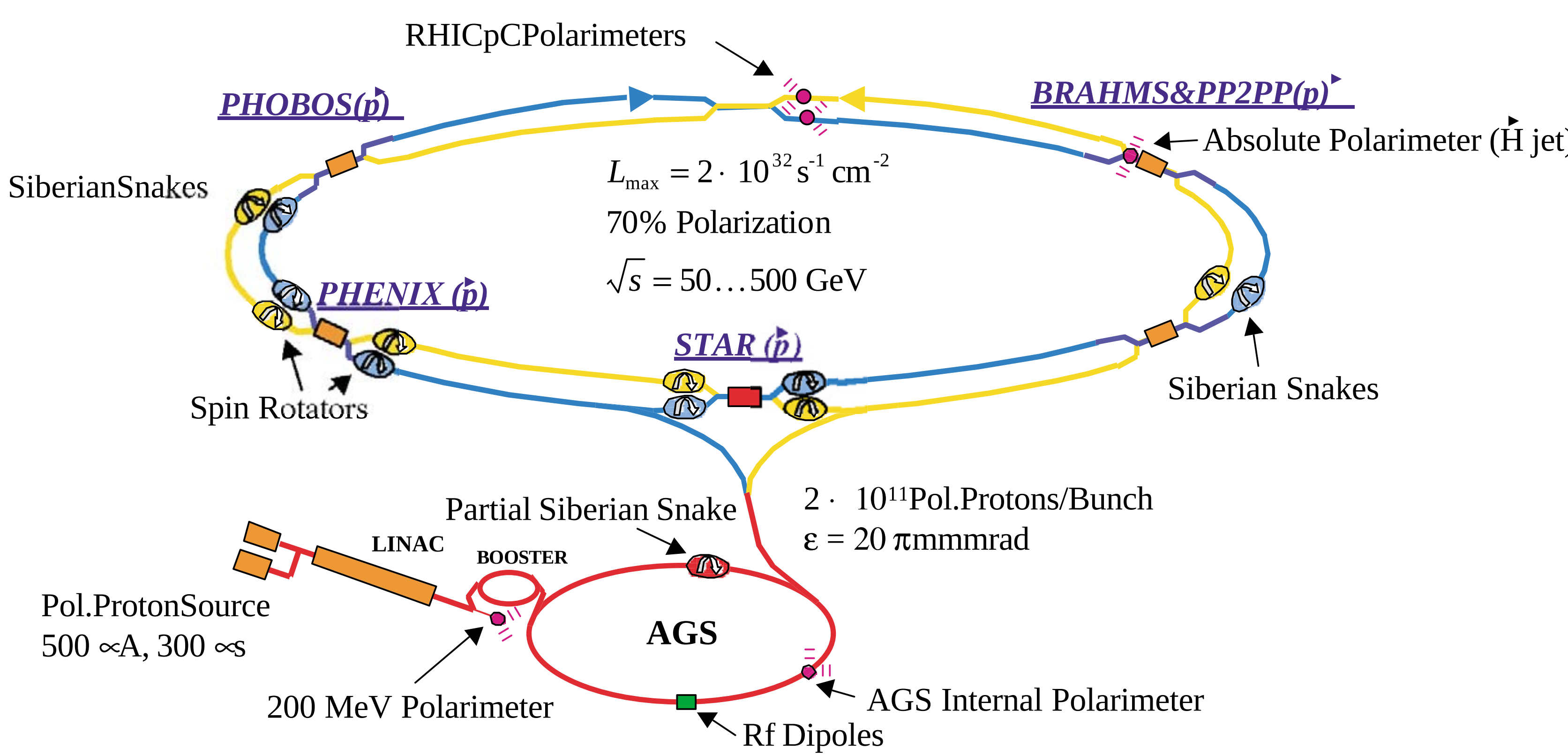

Figure 2-1: The facilities which produce, accelerate and collide polarized protons at BNL

Five experiments ran at RHIC during 2005: PHOBOS[10], BRAHMS[11], PHENIX[12], pp2pp[13] and STAR[14]. pp2pp investigated elastic scattering of proton-proton collisions. BRAHMS and PHOBOS were interested solely in heavy ion collisions, which create the QGP, whereas PHENIX and STAR were concerned with both heavy ion collisions to study the QGP as well as proton-proton collisions to study the spin structure of the proton.

Polarized protons started their journey in the $500\mu A$, $300\mu s$ source[15] where they were made by stripping Hydrogen atoms. The polarized proton source injected H^- ions into the 200 MHz LINAC, where they were accelerated to 200 MeV. The Alternating Gradient Synchrotron (AGS) Booster collected proton bunches and accelerated them up to 1.5 GeV. Then they were injected into the AGS where they were accelerated up to 25 GeV. After the AGS, protons entered the RHIC ring and, once it was completely filled, the protons were accelerated up to their full energy (100-250 GeV).

Two beams of protons circled the RHIC ring. The proton beams had transverse polarization (polarization vector perpendicular to velocity vector). Spin Rotators located before and after the interaction points at PHENIX and STAR allowed beam collisions in both transverse and longitudinal orientations. The beams were brought together at six interaction points (4 experimental halls, one polarimeter hall and one empty slot). These six interaction points were determined by the pre-existing ring that was used by RHIC.

Four Siberian snakes[16] in the ring helped the beam maintain its polarization. Since the proton's gyromagnetic ratio[1] is not 2[2], if the proton's spin is not aligned with the magnetic field it will precess. The Siberian Snakes contained helical magnets that rotated the proton's spin 180° around the longitudinal direction. This allowed one to maintain proton polarization in the ring.

Carbon polarimeters[17, 18] were placed in each beam at regular intervals to measure its polarization. An asymmetry occurs in proton-carbon scattering that

[1] A particle's gyromagnetic ratio is the particle's magnetic dipole moment divided by its angular momentum.

[2] $\gamma_p = 2.68 s^{-1} T^{-1}$

depends on the amount of polarization of the protons. By looking at the scattering from the carbon nuclei and using the analyzing powers of proton-carbon elastic scattering, the proton beams' polarization was determined.

2.3 The STAR Detector

Figure 2-3 gives a view of the STAR[14] detector. A cutaway side view can be seen in Fig. 2-2. The STAR detector was built to examine the QGP and study the proton structure.

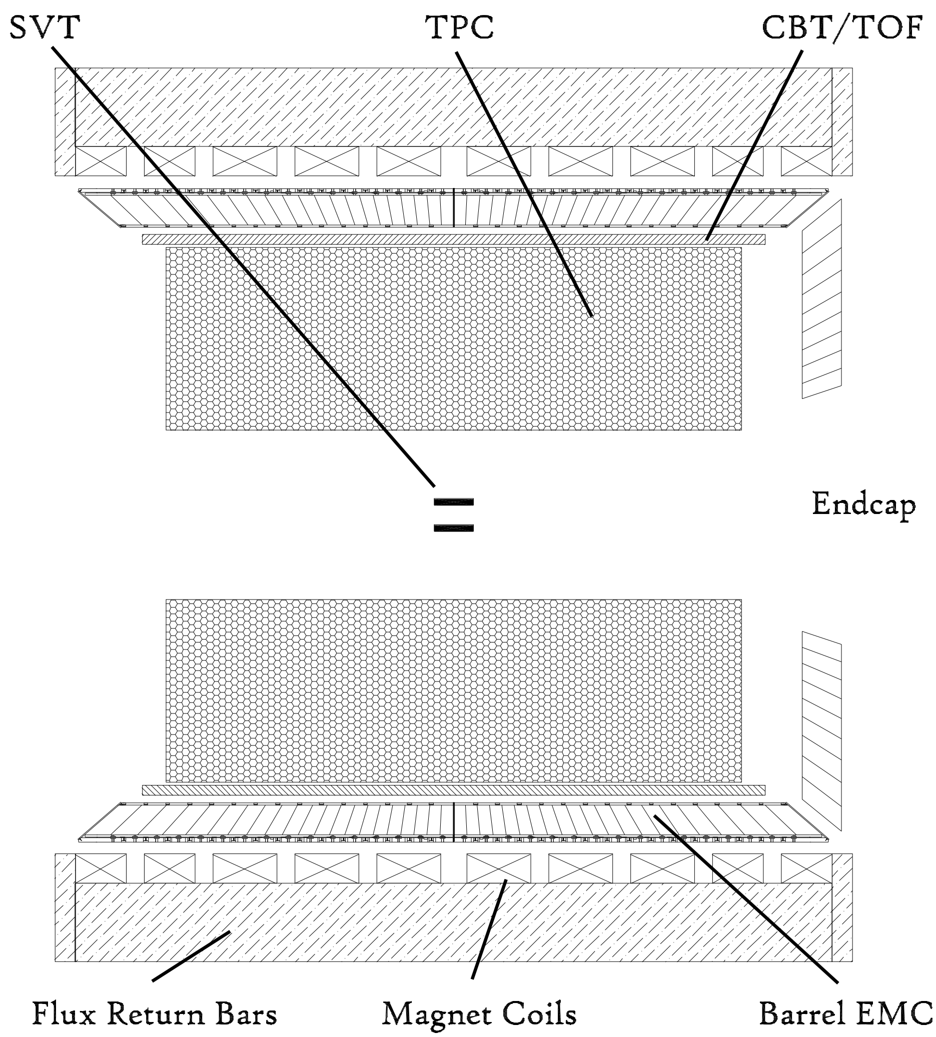

Figure 2-2: The STAR detector cross section

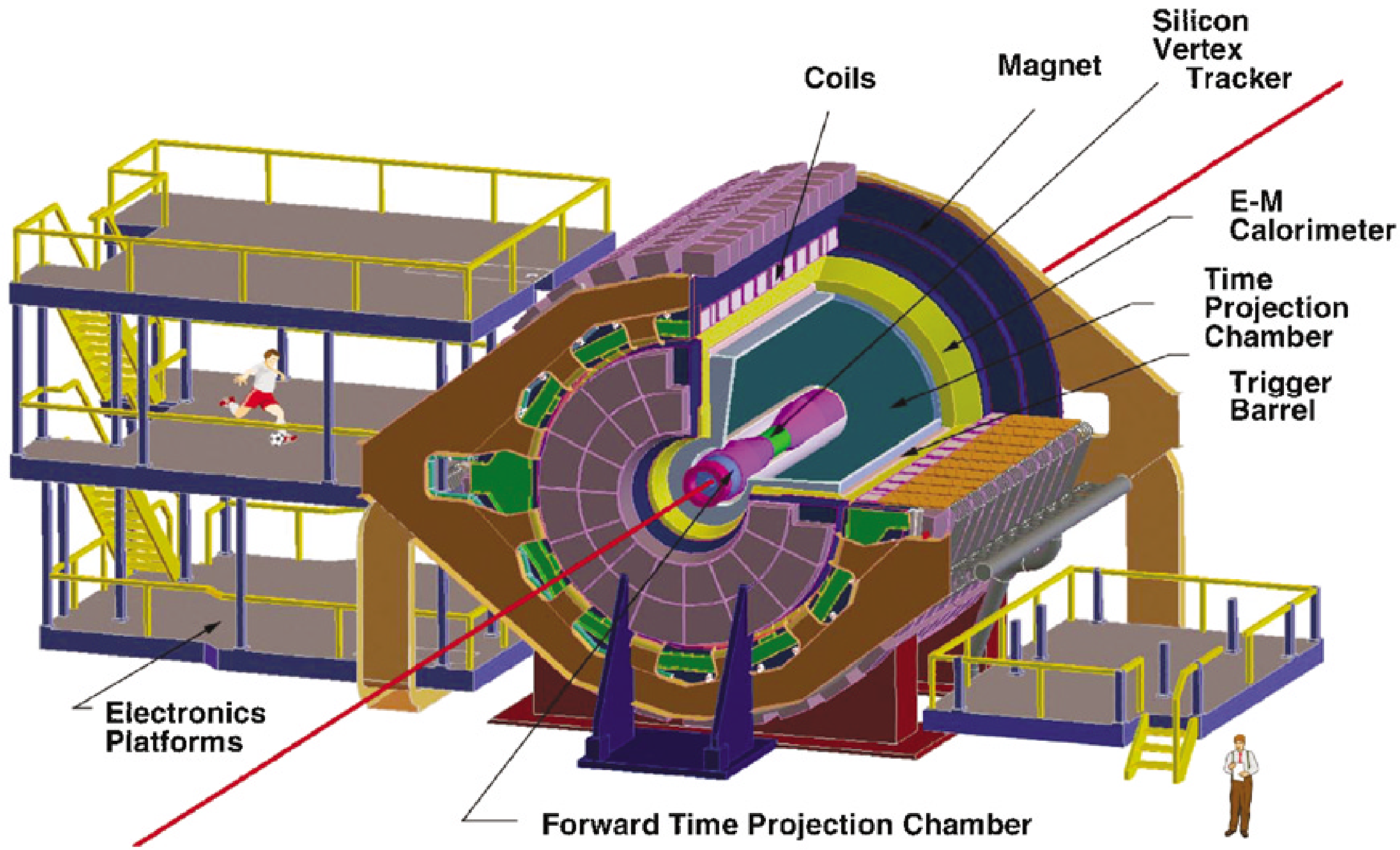

Figure 2-3: The STAR detector

A Solenoidal magnet[19] with $0.25 < |B_z| < 0.5T$ was located outside the Barrel Electro-magnetic Calorimeter (BEMC)[20] along the pole-tip. It enabled momentum measurements of charged particles. The Silicon Vertex Tracker (SVT)[21] , Central Barrel Trigger (CBT)[22] and Time of Flight (TOF)[23] were detector elements used for heavy ion collisions.

Charged particle tracking and identification were done by a large volume Time Projection Chamber (TPC)[24]. The TPC extended from 50 to 200 cm radially and was 4 m long. It had complete azimuthal symmetry ($0 < \phi \leq 2\pi$) and covered $|\eta| \leq 1.8$ where η is the pseudorapidity. 136,608 channels of front-end electronics gave the equivalent of 70 million voxels.[3]

The Barrel Electromagnetic Calorimeter (BEMC) measured the transverse energy of events and enabled triggering on high-transverse-momentum particles. Shower maximum detectors provided discrimination between single photons and photon pairs. Also, prompt charged-particles signals allowed discrimination due to pileup of TPC tracks when beam crossings fell within the drift time.

The STAR data acquisition system (DAQ)[25] took data from many detectors that had a large range of readout rates. Event sizes could be of the order 20 MB with 100 Hz maximum input rates. The trigger system had four levels. Fast detectors made up the lower level, whereas slower detectors applied more sophisticated criteria at the higher levels.

2.3.1 The Beam-Beam Counter

The Beam-beam counter (BBC)[26] consisted of two pieces of 1 cm thick scintillator located at the ends of the detector around the beam pipe at $2 < |\eta| < 5$. Scintillator light from the tiles was channeled to PMTs that connected up to 3 tiles. The BBC's were further segmented as shown in Fig. 2-4 and the region of $3.4 < |\eta| < 5$ was used to check for the minimum bias (MINB) trigger.

Charged particles that went down the beam line after the collision of two protons were incident on the BBC. A coincidence in the two counters was an indication of a

[3] A voxel is a volume element. The 2-D equivalent is a pixel.

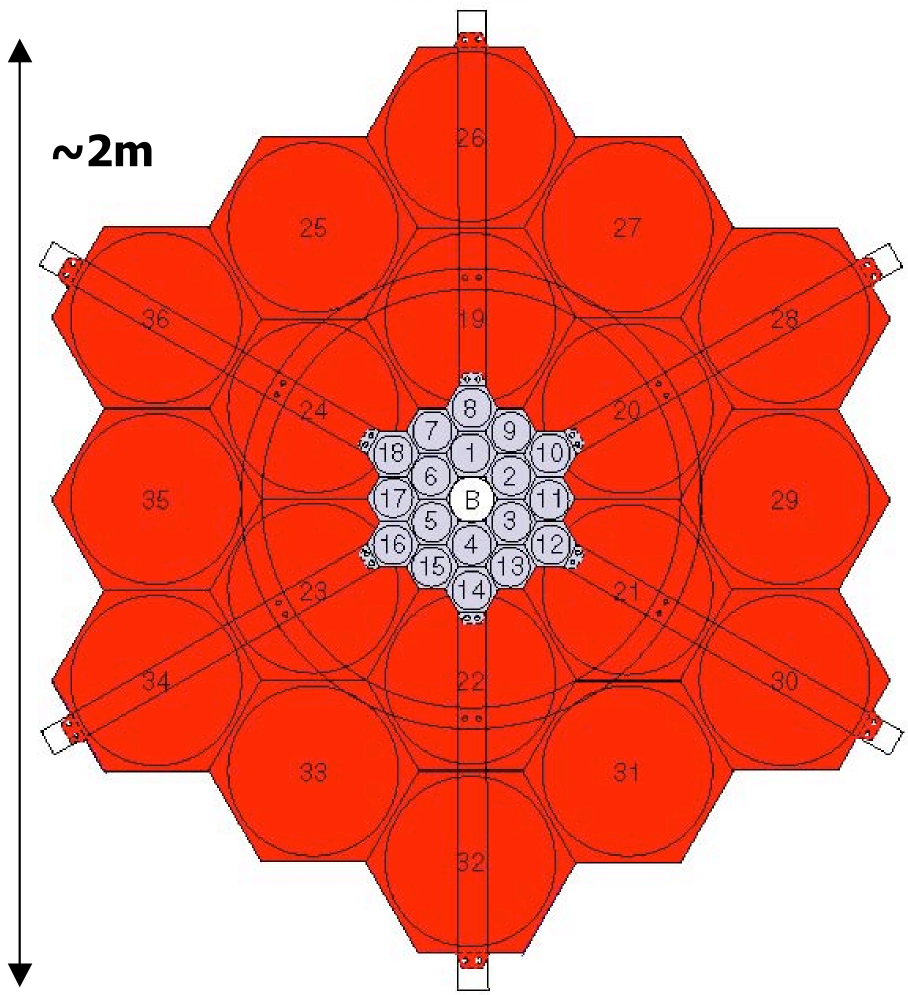

Figure 2-4: The STAR BBC Schematic Front View

collision between two protons as opposed to a collision between a proton and beam gas or background. The BBC was also used to measure the relative luminosity of the spin states and could be used to measure polarization.

2.3.2 The Scalar Boards

A 24-bit 10-MHz VME memory module[26] made up the scalar boards. The 10 MHz was due to RHIC's 107 ns bunch crossing frequency. There were 2^{24} cells with each cell having 40 bits, which allowed continuous recording up to 24 hours. Both bunch crossing information and physics information from the fast detectors (such as the BBC) and trigger were stored in the scalar boards.

The BBC and scalar boards were used to measure the relative luminosity. There were four spin states that circulated in the beam: UU, UD, DU and DD where the first letter is for one proton beam and the second letter is for the other proton beam. U (D) is for spin up (down) and means the proton spin was vertically pointing upwards (downwards) while moving around the ring and the spin was rotated to parallel (anti-parallel) to the velocity just before collision. Ideally there would have been an equal number of collisions for all four spin states. But inevitably there were different numbers of collisions for the different spin states. The relative luminosity of these states was measured by the BBC and recorded by the scalar boards.

2.3.3 The Time Projection Chamber

The Time Projection Chamber (TPC) was the main tracking detector for STAR. It identified particles through a measurement of their ionization loss (dE/dx), found their momentum, and tracked them. Its range was $|\eta| < 1.8$ in pseudorapidity and $0 < \phi < 2\pi$ in the azimuthal angle. Particle identification was possible in the range $100MeV/c < p < 1GeV/c$ in momentum, and momentum was measured in the range $100MeV/c < p < 30GeV/c$. For the jet analysis, particle identification was not used and it was assumed that any particle with a charged track was a pion. A schematic view of the STAR TPC is shown in Fig. 2-5.

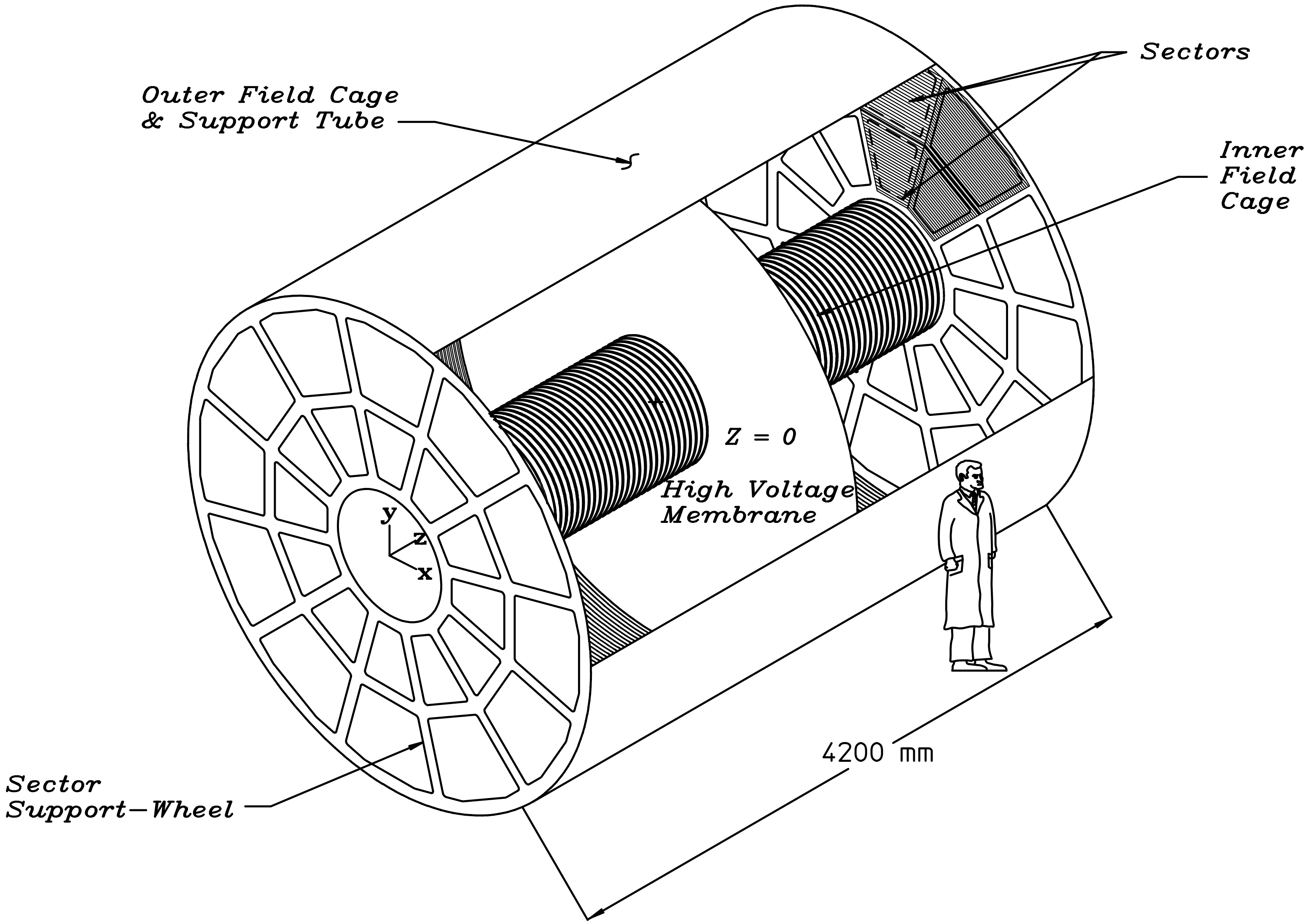

Figure 2-5: The STAR TPC

The TPC was contained within a 0.5 T solenoidal magnet. The dimensions were 4.2 m in length and 4 m in diameter. A thin conductive Central Membrane at the center of the TPC, readout end caps, and concentric field-cage cylinders created a well defined, uniform, 135 V/cm electric field. The uniform electric field allowed for sub-millimeter track reconstruction with drift paths up to 2.1 m.

The primary ionizing particle tracks were reconstructed from the freed electrons, which drifted in the electric field to readout end caps located on the ends of the chamber. The end caps were divided into 12 sectors. A diagram of a sector is shown in Fig. 2-6 and a close up view of one sub-sector is shown in Fig. 2-7.

$20\mu m$ anode wires caused the drifting electrons to avalanche, which gave an amplification of 1000-3000. A temporary image charge was induced on the pads from the positive ions formed in the avalanche. This image charge went away when the ions moved away from the anode wires. A preamplifier/shaper/waveform digitizer system measured the image charge. Several adjacent pads shared the avalanche's induced charge. This allowed a resolution of a small fraction of a pad width for the original track position.

P10 gas (10% methane, 90% argon) kept at 2 mbar above atmospheric pressure filled the TPC. This gas has the advantage of fast drift velocity with a maximum at low electric field. Drift velocity stability and insensitivity to small temperature and pressure variations were the advantages of operating at the drift velocity peak.

Gas limitations and financial constraints guided the design of the TPC. The number of and diffusion of drifting electrons determined position resolution. Finite track lengths and ionization fluctuations limited dE/dx particle identification.

A particle traveling at mid-rapidity would have been sampled by at most 45 rows of pads (see Fig. 2-6). The number of rows a particle crossed depended on its track's radius of curvature, track pseudorapidity, fiducial cuts near the sector boundaries and other aspects of the particle's path.

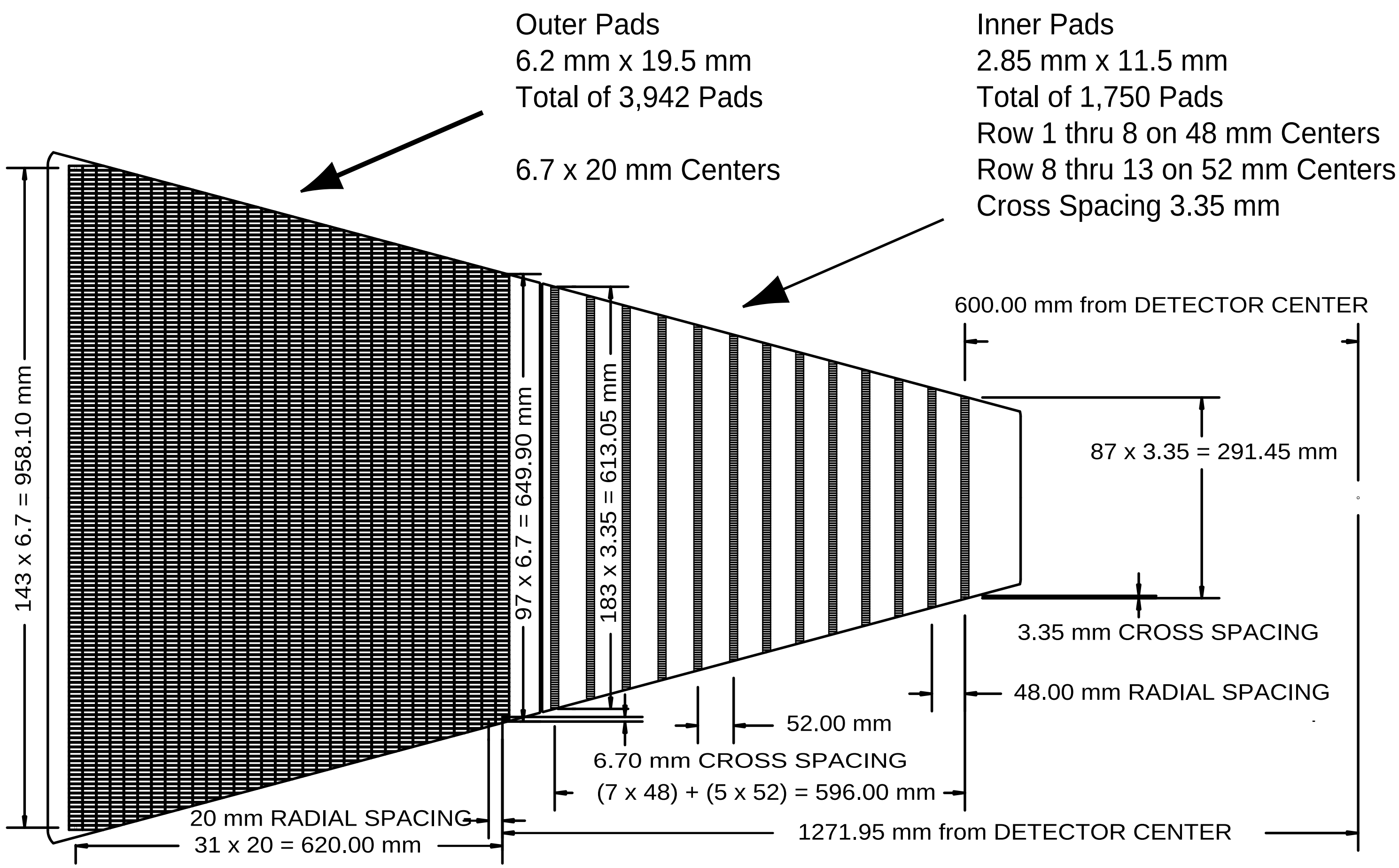

Figure 2-6: A STAR TPC readout sector.

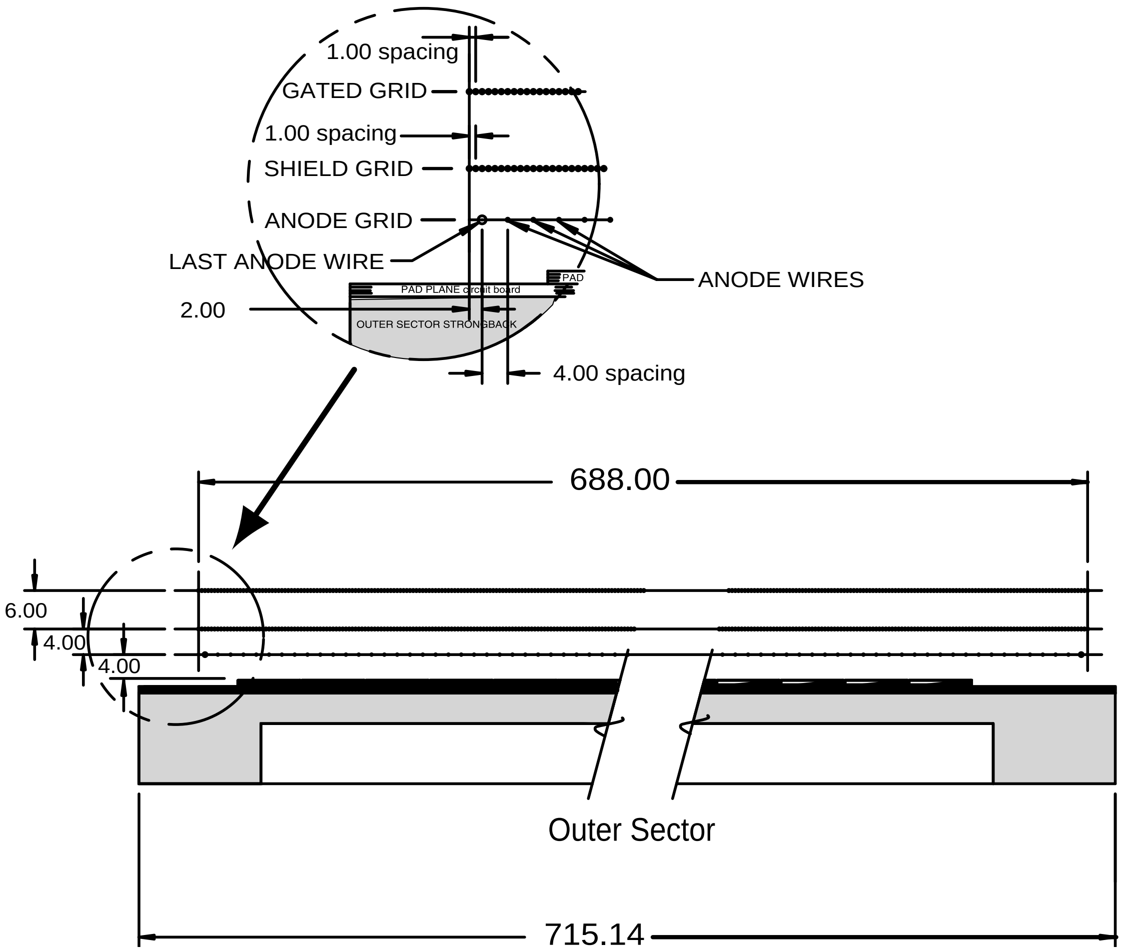

Figure 2-7: A STAR TPC readout subsector cross-section.

Primary particles that passed through the TPC were reconstructed by identifying ionization clusters along the track. Clusters were found in x,y and z independently. The z-axis was along the beam line. See Fig. 2-5 for the x and y directions. Generally, total ionization of the cluster was found by summing the energy from all the pads. If tracks were close together, their clusters overlapped. This type of cluster was found by looking for two peaks separated by a valley. The cluster was then split in two with the energy divided between the two. These clusters were only used for tracking since the uncertainty in how much energy goes into each track made particle identification difficult.

A cluster's z coordinate was found by timing how long it took the cluster to drift to the end, and using the average drift velocity. A cluster's x and y coordinates were found by fitting a Gaussian to the charge measured on the pads. Figure 2-8 gives the resolution achieved for the fit.

Half field is 0.25 T and full field is 0.5 T. The crossing angle was the angle between the particle's momentum and the direction of the pad row. The dip angle was the angle between the particle's momentum and the drift direction.

2.3.4 The Barrel Electromagnetic Calorimeter

At the time that the data for this thesis were taken, the entire BEMC had not been installed and commissioned. So only half the calorimeter ($0 < \eta < 1, 0 < \phi \leq 2\pi$) was used to find jets. The depth of the calorimeter was about 20 radiation lengths at $\eta = 0$. Over 60 m^2 had to be covered so, to keep costs low, a Pb-plastic sampling calorimeter was chosen. The BEMC was comprised of many modules, enabling it to be installed over time after the completion of the main detector components (TPC, magnet, etc.).

There was not enough space within the magnet to contain all of the photomultiplier tubes (PMT) and their necessary high voltage sources and electronics. The scintillation light was piped out of the calorimeter using wavelength shifting fibers and clear optical fibers. So the PMTs were operated outside the magnetic field.

The BEMC had a very large surface area, so it was not feasible to choose the tower

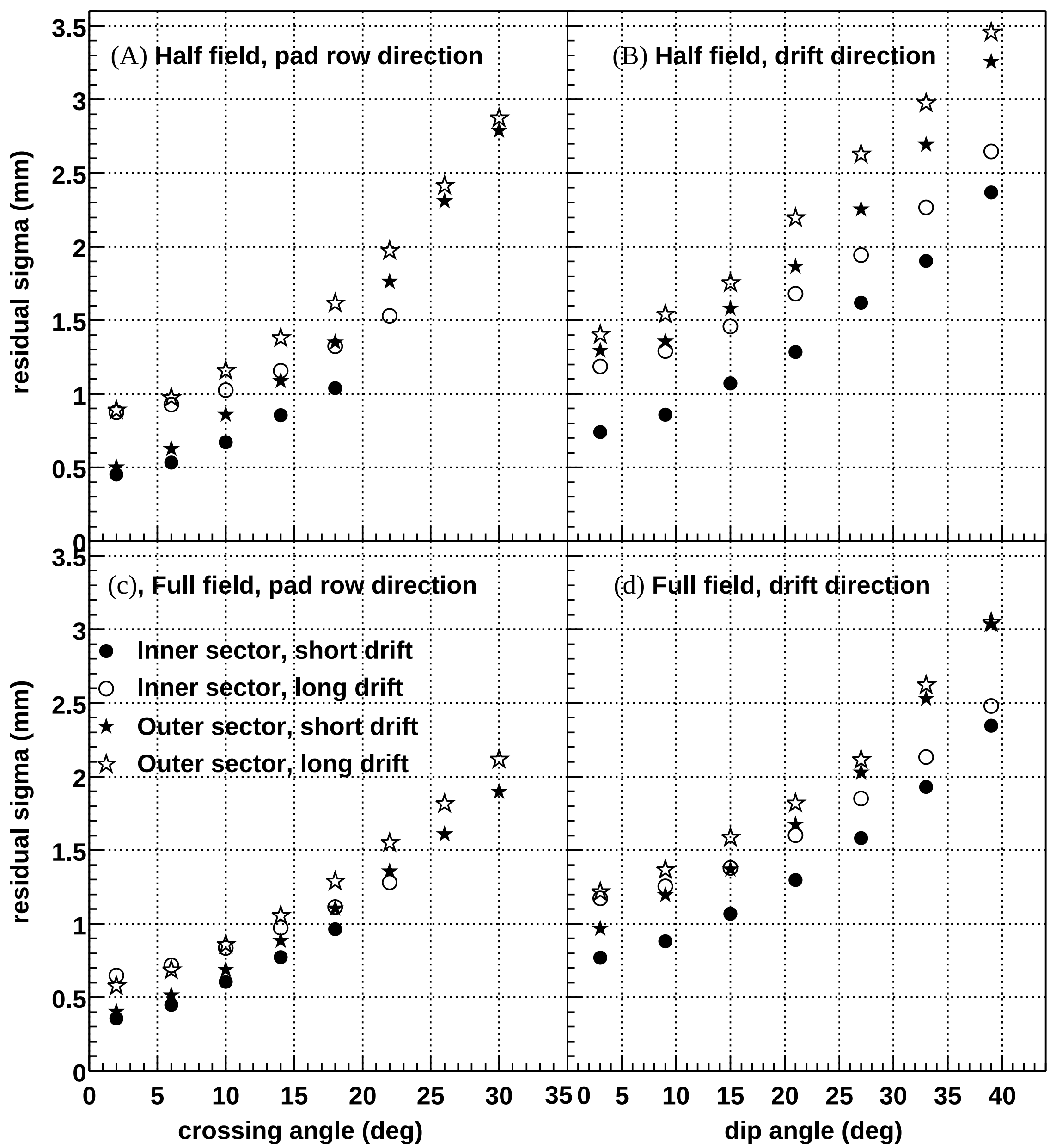

Figure 2-8: The STAR TPC Position Resolution

size based on the Molière radius[4]. But good spatial resolution was necessary in order to reconstruct pions, single photons and electron versus electron pairs. A shower max detector was incorporated into the calorimeter. The shower max detectors were two layers of gas wire pad chambers. Because there were shower max detectors, the tower sizes were chosen to be small enough to give reasonable particle occupancies for typical interesting events.

Pre-shower detectors were at the beginning of each tower. This was to help distinguish pions from single photons and electrons from hadrons. Located within 1 - 1.5 radiation lengths, most electrons showered in the pre-shower detectors, whereas most hadrons did not start showering yet. A schematic of one of the BEMC modules is shown in Fig. 2-9.

Optical Structure

The module starts with 2 layers of 6 mm-thick plastic scintillator[5] for the pre-shower followed by 19 layers of 5 mm-thick plastic scintillator[20]. Each layer of scintillator was separated by 5 mm of Pb, and was divided into 40 optically-isolated parts, as shown in Fig. 2-11. The parts were separated by removing 95% of the scintillator material and filling it in with an optically isolating epoxy. A black line painted on the remaining scintillator material between parts further reduced the amount of light traveling between parts. Edges of a scintillation layer were painted white [6] and white bond paper was placed on both sides of the scintillator layer that, in addition to having a high coefficient of friction, has diffuse reflectivity.

Light from all 21 layers comprising a tower was transferred to one PMT as shown in Fig. 2-10. A wavelength shifting fiber left each tile and joined with the other fibers in a multi-fiber optical connector. Optical fibers then carried the light outside the magnet to boxes mounted outside the detector that contained PMTs.

[4]The Molière radius is a measure of the transverse size of an electron's shower.
[5]Kuraray SCSN81
[6]Bicron BC260 reflective paint

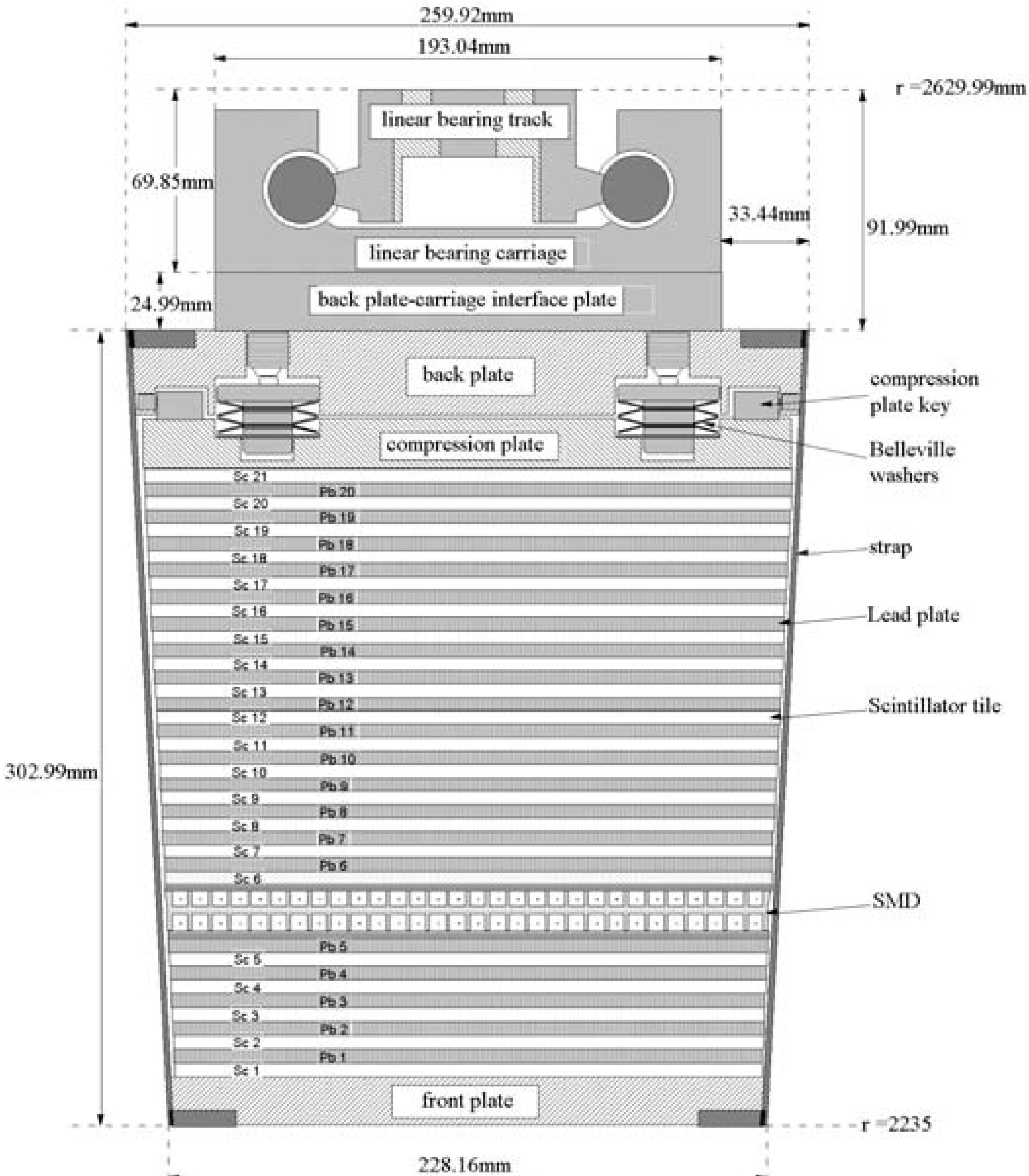

Figure 2-9: A STAR BEMC module

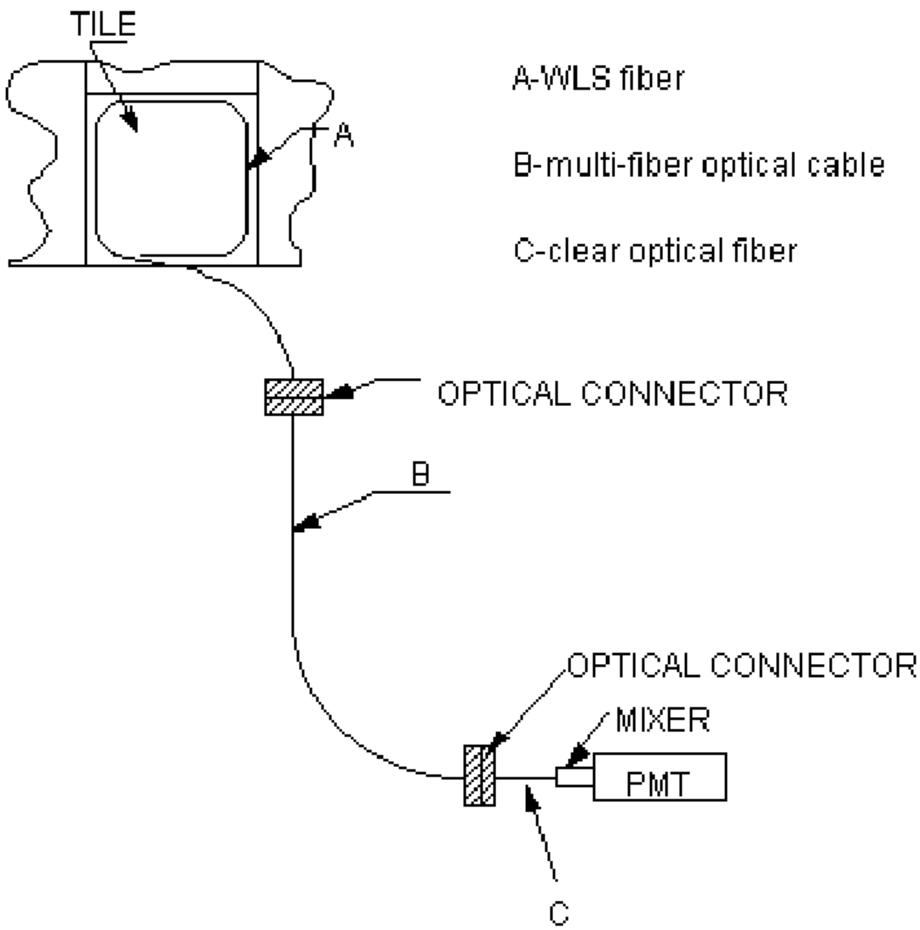

Figure 2-10: The STAR BEMC Optical System

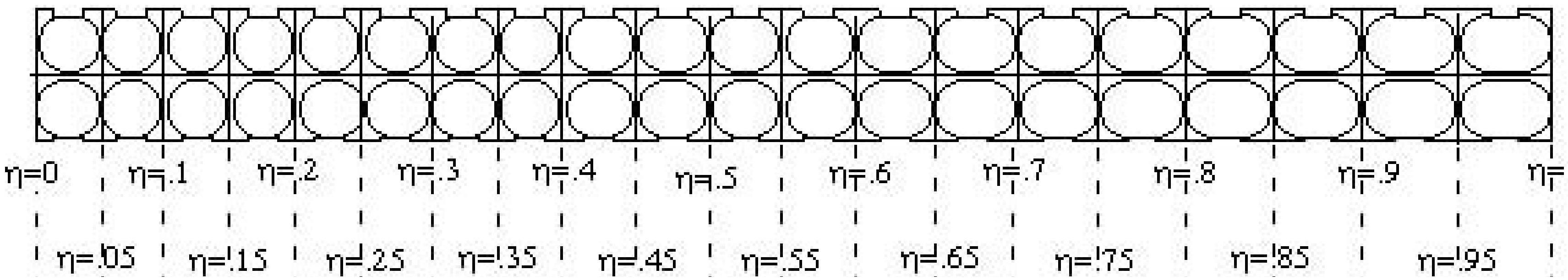

Figure 2-11: The STAR BEMC Scintillator tile division

Shower Max Detector

The towers covered an area of $\Delta\eta \times \Delta\phi = 0.05 \times 0.05$, which translated to a physical area of $10 \times 10cm^2$ at $\eta = 0$. This was larger than the typical electromagnetic shower size. Since pions needed better resolution than this to be reconstructed, a shower max detector was located about 5.6 radiation lengths inside the detector.[7]

The shower max detector was a wire proportional counter that used gas amplification and strip readout. A cross-sectional view is shown in Fig. 2-12. $50\mu m$ gold-plated tungsten wires ran down the center of the extrusion channels. Each strip covered 30 wires. The strip size was $\Delta\eta \times \Delta\phi = 0.0064 \times 0.1 \approx 1.5cm$[8] $\times 23cm$ (which is the strip length). There was another set of strips that was parallel to the aluminum extrusions and parallel to the wire channel.

Pre-shower Detector

The first two strips of the detector served as a pre-shower detector. Two fibers left the strips, one going to combine with the other 19 strips and the other going to a multi-anode PMT pixel. Light in each fiber was reduced 20% by using two fibers instead of one. This was compensated for by making the scintillator size 20% longer, or 6 mm instead of 5 mm.

2.3.5 The Zero-Degree Calorimeter

The Zero-Degree Calorimeter (ZDC), which had two pieces located along the beam line at $\theta < 2$ mrad[14] on opposite sides of the interaction region, was used for triggering and measuring relative luminosities[27]. Each piece was a hadron calorimeter with three modules. The modules contained a series of tungsten plates alternating with wavelength shifting fibers layers[22]. Space constraints restricted the ZDC's width to 10 cm.

[7] The depth of the shower max detector varied with η, with its location being 4.6 radiation lengths inside the detector at $\eta = 0$ and 7.1 radiation lengths at $\eta = 1$.

[8] at low η

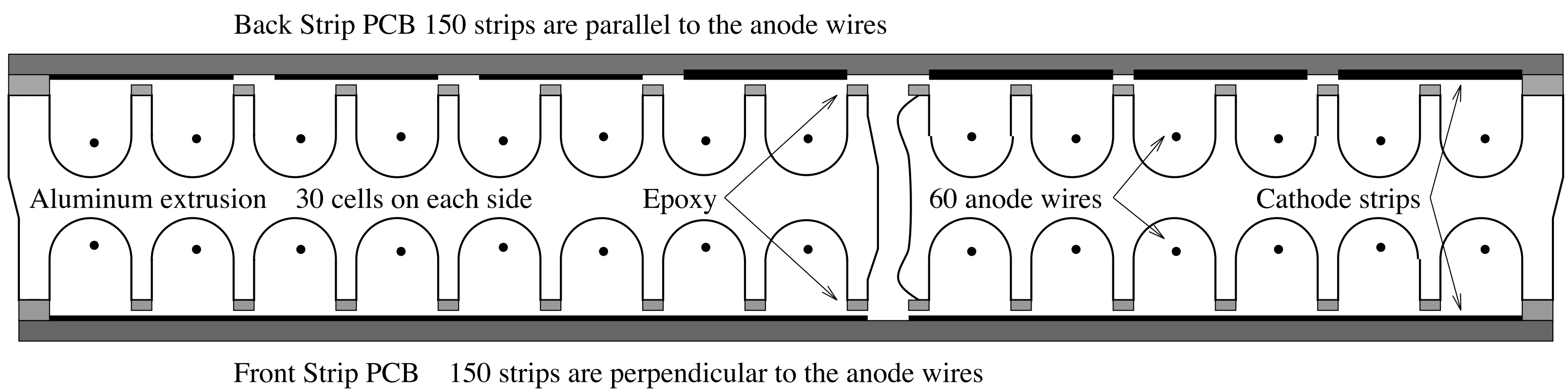

Figure 2-12: The STAR BEMC Shower Max Detector cross-section

Chapter 3

Data Selection

3.1 Jet Definition

When protons collided at RHIC, the interaction was between a gluon (or quark) in one proton and a gluon (or quark) in the other proton. Gluons and quarks do not exist as free particles, and shortly after the collision the quarks and gluons hadronized into many other particles. These particles traveled in roughly the same direction and could be clustered together or fit into a cone. This collection of particles was called a jet.

Jets were defined using a mid-point Cone algorithm[28] with starting energy seeds of 0.5 GeV. A radius of 0.4, where the radius is defined as $\sqrt{(\Delta\eta)^2 + (\Delta\phi)^2}$ where η is the pseudorapidity and ϕ is the azimuthal angle, was chosen because the completely installed part of the BEMC extended from $0 < \eta < 1$.

Jets were formed by clustering TPC tracks and BEMC tower energies. BEMC tower energies had the charged hadron contribution subtracted to prevent double counting, as this energy was already taken into account in the tracks, and were required to have a minimum transverse energy of 0.2 GeV/c. TPC tracks were required to point to the primary vertex and needed a minimum transverse momentum of 0.2 GeV/c. The jets formed in this way are called detector jets.

In converting from transverse energy to transverse momentum, the particle mass of charged tracks was taken as that of the pion and for BEMC towers a photon mass was assumed. A cut on reconstructed jet momentum of 5 GeV/c was made.

For some Monte-Carlo simulations, jets were formed from the stable particles created when the partons involved in the collision hadronized. These jets are called particle jets. Particle jets were defined using the same algorithm and starting energy seeds as the detector jets.

3.2 Run Selection

At STAR, data were divided into runs. A run was a short period of time, anywhere from two minutes to two hours, where data were being recorded. When two protons collide at a center of mass collision energy of $\sqrt{s} = 200$ GeV, the interaction is usually between quarks and/or gluons in the protons. The spectator particles continue down the beam line only slightly deflected and hit the BBC. A coincidence of BBC hits is considered an event. Events within a run had identical conditions. Magnetic field strength and which detectors were turned on were just two of the things that were constant over a run. Selecting runs for the analysis was a way of selecting data that met certain criteria.

For the asymmetry measurement, several people reviewed the runs and came up with a common list of runs to be used in analyzing the data. For the cross-section a slightly different run list was used. The asymmetry run list contained runs that had large blocks of the BEMC towers with bad status. These runs were excluded from the cross-section run list by excluding runs that had more than 3.3% of the BEMC towers marked as bad. The reason for excluding these runs was that they would have greatly increased the systematic uncertainty due to the BEMC tower status changing from run to run without greatly decreasing the statistical uncertainty.

Some runs were taken that only included MINB[1] events. None of these runs was on the asymmetry list as the asymmetry was not calculated for MINB. Some of these runs were added into the cross-section run list. From the initial list of MINB runs, runs that were found bad by other reviewers were excluded. Then any runs where

[1] MINB - minimum bias trigger, which is defined later.

the BEMC was malfunctioning, the BEMC data were not recorded, there was high beam background, and/or there were trigger rate problems were excluded. Finally, runs that had the magnetic field at full value were selected as the run list for the MINB data.

3.3 Event Selection

The center of mass collision energy for the data presented here, $\sqrt{s} = 200$ GeV, was sufficient to allow for a hard interaction between two partons (quark-quark, quark-gluon, or gluon-gluon). The spectator particles (the quarks and gluons that did not collide) traveled down the beam line and were incident on the BBC, which is described previously. In this way, the BBC served as a minimum bias trigger (MINB), sampling $\sim 87\%$ (26.1 ± 2.0 mb[29]) of the non-singly diffractive cross-section.

The majority of MINB events had jets whose transverse momentum was less than 15 GeV/c. In order to record jets with higher transverse momentum, four additional triggers were used. Barrel High Tower (BHT) required, in addition to the MINB trigger, that one of the BEMC towers measuring $\Delta\eta \times \Delta\phi = 0.05 \times 0.05$ had transverse energy $E_T > 2.9$ GeV (BHT1) or 3.7 GeV (BHT2). The Barrel Jet Patch (BJP) trigger required, in addition to the MINB trigger, patches roughly the size of a jet ($\Delta\eta \times \Delta\phi = 1 \times 1$) had $E_T > 4.6$ GeV (BJP1) or 7.9 GeV (BJP2).

Not all events that satisfied the above triggers were recorded. For each run, it was decided what percentage of each trigger's events would be recorded. These percentages were set in general to record more BJP2 and BJP1 events than MINB.

3.4 BEMC status

Figure 3-1 is a 2-D histogram of the BEMC tower status. The x-axis (run reference) refers to the runs in the cross-section run list. There were 2400 BEMC towers used for 2005 and the y-axis, labeled tower id, refers to the BEMC tower. For each tower in a run, if the tower had a status of good then the histogram was filled with 0 (white) at the location of the run reference and tower id; otherwise it was filled with 1 (black). The plot shows that some towers were not good for all runs and that the variation from run to run was small.

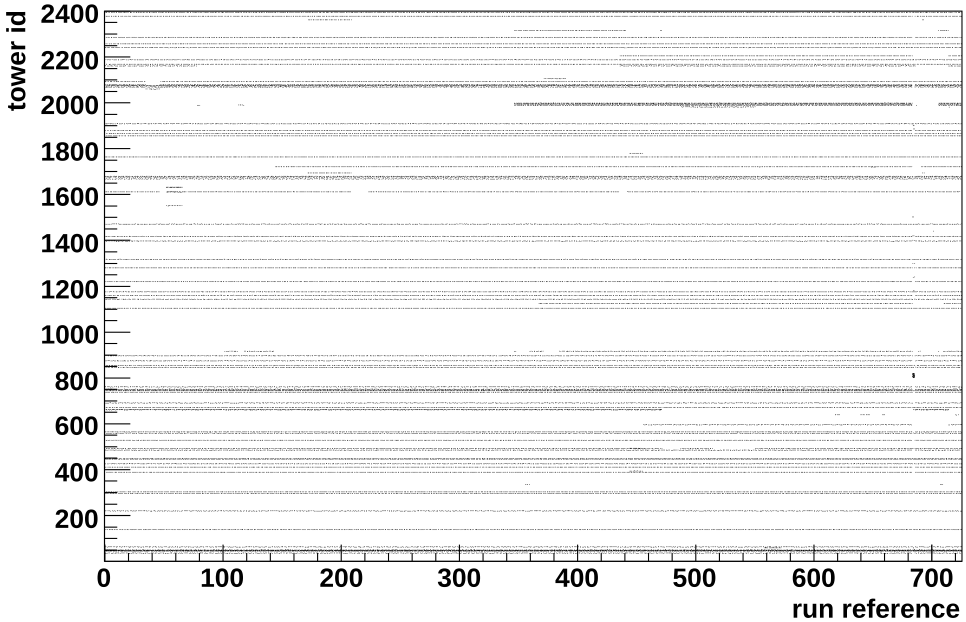

Figure 3-1: Tower status for the west half of BEMC

Figure 3-2 is a graph of the fraction of towers that were not good for a run. Only the west half of the BEMC (towers 1-2400) was considered, since that is the only part used in this analysis. The difference in the runs is small, varying from 2.7% to 3.2%. The runs spanning from run reference=0 to approximately run reference=680 in Fig. 3-2 are for those used for the BHT1, BHT2, BJP1 and BJP2 triggers. Starting at approximately run reference=680 are the MINB runs. So this graph increases in time as run reference increases, with a break at approximately run reference=680 where the timeline restarts. That is the reason the runs have a lower percentage starting again at run reference=680.

For Monte-Carlo studies, an average table was made. Figure 3-3 shows the average table's BEMC tower status. For the average status table, 2.79% of the towers are marked as bad.

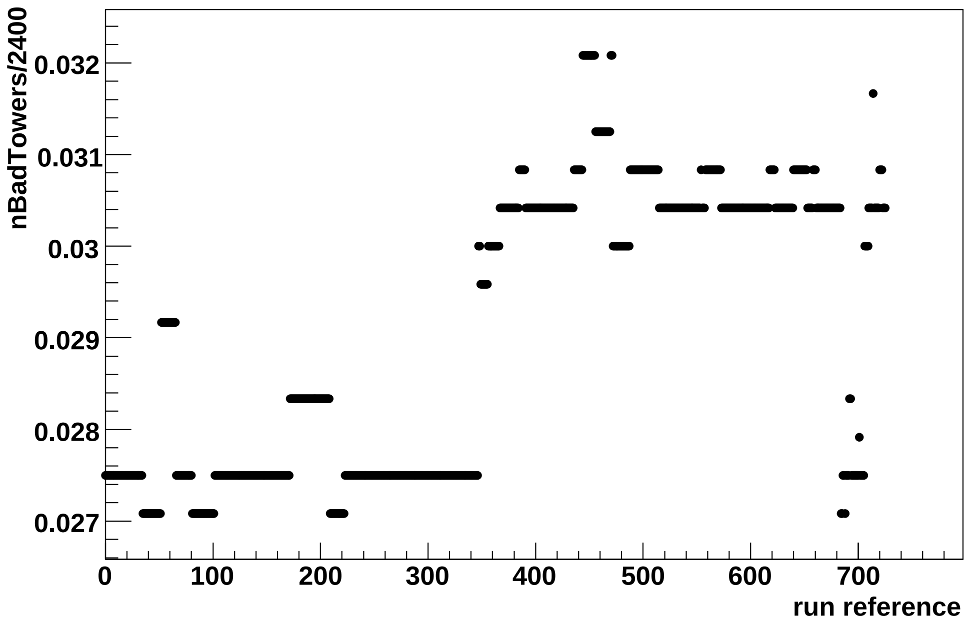

Figure 3-2: Fraction of BEMC towers which were not marked as good

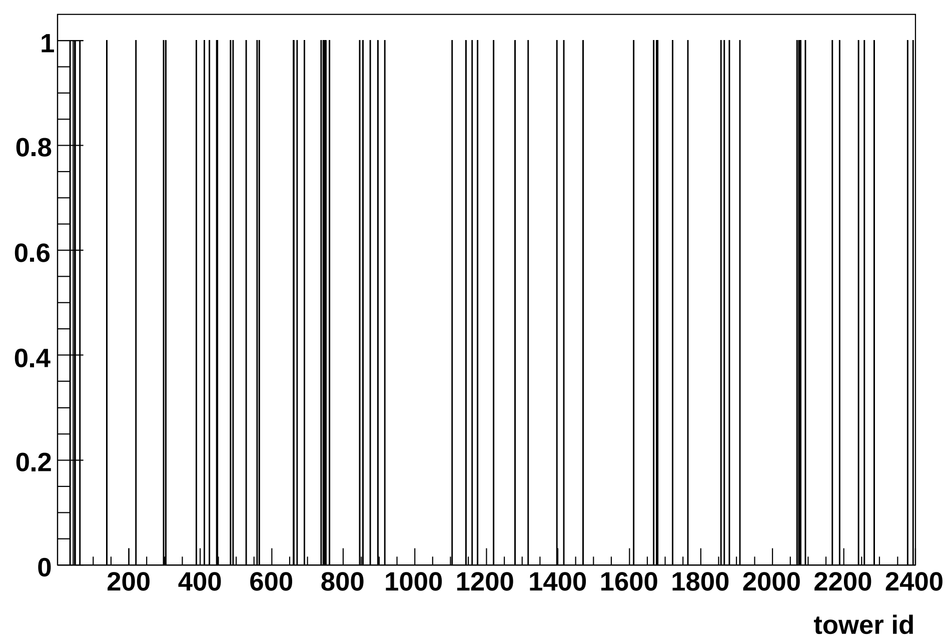

Figure 3-3: Average BEMC tower status which was used for Monte-Carlo calculations

3.5 Hot Tower Elimination

Sometimes a BEMC tower had problems that caused it to record an abnormally high transverse energy and consequently satisfied the trigger conditions more often than other towers. These towers were excluded from the analysis to prevent them from biasing the results. A search for these "hot" towers was made for each run in the run list.

For each run the amount of transverse energy, how often a tower had the maximum transverse energy, and how often a tower had transverse energy above the pedestal, were filled in histograms. Figure 3-4 shows an example of what was found for a hot tower.

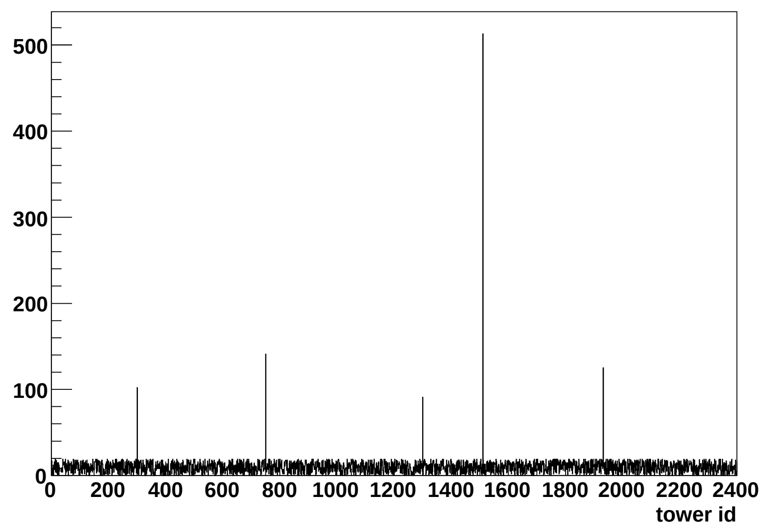

Figure 3-4: A Simulation Histogram of how often a BEMC tower had energy above the pedestal

The histograms were then checked to see if any towers stood out from the others. In Fig. 3-4 BEMC tower 1500 is seen to be hot because it had energy above the pedestal more often than that of the next most active tower. The criterion for throwing out a tower was if for one of these histograms it had 10 times or more counts than for the next largest tower. Towers that were determined to be hot were marked as bad and were not used in the analysis.

3.6 Data Cuts

3.6.1 Trigger Threshold

During data taking trigger thresholds were set based on tower (patch) ADC values. Ideally, for the same amount of transverse energy striking a tower (patch) the same ADC value would result. But variations between towers meant that different amounts of transverse energy were needed to cause the tower (patch) to have the minimum ADC to satisfy the trigger. This was due to the tower gains varying between towers. If this had not been corrected, biases would have been introduced into the cross-section. Since the cross-section is a steeply falling function, any deviation in trigger threshold could have caused changes in the jet yield that were difficult to understand.

To get around this problem a cut was placed on events, based on the transverse energy of the triggered tower (patch). It was done so that all trigger towers (patches) had at least the minimum transverse energy to fire any of the towers (patches); otherwise the event was discarded for that trigger. This cut was applied only to the cross-section data and not to the asymmetry data.

The appropriate offline software trigger threshold to apply was determined by the following procedure. Two histograms were made. If an event fired the trigger, both histograms were filled with the transverse energy of the tower (patch) that fired the trigger. Otherwise, only one histogram was filled with the transverse energy of the tower (patch) with the highest transverse energy. Then the histogram with the triggered events was divided by the histogram with all events. The resulting histogram gave the turn-on curve for the various triggers. Figure 3-5 shows the turn-on curve for the four triggers. Monte-Carlo simulations were used since, if the event did not fire a trigger, it was not recorded. By using Monte-Carlo simulations, events that did not fire the trigger were preserved.

A cut of $\frac{\text{nTriggerEvents}}{\text{nEvents}} \geq 0.99$ was placed on the minimum transverse energy. The values are 4.75 GeV/c (BHT1), 5.75 GeV/c (BHT2), 6.25 GeV/c (BJP1) and 9.00 GeV/c (BJP2). So the BEMC tower (patch) which fired the trigger must have at least 4.75 GeV/c (6.25 GeV/c) in order for it to be kept as a BHT1 (BJP1) event.

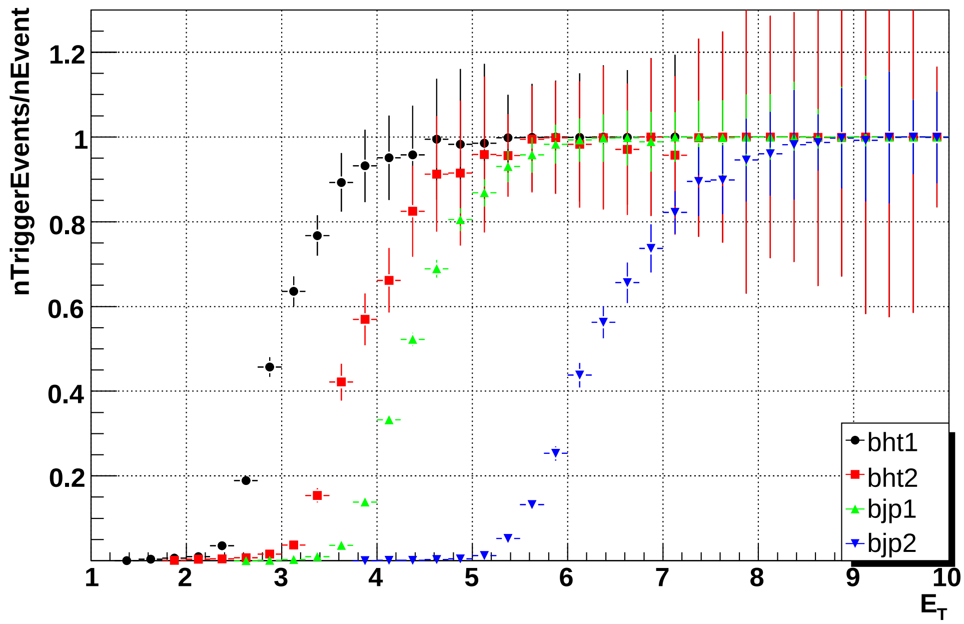

Figure 3-5: Turn-On Curve

Placing this cut resulted in a drastic decrease in statistics. Figure 3-6 shows the jet yield sorted by p_T spectrum without the trigger threshold cut and Fig. 3-7 shows the jet yield after the trigger threshold cut. Although the higher transverse momentum jets were not affected by this cut, the lower transverse momentum jets were reduced by a factor of about 10.

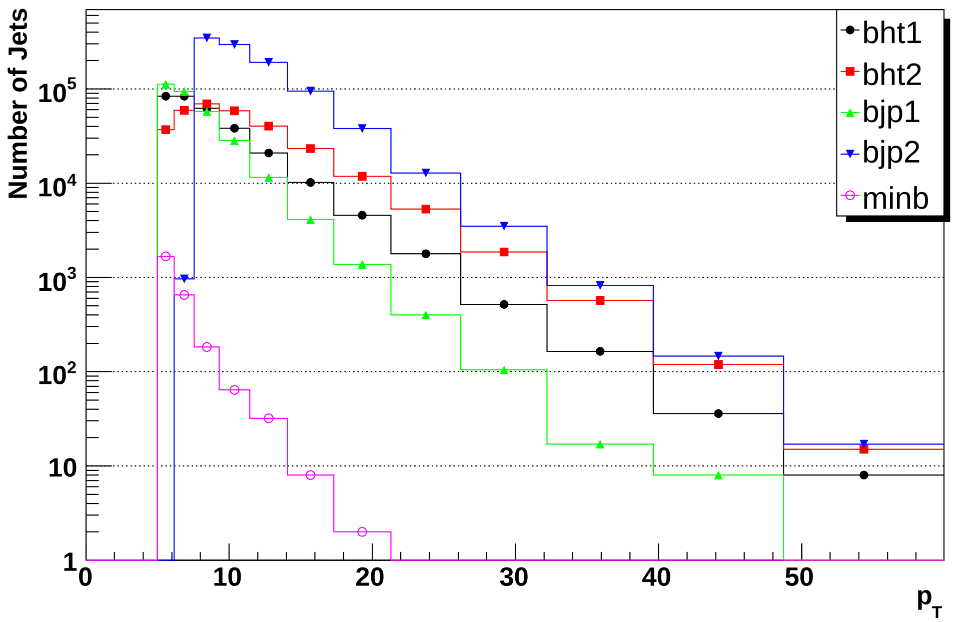

Figure 3-6: Jet Yield without the threshold cut

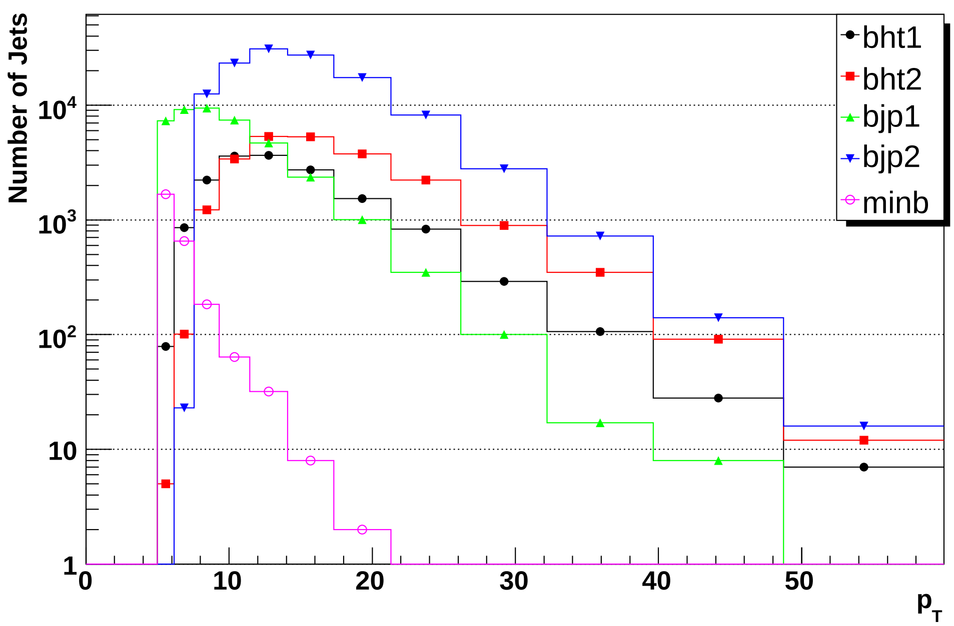

Figure 3-7: Jet Yield with the threshold cut

3.6.2 Geometry and Software Trigger

Multiple jets could occur within an event. In order to make sure that the jets used in the analysis were the jets that satisfied the trigger, jets were required to contain the BEMC tower that satisfied the trigger for BHT1 and BHT2 triggers. The jets were required to point in the direction of the patch for BJP1 and BJP2 triggers. This was the geometry cut.

Also, to make sure that the trigger thresholds were applied correctly, BEMC towers and patches were checked after being recorded that they satisfied the trigger. If they did not they were discarded. No cuts were placed on the MINB jets.

3.6.3 Neutral Energy

Sometimes the protons collided with beam line gas or parts of the detector. This created showers of particles that could have hit the detector and been recorded as background jets. In general, these background jets did not originate from the center of the detector. One way of eliminating background jets was to look at how much energy the jet deposited in the BEMC compared to the total jet energy. A jet that deposited most of its energy in the TPC or BEMC was probably coming from background. The neutral energy was defined as the fraction of the jet's energy deposited in the BEMC compared to the total jet energy. Or

$$R = \frac{\text{Jet Energy deposited in BEMC}}{\text{Jet Energy}}.$$

Particles passing through the detector left charged tracks in the TPC and deposited energy in the BEMC. Each jet contained a finite number of tracks and towers. The average number of tracks and towers in a jet should have been constant from one run to the next if there was no background. Varying amounts of background in a run affected this average, as background jets were not expected to be similar in terms of the number of towers and the number of tracks.

For each run the average number of tracks and the average number of towers were found. A constant line was fit to these average numbers. How good of a fit this yielded gave an idea of how much background was in the runs. A fit with $\chi^2/NDF \approx 1$, where NDF is the number of degrees of freedom, meant that there was no observable background in the run from this method. However, a large χ^2/NDF meant that the average was varying a lot from run to run and thus background was not being excluded as much. For the asymmetry measurement a cut of $0.1 < R < 0.8$ was imposed. For the cross-section, a more conservative cut $0.2 < R < 0.8$ was used.

3.6.4 BEMC Pseudorapidity

The jets had a maximum size of 0.4 in pseudorapidity. In order that the majority of the jet was contained within the BEMC, which extended from $0 < \eta < 1$ when the data were taken, a cut was placed on the jets based on where they hit the BEMC. The cut was $0.2 < \eta_{BEMC} < 0.8$ where η_{BEMC} is the pseudorapidity of the BEMC where the jet hit it and not the pseudorapidity of the jet. The jet energy for the jets hitting the edge of the BEMC was still systematically low, but the amount was negligible for the asymmetry analysis and was accounted for via simulations for the cross-section.

3.6.5 Bunch Crossing

The proton beam was filled at RHIC in bunches of protons. There were up to 120 bunches of protons and 120 bunch crossings in a run. A bunch crossing was when two bunches of protons collided at the STAR interaction point. The proton spin alignment was determined from knowing which bunch it was in. For four of the 120 bunch crossings there were some problems with events being recorded in the wrong bunch crossings. So these four bunch crossings were discarded for the asymmetry measurement. For the cross-section the spin alignment did not matter so these four bunch crossings were included.

3.6.6 Vertex Location

A cut requiring the event vertex to be within 60 cm of the TPC center was applied to the cross-section to obtain uniform tracking efficiency. For the asymmetry measurement the cut was applied not through the vertex location but through the BBC timing bin, which is equivalent to the same vertex cut. Figure 3-8 is a 2-D histogram of z-vertex and BBC time bin for approximately two million events. It shows the relationship

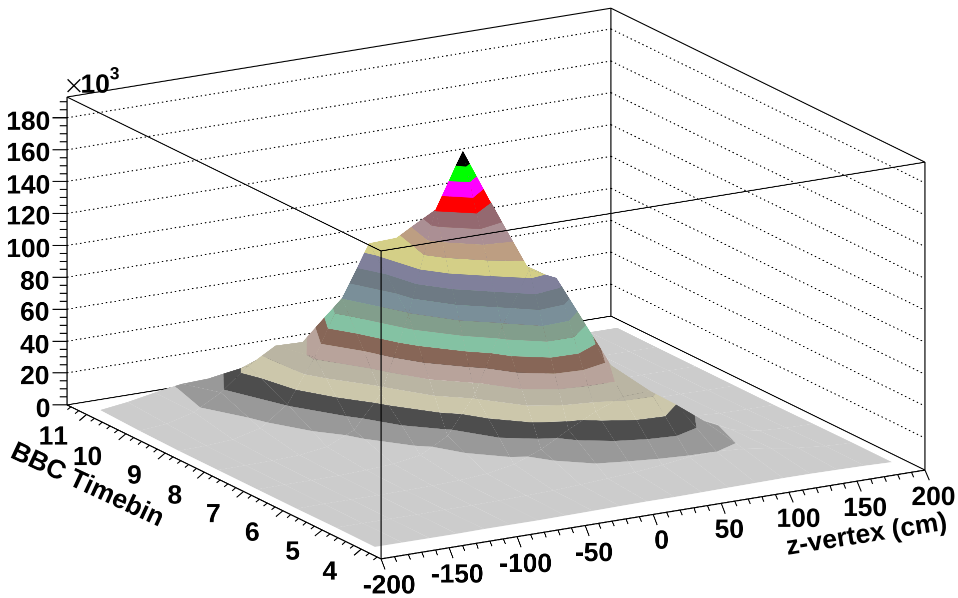

Figure 3-8: Relation between z-vertex and BBC time bin

between the z-vertex and the BBC time bin where z-vertex is the distance along the beam line from the TPC center.

The BBC had two pieces located on each side of the detector. One way of finding the location of the collision of the protons within the detector is to look at the timing difference between the spectator partons hitting the east BBC versus the west BBC. The difference in timing is called the BBC time bin. For the asymmetry the cut that the event had to be in time bin 7,8 or 9 was made. The time bins record a difference in time between the proton remnants hitting the east and west BBC. The time differences for time bins 7,8 and 9 are $(-\frac{2}{3} \pm \frac{1}{3})$ ns, $(0 \pm \frac{1}{3})$ ns, and $(\frac{2}{3} \pm \frac{1}{3})$ ns respectively.

3.6.7 Jet Transverse Momentum

A cut on BJP2 jets was made such that they had $p_T > 7.6$ GeV/c. When looking at the Monte-Carlo Simulation for the two lowest transverse momentum bins, the simulation predicted more jets for the lowest transverse energy bin than for the next transverse momentum bin. This was not seen in data. A cut was made on the trigger jets requiring their patch energy to be at least 9 GeV/c, so it was expected that the number of jets would increase until the 9 GeV/c cut at which point the number of jets would then decrease. So the first two transverse momentum bins ($p_T < 7.6$GeV/c) were removed.

THIS PAGE INTENTIONALLY LEFT BLANK

Chapter 4

The Longitudinal Double Spin Asymmetry

4.1 Calculation Method

The double spin asymmetry (A_{LL}) is defined as

$$A_{LL} = \frac{\sigma^+ - \sigma^-}{\sigma^+ + \sigma^-}$$

where σ^+ (σ^-) is the cross-section for proton-proton collisions where the product of the helicities[1] is +1 (-1). After canceling quantities that are common to both σ^+ and σ^-, the formula is simplified to

$$A_{LL} = \frac{N^+R - N^-}{P(N^+R + N^-)},$$

where N^+ (N^-) is the number of jets for a proton-proton collision where the helicities are the same (opposite), P is the product of the beam polarizations, and R is the relative luminosity of the two spin configurations.

The proton beams were not 100% polarized. This did not affect the sum of the jets, but it did affect the difference. So the difference was divided by the polarization

[1] A particle has +1 (-1) helicity if the spin and velocity are parallel (anti-parallel).

of the beams to account for this.

The polarization and relative luminosity were both changing over time, so A_{LL} was measured for the various runs[2] and the values were combined using a weighted mean. The weighted mean of A_{LL} over these various runs was

$$A_{LL} = \frac{\sum_{run} \frac{N^+_{run} R_{run} - N^-_{run}}{P_{run}(N^+_{run} R_{run} + N^-_{run})} \frac{1}{\sigma^2_{run}}}{\sum_{run} \frac{1}{\sigma^2_{run}}},$$

where σ_{run} was the uncertainty on the asymmetry for the run.

$$\sigma^2_{run} = \left(\frac{\partial A_{LL}}{\partial N^+}\right)^2 \sigma^2_{N^+} + \left(\frac{\partial A_{LL}}{\partial N^-}\right)^2 \sigma^2_{N^-} + \left(\frac{\partial A_{LL}}{\partial P}\right)^2 \sigma^2_P + \left(\frac{\partial A_{LL}}{\partial R}\right)^2 \sigma^2_R.$$

This was simplified by making a few assumptions. The first assumption was that the uncertainties on the polarization and the relative luminosity were much smaller than the statistical uncertainties and thus could be ignored. These uncertainties were calculated and were indeed much smaller than the statistical uncertainty. Next, Poisson statistics were assumed.

$$\begin{aligned}
\sigma^2_{run} &= \left(\frac{\partial A_{LL}}{\partial N^+}\right)^2 N^+ + \left(\frac{\partial A_{LL}}{\partial N^-}\right)^2 N^-, \\
\frac{\partial A_{LL}}{\partial N^+} &= \frac{(N^+R + N^-)(PR) - (N^+R - N^-)(PR)}{P^2(N^+R + N^-)^2}, \\
\frac{\partial A_{LL}}{\partial N^-} &= \frac{(N^+R + N^-)(-P) - (N^+R - N^-)(P)}{P^2(N^+R + N^-)^2}.
\end{aligned}$$

The next assumption was that $A_{LL} \ll 1$. The asymmetry was measured in 2004 and was found to be much less than one. This meant that $N^+R - N^- \ll N^+R + N^-$.

$$\begin{aligned}
\frac{\partial A_{LL}}{\partial N^+} &= \frac{R(N^+R + N^-)}{P(N^+R + N^-)^2} = \frac{R}{P(N^+R + N^-)}, \\
\frac{\partial A_{LL}}{\partial N^-} &= \frac{(N^+R + N^-)(-1)}{P(N^+R + N^-)^2} = \frac{-1}{P(N^+R + N^-)}, \\
\sigma^2_{run} &= \left(\frac{R}{P(N^+R + N^-)}\right)^2 N^+ + \left(\frac{-1}{P(N^+R + N^-)}\right)^2 N^-,
\end{aligned}$$

[2] A run is a period of time lasting up to two hours during which the beam and detector conditions remain constant.

$$= \frac{N^+R^2 + N^-}{P^2(N^+R + N^-)^2}.$$

Then the assumption that $R^2 \approx R$ was made. For 2005, most relative luminosities varied by $0.9 < R < 1.1$.

$$\begin{aligned}
\sigma^2_{run} &= \frac{N^+R + N^-}{P^2(N^+R + N^-)^2} = \frac{1}{P^2(N^+R + N^-)}, \\
A_{LL} &= \frac{\sum_{run} \frac{N^+_{run}R_{run} - N^-_{run}}{P_{run}(N^+_{run}R_{run} + N^-_{run})} \frac{1}{\sigma^2_{run}}}{\sum_{run} \frac{1}{\sigma^2_{run}}}, \\
&= \frac{\sum_{run} \frac{N^+_{run}R_{run} - N^-_{run}}{P_{run}(N^+_{run}R_{run} + N^-_{run})} P^2_{run}(N^+_{run}R_{run} + N^-_{run})}{\sum_{run} P^2_{run}(N^+_{run}R_{run} + N^-_{run})}.
\end{aligned}$$

The expression used to calculate A_{LL} is as follows.

$$A_{LL} = \frac{\sum_{run} P_{run}(N^+_{run}R_{run} - N^-_{run})}{\sum_{run} P^2_{run}(N^+_{run}R_{run} + N^-_{run})}.$$

4.2 Uncertainty Calculation

Poisson statistics were assumed in calculating this value and once again it was assumed that the uncertainties on the polarization and relative luminosity were insignificant compared to the uncertainty on the number of jets.

$$\begin{aligned}
A_{LL} &= \frac{\sum_{run} P_{run}(N^+_{run}R_{run} - N^-_{run})}{\sum_{run} P^2_{run}(N^+_{run}R_{run} + N^-_{run})}, \\
\frac{\sigma^2_{A_{LL}}}{A^2_{LL}} &= \sum_{run} \left[\left(\frac{\partial A_{LL}}{\partial N^+_{run}} \right)^2 \sigma^2_{N^+_{run}} + \left(\frac{\partial A_{LL}}{\partial N^-_{run}} \right)^2 \sigma^2_{N^-_{run}} \right], \\
&= \sum_{run} \left[\left(\frac{\partial A_{LL}}{\partial N^+_{run}} \right)^2 N^+_{run} + \left(\frac{\partial A_{LL}}{\partial N^-_{run}} \right)^2 N^-_{run} \right], \\
\frac{\partial A_{LL}}{\partial N^+_{run'}} &= \frac{P_{run'}R_{run'}(1 - A_{LL}P_{run'})}{\sum_{run} P^2_{run}(N^+_{run}R_{run} + N^-_{run})}, \\
\frac{\partial A_{LL}}{\partial N^-_{run'}} &= \frac{-P_{run'}(1 + A_{LL}P_{run'})}{\sum_{run} P^2_{run}(N^+_{run}R_{run} + N^-_{run})}, \\
\frac{\sigma^2_{A_{LL}}}{A^2_{LL}} &= \sum_{run'} \left[\left(\frac{P_{run'}R_{run'}(1 - A_{LL}P_{run'})}{\sum_{run} P^2_{run}(N^+_{run}R_{run} + N^-_{run})} \right)^2 N^+_{run'} \right.,
\end{aligned}$$

$$
\begin{aligned}
& + \left(\frac{-P_{run'}(1 + A_{LL}P_{run'})}{\sum_{run} P^2_{run}(N^+_{run}R_{run} + N^-_{run})} \right)^2 N^-_{run'} \Bigg] , \\
\frac{\sigma^2_{A_{LL}}}{A^2_{LL}} \quad = \quad & \sum_{run'} \left(\frac{P_{run'}}{\sum_{run} P^2_{run}(N^+_{run}R_{run} + N^-_{run})} \right)^2 , \\
& \times \left[R^2_{run'}(1 - A_{LL}P_{run'})^2 N^+_{run'} + (1 + A_{LL}P_{run'})^2 N^-_{run'} \right] .
\end{aligned}
$$

4.3 Spin State Determination

Two proton beams, consisting of up to 110 bunches, circulated in RHIC. Each bunch contained up to 2×10^{11} protons. In addition, an abort gap the width of 10 bunches was in the beams in order to facilitate dumping of the beam. Within each bunch, the protons' spins were polarized, either with the spins vertically upwards or downwards. Just before the STAR interaction region, the protons' spins were rotated to be either parallel to the proton's velocity (positive helicity) or anti-parallel (negative helicity). Then the beams were made to intersect so that protons from one beam could collide with the other beam's protons.

For the asymmetry measurement, it was important to know whether the colliding protons had the same or opposite helicity. Each bunch's proton spin direction was known when it was injected into the ring. This ideal spin pattern was recorded and varied by fill. The protons were injected into the RHIC ring and circulated in it for up to eight hours before being discarded. The time from injection to dumping was considered a fill.

The two beams collided at the STAR interaction region. Each bunch in one beam collided with only one bunch in the other beam. The bunches collided with the exact same bunch from the other beam every time. This produced a bunch crossing pattern consisting of 120 bunch crossings. The pattern stayed the same throughout the fill. What needed to be known was how the ideal patterns for the two beams were overlapping to produce the bunch crossing pattern. Once that was known, it was possible to know the helicity of the colliding protons by knowing where in the bunch crossing pattern it was.

First an ideal bunch crossing pattern was formed by assuming that the first bunch of the one beam collided with the first bunch of the other beam. The bunch crossing pattern was offset from the ideal bunch crossing pattern. Then the scalar boards[3] were used to determine the offset. The scalar boards recorded, at the bunch crossing frequency, if a collision occurred. Figure 4-1 gives the event rate where the histogram was filled if a collision, as determined by the BBC, occurred. Figure 4-1 is from simulation of the data and not from actual events. The bunch crossing on the x-axis runs from 0 to 119.

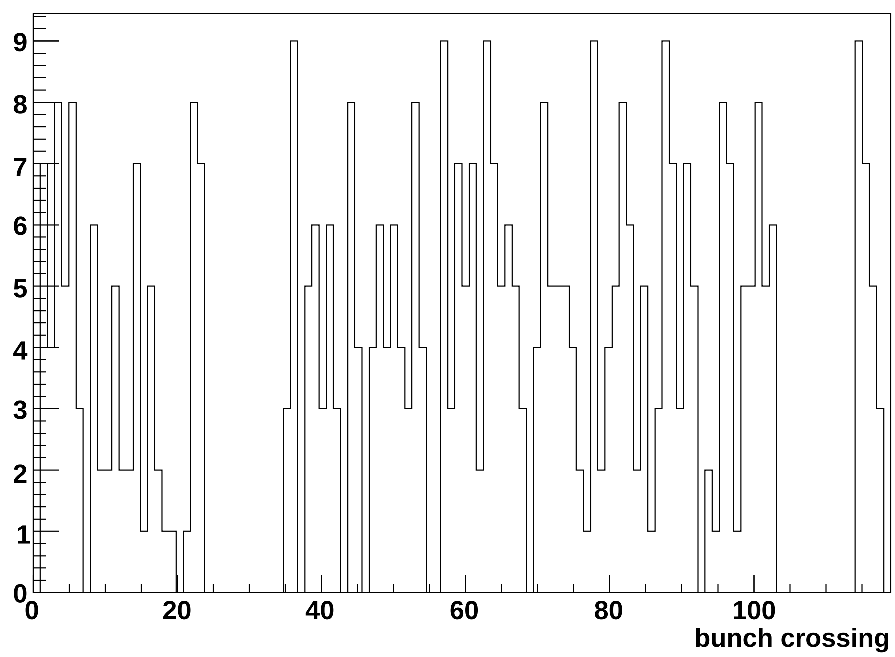

Figure 4-1: Simulated Event Rate

Collisions did not occur when one beam was intersecting with the other beam at the location of that beam's abort gap. This shows up in Fig. 4-1 as the two gaps from 25-35 and 105-115. These gaps were used to determine the offset between the ideal bunch crossing pattern and the bunch crossing pattern. A computer program looped over the 120 possible offsets and compared the event rate (shown in Fig. 4-1)

[3]Described in an earlier chapter

to the ideal bunch crossing pattern and calculated the χ^2/NDF of the fit of the two. When the bunch crossing pattern was lined up with the ideal bunch crossing pattern the best fit and consequently the smallest χ^2/NDF occurred.

4.4 Beam Polarization

Carbon polarimeters[4] were used to measure the beam's polarization at intervals lasting up to two hours. When the polarized protons hit the carbon target, they scattered. Depending on the direction and magnitude of the polarization, they scattered preferentially in one direction over the other. This is called the x-asymmetry. Previous experiments have measured the relation between the proton's polarization and the x-asymmetry. This ratio is called the analyzing power and depends on the proton's energy. The x-asymmetry from these measurement and analyzing power were used to calculate the polarization.

$$P = \frac{x}{A},$$

where P is the polarization, x is the x-asymmetry, and A is the analyzing power. Figure 4-2 shows the polarizations for the two beams. Only the fills used in calculating the asymmetry are shown. Although several measurements were made during the fill, the average over the fill was used.

4.5 Results

Figure 4-3 shows the measured asymmetry. The black bars are the statistical uncertainties on the asymmetry and the vertical size of the gray box is the systematic uncertainty. The points were plotted at the particle jet's transverse momentum and the gray band's horizontal size reflects the uncertainty in the transverse momentum of the parton jet[7]. Table 4.1 gives the values for each point.

[4]described in a previous chapter

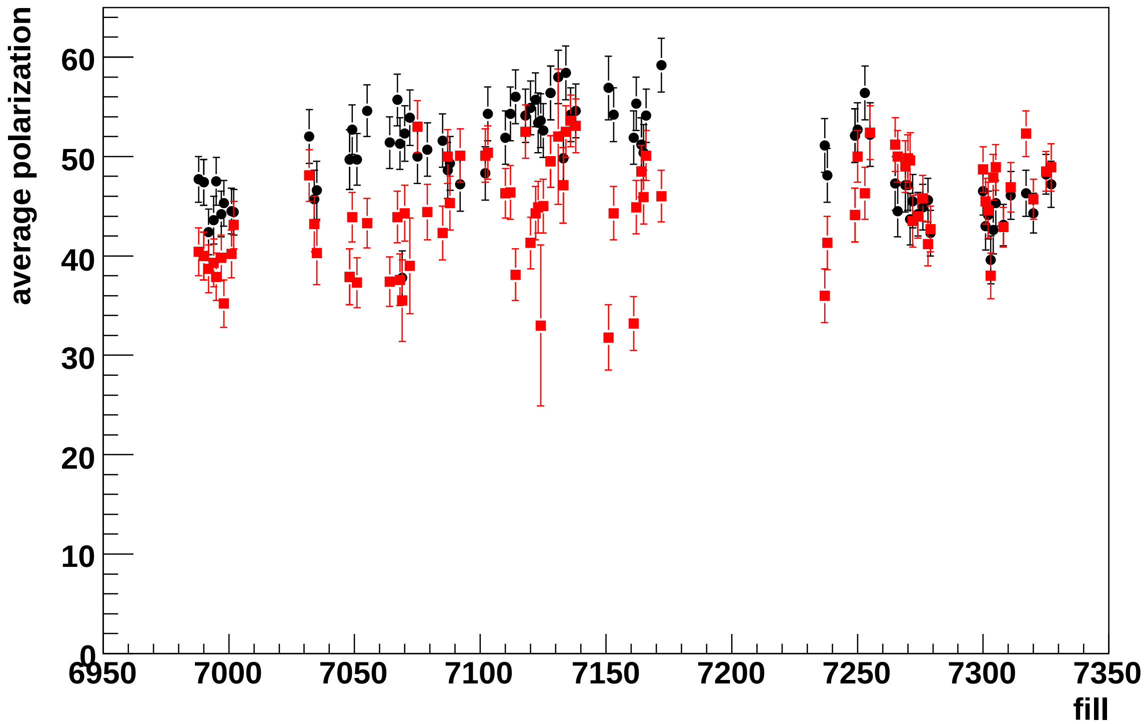

Figure 4-2: 2005 RHIC Beam Polarization. The black circles are for one beam and the red squares are for the other beam.

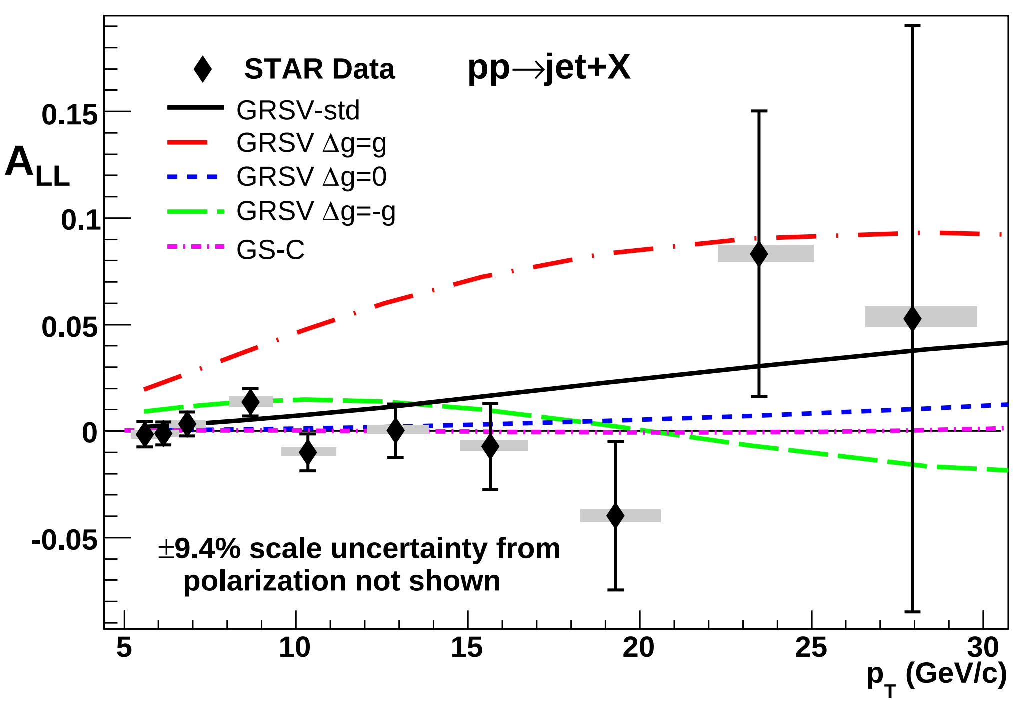

Figure 4-3: Experimentally measured value of A_{LL}

p_T^M (GeV/c)	p_T+sys-sys (GeV/c)	$A_{LL}\pm$ stat + sys-sys $\times 10^{-3}$
5.58	5.60 + 0.33 - 0.38	$-1.30 \pm 5.72 + 2.43 - 2.43$
6.84	6.14 + 0.36 - 0.39	$-1.01 \pm 5.27 + 2.34 - 2.34$
8.38	6.83 + 0.41 - 0.42	$3.25 \pm 5.42 + 2.21 - 2.49$
10.26	8.67 + 0.52 - 0.47	$13.22 \pm 6.33 + 3.76 - 2.61$
12.57	10.34 + 0.63 - 0.53	$-9.71 \pm 8.31 + 3.42 - 2.32$
15.41	12.89 + 0.79 - 0.62	$0.20 \pm 12.17 + 3.61 - 2.30$
18.90	15.65 + 0.97 - 0.73	$-7.03 \pm 19.49 + 5.46 - 2.51$
23.20	19.30 + 1.20 - 0.86	$-38.48 \pm 33.54 + 4.45 - 2.96$
28.39	23.48 + 1.47 - 1.03	$80.41 \pm 64.73 + 3.80 - 3.80$
34.81	27.94 + 1.76 - 1.20	$50.87 \pm 132.86 + 4.17 - 4.17$

Table 4.1: Double Longitudinal Spin Asymmetry Results

The curves represent theoretical predictions for NLO pQCD parton jets from the GRSV[2] and GS-C[8] global analysis. GRSV-std was calculated based on the best fit to polarized inclusive DIS experimental data. GRSV $\Delta g = 0$ ($\Delta g = \pm g$) was calculated assuming no (maximum/minimum) gluon polarization, $\Delta g = 0$ ($\Delta g = \pm g$). An initial scale of $Q_0^2 = 0.4 GeV^2/c^2$ was used and the expressions were evaluated at factorization and renormalization scales of$\mu_F = \mu_R = p_T$. The GS-C curve is similar to the GRSV-std curve. The main difference is that its functional form has a node at $x \sim 0.1, Q^2 = 1 GeV^2/c^2$.

The 2005 Asymmetry measurement was consistent with the previous measurement from combined data from 2003 and 2004 (see Fig. 4-4). The transverse momentum range was extended for 2005 and the statistical uncertainties were smaller.

The asymmetry value was compared to the GRSV theory curves and confidence levels (see Fig. 4-5) were determined[7, 2, 30]. The yellow band gives the confidence level uncertainty due to the polarization uncertainty. $\Delta G > 0.33$ ($\Delta G = -G$) was ruled out within the GRSV framework with a confidence level of 90% (94%).

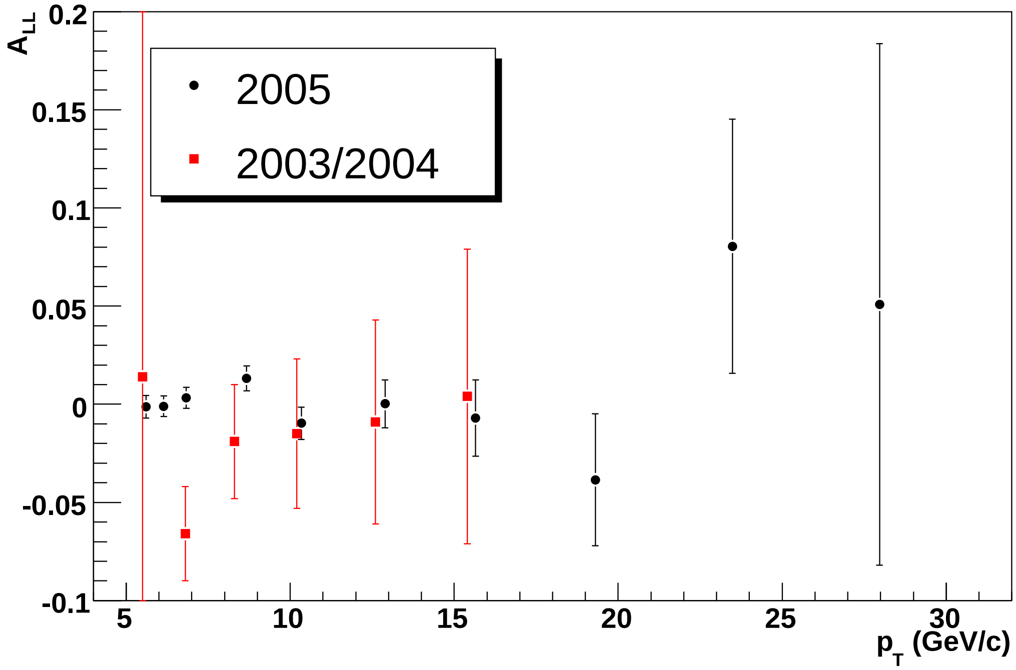

Figure 4-4: The 2003/2004 and 2005 Longitudinal Double-Spin Asymmetries

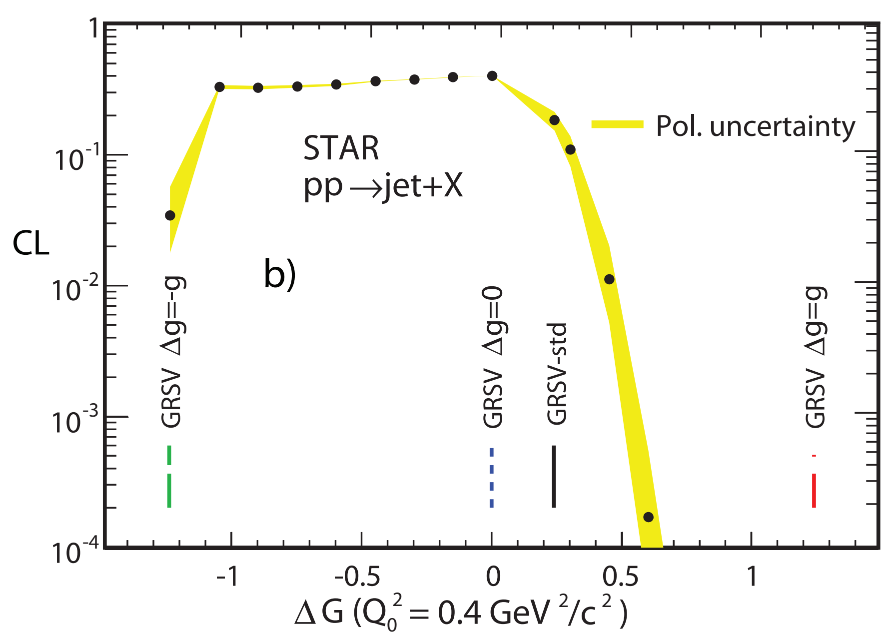

Figure 4-5: Confidence Levels

THIS PAGE INTENTIONALLY LEFT BLANK

Chapter 5

The Inclusive Jet Cross-section

5.1 Calculation Method

The differential cross-section is defined as

$$d\sigma = \frac{dN}{\text{flux } d\eta d\phi dp_T} \frac{1}{\text{correction Factor}}.$$

It was calculated for inclusive jets produced from proton-proton collisions at $\sqrt{s} =$ 200 GeV. Jets were formed using a mid-point Cone algorithm[28] with a radius of 0.4[1]. It was calculated separately for each transverse momentum bin and trigger (where triggers are defined in a previous chapter). $d\eta = 0.8$ and $d\phi = 2\pi$ are the pseudorapidity and azimuthal range, respectively, of the jets. The correction factors are described in section 5.2, the number of jets (dN) is described in section 5.3, and the flux is described in section 5.4.

The transverse momentum bin width (dp_T) varied from bin to bin. The transverse momentum binning used was [5.0, 6.2, 7.6, 9.3, 11.4, 14.1, 17.3, 21.3, 26.2, 32.2, 39.6, 48.7, 60.0] GeV/c.

[1] A more complete jet definition is in a previous chapter.

5.2 Correction Factors

The jets used in this analysis were made by grouping together BEMC tower energies and charged tracks. In order to compare the cross-section with theory predictions, the cross-section needed to be calculated in terms of jets composed of particles. Monte-Carlo simulations were used to find the relation between the number of jets composed of BEMC tower energies and charged tracks, and the number of jets composed of particles.

PYTHIA 6.205[31] generated the events using CDF 'Tune A' settings[32]. Jets were formed using the same algorithm as for the data jets[2]. The following cuts were applied to the jets: event vertex found, jet pseudorapidity between $0.2 < \eta < 0.8$, and the vertex was within 60 cm of the center of the BEMC.

The STAR detector response package, which is based on GEANT 3[33], was used to get the detector response to the PYTHIA generated particles. Jets were calculated from the detector response in the exact same way they were calculated using data. The same cuts were made on the jets as on the jets from the data[3]. A comparison of the simulated jets to the data jets is given in a later chapter.

The correction factor was defined as the ratio of the number of jets from PYTHIA particles to the number of jets from the detector response. Correction factors were calculated for each trigger as a function of p_T. Figure 5-1 shows the correction factors as a function of transverse momentum. Table 5.1 gives the numerical values of the correction factors.

[2] The algorithm is described in a previous chapter

[3] Cuts are described in a previous chapter

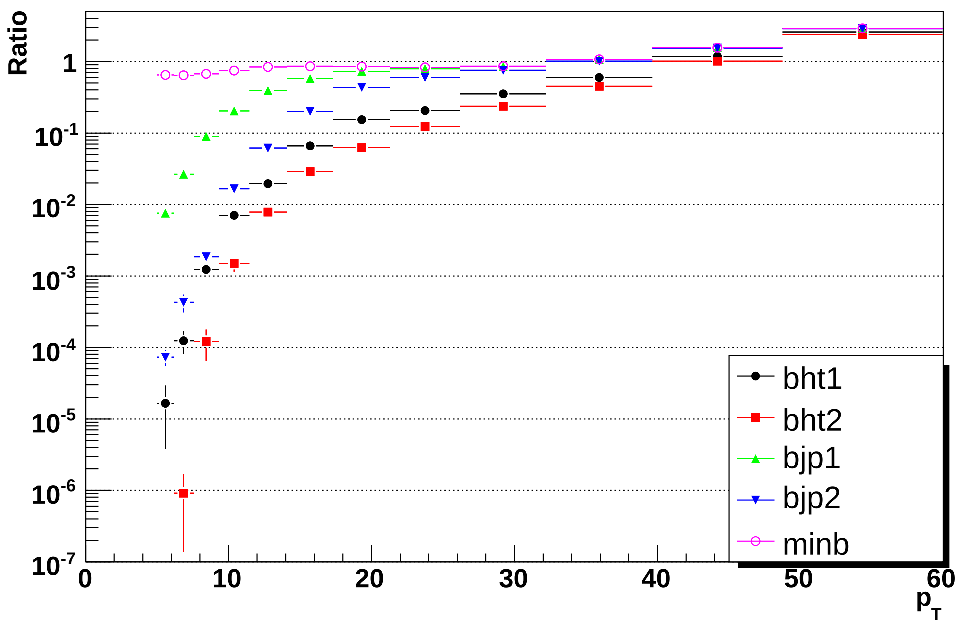

Figure 5-1: Correction Factors for various triggers.

p_T range (GeV/c)	bht1	bht2	bjp1	bjp2	minb
5.0 - 6.2	$(1.7 \pm 1.3) \times 10^{-5}$	$(4.1 \pm 4.1) \times 10^{-10}$	$(7.6 \pm 0.8) \times 10^{-3}$	$(7.3 \pm 1.8) \times 10^{-5}$	$(6.5 \pm 0.1) \times 10^{-1}$
6.2 - 7.6	$(1.2 \pm 0.4) \times 10^{-4}$	$(9.1 \pm 7.7) \times 10^{-7}$	$(2.7 \pm 0.2) \times 10^{-2}$	$(4.3 \pm 1.2) \times 10^{-4}$	$(6.4 \pm 0.1) \times 10^{-1}$
7.6 - 9.3	$(1.2 \pm 0.2) \times 10^{-3}$	$(1.2 \pm 0.6) \times 10^{-4}$	$(9.0 \pm 0.5) \times 10^{-2}$	$(1.9 \pm 0.3) \times 10^{-3}$	$(6.7 \pm 0.1) \times 10^{-1}$
9.3 - 11.4	$(7.0 \pm 0.9) \times 10^{-3}$	$(1.5 \pm 0.4) \times 10^{-3}$	$(2.0 \pm 0.1) \times 10^{-1}$	$(1.6 \pm 0.1) \times 10^{-2}$	$(7.5 \pm 0.2) \times 10^{-1}$
11.4 - 14.1	$(2.0 \pm 0.2) \times 10^{-2}$	$(7.8 \pm 1.4) \times 10^{-3}$	$(3.9 \pm 0.2) \times 10^{-1}$	$(6.1 \pm 0.3) \times 10^{-2}$	$(8.3 \pm 0.3) \times 10^{-1}$
14.1 - 17.3	$(6.6 \pm 0.8) \times 10^{-2}$	$(2.9 \pm 0.5) \times 10^{-2}$	$(5.8 \pm 0.2) \times 10^{-1}$	$(2.0 \pm 0.1) \times 10^{-1}$	$(8.6 \pm 0.5) \times 10^{-1}$
17.3 - 21.3	$(1.5 \pm 0.2) \times 10^{-1}$	$(6.2 \pm 1.0) \times 10^{-2}$	$(7.3 \pm 0.3) \times 10^{-1}$	$(4.4 \pm 0.3) \times 10^{-1}$	$(8.5 \pm 0.3) \times 10^{-1}$
21.3 - 26.2	$(2.0 \pm 0.1) \times 10^{-1}$	$(1.2 \pm 0.1) \times 10^{-1}$	$(7.9 \pm 0.2) \times 10^{-1}$	$(6.0 \pm 0.2) \times 10^{-1}$	$(8.3 \pm 0.2) \times 10^{-1}$
26.2 - 32.2	$(3.5 \pm 0.2) \times 10^{-1}$	$(2.4 \pm 0.1) \times 10^{-1}$	$(8.5 \pm 0.3) \times 10^{-1}$	$(7.5 \pm 0.3) \times 10^{-1}$	$(8.6 \pm 0.3) \times 10^{-1}$
32.2 - 39.6	$(6.0 \pm 0.3) \times 10^{-1}$	$(4.5 \pm 0.3) \times 10^{-1}$	1.1 ± 0.0	1.0 ± 0.0	1.1 ± 0.0
39.6 - 48.7	1.2 ± 0.1	1.0 ± 0.1	1.6 ± 0.1	1.5 ± 0.1	1.6 ± 0.1
48.7 - 60.0	2.6 ± 0.2	2.4 ± 0.2	2.9 ± 0.2	2.9 ± 0.2	2.9 ± 0.2

Table 5.1: Correction Factors for various triggers

5.3 Number of jets

For each run the number of jets for a given trigger was multiplied by that run's trigger prescale. That gave the "true" number of jets for that run (the number we would have had if every event was recorded). The number of true jets for each run was added together for the respective transverse momentum bin to give dN.

Figure 5-2 is the jet yield sorted by transverse momentum. The triggered data has a turn-on curve because, as the jet transverse momentum increased, the jet was more likely to satisfy the trigger. However, there is a peak because the higher the transverse momentum, the less likely it was that a jet was produced. Figures B-1 -

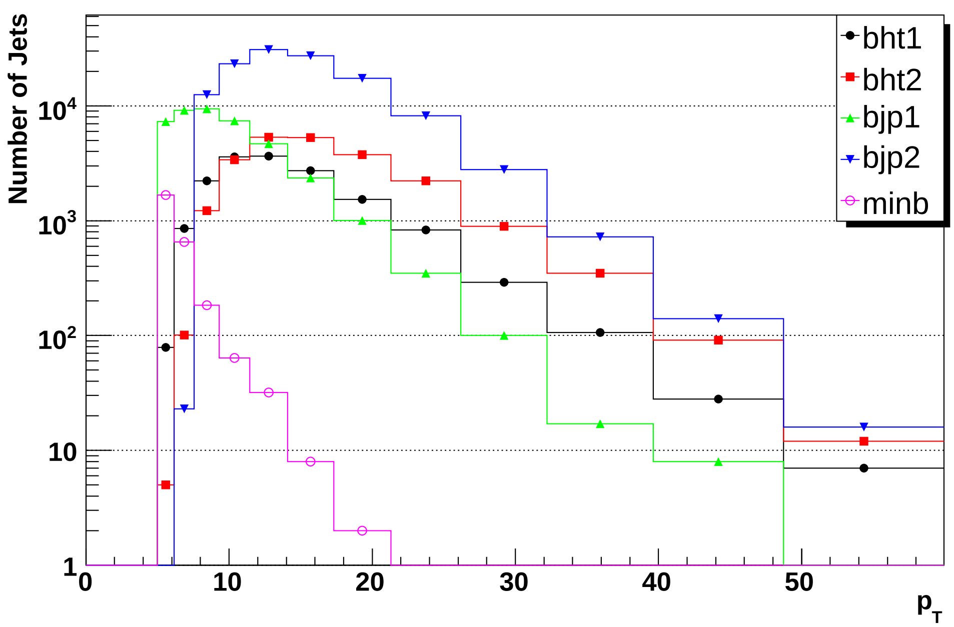

Figure 5-2: Jet Yield sorted by transverse momentum

Fig. B-3 show the jet yield as a function of jet pseudorapidity, azimuthal angle, and neutral energy ratio.

5.4 Proton Flux

The flux of protons is defined as

$$\text{Flux} = \frac{\text{Number of Events}}{\sigma_{BBC} V_{eff}}$$

where σ_{BBC} is the BBC cross-section[4]. V_{eff}, the MINB vertex finding efficiency, is described in section 5.5.

Figure B-4 (B-5) shows the event distribution (with a vertex cut). Figure 5-3 gives

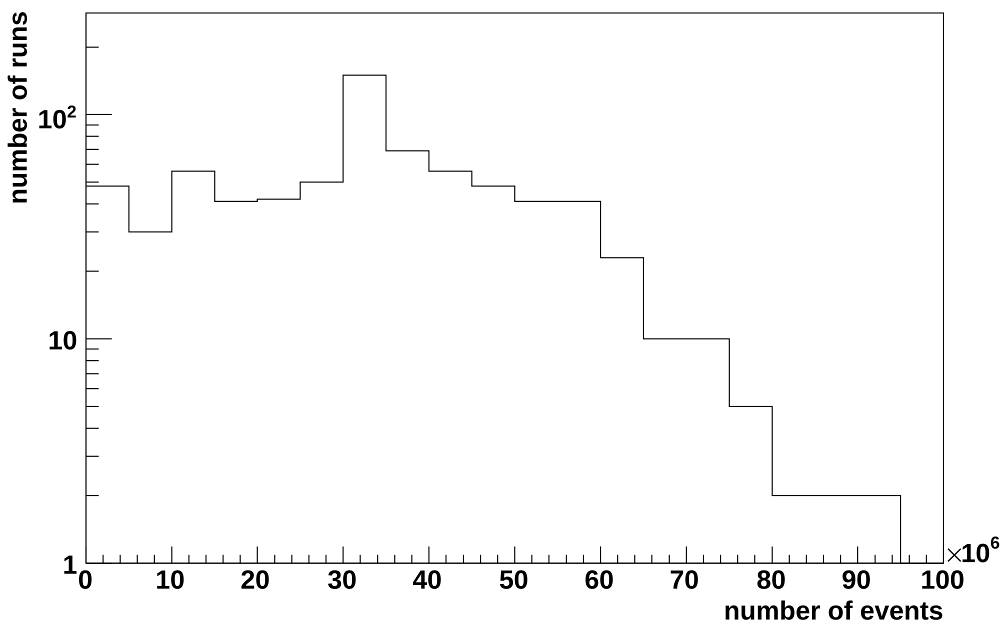

Figure 5-3: Number of MINB events with vertex cut applied

the total number of events used for the analysis. These are the events from Fig. B-5, which have cuts applied, multiplied by the prescale for the run. This corresponds to the number that went into Number of Events in the flux formula.

[4] $\sigma_{BBC} = (26.1 \pm 2.0) mb$[29]

5.5 Vertex Efficiency

The vertex efficiency is defined as the ratio of the number of events with a reconstructed vertex to all events.

$$V = \frac{N_f}{N_T} = \frac{N_f}{N_f + N_n},$$

where V is the vertex efficiency, N_n is the number of events without a found vertex, N_f is the number of events with a found vertex, and N_T is the total number of events. The vertex efficiency was sorted by trigger (where triggers are defined in a previous chapter). So only the MINB events were considered in finding the MINB vertex efficiency.

The efficiency was calculated for each run and then plotted. A constant line was fit to the data to come up with an overall vertex efficiency and error. Figure 5-4 gives the results for MINB data, which is the number that was used in the cross-section calculation. A vertex efficiency of 64% was found for the MINB data.

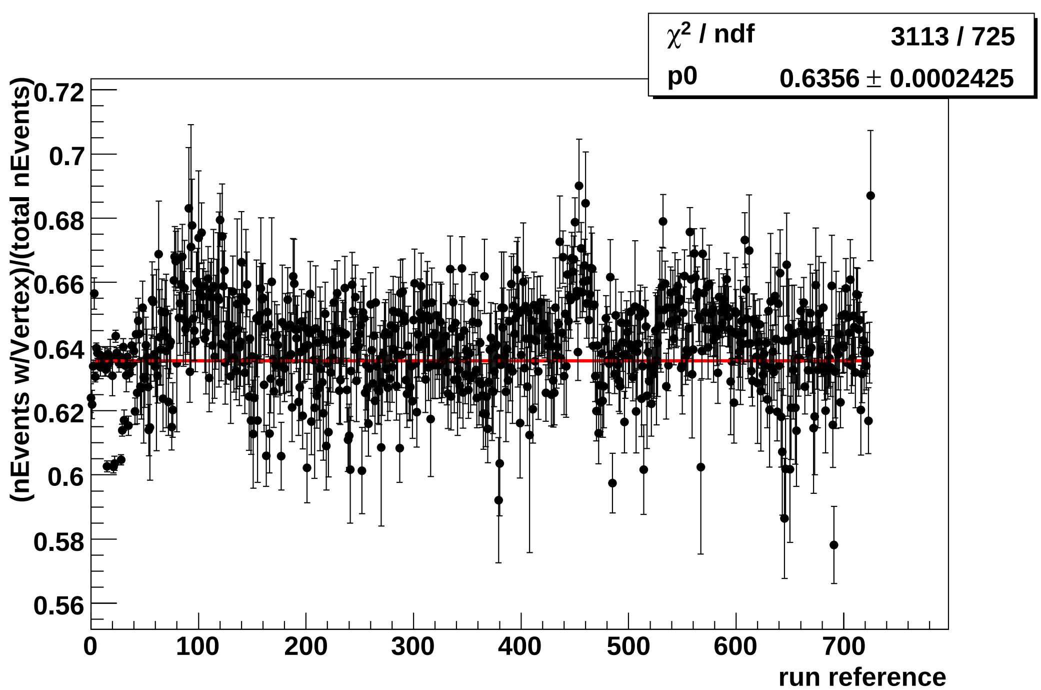

Figure 5-4: Vertex Efficiency for MINB

5.5.1 The BJP2 Vertex Efficiency

One of the triggers used was BJP2 (Barrel Jet Patch 2). The BJP2 trigger required, in addition to the MINB trigger, patches roughly the size of a jet ($\Delta\eta \times \Delta\phi = 1 \times 1$) had $E_T > 7.9$ GeV. From the plot of vertex efficiency for BJP2 (Fig. 5-5), a structure was seen within it. After sorting by fill[5], it was seen that the efficiency increased as

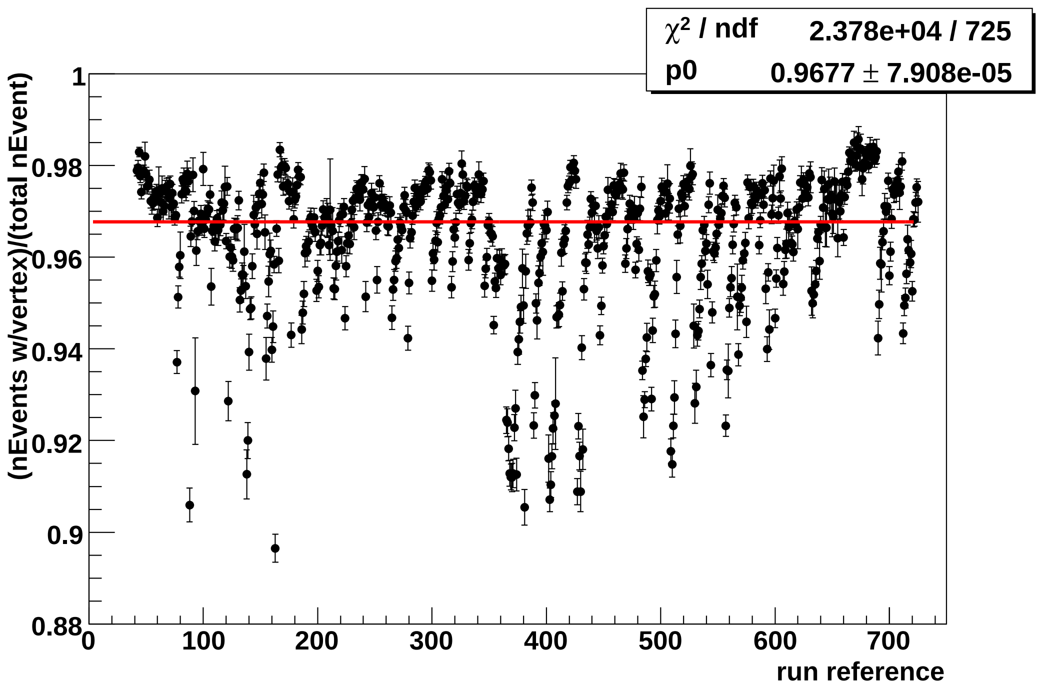

Figure 5-5: Vertex Efficiency for BJP2

the fill progressed (see Fig. 5-6).

Although the BJP2 vertex efficiency was not used explicitly in the cross-section calculation, one concern was that it might have affected the cross-section measurement, since if a vertex was not found no jets from that event were used.

This was checked first by dividing the run list into two parts: the runs that had a vertex efficiency within one standard deviation of the average; and the runs that had a vertex efficiency outside one standard deviation of the average. The cross-section was then calculated for each run list (see Fig. 5-7) and a p_T bin-by-bin comparison

[5] A fill is the period of time that the same protons are circulating in the RHIC ring.

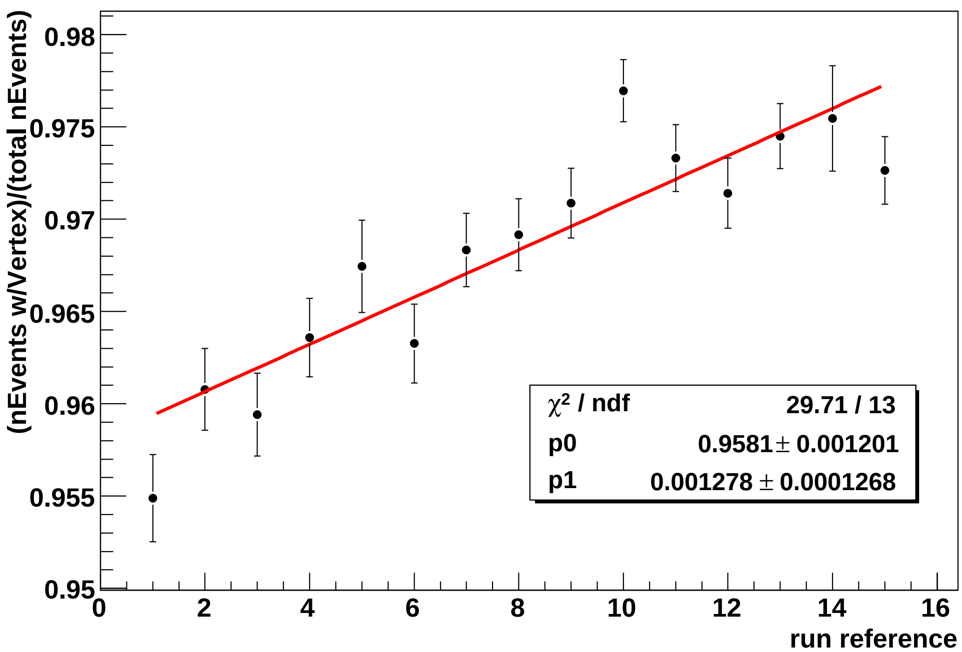

Figure 5-6: Vertex Efficiency for BJP2 Fill 7125

was made. There was no difference that could be seen within statistical error.

This was then repeated with the run list divided into runs where the vertex efficiency was above or below the average vertex efficiency. Once again the cross-sections were compared (see Fig. 5-8) and no difference was observed.

5.5.2 The BBC Timebin Dependence of the Vertex Efficiency

Another concern was that the vertex efficiency might have been changing as the vertex changed. If the vertex was not found its location was unknown, which prevented this from being directly tested. However, by looking at the BBC timebin for the event this could be determined. The timebin gives a measure of the time difference between the proton remnants hitting the BBC. A vertex between -60 cm and +60 cm corresponds to BBC timebins 7-9. Greater or lesser timebins have vertices outside -60 cm to +60 cm. So the vertex efficiency was checked for any vertex dependence by calculating the vertex efficiency for each timebin.

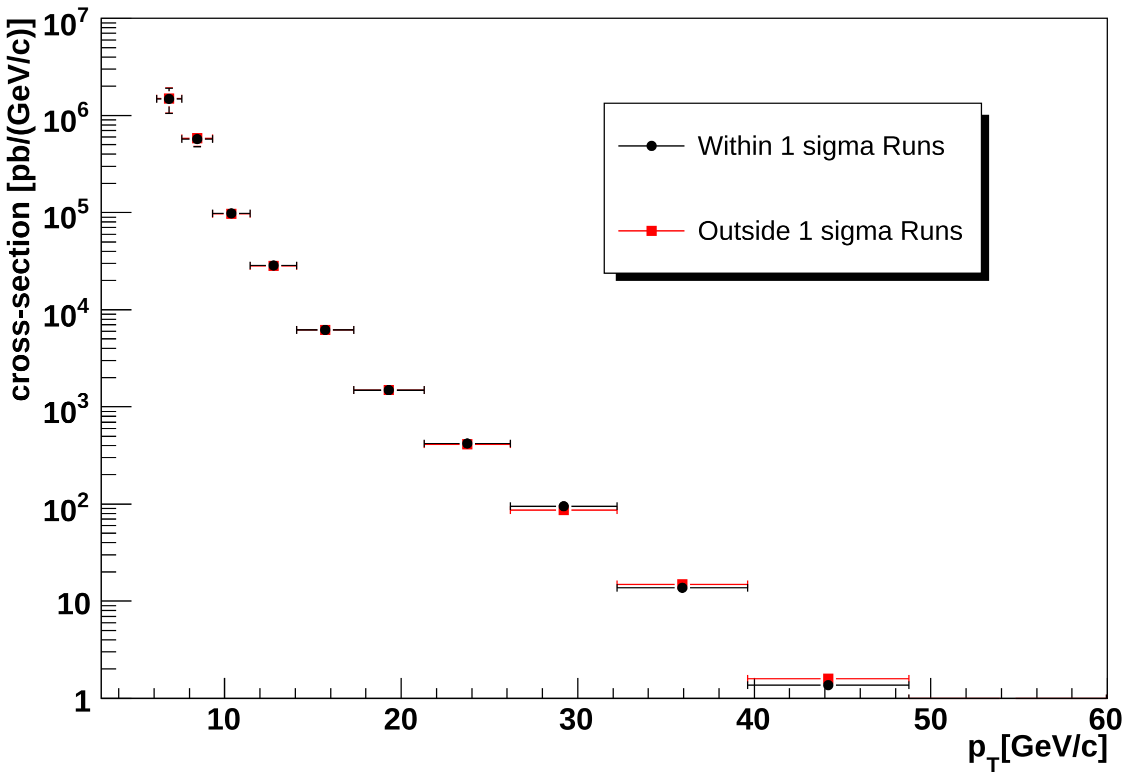

Figure 5-7: Cross-section for runs within and outside one standard deviation of the average vertex efficiency

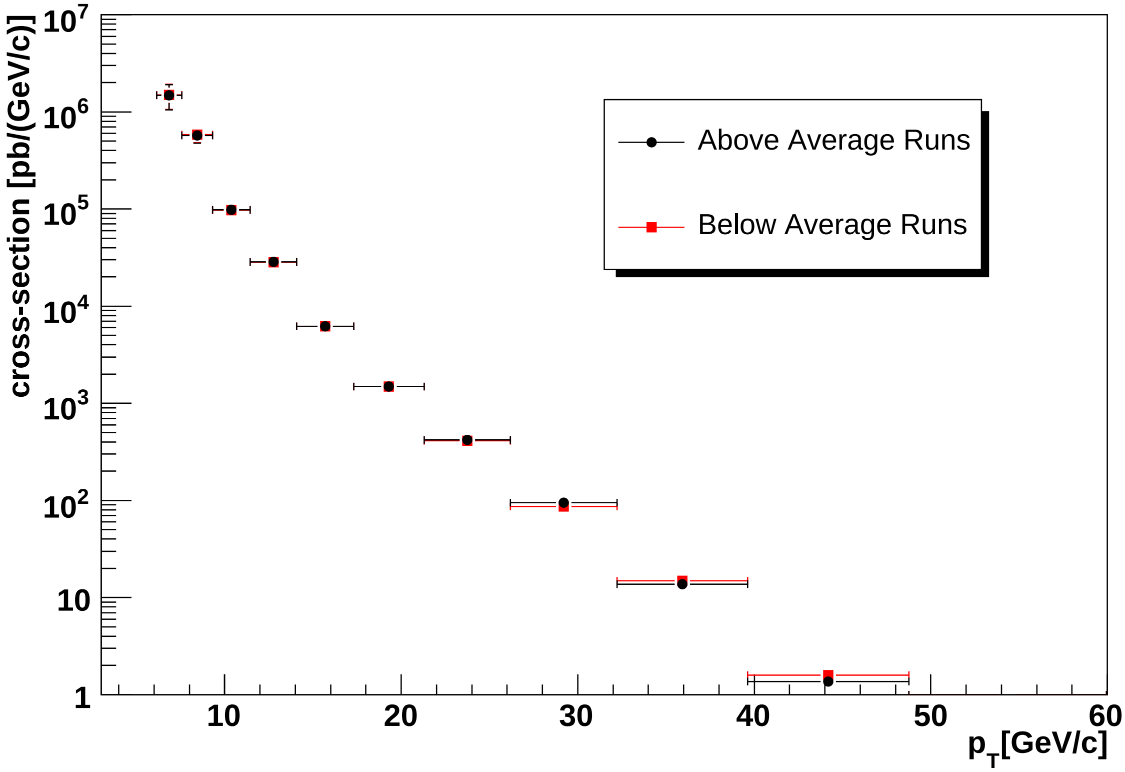

Figure 5-8: Cross-Section for runs with above and below average vertex efficiency

The vertex efficiency was found for timebins 4-11. Figure B-6 and Fig. B-7 show the vertex efficiency for each run sorted by timebin. The red line is the best fit. Figure 5-9 is a plot of the vertex efficiency as a function of BBC timebin. Figure 5-9

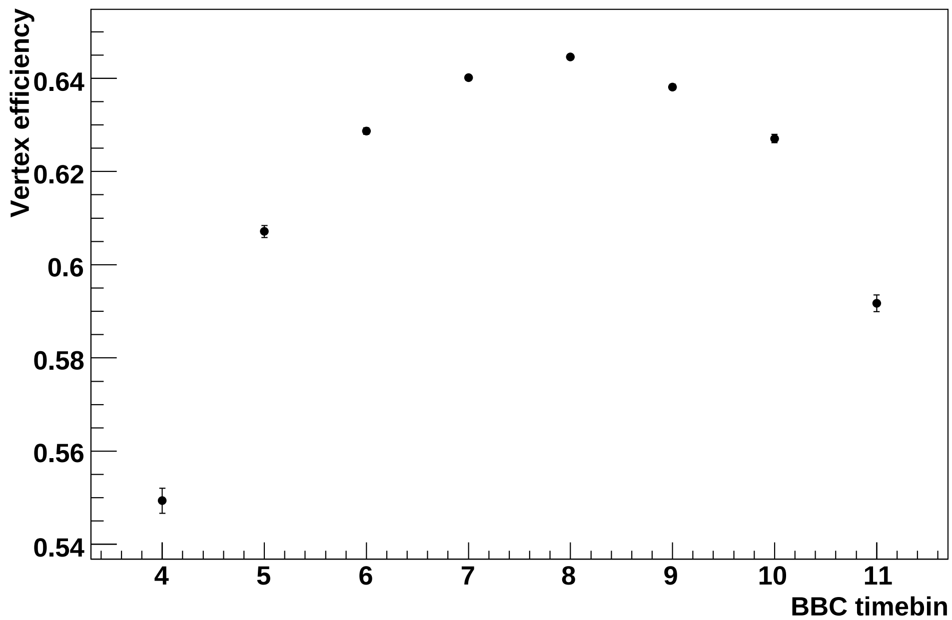

Figure 5-9: Vertex Efficiency for the various time bins

shows that the vertex efficiency was changing as the vertex changed. However, the change for the region of the measured vertex cut was within 1% of itself so any vertex dependency of the vertex efficiency could be ignored.

5.6 Results

Figure B-8 shows the cross-section sorted by trigger and Fig. 5-10 has all the triggers on one plot. Table B.4 gives the numerical values. The points agree with each other fairly well from trigger to trigger. Comparison of the cross-section to theory and previous results is in a following chapter.

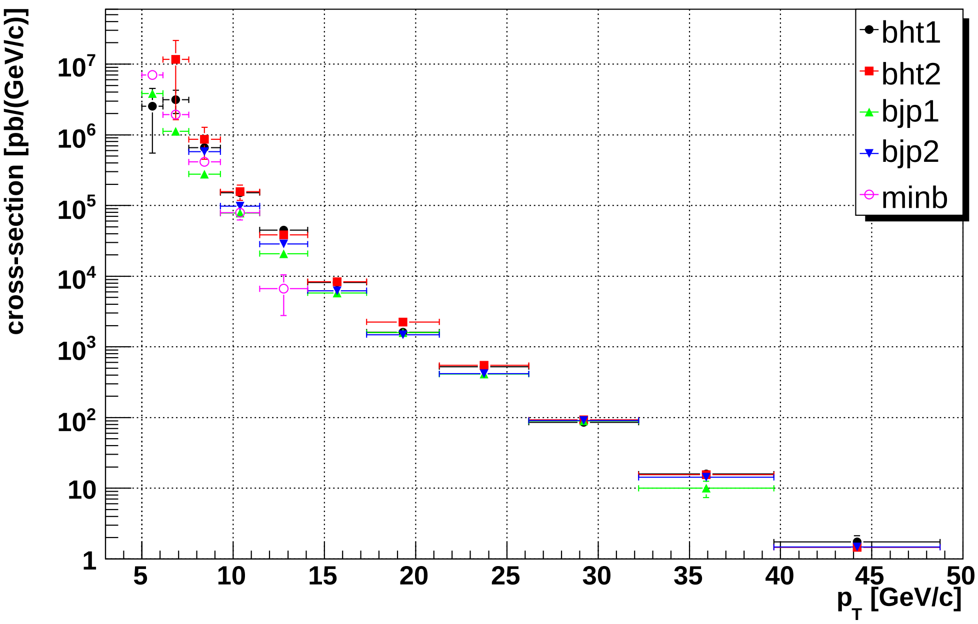

Figure 5-10: Inclusive Jet Cross-section

THIS PAGE INTENTIONALLY LEFT BLANK

Chapter 6

The Cross-section Systematic Uncertainties

6.1 Monte-Carlo Data Comparison

Monte-Carlo simulation was used to calculate the correction factors, which are discussed in a previous chapter. So it is important that the Monte-Carlo was reproducing what was happening in the data. This was checked by comparing the Monte-Carlo distributions to the data distributions. Because the data and Monte-Carlo had different numbers of events, the distributions were weighted so that the integral of the curve was unity.

Figure 6-1 is a plot of the transverse momentum distribution for the data and Monte-Carlo. The red filled squares are the BHT2 data points and the brown hollow squares are the Monte-Carlo Simulation. There is good agreement for the transverse momentum region that contains the majority of the statistics. The appendix contains more figures of the comparisons that were made. Most comparisons show reasonable agreement between Monte-Carlo and data.

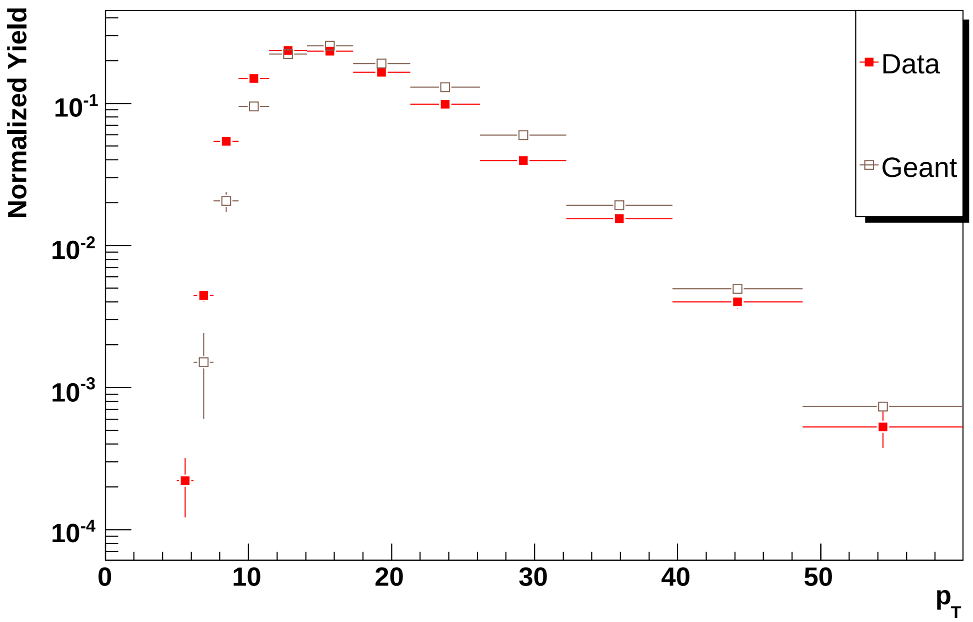

Figure 6-1: Data-Monte Carlo transverse momentum comparison for BHT2

6.2 Jet Energy Scale

The cross-section's uncertainty due to the jet transverse momentum uncertainty was found by adding in quadrature the BEMC gain uncertainty (described in section 6.2.1) and the charged track momentum uncertainty (described in section 6.2.2). Results are shown in Table 6.1. The low (high) column is the amount the cross-section was decreased (increased). Figure 6-3 gives the cross-section's fractional change for BJP2 trigger. The blue triangles (black squares) are the fractional increase (decrease). Figure C-11 shows the results for all five triggers.

The major contributor to the jet energy scale uncertainty was the BEMC gains for the low transverse momentum range. At the higher transverse momentum range the BEMC gains and charged track momentum contributed about equally to the uncertainty. This uncertainty was a major contributor to the cross-section's uncertainty.

p_T^M (GeV/c)	bht1		bht2		bjp1		bjp2		minb	
	low	high	low	high	low	high	low	high	low	high
5.58	-27.9	25.5	-0.0	0.0	-31.7	2.9	-0.0	0.0	-20.7	10.9
6.86	-30.9	10.2	-25.4	29.7	-27.3	2.5	-0.0	0.0	-23.9	34.0
8.43	-26.9	10.3	-25.7	15.1	-27.1	25.3	-34.8	6.8	-21.1	37.6
10.37	-27.9	2.0	-24.7	5.8	-25.2	24.5	-28.8	6.0	-23.1	80.3
12.76	-22.8	22.6	-25.2	3.3	-23.3	19.6	-26.3	1.4	-0.0	372.6
15.70	-23.0	19.8	-22.4	20.7	-23.2	18.7	-23.5	23.1	-0.0	0.0
19.31	-20.8	22.7	-23.4	22.3	-24.3	24.9	-23.8	21.4	-0.0	0.0
23.75	-23.3	16.8	-22.1	19.3	-25.7	21.4	-23.1	20.2	-0.0	0.0
29.21	-27.2	33.0	-23.5	28.5	-34.7	22.8	-27.2	28.8	-0.0	0.0
35.92	-20.6	20.4	-27.6	31.0	-18.9	36.2	-30.7	30.8	-0.0	0.0
44.19	-37.5	19.5	-34.2	23.8	-0.0	0.0	-38.0	30.4	-0.0	0.0

Table 6.1: Total Jet Energy Scale Uncertainty (percentage)

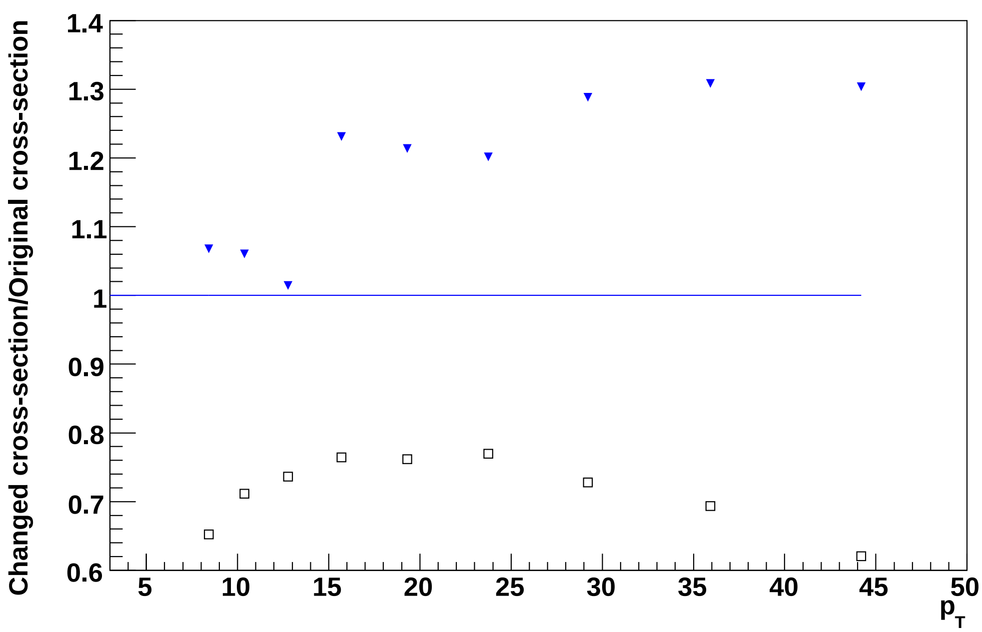

Figure 6-2: Cross-section's fractional change due to Jet Energy Scale for BJP2

p_T^M	bht1		bht2		bjp1		bjp2		minb	
(GeV/c)	low	high	low	high	low	high	low	high	low	high
5.58	-20.0	50.2	0.0	0.0	-29.1	26.7	0.0	0.0	-15.7	10.9
6.86	-28.6	23.9	-8.9	8.9	-27.1	27.2	0.0	0.0	-8.8	25.1
8.43	-26.3	26.4	-23.2	15.3	-27.0	25.3	-32.1	32.5	5.1	22.2
10.37	-27.6	28.3	-23.9	21.7	-24.8	24.1	-28.4	30.0	76.9	11.5
12.76	-22.8	22.6	-25.0	25.7	-22.3	18.5	-26.2	24.4	366.5	66.6
15.70	-22.5	19.4	-22.4	20.7	-20.7	15.7	-23.4	23.0	0.0	0.0
19.31	-19.7	20.5	-22.8	21.5	-19.6	18.2	-22.5	20.1	0.0	0.0
23.75	-21.3	15.3	-20.7	18.4	-18.4	12.2	-19.8	16.6	0.0	0.0
29.21	-24.1	24.5	-21.4	23.9	-24.8	8.3	-20.6	20.2	0.0	0.0
35.92	-16.1	10.4	-22.1	22.6	-11.8	13.3	-21.5	16.9	0.0	0.0
44.19	-22.2	8.7	-24.2	19.8	0.0	0.0	-25.0	20.0	0.0	0.0

Table 6.2: BEMC Gain Variation Uncertainty (percentage)

6.2.1 The BEMC Gain Uncertainty

The BEMC was calibrated with an uncertainty of 4.8% [34] in the gain. Gains were used to convert the tower ADC readings into transverse energy. So an uncertainty in the gain resulted in an uncertainty in the BEMC tower's transverse energy and consequently an uncertainty in the jets' transverse energy and transverse momentum. Because the jets' transverse momentum spectrum was a sharply falling function, a shift in the transverse momentum of the jets would result in a different number of jets found for each transverse momentum bin and consequently a different cross-section.

Since the only variable in the cross-section that would change if the gain was changed is the number of jets per transverse momentum bin, the fraction $\frac{dN_{ch}-dN_0}{dN_0}$, where dN_{ch} is the number of jets with the gain increased (decreased) by 4.8% and dN_0 is the number of jets without the gain changed, is equivalent to $\frac{d\sigma_{ch}-d\sigma_0}{d\sigma_0}$ where $d\sigma$ is the differential cross-section.

For this study, $\frac{dN_{ch}-dN_0}{dN_0}$ was calculated as it is equivalent to $\frac{d\sigma_{ch}-d\sigma_0}{d\sigma_0}$. The values of $\frac{dN_{ch}-dN_0}{dN_0}$ are recorded in Table 6.2. p_T^M is the average transverse momentum for the bin. The low (high) value is for when the gain is lowered (raised) by 4.8%. A negative (positive) value means that fewer (more) jets were found than when the gain was unchanged. Values of zero are where there were less than 10 jets found and so the cross-section was not calculated.

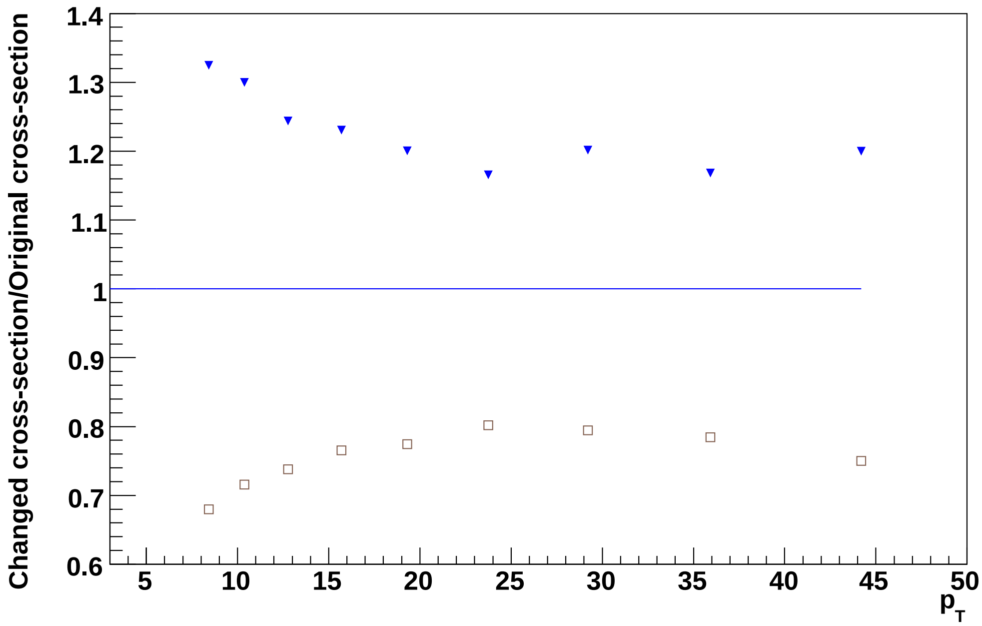

Figure 6-3: Cross-section's fractional change due to BEMC gain variation for BJP2

Figure 6-3 shows the fraction $\frac{d\sigma_{ch}}{d\sigma_0}$ for both the raised and lowered gains. The fraction was calculated as $\frac{dN_{ch}}{dN_0}$.

6.2.2 The Charged track effects

Another uncertainty in the jet energy scale was from the charged track momentum uncertainty. TPC tracks had a momentum uncertainty of 1% and the TPC tracking efficiency uncertainty was 5%.

Charged hadrons, after passing through the TPC, passed through the BEMC and deposited on average energy equal to 20%[34] of their momentum. To eliminate double counting of the energy, this energy was subtracted out. The uncertainty of the average BEMC charged hadron response found from Monte-Carlo simulations was 10%[34]. Combining this with a 90% tracking efficiency in the TPC[24] led to an uncertainty in the track energy due to hadrons in the BEMC of $\frac{0.20}{0.90}0.1 \times 100\% = 2.2\%$.

p_T^M	bht1		bht2		bjp1		bjp2		minb	
(GeV/c)	low	high	low	high	low	high	low	high	low	high
5.58	25.5	-19.4	0.0	0.0	2.9	-12.4	0.0	0.0	-13.5	-11.2
6.86	10.2	-11.5	29.7	-23.8	2.5	-2.5	0.0	0.0	-22.2	22.9
8.43	10.3	-5.8	15.1	-11.1	-0.6	0.4	6.8	-13.5	-21.1	30.3
10.37	2.0	-4.4	5.8	-6.3	-4.0	4.0	6.0	-4.9	-23.1	23.1
12.76	-1.0	-0.0	3.3	-3.5	-6.9	6.4	1.4	-2.5	-0.0	66.7
15.70	-4.9	3.8	-1.2	-0.5	-10.4	10.1	-2.2	2.1	0.0	0.0
19.31	-6.5	9.7	-5.1	6.0	-14.3	17.0	-7.8	7.3	0.0	0.0
23.75	-9.3	7.0	-7.5	5.9	-17.9	17.6	-11.8	11.5	0.0	0.0
29.21	-12.7	22.2	-9.7	15.5	-24.3	21.2	-17.8	20.6	0.0	0.0
35.92	-12.9	17.5	-16.6	21.2	-14.8	33.6	-21.8	25.8	0.0	0.0
44.19	-30.2	17.5	-24.2	13.2	0.0	0.0	-28.6	22.9	0.0	0.0

Table 6.3: Charged Track Variation Uncertainty (percentage)

Adding these three uncertainties in quadrature gave an uncertainty in the track energy of 5.6%. The track energy uncertainty resulted in an uncertainty in the jet energy and transverse momentum as follows where E' is the new energy, E_T is the energy in the tracks, E_B is the rest of the jet energy, R is the neutral energy ratio, and $a = 0.056$ is the track energy uncertainty.

$$\begin{aligned} E &= E_B + E_T = RE + (1-R)E \\ E' &= E_B + E_T(1 \pm a) = RE + (1-R)E(1 \pm a) = [1 \pm a(1-R)]E \\ p'_T &= [1 \pm a(1-R)]p_T \end{aligned}$$

Results are shown in table 6.3. All jet cuts remained the same. The uncertainty is small compared to the BEMC Gain Uncertainty for the low transverse momentum region, but becomes the leading uncertainty in the high transverse momentum region. Figure 6-4 shows the fraction of the changed cross-section to the original cross-section for both raising and lowering the track energy.

A cut on the minimum energy of the trigger tower (patch) affected the uncertainty for the low transverse momentum range. If no cuts had been made on the jets, increasing (decreasing) the track energy would have increased (decreased) the cross-

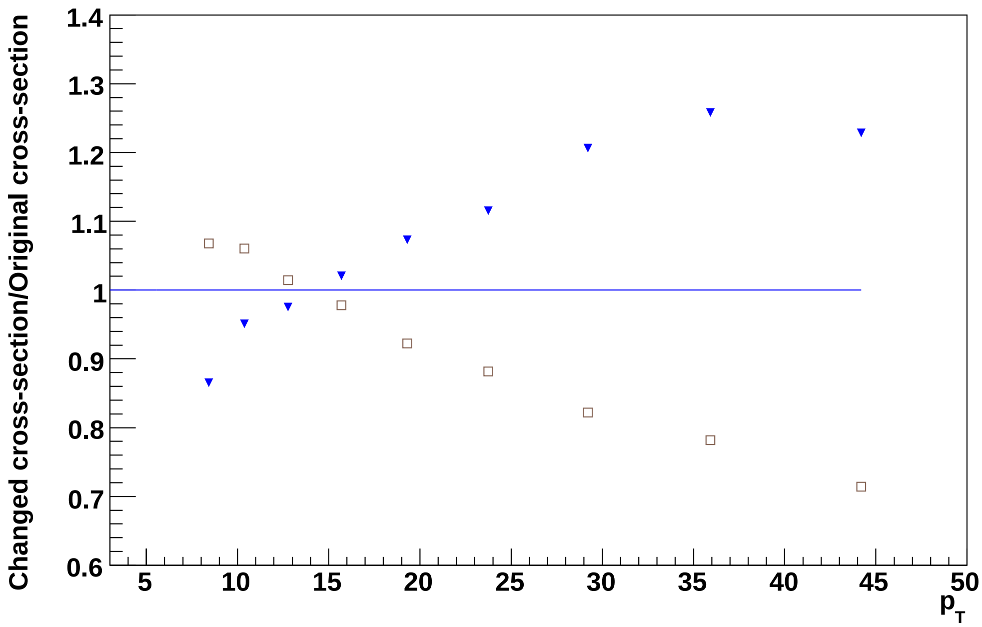

Figure 6-4: Cross-section's fractional change due to Charged Track energy uncertainty for BJP2

section. Figure C-10 shows the results when the cut on minimum energy of a tower (patch) was removed. It can be seen that now an increase (decrease) in track energy

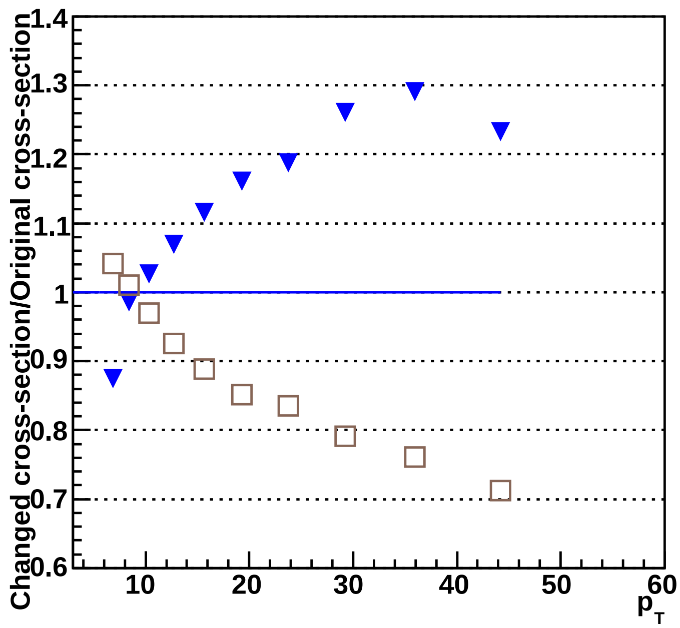

Figure 6-5: Cross-section's fractional change due to Charged Track energy uncertainty for BJP2 with no transverse energy cut on the trigger patch

resulted in an increase (decrease) of the cross-section for all but the lowest transverse momentum point.

The lowest transverse momentum point was lower because there was a cut on jet transverse momentum of $p_T > 5$ GeV/c which was applied before this study raised or decreased the energy. So jets left the first transverse momentum bin when the track energy was raised and there were no jets below that bin to be raised into it.

One of the reasons for the transverse momentum dependence is because as seen in Fig. 6-6 the neutral energy ratio is transverse momentum dependent. Figure 6-6 gives the average neutral energy ratio of the cut jets. Jet patch triggers were much more affected than the high tower triggers because the high tower triggers rejected many jets in the low transverse momentum bins because the jet's neutral energy ratio was greater than 0.8. By lowering (raising) the track energy, the neutral energy ratio was increased (decreased) and so fewer (more) jets survived the cut. This was the

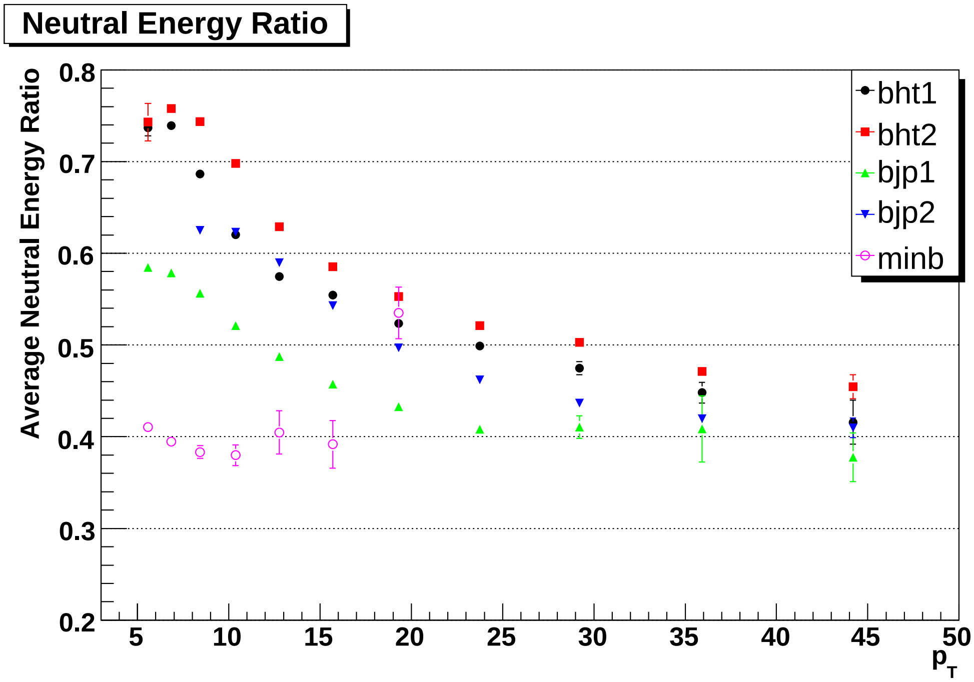

Figure 6-6: Neutral Energy ratio as function of transverse momentum

opposite effect from the minimum transverse energy cut and the two tended to cancel each other.

6.3 Z-Vertex Dependence

The proton collisions did not necessarily take place in the center of the detector. A cut was made on the jets to restrict them to events where the collision occurred within 60 cm of the center of the detector along the beam line. The cross-section was expected to be independent of the location of the collision with respect to the detector. A check was made that this was the case, and it was found that the cross-section was independent of the location of the collision with respect to the detector's center.

For this study, the distance from the center of the detector that jets were allowed to have was extended from 60 cm to within 100 cm of the center. To reduce error correlations, the cross-section was calculated for jets that fell within 20 cm of each other. So the cross-section was calculated for jets from -100 cm to -80 cm, -80 cm to -60 cm, -60 cm to -40 cm, $\cdots$, 80 cm to 100 cm, where the distance is from the center of the detector. Cross-sections from the different vertex regions were compared to each other sorted by trigger and p_T. A constant line was fit to the points and the χ^2 of this line was looked at to see how well the points fit. No difference in cross-section can be seen within statistics. The comparison can be seen in Fig. 6-7. Additional figures are in the appendix.

6.4 Phi Dependence

When the unpolarized or longitudinally polarized protons collide, symmetry says that there should not be any phi preference where the phi is the azimuthal angle with respect to the beams. A check that the cross-section was independent of phi was made. Divisions were made for 2,3,4,6 and 12 divisions, and no systematic shift was noticed. The results for two divisions are shown in Fig. 6-8. The plots for additional triggers and transverse momentum range are found in the appendix.

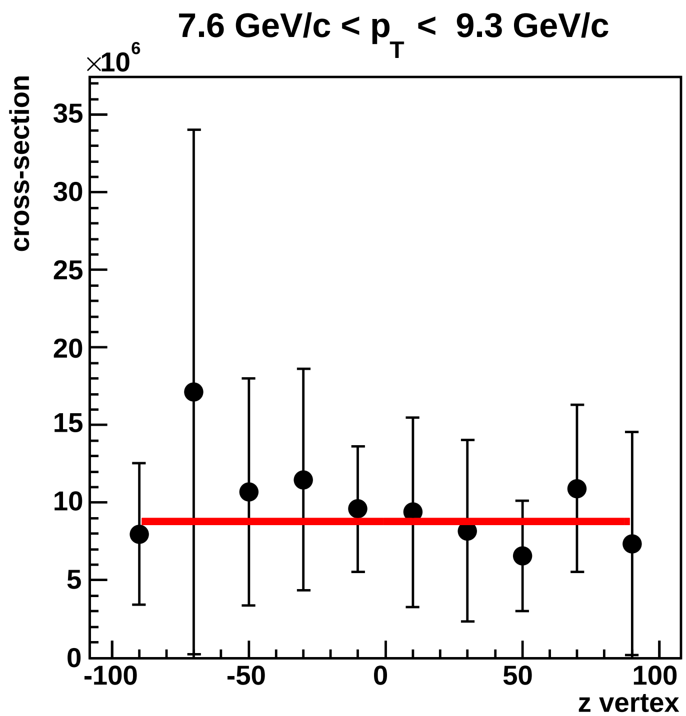

Figure 6-7: Cross-section Comparison of different z-vertices for bht1 trigger 7.5GeV/c $< p_T <$ 9.3GeV/c

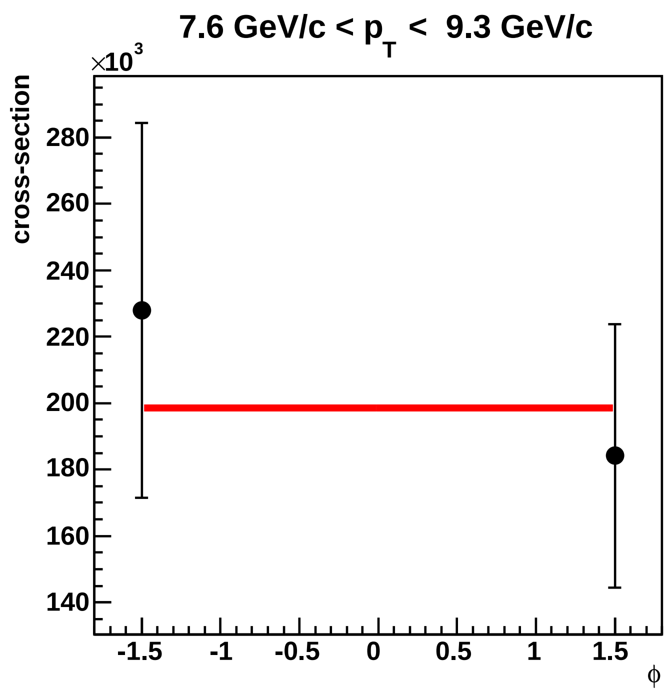

Figure 6-8: Cross-section Comparison for negative phi and positive phi for bht1 trigger 7.5GeV/c $< p_T <$ 9.3GeV/c

6.5 Spin State Dependence

Protons were collided in four different spin configurations: both spins pointing east; both spins pointing west; one pointing east and one pointing west. Different cross-sections are expected for the different spin configurations. If there are more collisions from one spin configuration, the overall measurement would be polarized and this can affect the cross-section. The cross-section was calculated separately for the four spin configurations and was found to be the same within statistical uncertainties.

Figure 6-9 shows the result for BHT1 for one transverse momentum bin. Additional plots are in the appendix. Each plot was sorted by transverse momentum as the cross-section was transverse momentum dependent. A constant line was fit to the four cross-sections found from the four different spin states.

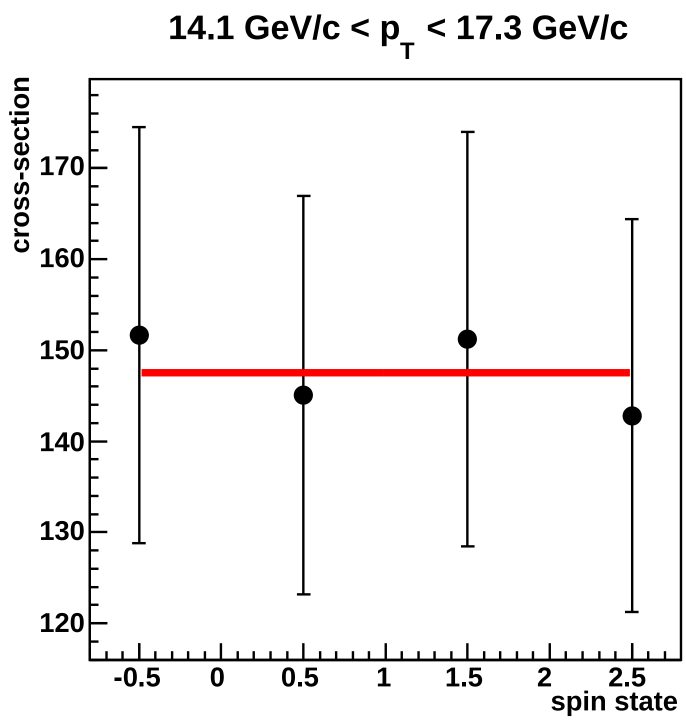

Figure 6-9: Spin State Cross-section Comparison for BHT1 trigger

6.6 Total Systematic Uncertainty

Only the jet energy scale had a non-negligible uncertainty. Therefore, the total systematic uncertainty on the cross-section is due to the jet energy scale. Table 6.6 shows the total uncertainty on the cross-section.

p_T range (GeV/c)	bht1 (± stat + sys - sys) (pb/GeV)	bht2 (± stat + sys - sys) (pb/GeV)
5.0 - 6.2	$(2.5 \pm 2.0 + 0.6 - 0.7) \times 10^6$	—
6.2 - 7.6	$(3.1 \pm 1.1 + 0.3 - 1.0) \times 10^6$	$(1.2 \pm 1.0 + 0.4 - 0.3) \times 10^7$
7.6 - 9.3	$(6.6 \pm 1.2 + 0.7 - 1.8) \times 10^6$	$(8.6 \pm 4.1 + 1.3 - 2.2) \times 10^6$
9.3 - 11.4	$(1.5 \pm 0.2 + 0.0 - 0.4) \times 10^5$	$(1.6 \pm 0.4 + 0.1 - 0.4) \times 10^5$
11.4 - 14.1	$(4.5 \pm 0.6 + 1.0 - 1.0) \times 10^5$	$(3.8 \pm 0.7 + 0.1 - 1.0) \times 10^5$
14.1 - 17.3	$(8.2 \pm 1.1 + 1.6 - 1.9) \times 10^4$	$(8.4 \pm 1.5 + 1.7 - 1.9) \times 10^4$
17.3 - 21.3	$(1.6 \pm 0.2 + 0.4 - 0.3) \times 10^3$	$(2.3 \pm 0.4 + 0.5 - 0.5) \times 10^3$
21.3 - 26.2	$(5.3 \pm 0.5 + 0.9 - 1.2) \times 10^3$	$(5.5 \pm 0.5 + 1.1 - 1.2) \times 10^3$
26.2 - 32.2	$(8.6 \pm 0.9 + 2.8 - 2.3) \times 10^2$	$(9.3 \pm 0.9 + 2.7 - 2.2) \times 10^2$
32.2 - 39.6	$(1.6 \pm 0.2 + 0.3 - 0.3) \times 10^1$	$(1.6 \pm 0.2 + 0.5 - 0.4) \times 10^1$
39.6 - 48.7	$(1.7 \pm 0.4 + 0.3 - 0.6) \times 10^0$	$(1.5 \pm 0.2 + 0.4 - 0.5) \times 10^0$
	bjp1 (± stat + sys - sys)	bjp2 (± stat + sys - sys)
5.0 - 6.2	$(3.8 \pm 0.5 + 0.1 - 1.2) \times 10^7$	—
6.2 - 7.6	$(1.1 \pm 0.1 + 0.0 - 0.3) \times 10^6$	—
7.6 - 9.3	$(2.8 \pm 0.3 + 0.7 - 0.8) \times 10^5$	$(5.8 \pm 1.0 + 0.4 - 2.0) \times 10^6$
9.3 - 11.4	$(7.8 \pm 0.7 + 1.9 - 2.0) \times 10^5$	$(9.8 \pm 1.1 + 0.6 - 2.8) \times 10^5$
11.4 - 14.1	$(2.1 \pm 0.2 + 0.4 - 0.5) \times 10^4$	$(2.8 \pm 0.3 + 0.0 - 0.7) \times 10^4$
14.1 - 17.3	$(5.8 \pm 0.5 + 1.1 - 1.3) \times 10^4$	$(6.2 \pm 0.6 + 1.4 - 1.5) \times 10^4$
17.3 - 21.3	$(1.6 \pm 0.1 + 0.4 - 0.4) \times 10^3$	$(1.5 \pm 0.1 + 0.3 - 0.4) \times 10^3$
21.3 - 26.2	$(4.1 \pm 0.4 + 0.9 - 1.1) \times 10^3$	$(4.2 \pm 0.3 + 0.8 - 1.0) \times 10^3$
26.2 - 32.2	$(8.9 \pm 1.2 + 2.0 - 3.1) \times 10^2$	$(9.1 \pm 0.8 + 2.6 - 2.5) \times 10^2$
32.2 - 39.6	$(10.0 \pm 2.6 + 3.6 - 1.9) \times 10^1$	$(1.4 \pm 0.1 + 0.4 - 0.4) \times 10^1$
39.6 - 48.7	—	$(1.5 \pm 0.2 + 0.5 - 0.6) \times 10^0$
	minb (± stat + sys - sys)	
5.0 - 6.2	$(7.0 \pm 0.6 + 0.8 - 1.4) \times 10^7$	
6.2 - 7.6	$(1.9 \pm 0.2 + 0.6 - 0.5) \times 10^6$	
7.6 - 9.3	$(4.1 \pm 0.5 + 1.5 - 0.9) \times 10^6$	
9.3 - 11.4	$(7.9 \pm 1.7 + 6.3 - 1.8) \times 10^5$	
11.4 - 14.1	$(6.6 \pm 3.9 + 31.2 - 0) \times 10^4$	

Table 6.4: The 2005 Inclusive Jet Cross-section Values with Statistical and Systematic Errors

Chapter 7

Cross-section Comparisons

The Inclusive Jet cross-section at STAR was also measured in 2003 and 2004. The 2003 and 2004 data were combined into a measurement of one cross-section[35]. The BEMC was being installed and commissioned between 2003 and 2005. However, if the changes to the BEMC were correctly taken into account, the cross-section from 2003, 2004 and 2005 should be equivalent as they describe the same physics. A check for consistency between the years is done in Section 7.1.

The motivation behind measuring the cross-section is to check that the data follow NLO pQCD predictions. ΔG, which was the value the experiment was measuring, is obtained from the asymmetry measurement assuming NLO pQCD. If the data did not follow NLO pQCD predictions, then that would put into question the abstraction of ΔG from the asymmetry measurement.

7.1 Comparison to Previous Results

Figure 7-1 is the same as Fig. 7-7 but with the 2003/2004 cross-section also included[35]. The 2003 and 2004 data were combined into one cross-section measurement. In 2003/2004 there were two triggers used for publication, high tower (HT) and MINB. The 2003/2004 MINB trigger was identical to the 2005 MINB trigger. The 2003/2004 HT trigger differed from 2005 in that it had a trigger threshold of 2.2 GeV for 2003 and varied between 2.2 GeV and 3.4 GeV depending on the pseudorapidity of the

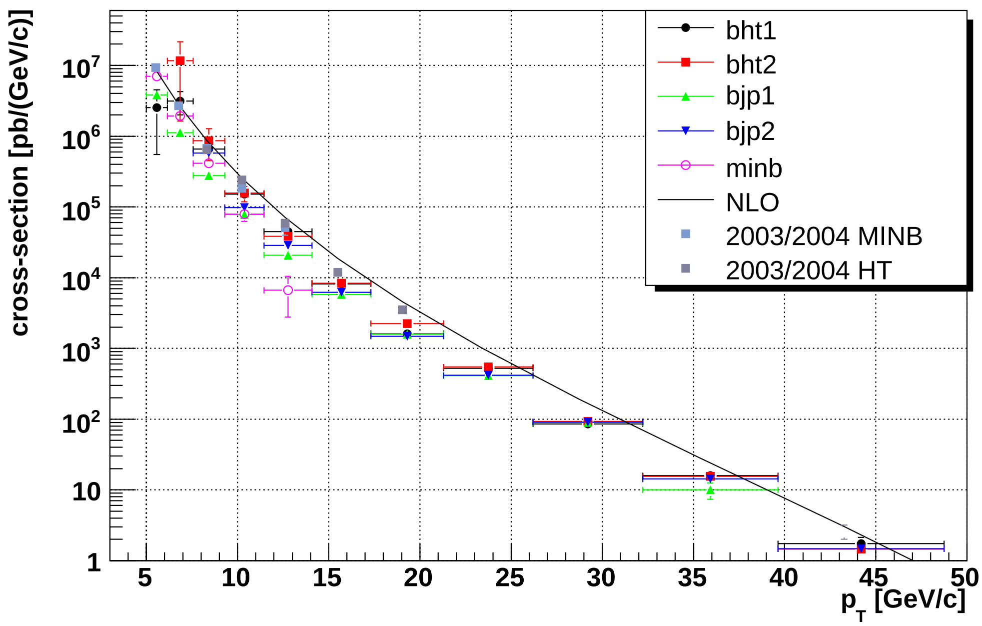

Figure 7-1: 2005 and 2003/2004 Cross-section

BEMC tower for 2004[1]. A cut was placed on the jets for 2003/2004 (2005) such that the trigger tower had to have at least 3.5 GeV (4.75 GeV). The 2003/2004 points are not plotted at the center of the transverse momentum range, but at a point determined from using an integral equation for a rapidly decreasing distribution[36]. The 2003/2004 cross-section is also systematically low compared to the theory prediction. However it agrees better with the theory prediction than the 2005 cross-section does.

Figure 7-2 shows the ratio of the cross-section from data to the theoretical cross-section for 2005 along with the 2003/2004 points and their systematic uncertainties. The black bars are the statistical uncertainties. The blue band represents the 2003/2004 systematic uncertainties. The major systematic uncertainty for 2003/2004 was the jet energy scale, which was a combination of the BEMC gain uncertainty and the charged track momentum uncertainty. Although the 2005 points are systematically low compared to 2003/2004, the 2005 points fall within the 2003/2004 systematic

[1] In 2004 the BEMC tower high voltages were accidentally set with a $\sin^2\theta$ dependence. A varying trigger threshold was needed to keep the high pseudorapidity jets from dominating the sample.

uncertainties. The 2003 and 2004 cross-sections were also individually systematically different from each other by 20%. The 2003/2004 MINB cross-section also disagrees more with theory as the momentum increases, just like the 2005 MINB cross-section.

Figure 7-3 shows the 2003/2004 and 2005 cross-sections with the 2005 systematic uncertainty. The 2005 systematic uncertainty was much smaller than the 2003/2004 systematic uncertainty and the 2003/2004 points do not fall within the 2005 systematic uncertainty. The smaller 2005 systematic uncertainty was due to a smaller jet energy scale uncertainty for 2005 compared to 2003/2004.

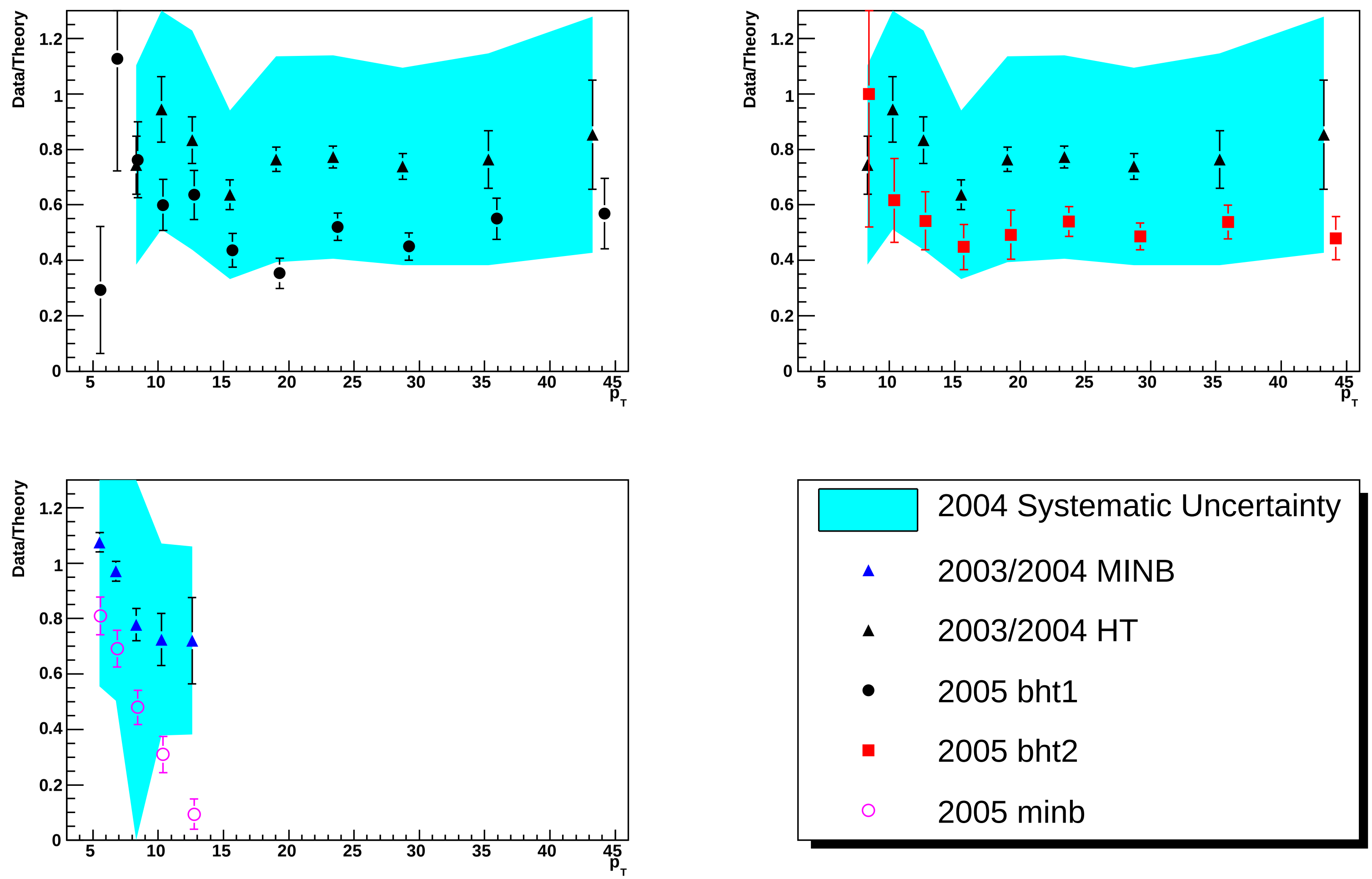

Figure 7-2: 2005 Inclusive Jet Cross-section divided by NLO pQCD value for cross-section

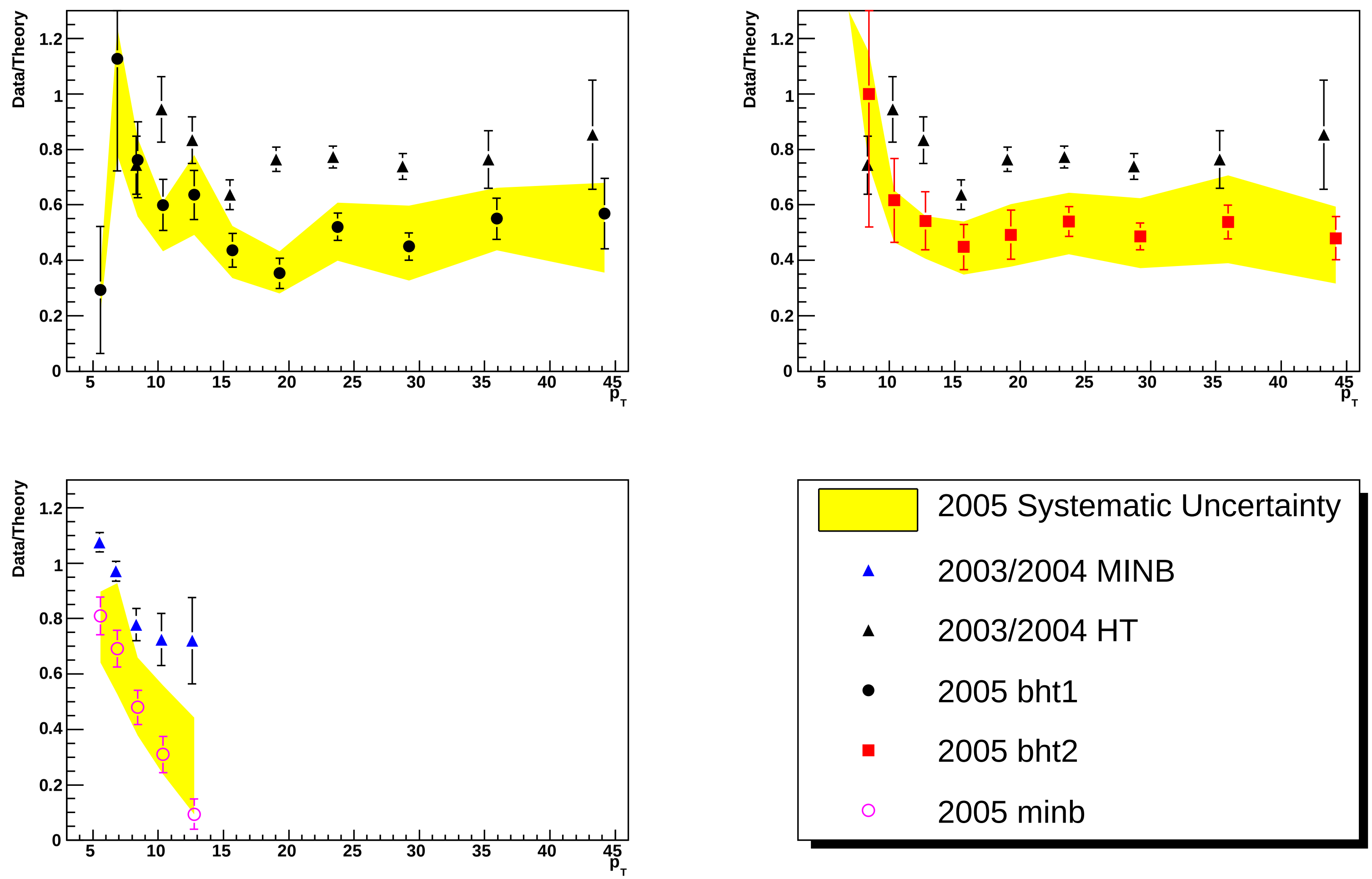

Figure 7-3: 2005 Inclusive Jet Cross-section divided by NLO pQCD value for cross-section

7.2 Neutral Energy Study

Since the Jet Energy Scale systematic uncertainty was the largest systematic uncertainty, it was the most likely cause of the differences between the 2003/2004 cross-section and the 2005 cross-section. The cross-section was divided into regions of low neutral energy and high neutral energy, where neutral energy (R) is defined in a previous chapter, in order to test whether the BEMC gain uncertainty was causing the difference between the 2003/2004 cross-section and the 2005 cross-section. At the extreme of R = 0, none of the jet energy was from the BEMC, and so the cross-section would not have been affected at all and it was expected that the 2004 and 2005 cross-sections would agree. At the opposite extreme of R = 1, the maximum disagreement was expected to occur.

The two extremes of R = 0 and R = 1 contained a lot of background and the jets with these values of neutral energy were not used in calculating the cross-section. So a cross-section comparison between 0.2 < R < 0.5 and 0.5 < R < 0.8 was made instead, with the expectation that the cross-sections from the lower neutral energy region would be more in agreement than the cross-sections from the higher neutral energy region.

As a test of this idea, a simulation was conducted using only 2005 data. The jets were found in the data with the BEMC gain systematically too high, or too low, by 4.8%. The cross-sections were calculated for the regions of low and high neutral energy, and the cross-section from the high, low and normal gains were compared. Figure 7-4 (7-5) gives the results for the gain systematically too high (low). In each case the cross-section with the higher gains was divided by the cross-section with the lower gains. One run list was used for the jets that had their BEMC gains changed and a different run list was used for runs with the standard gains so that the ratio uncertainty was easier to calculate. For both Fig. 7-4 and Fig. 7-5 the ratio of cross-sections for $R > 0.5$ is always greater than for $R < 0.5$ or consistent with it. So this method can distinguish if the difference is due to BEMC gains.

This method can also test whether or not the systematic shift was due to the

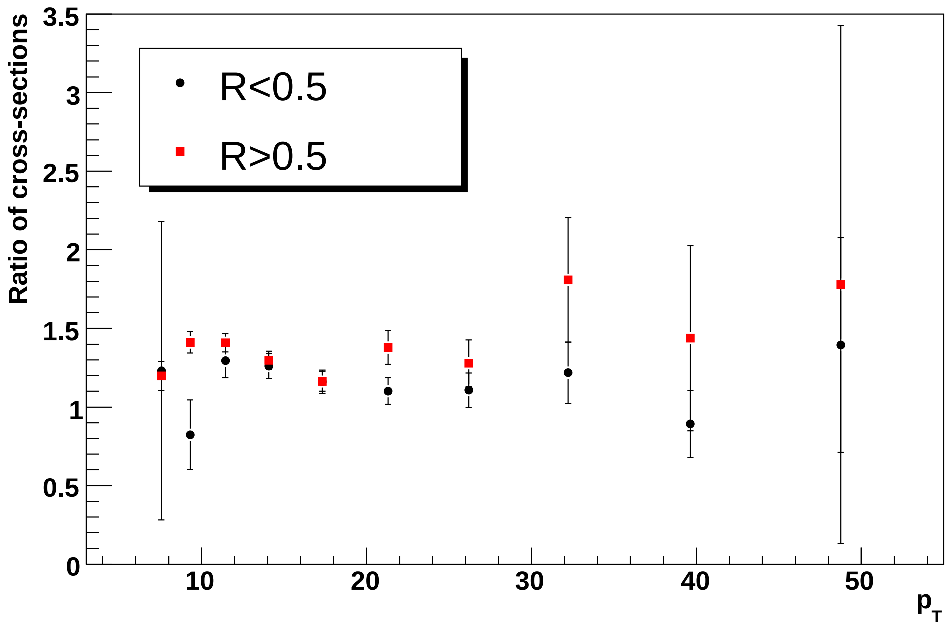

Figure 7-4: Simulated Neutral Energy Sorted Cross-section comparison for raised BEMC gains

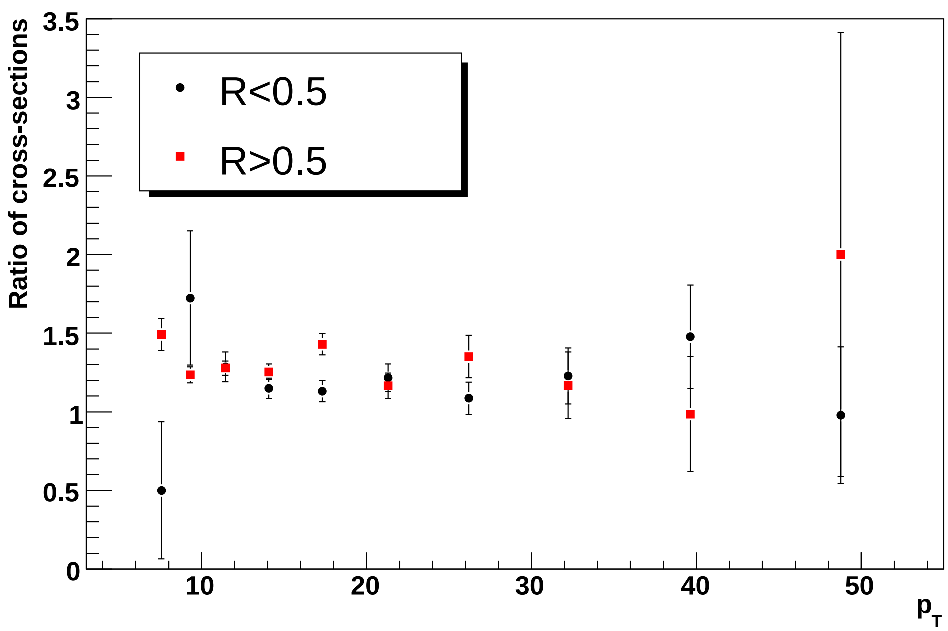

Figure 7-5: Simulated Neutral Energy Sorted Cross-section comparison for lowered BEMC gains

charged track momentum uncertainty as the charged track momentum uncertainty is expected to act in the opposite direction of the BEMC gain uncertainty. So a positive slope was due to the BEMC gain uncertainty and a negative slope would have been due to the charged track momentum uncertainty.

The ratio of cross-sections sorted by neutral energy for 2004 and 2005 was looked at. The cross-section was simplified to the ratio of jet yields for the two regions. This made the assumption that the ratio of correction factors for 2004 and 2005 remained constant (or changed negligibly) as the neutral energy changed. Eight out of ten transverse momentum ranges had the disagreement between 2004 and 2005 get worse as the neutral energy increased. Figure 7-6 shows the ratios.

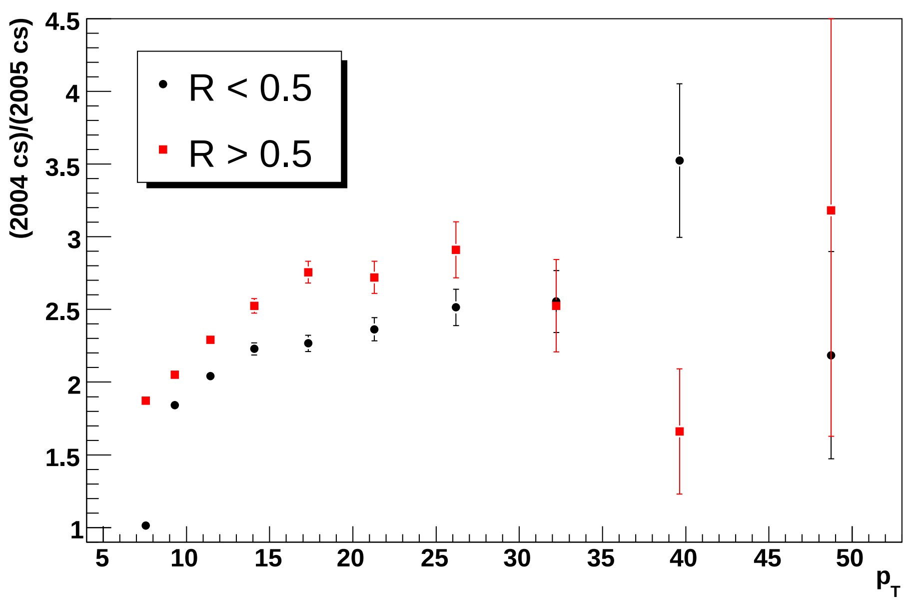

Figure 7-6: Neutral Energy Sorted Cross-section comparison

7.3 Comparison to Theory

Figure 7-7 shows the 2005 inclusive jet cross-section with the theory prediction from NLO pQCD[30]. Figure D-1 shows the cross-section separated by the different trigger data. The theory curve was calculated using CTEQ6M[37] parton distributions. The cross-sections for the five triggers agree fairly well with each other. This suggests that

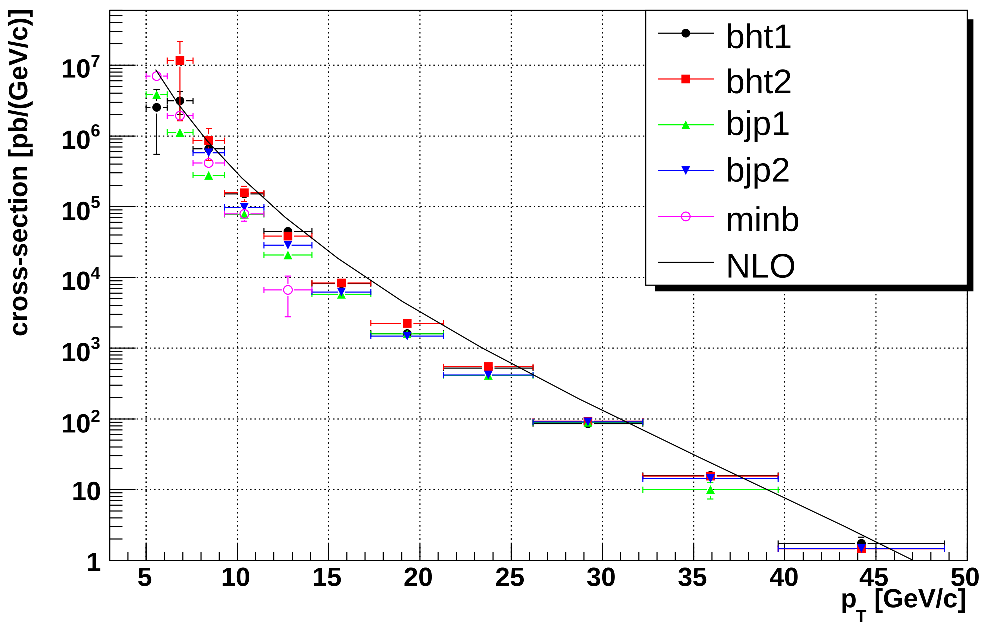

Figure 7-7: 2005 Inclusive Jet Cross-section

the correction factors are handling trigger inefficiencies and trigger bias well. The cross-sections are systematically low with respect to the theory prediction. However, the theory line passes through the horizontal bars, which represent the transverse momentum range of the points. The points were plotted at the center of the momentum range.

Figure 7-8 shows the ratio of the cross-section to the theoretical prediction[30] for the BHT1 trigger data. The yellow band is the cross-section's systematic uncertainty and the black bars are its statistical uncertainty. Figure 7-9 gives the comparisons for all five triggers. The BHT1, BHT2 and BJP2 cross-sections, other than the first few points, are about half of the theory prediction. For the BJP1 cross-section the ratio is about 0.4. The MINB trigger data disagreement with the theory prediction increases as the transverse momentum increases. This is also seen in the trigger data in the region of $p_T < 12$ GeV/c, which is the region the MINB trigger data covers.

Figure 7-10 shows the difference between the theory prediction and the 2005 cross-section for all five triggers on one graph. Figure D-2 shows the difference trigger

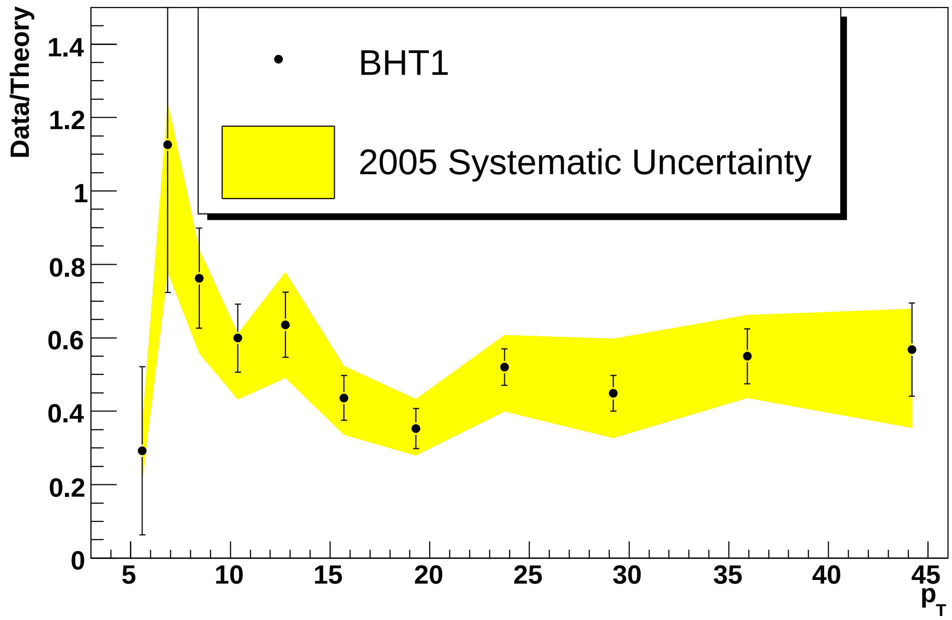

Figure 7-8: Data Theory Ratio for BHT1

sorted. Since this is a difference, agreement between theory and the 2005 cross-section would give points of zero on the y-axis. This shows that, other than the low transverse momentum region, the five triggers agree fairly well on their difference between theory and the 2005 cross-section.

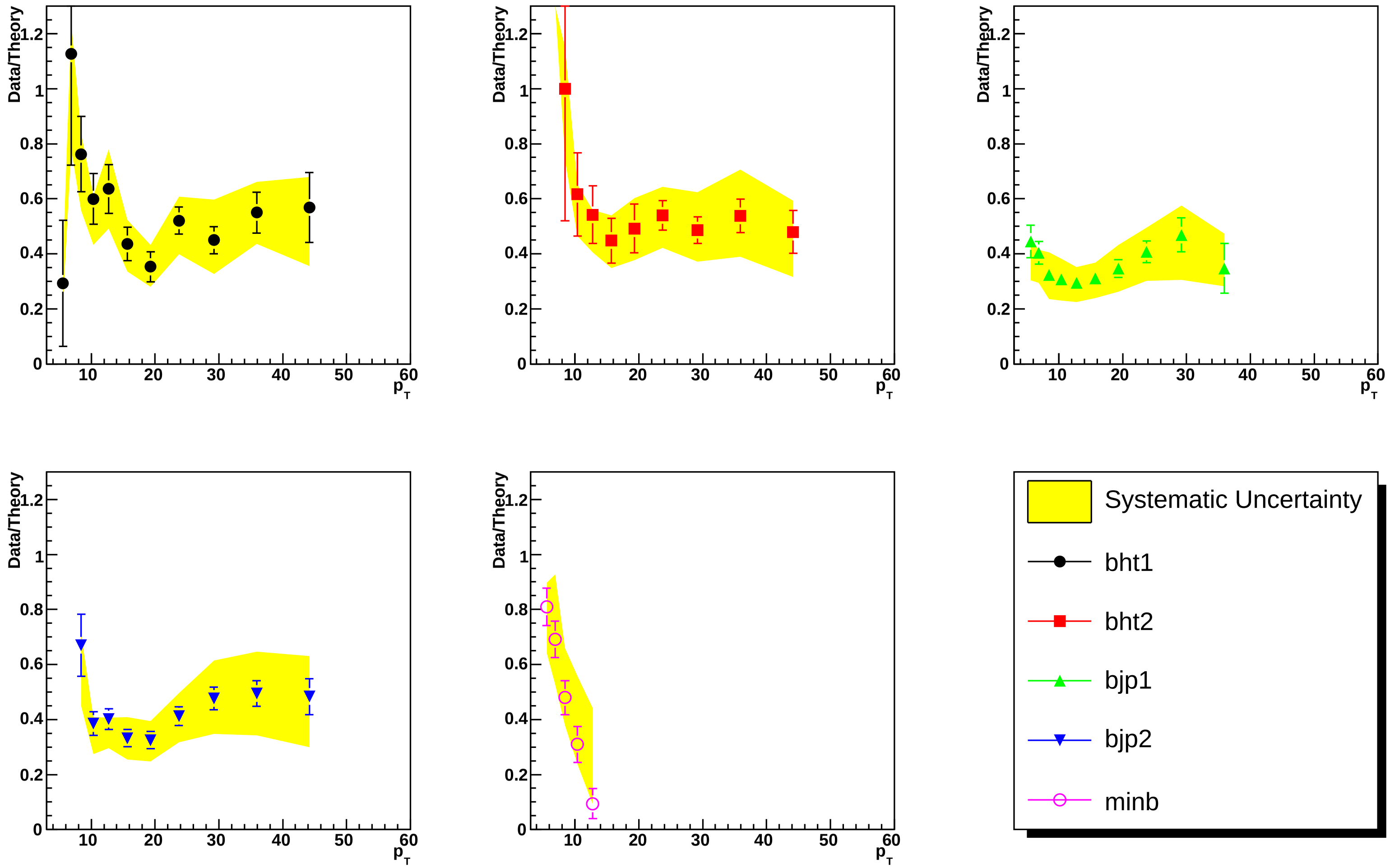

Figure 7-9: 2005 Inclusive Jet Cross-section divided by the NLO pQCD prediction

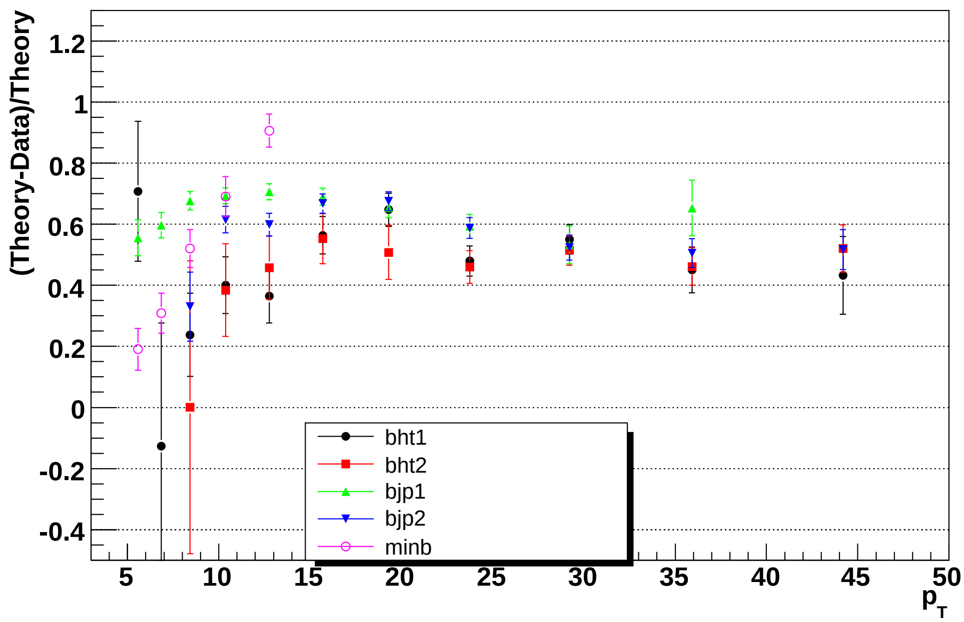

Figure 7-10: Difference between Data and Theory

7.4 Discussion

The 2005 cross-section falls within the 2003/2004 cross-section systematic uncertainties and so the 2003/2004 and 2005 cross-sections agree with each other. The 2005 systematic uncertainties are smaller than the 2003/2004 systematic uncertainties due to a better understanding of the BEMC gains and a less cautious treatment of the systematic uncertainties.

The reason the 2005 cross-section was systematically low compared to the 2003/2004 cross-section is most likely due to the uncertainty in the BEMC gains. In 2003 (2004) the BEMC was calibrated using d-Au (Au-Au) collisions, whereas in 2005 the BEMC was calibrated using proton-proton collisions. This was the most likely cause for the three cross-sections being systematically offset from each other.

The cross-section was approximately half of the theory prediction, which is fairly close to the prediction since the cross-section is a steeply falling function. Measurements of the 2003, 2004 and 2005 inclusive jet cross-sections are all systematically lower than the theoretical prediction. The disagreement between experiment and theory is most likely due to a lack of insight in how to apply NLO pQCD to the experiment. For instance, the renormalization and factorization scales were set to $\mu_F = \mu_R = p_T$. Changing these scales results in a different theoretical prediction. It is also possible that a different parton distribution function should be used as this also affects the cross-section.

Although the measured cross-section is close to theoretical predictions, they do not completely agree. More work is needed to obtain agreement between the measured cross-section and theoretical predictions. The input of theorists will be necessary in determining the reason for the disagreement between measurement and theoretical predictions.

THIS PAGE INTENTIONALLY LEFT BLANK

Chapter 8

Summary and Conclusion

8.1 The Gluon's Contribution to the Proton's Spin

Ellis and Jaffe used a sum-rule to estimate that the quarks contribute 60% of the proton's spin. The remaining 40% comes from the orbital angular momentum of the quarks and gluons[5]. DIS experiments found the percentage from the quark contribution to be closer to 30%[4, 1]. The remaining 70% needs to come from the gluons and/or the orbital angular momentum.

DIS experiments also measured the contribution from the gluons[1]. However, due to the fact that leptons couple to gluons only at next-to-leading order, the DIS experimental measurement of the gluon contribution to the proton's spin had large uncertainties. Experiments[35, 38] using polarized protons were better able to constrain the gluon contribution, since the quarks and gluons inside the protons couple in leading order to each other.

The Double Spin Longitudinal Asymmetry was used to measure the gluon's contribution to the proton's spin. The asymmetry was defined as the ratio of the polarized cross-section to the unpolarized cross-section. The polarized (unpolarized) cross-section is the difference (sum) of the cross-sections from collisions where the product of the proton helicities was +1 and -1.

The factorization theorem says that the polarized cross section for jets ($d\Delta\sigma$), can be written as

$$\frac{d\Delta\sigma}{dp_T d\eta} = \sum_{a,b} \Delta f_a(x_a,\mu) \bigotimes \Delta f_b(x_b,\mu) \bigotimes \frac{d\Delta\hat{\sigma}_{ab}}{dp_T d\eta}(x_a, x_b, p_T, \eta, \mu)[3],$$

where convolutions are represented as $\otimes$ and the sum is over all participating partons. Δf_a and Δf_b are the two partons interacting in the collision. They could be quarks (Δq) and/or gluons (Δg).

In order to extract the gluon contribution to the proton's spin at least one gluon had to be participating in the interaction between protons. In the STAR kinematic region, most low transverse momentum collisions were between two gluons. In the mid-transverse momentum range, the interactions were mostly quark-gluon collisions. Quark-quark collisions were only a small fraction of the collisions for the transverse momentum range at STAR.

Theorists calculated the value of the asymmetry for different values of Δg[30]. The experimentally measured asymmetry was then compared to the theorists' calculations of the asymmetry. Since NLO pQCD was assumed in the theorists' calculation of the asymmetries, a cross-section that was consistent with NLO pQCD became necessary.

8.2 The STAR Experiment

The STAR experiment at BNL was designed to detect the Quark-Gluon Plasma and to measure the contribution of gluons to the proton's spin. Polarized protons with center-of-mass energies up to 500 GeV were collided. Collisions between protons at center-of-mass energy equal to 200 GeV were used for this analysis.

A large time-projection-chamber (TPC) and a barrel-electromagnetic-calorimeter (BEMC) were the main components of the detector. The TPC covered a range of $|\eta| < 1.8$ in pseudorapidity and measured the momentum of particles in the range $100 MeV/c < p < 30 GeV/c$. The BEMC was a Pb-plastic sampling calorimeter that covered a region of $|\eta| < 1$ and $0 < \phi \leq 2\pi$. It was approximately 20 radiation lengths at $\eta = 0$. Plastic-scintillator beam-beam counters located at $3.3 < |\eta| < 5.0$ were used to detect that a collision occurred, make spin dependent relative luminosity measurements, and measure non-longitudinal spin components of the beam. The detectors all covered the full azimuthal angle.

8.3 Cross-section

ΔG was extracted from the asymmetry using NLO pQCD. The Inclusive Jet cross-section measurement was made to verify that the data followed NLO pQCD predictions. The differential cross-section was defined as

$$d\sigma = \frac{dN}{\text{flux } d\eta d\phi dp_T} \frac{1}{\text{correction factor}}$$

where dN was the number of jets, $d\eta = 0.8$ was the jet pseudorapidity range, $d\phi = 2\pi$ was the azimuthal range and p_T is the transverse momentum. The correction factors were obtained from Monte-Carlo Simulation and converted jets composed of TPC tracks and BEMC towers into jets composed of particles, corrected for detector resolution, and corrected trigger inefficiencies. The major systematic uncertainty for 2005 was the jet energy scale that had contributions from the jet momentum uncertainty and the jet transverse energy uncertainty.

The 2005 cross-section was within the systematic uncertainty of the 2003/2004 cross-section. However, it was systematically low compared to the 2003/2004 results. This could be accounted for by 2003/2004 BEMC gains fluctuating 10% too high. The 2005 systematic uncertainties are smaller than the 2003/2004 systematic uncertainties due to a better understanding of the BEMC gains and a more careful treatment of the systematic uncertainties.

The cross-section was approximately half of the theory prediction, which is fairly close to the prediction since the cross-section is a steeply falling function. Measurements of the 2003, 2004 and 2005 inclusive jet cross-sections are all systematically lower than the theoretical prediction. The disagreement between experiment and theory is most likely due to a lack of insight in how to apply NLO pQCD to the experiment. For instance, the renormalization and factorization scales were set to $\mu_F = \mu_R = p_T$. Changing these scales would result in a different theoretical prediction. It is also possible that a different parton distribution function should be used as this also affects the cross-section.

8.4 Longitudinal Double Spin Asymmetry

The gluon contribution to the proton was determined by measuring the longitudinal double-spin asymmetry. The double spin asymmetry, defined as

$$A_{LL} = \frac{\sigma^+ - \sigma^-}{\sigma^+ + \sigma^-},$$

where $\sigma^+(\sigma^-)$ was the cross-section for protons with same (opposite) sign helicity was calculated as

$$A_{LL} = \frac{\sum_{run} P_{run}(N^+_{run}R_{run} - N^-_{run})}{\sum_{run} P^2_{run}(N^+_{run}R_{run} + N^-_{run})},$$

where P is the product of the beam polarizations, $N^+(N^-)$ was the number of jets for collisions with same (opposite) helicity, and R was the relative luminosity between the two helicity states. The measurement had an average polarization of 45% - 50% and a sampled luminosity of 2 pb^{-1}. The largest systematic uncertainty was from trigger and reconstruction bias that was transverse momentum dependent and varied from 0.0015 to 0.008. The other non-zero systematic uncertainties were from background, relative luminosity, and non-longitudinal beam components. The asymmetry was calculated for inclusive jets for a transverse momentum range of $5GeV/c < p_T < 30GeV/c$. Values of $\Delta G > 0.33$ were ruled out with a confidence of 90% and the minimum scenario of $\Delta G = -G$ was ruled out with a confidence of 94%. The result was consistent with the measurement from 2003/2004.

Figure 8-1 shows the confidence levels of the asymmetry for various measurements of Δ G. GRSV-std on the picture is the most likely value of Δ G from previous experimental measurements. The 2005 measurement shown in this thesis rules out that value with a confidence level of 90%. GRSV-std corresponds to Δ G = 0.24 with

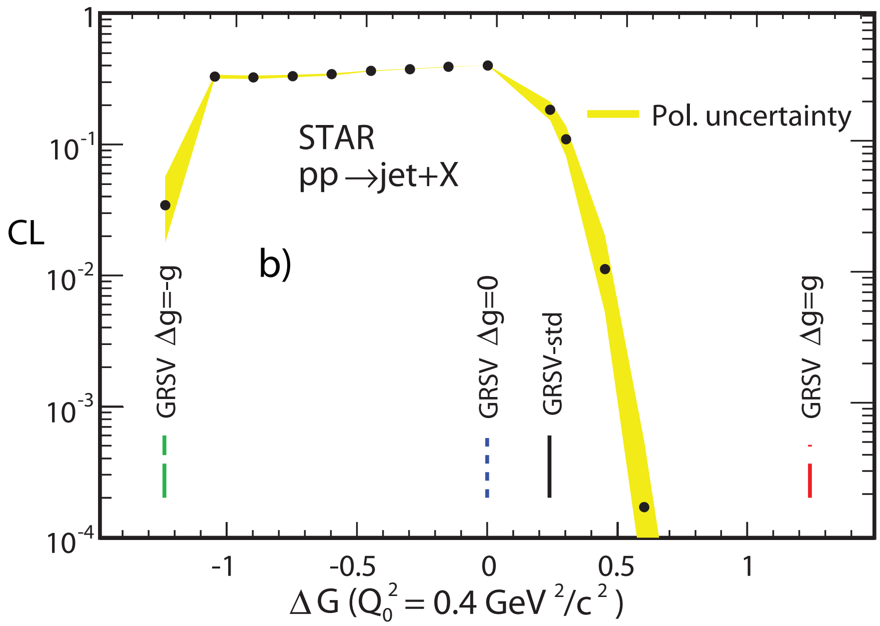

Figure 8-1: Confidence Levels

a range of $-0.45 < \Delta G < 0.7$[2]. The asymmetry measurement in this thesis rules out $\Delta G > 0.33$ with at least 90% confident level.

THIS PAGE INTENTIONALLY LEFT BLANK

Appendix A

The Double-Spin Asymmetry Systematic Uncertainties

The single-spin asymmetry uncertainty was described in a previous chapter. This chapter contains the systematic uncertainty studies for the asymmetry measurement made by members of the STAR collaboration, including the author.

A.1 Single-Spin Asymmetry Uncertainty

The proton beams had positive or negative helicity when they collided. A single-spin asymmetry was defined as

$$A_L = \frac{\sigma_+ - \sigma_-}{\sigma_+ + \sigma_-},$$

where σ_+ (σ_+) is the cross-section for one beam having positive (negative) helicity and the other beam unpolarized. In practice, the unpolarized beam was made from using the polarized beam and summing over the negative and positive helicity states, taking into account the relative luminosities. The single-spin asymmetry was expected to be zero due to conservation of parity. There is a parity violating term in the cross-section, but it is negligible at the center of mass energy for this thesis. It was measured for both beams (labeled yellow and blue for reference) and found to be consistent with zero. Table A.1 gives the values and Figs. A-1 - A-4 show plots of the asymmetry as

$p_T(GeV/c)$	Blue $\times 10^{-3}$	Yellow $\times 10^{-3}$
5.0 - 6.2	-0.1 $\pm$ 3.2	4 $\pm$ 4
6.2 - 7.6	-2 $\pm$ 3	-4 $\pm$ 3
7.6 - 9.3	5 $\pm$ 3	0.4 $\pm$ 3
9.3 - 11.4	1 $\pm$ 4	9 $\pm$ 4
11.4 - 14.1	2 $\pm$ 5	3 $\pm$ 5
14.1 - 17.3	7 $\pm$ 7	-0.2 $\pm$ 75
17.3 - 21.3	10 $\pm$ 10	4 $\pm$ 120
21.3 - 26.2	-10 $\pm$ 20	50 $\pm$ 20
26.2 - 32.2	-10 $\pm$ 40	10 $\pm$ 40
32.2 - 39.6	60 $\pm$ 70	-40 $\pm$ 80
39.6 - 48.7	-100 $\pm$ 200	-400 $\pm$ 200

Table A.1: Single-Spin Asymmetry Values

a function of transverse momentum.

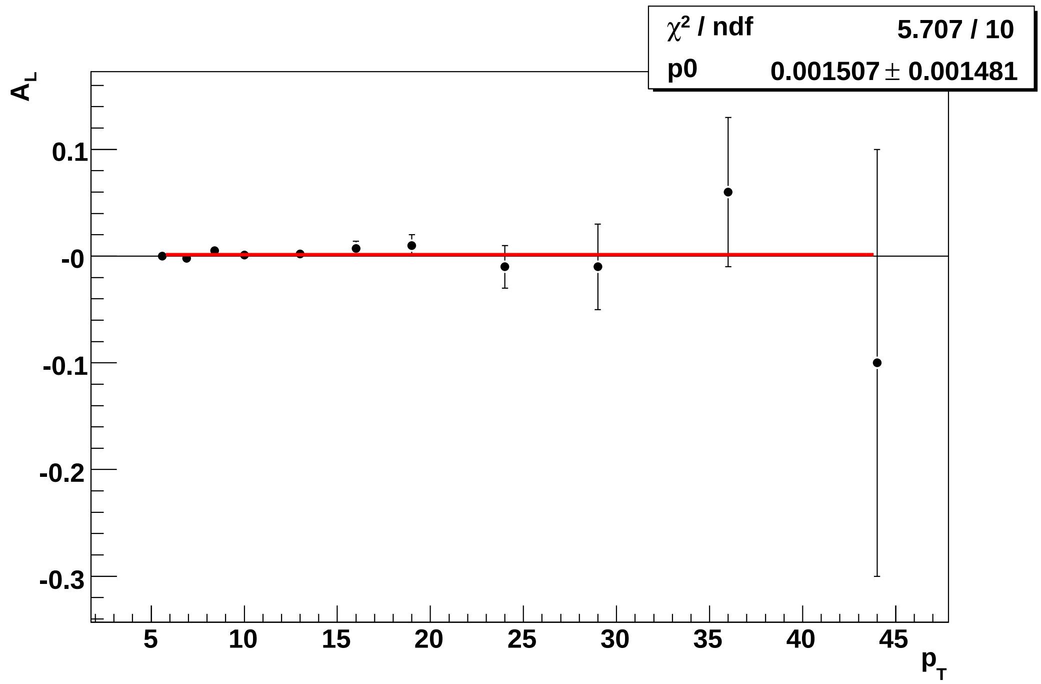

Figure A-1: Single-Spin Asymmetry for Blue Beam

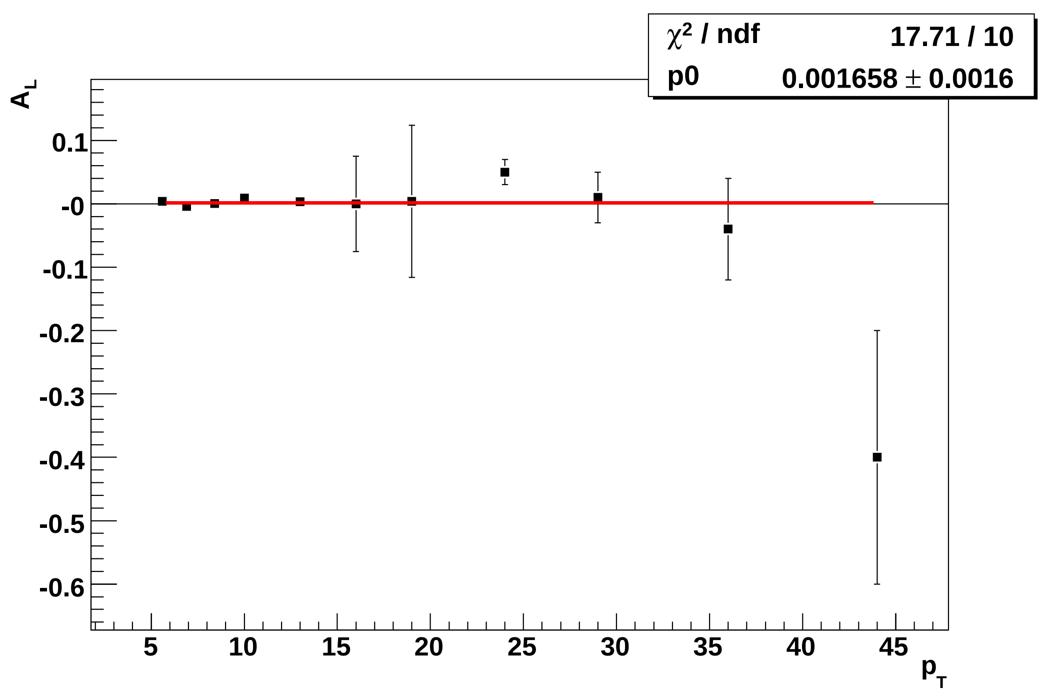

Figure A-2: Single-Spin Asymmetry for Yellow Beam

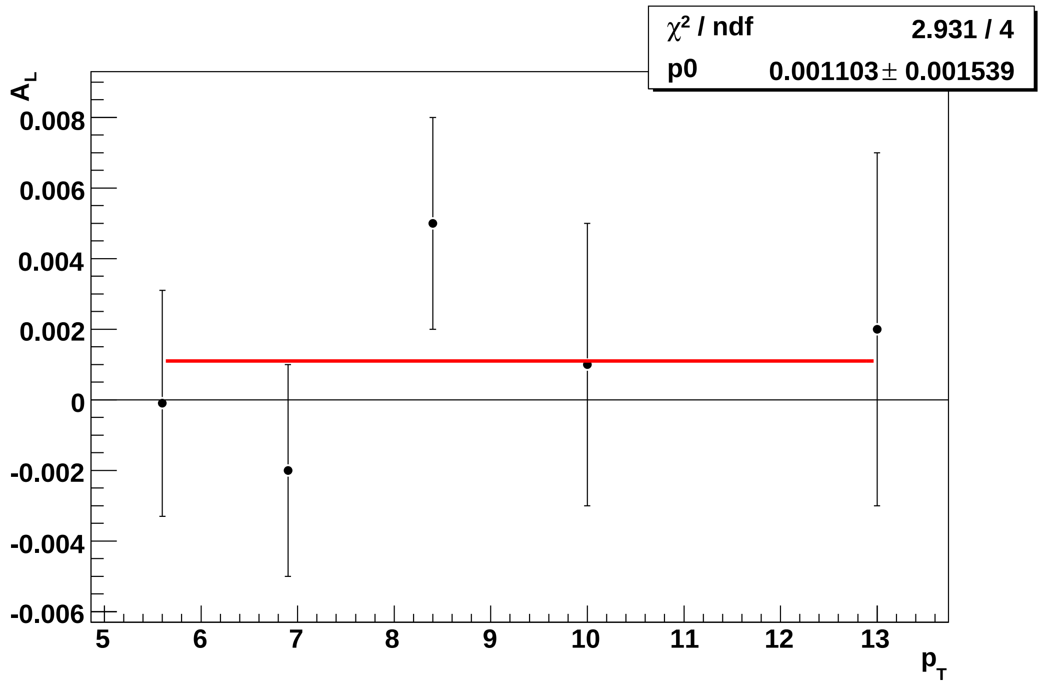

Figure A-3: Blue Beam Single-Spin Asymmetry for low transverse momentum

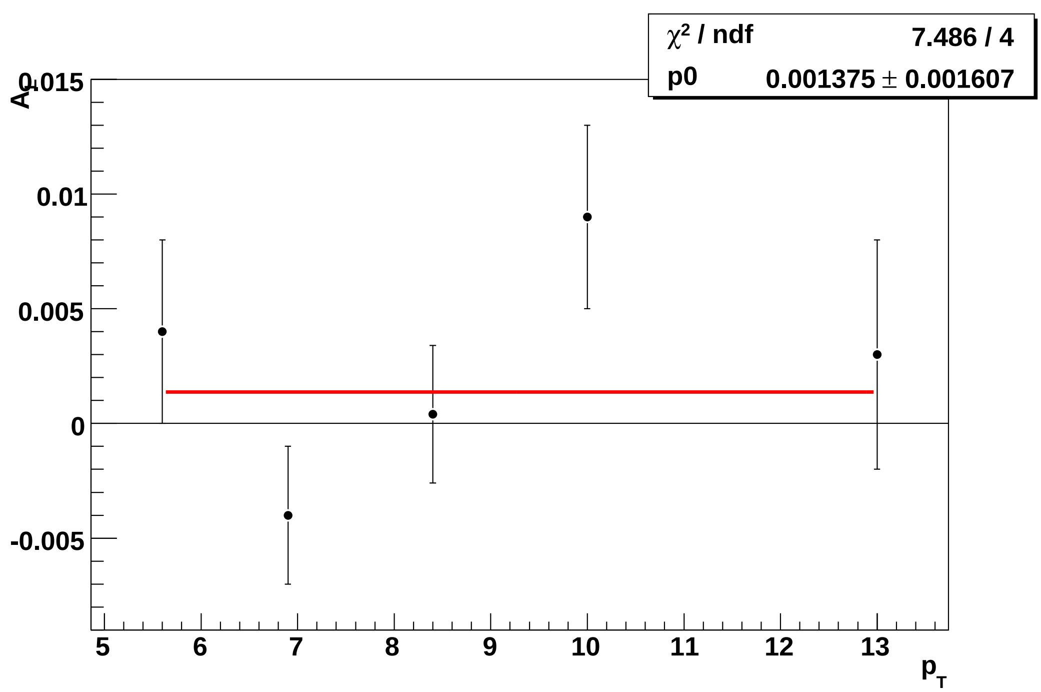

Figure A-4: Yellow Beam Single-Spin Asymmetry for low transverse momentum

A.2 Relative Luminosity Uncertainty

The luminosities of the positive and negative helicity collisions were kept as close to each other as possible. However, the luminosities varied between helicity states, and this difference was measured by the relative luminosity. For the asymmetry measurement, the relative luminosities were measured by looking at how many events occurred as measured by remnant particles hitting the BBC for the different helicity states.

The ZDC was also able to measure the relative luminosity. The uncertainty on the relative luminosity was found by measuring it using the BBC and the ZDC[1]. This was done four ways: all BBC timebins compared to ZDC Board 5, BBC timebins 7-9 compared to ZDC Board 5, all BBC timebins compared to ZDC Board 6, and BBC timebins 7-9 compared to ZDC Board 6. The results for BBC timebins 7-9 compared to ZDC Board 5 are shown in Fig. A-5. For each run, the relative luminosity difference was calculated for the four different ways. Four histograms were filled with the results and a Gaussian was fit to the data. The maximum mean from the four histograms set the limit on the relative luminosity uncertainty. The difference in measurements gave an uncertainty on the relative luminosity of less than 2.45×10^{-4}. An uncertainty in relative luminosity (R) led to an uncertainty in the asymmetry (A) of less that 5.0×10^{-4}, as follows.

$$A = \frac{N_+R - N_-}{P(N_+R + N_-)},$$

where N_+ (N_-) is the number of jets from collisions with positive (negative) helicity and P is the beam polarization.

$$\begin{aligned} A + \delta A &= \frac{N_+(R+\delta R) - N_-}{P[N_+(R+\delta R) + N_-]} = \frac{N_+R + N_+\delta R - N_-}{P[N_+R + N_+\delta R + N_-]}, \\ &= \frac{N_+R + N_+\delta R - N_-}{P(N_+R + N_-)} \frac{1}{1 + \frac{N_+}{N_+R+N_-}\delta R} \approx \frac{N_+R + N_+\delta R - N_-}{P(N_+R + N_-)}, \end{aligned}$$

[1]The BBC and ZDC are described in a previous chapter

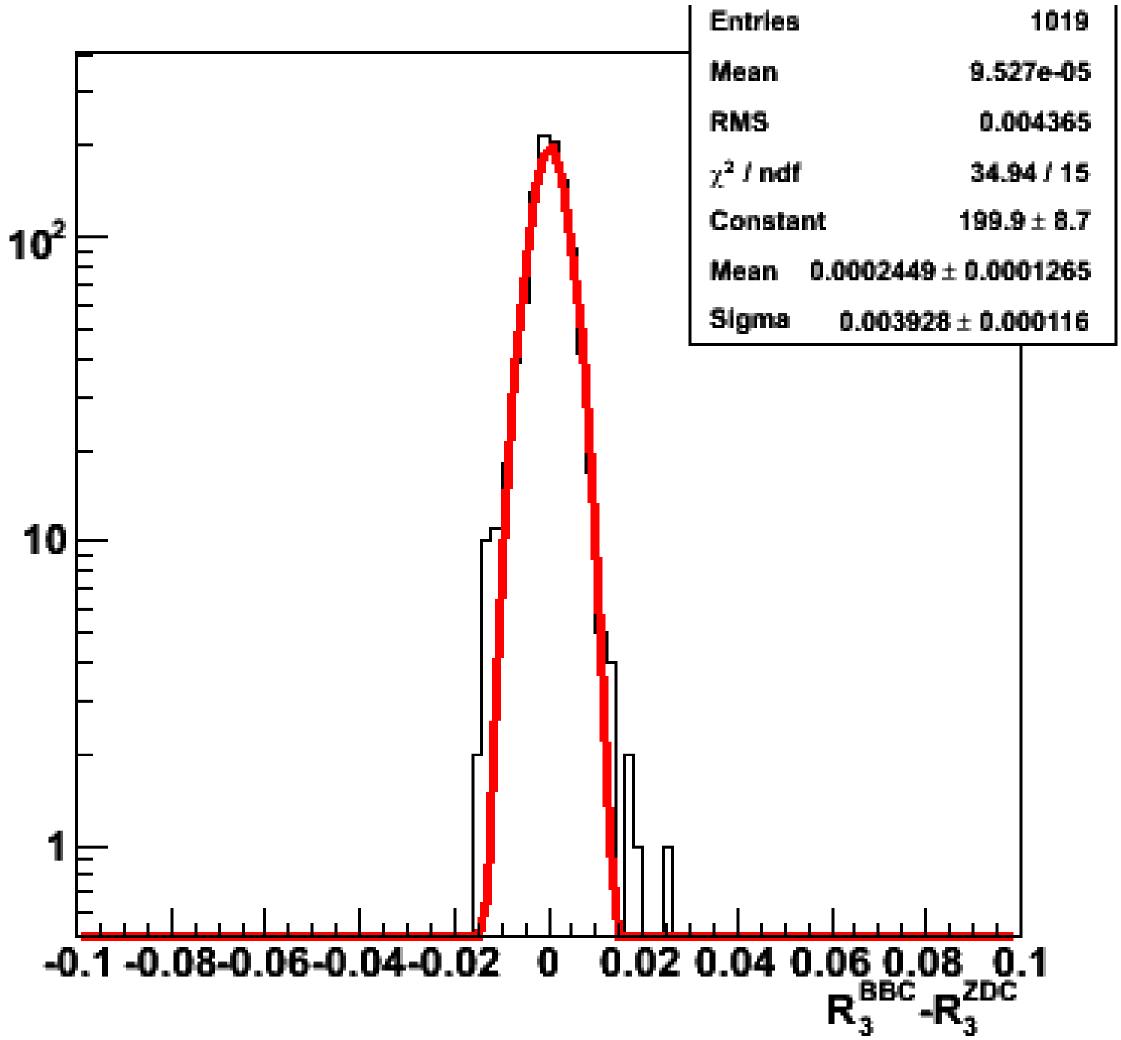

Figure A-5: Relative Luminosity difference between BBC timebins 7-9 and ZDC Board 5

$$
\begin{aligned}
&= \frac{N_+R - N_-}{P(N_+R + N_-)} + \frac{N_+\delta R}{P(N_+R + N_-)} = A + \frac{N_+}{N_+R + N_-}\frac{\delta R}{P} \approx A + \frac{1}{2}\frac{\delta R}{P}, \\
\Rightarrow \delta A &\approx \frac{\delta R}{2P} < 5.0 \times 10^{-4}.
\end{aligned}
$$

A.3 Background Uncertainty

A.3.1 Asymmetry Effect

The measured asymmetry contained jets from background events. This affected the asymmetry measurement as follows.

$$
A_{LL}^M = \frac{N_+^M - N_-^M}{N_+^M + N_-^M} = \frac{(N_+ + N_+^B) - (N_- + N_-^B)}{(N_+ + N_+^B) + (N_- + N_-^B)},
$$

where A_{LL} is the double spin asymmetry, N_+ (N_-) is the number of jets for the product of the helicities equal to +1 (-1), M (B) stands for measured (background), and no superscript means for proton-proton collisions.

$$
\begin{aligned}
A_{LL}^M &= \frac{(N_+ - N_-) + (N_+^B - N_-^B)}{(N_+ + N_-) + (N_+^B + N_-^B)}, \\
&= \frac{A_{LL}(N_+ + N_-) + A_{LL}^B(N_+^B + N_-^B)}{(N_+ + N_-) + (N_+^B + N_-^B)}, \\
&= \frac{A_{LL} + A_{LL}^B f}{1 + f},
\end{aligned}
$$

where $f = \frac{N_+^B + N_-^B}{N_+ + N_-}$ is the fraction of jets due to background.

It was shown in the 2004 asymmetry measurement that the beam background was correlated with the percentage of events in the abort gaps. Figure A-6 shows the fraction of events in the abort gaps for each run. Figure A-7 shows the distribution of fraction of beam background in the abort gaps for the runs. The runs with 8% or more of their events in the abort gaps, 21% of the runs, were set to be high background runs.

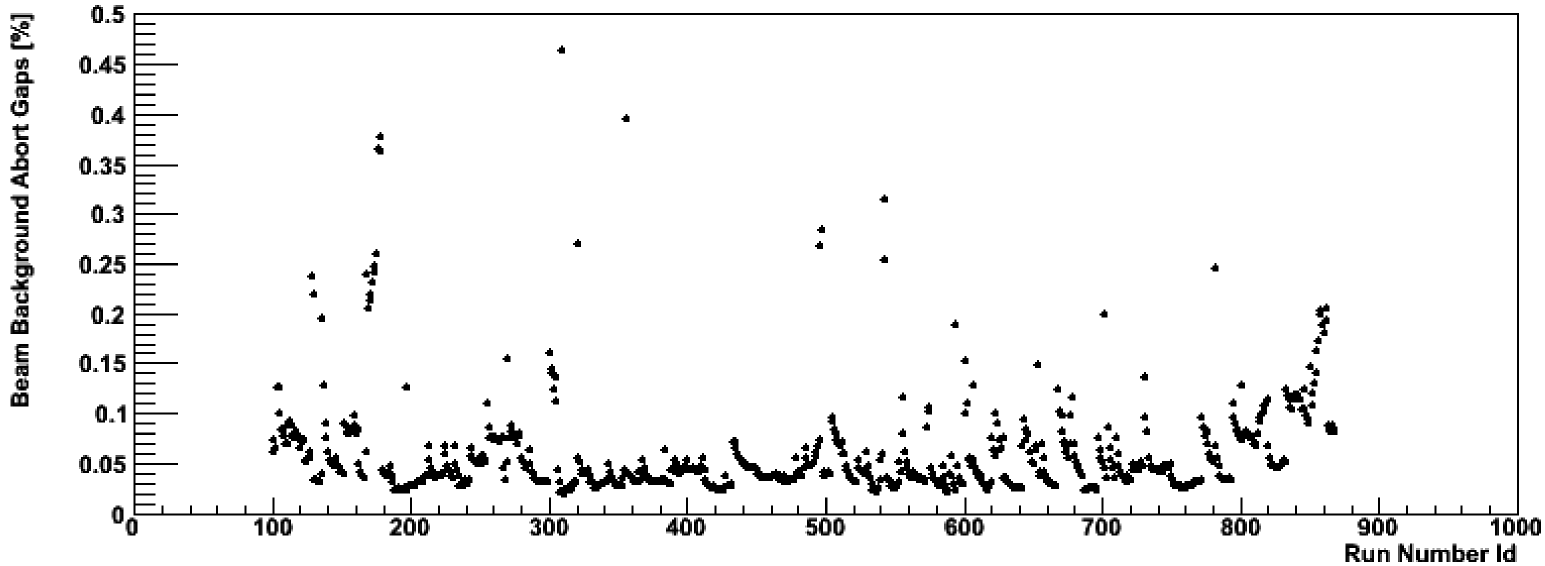

Figure A-6: The fraction of events in the abort gaps for each run

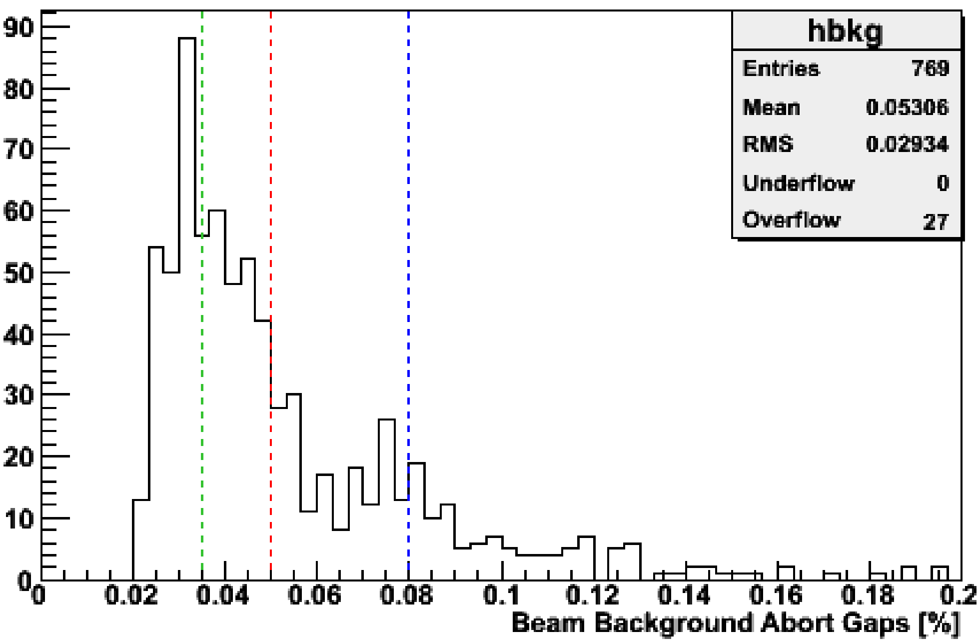

Figure A-7: Histogram of fraction of events in the abort gaps

A histogram with the number of jets as a function of neutral energy ratio[2] was filled for the high background runs and the low background runs (see Fig. A-8). The two histograms were normalized and subtracted to find the maximum contribution of background to the number of jets (see Fig. A-9).

The asymmetry was then calculated for the background contribution. Because the background asymmetry was found to be independent of transverse momentum, a constant line was fit to the found asymmetries for the various transverse momentum bins. The value of this constant line was the maximum contribution of the background to the asymmetry and had a value of 0.7×10^{-3}.

A.3.2 Relative Luminosity Effect

Background also affected the asymmetry measurement by altering the relative luminosity measurement. To estimate the background, the beam abort-gaps were used. If there

[2]defined in a previous chapter

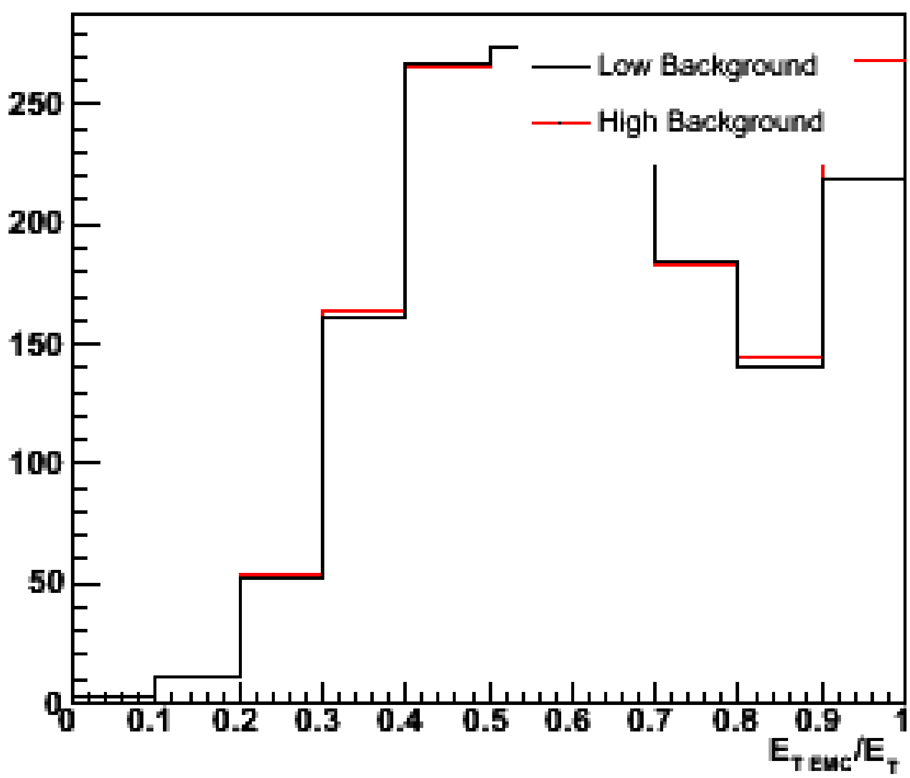

Figure A-8: Normalized number of jets for high and low background runs

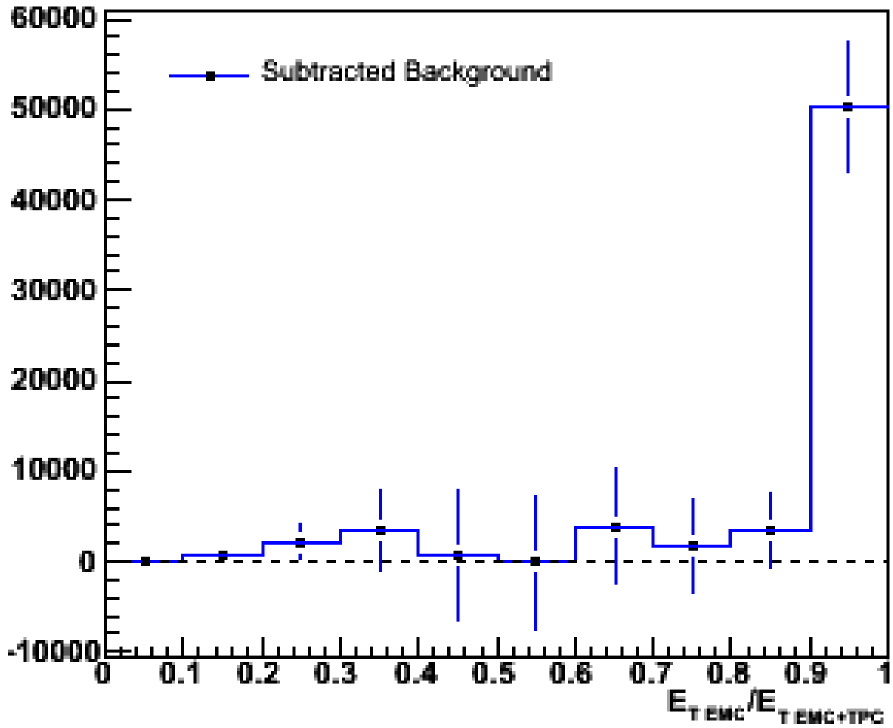

Figure A-9: Subtracted background as a function of neutral energy ratio

were no background, no BBC counts[3] would occur in the abort gaps. By looking at how many BBC counts were recorded in the abort gaps, an estimate of the error on the counts was calculated.

Relative luminosities were calculated by dividing the number of BBC counts for events where the product of the proton helicities was +1 by the number of BBC counts for events where the product of the proton helicities was -1. Background increased the number of BBC counts and thus changed the ratio. Background was estimated by adding the counts in the abort gaps and normalizing to the number of bunches in the abort gaps.

The relative luminosities were recalculated for each run with the background contribution subtracted from the number of BBC counts.

$$R = \frac{N_+}{N_-} \rightarrow \frac{N_+ - N_+^B}{N_- - N_-^B},$$

[3] A BBC count is when the proton remnants hit the BBC, which is described in a previous chapter.

	A_{LL}	Corrected A_{LL}	Difference
BHT1	-0.00224	-0.00198	0.00026
BHT2	-0.00032	-0.00004	0.00028
BJP1	0.00040	0.00070	0.00030
BJP2	0.00365	0.00395	0.00030

Table A.2: Effect of changing Relative luminosity on the asymmetry

where N_+ (N_-) is the number of BBC counts where the product of the proton helicities is +1 (-1), and N_+^B (N_-^B) is the number of counts calculated for the background. The asymmetry was recalculated using the modified relative luminosities and the difference was the systematic uncertainty. Table A.2 shows the values calculated for each trigger. The asymmetry was calculated over all transverse momentum bins. It was found that the systematic uncertainty due to the background's effect on relative luminosity was less than 3.0×10^{-4}.

A.4 Random Pattern Uncertainty

There were 120 bunch crossings[4] between the proton beams. Each bunch crossing had a fixed helicity for the colliding protons. If the bunch crossings were randomly assigned helicities for the protons, the resulting asymmetry would be expected to average to zero over the different random patterns.

A test of this was performed. For each bunch crossing a helicity was randomly assigned to the proton beam's bunch crossings. Then the asymmetry was recalculated for each run. The asymmetry values were plotted as a function of run id and a constant line was fit. Figure A-10 shows the asymmetries calculated for the various runs for one of the fill patterns. This was done for 1000 possible combinations of different helicity patterns. The resultant fits were filled in a histogram (Fig. A-11). The RMS of the histogram was smaller than the asymmetry's statistical error, and the mean was equivalent to zero so this uncertainty was set to zero.

[4] Bunch crossings are explained in a previous chapter.

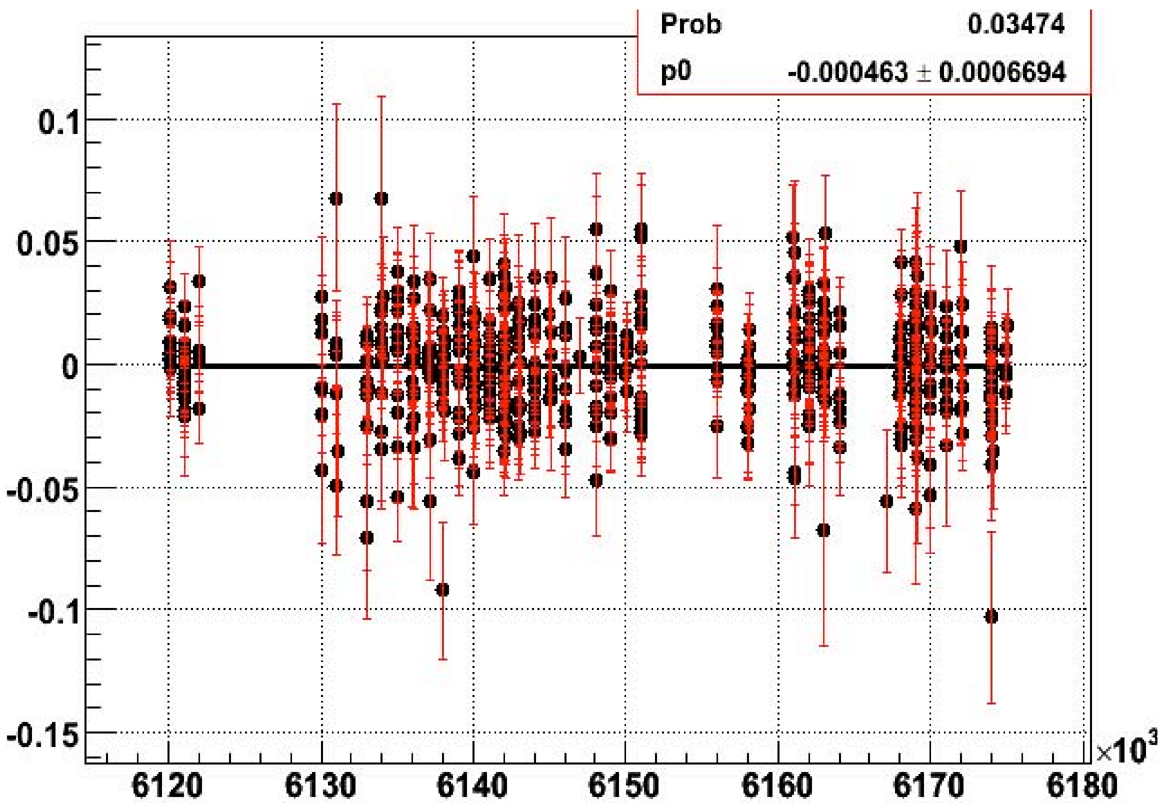

Figure A-10: Asymmetries for one random fill pattern

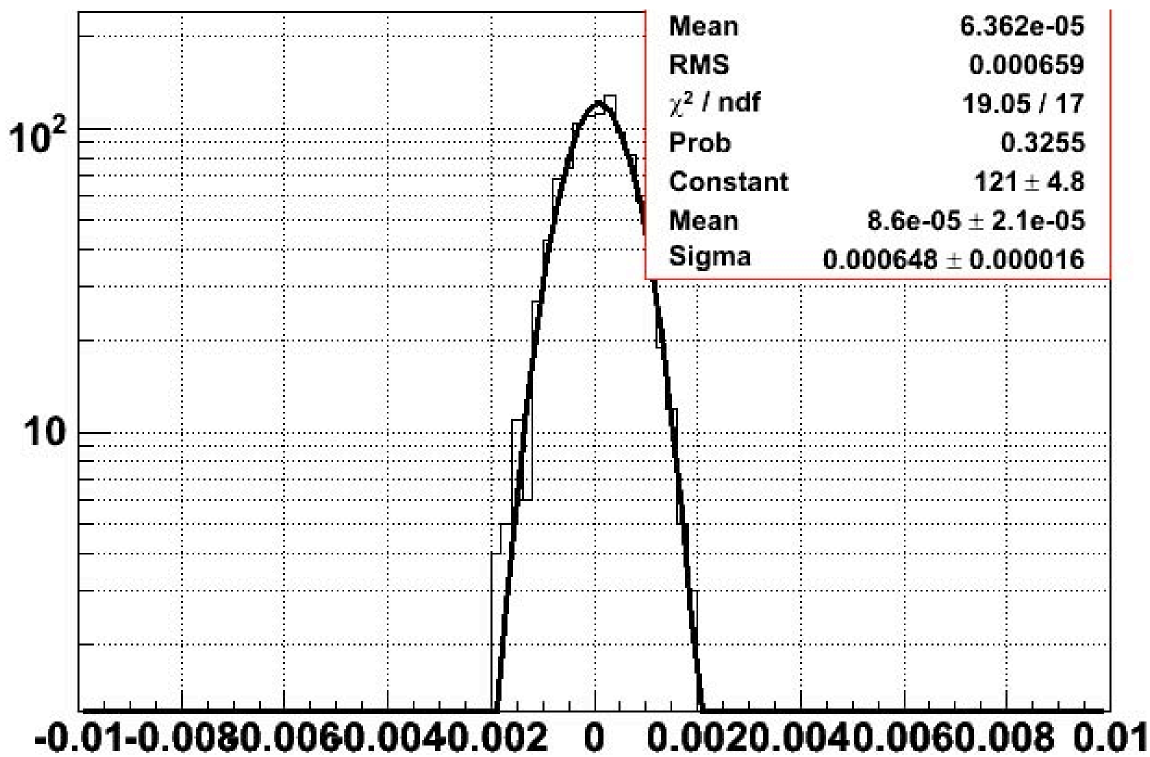

Figure A-11: Histogram of asymmetries from 1000 random patterns

A.5 Trigger Bias and Reconstruction Uncertainty

The measured jet's (detector jet) transverse momentum and the transverse momentum of the underlying parton (particle jet) that caused the jet were different. This difference is considered the reconstruction bias. This transverse momentum shift could have depended on whether the jet was caused by a quark-quark, quark-gluon, or gluon-gluon collision, since gluon jets usually fragmented more softly and therefore with higher multiplicity. In addition, different triggers could have favored jets from different underlying parton collisions. Four triggers were used to select data[5]. Each trigger potentially biased the data compared to the minimum bias trigger. This is called trigger bias. Also, jets were made from combining energies from BEMC towers and charged tracks, whereas in principle jets were made from particles generated in the collision.

These effects were treated together. Monte-Carlo simulations were used since the

[5]Triggers are defined in a previous chapter.

uncertainty depended on the value of ΔG, which was not known, and it was necessary to see the difference between what was reconstructed in the detector and what occurred at the particle level. The transverse momentum shift was calculated. Figure A-12 shows the amount of the shift for four different GRSV scenarios, and Fig. A-13 shows the uncertainty of the shift. Figure A-14 gives the relation between detector

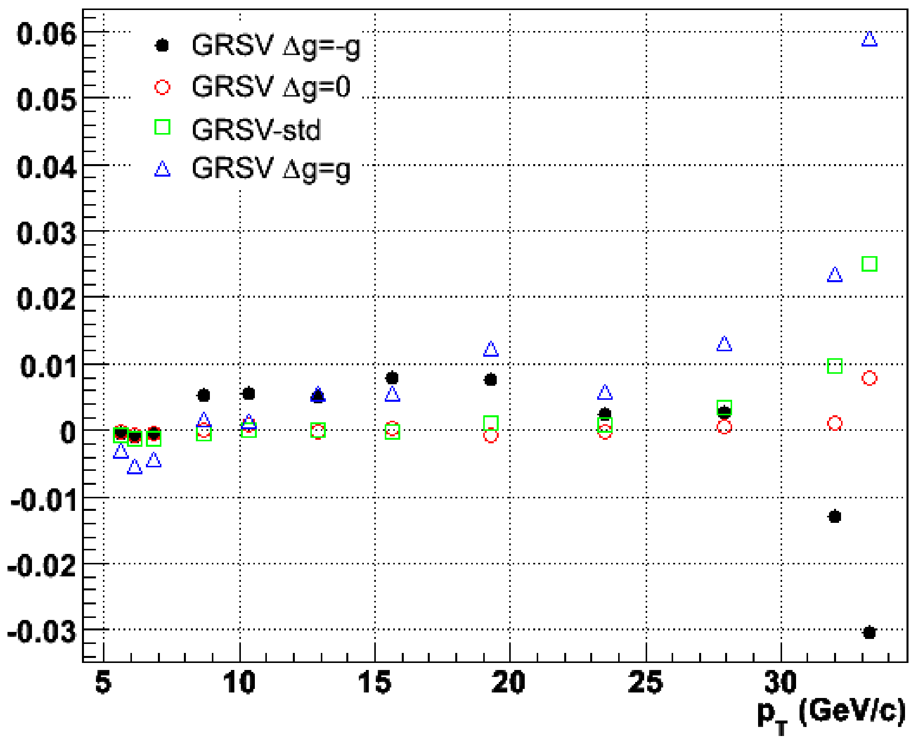

Figure A-12: Transverse momentum shift (Pythia jets - Detector jets)

jet transverse momentum and particle jet transverse momentum. The vertical error bar is the uncertainty on the particle jet transverse momentum.

The asymmetry was calculated for the jets composed of particles (A^P_{LL}), assuming gluon contributions of $\Delta G = 0, \Delta G = -G$ and GRSV standard. Then the asymmetry was calculated for jets composed of tower energies and charged tracks (A^T_{LL}), assuming the same gluon contributions.

Δ was defined as $\Delta(p_T) = A^P_{LL}(p_T) - A^T_{LL}(p_T)$ and had three different values for the three different chosen GRSV scenarios. Also, the asymmetry value from the detectors had three different uncertainties depending on the GRSV scenario. The uncertainty

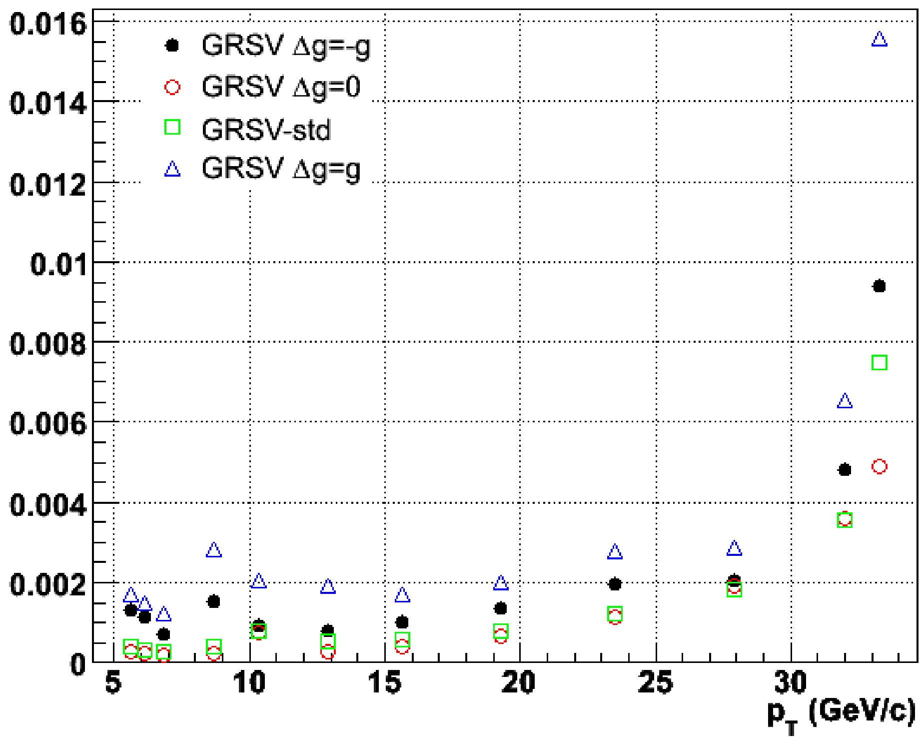

Figure A-13: Transverse momentum shift uncertainty

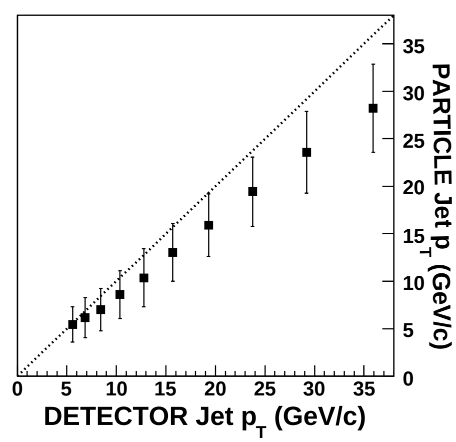

Figure A-14: Relation between detector jet transverse momentum and Particle jet transverse momentum was assigned to increase (decrease) the asymmetry by the maximum (minimum) of the three $\Delta(p_T)$ values or the maximum (minimum) of the asymmetry uncertainty, whichever was larger (most negative).

Different triggers contributed different numbers of jets to the asymmetry. This was taken into account in this uncertainty by weighting the uncertainty for the different triggers according to how many statistics they had in the asymmetry. The uncertainty was transverse momentum dependent and varied from -1.5×10^{-3} to 8×10^{-3}.

A.6 Non-longitudinal Beam Components Uncertainty

The polarized cross-section was proportional not only to the longitudinal double-spin asymmetry, but also to the transverse double and single spin asymmetries. If the beam polarization was not 100% longitudinal, but contained transverse and/or radial parts, the measured double-longitudinal spin asymmetry could have been systematically affected by the transverse components.

A transverse component of the beam polarization would have resulted in an asymmetry in the number of events hitting the BBC on the left side compared to the right side. If the beams had a radial component of polarization, there would have been an asymmetry in the number of events hitting the BBC on the top compared to the bottom. Measurements of these asymmetries found that the angle of the beam was $\theta = 7.9°, \phi = 74.0°$ for one beam and $\theta = 17.2°, \phi = 138.7°$ for the other beam[6].

The uncertainty on the double-spin longitudinal asymmetry due to the transverse single-spin asymmetry is

$$\delta A = \left| \frac{1}{P_1} \frac{\tan\theta_2}{\cos\theta_1} \sin(\phi_2 - \phi_R) + \frac{1}{P_2} \frac{\tan\theta_1}{\cos\theta_2} \sin(\phi_1 - \phi_R) \right| |A_N| \,,$$

where P is the beam polarization, and A_N is the single-spin transverse asymmetry. A line of the form $a_0 \cos\phi$ was fit to the single-spin transverse asymmetry where ϕ is the jet azimuthal angle. The amplitude of the fit (a_0), and consequently the transverse

[6]The ideal beam would have $\theta = 0°$ and the difference in beam azimulthal angle equal to 90°.

single-spin asymmetry, were consistent with zero.

The uncertainty due to the transverse double-spin asymmetry was

$$|\tan\theta_1 \tan\theta_2[\cos(\phi_1 - \phi_2)A_\Sigma + \cos(2\phi_R - \phi_Y - \phi_B)A_{TT}]|,$$

where A_Σ is the transverse double-spin asymmetry as a function of transverse momentum and A_{TT} is the transverse double-spin asymmetry as a function of jet azimuthal angle. A_{TT} was calculated from 2005 data as a function of jet azimuthal angle. The line $a_0 + a_1\cos(2\phi)$ was fit to the data and a_0 and a_1 were both consistent with zero. Figure A-15 shows the results for BHT1 data. This meant that A_{TT} was negligible

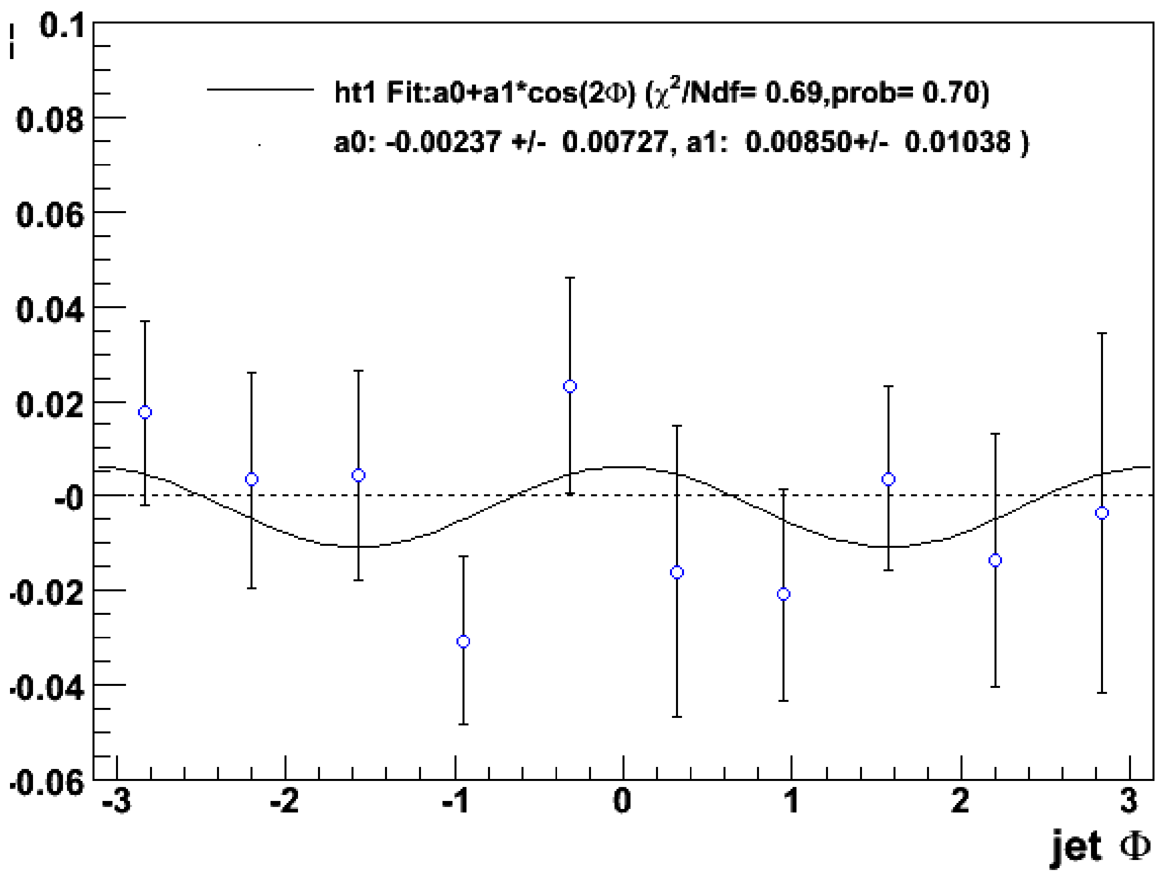

Figure A-15: Double-transverse spin asymmetry as a function of jet azimuthal angle

and did not contribute to the uncertainty on A_{LL}.

A_Σ is defined as

$$A_\Sigma = \frac{\sigma^+ - \sigma^-}{\sigma^+ + \sigma^-},$$

where σ^+ (σ^-) is the cross-section for proton-proton collisions where the spins of the protons are parallel (anti-parallel) to each other. It was calculated from data in 2006 where the protons were collided with their spins perpendicular to their velocity and found to be non-zero. This resulted in an uncertainty on the longitudinal double-spin asymmetry of 1.8×10^{-3}.

THIS PAGE INTENTIONALLY LEFT BLANK

Appendix B

Additional Cross-Section Graphs and Tables

This chapter contains graphs related to the cross-section. The plots are sorted by trigger. Five triggers were used: MINB, BHT1, BHT2, BJP1 and BJP2. MINB was a minimum bias trigger that required particles to be incident on the BBC[1]. BHT1[2] (BHT2) required, in addition to the MINB trigger, that one of the BEMC towers measuring $\Delta\eta \times \Delta\phi = 0.05 \times 0.05$ had transverse energy $E_T > 2.9$ GeV (3.7 GeV). The BJP1[3] (BJP2) trigger required, in addition to the MINB trigger, patches roughly the size of a jet ($\Delta\eta \times \Delta\phi = 1 \times 1$) had $E_T > 4.6$ GeV (7.9 GeV).

B.1 Number of Jets

Figure B-1 gives the distribution of jets by jet pseudorapidity. A cut was placed on the pseudorapidity value that the jet hit the BEMC, which indirectly gave a jet pseudorapidity cut. Figure B-2 shows the jet yield after cuts sorted by azimuthal angle. The structure seen as six peaks in the jet patch triggers is due to grouping towers into six patches in azimuthal angle. Figure B-3 is the jet yield sorted by neutral energy, where the neutral energy is the ratio of the jet energy deposited in the BEMC

[1]The BBC is described in a previous chapter.
[2]Barrel High Tower 1
[3]Barrel Jet Patch 1

to the total jet energy. Once again a turn-on curve is seen in the triggered data. This is because the trigger was satisfied based on how much energy was deposited in the BEMC. The less energy that was deposited in the BEMC, the less likely it was that the jet satisfied the trigger. Jets that satisfied the trigger at low neutral energy were highly energetic and were less likely to be produced.

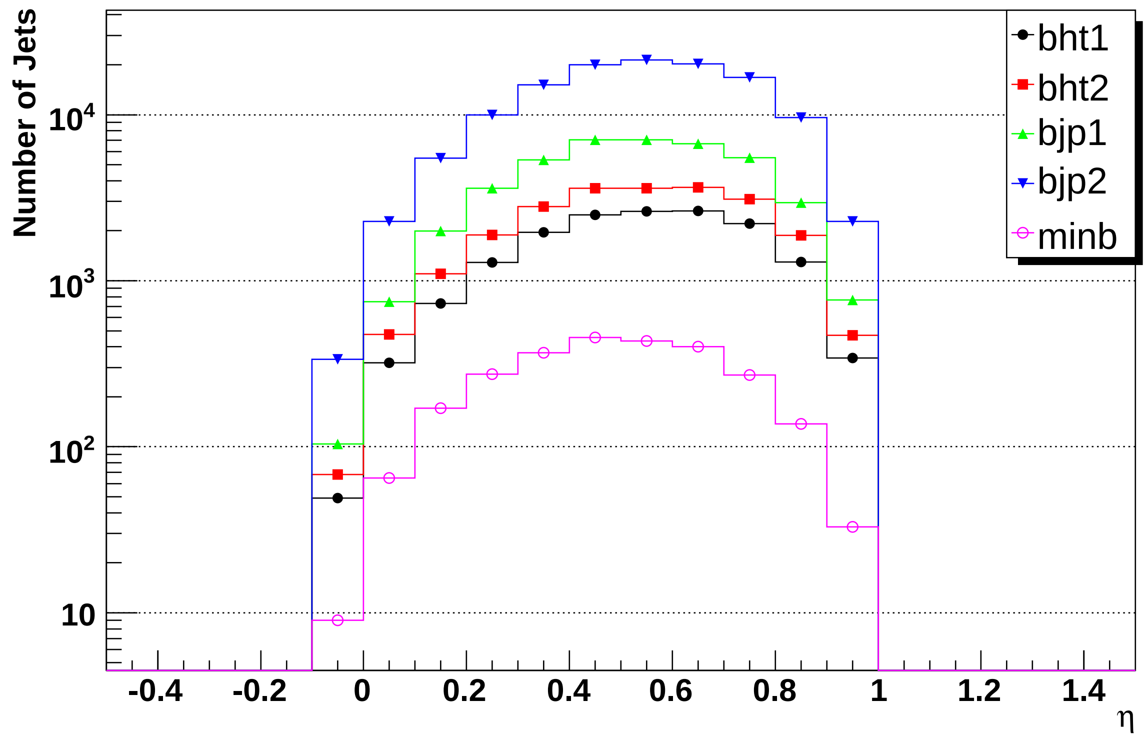

Figure B-1: Jet Yield sorted by jet pseudorapidity (η)

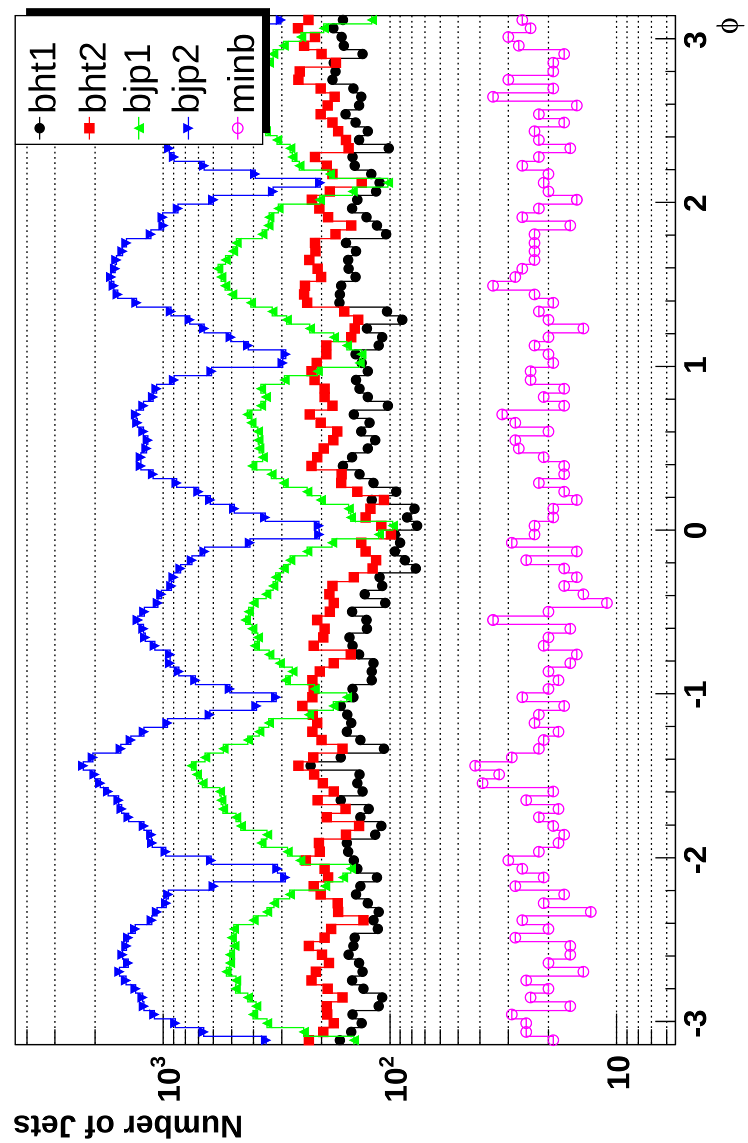

Figure B-2: Jet Yield sorted by azimuthal angle (ϕ)

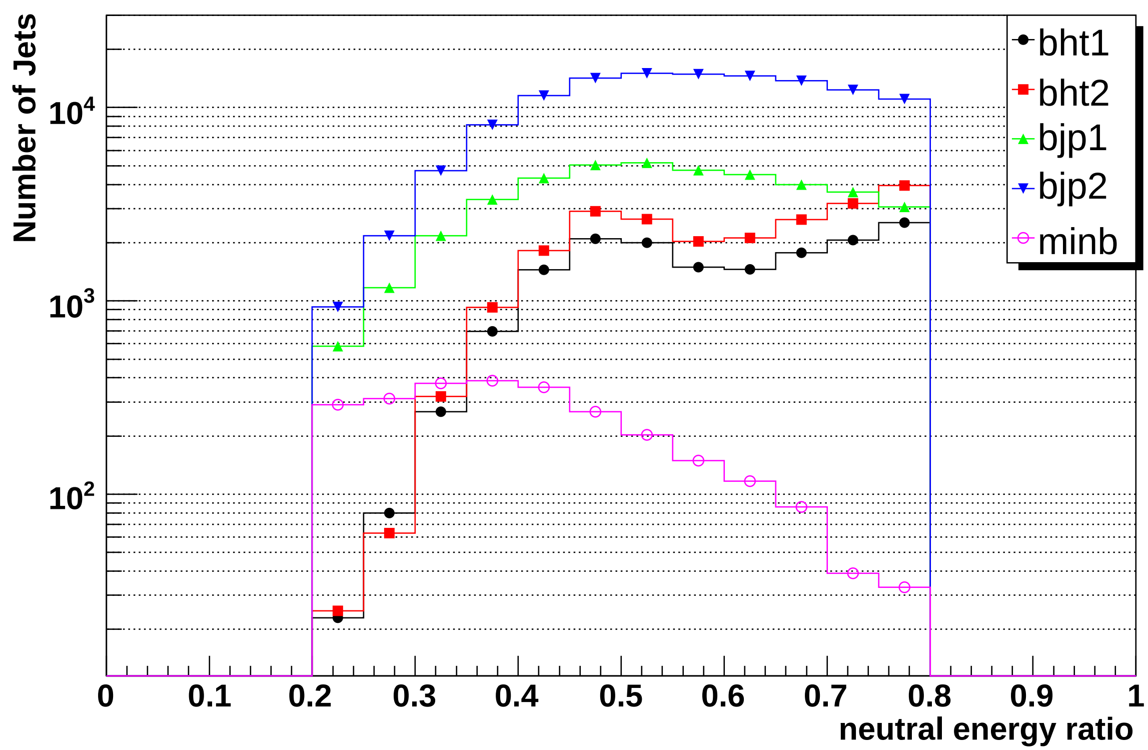

Figure B-3: Jet Yield sorted by neutral energy ratio

B.2 Proton Flux

Figure B-4 shows how the events recorded to tape were distributed for the runs used in the analysis[4]. Figure B-5 shows how the events recorded to tape were distributed in the runs for the runs used in the analysis with a vertex cut applied that required that the collisions were within 60 cm of the center of the BEMC.

[4] Run selection is described in a previous chapter.

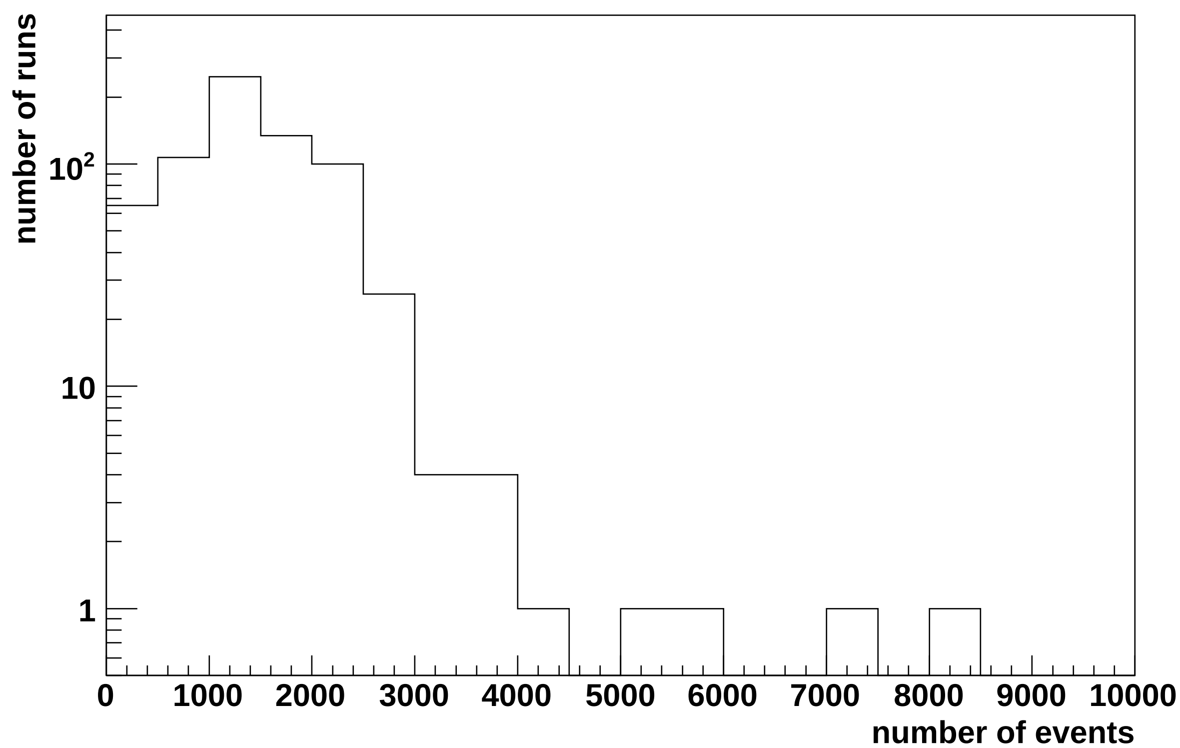

Figure B-4: Raw Number of MINB events with no cuts applied

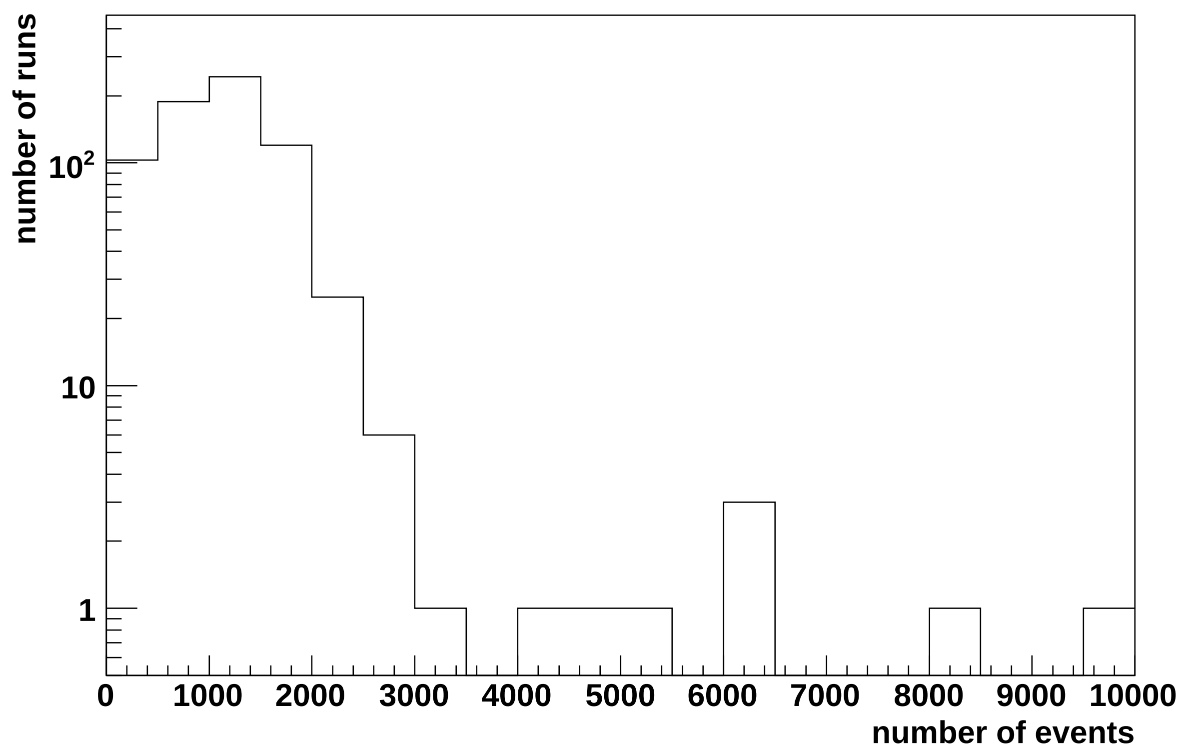

Figure B-5: Raw Number of MINB events with a vertex cut applied

B.3 BBC Timebin Dependence of the Vertex Efficiency

The BBC timebin gives a measure of the time difference between the proton remnants hitting the BBC. A vertex between -60 cm and +60 cm corresponds to BBC timebins 7-9. Greater or lesser timebins have vertices outside -60 cm to +60 cm. Figure B-6 and Fig. refverEff5b show the vertex efficiency for each run sorted by timebin. The red line is the best fit.

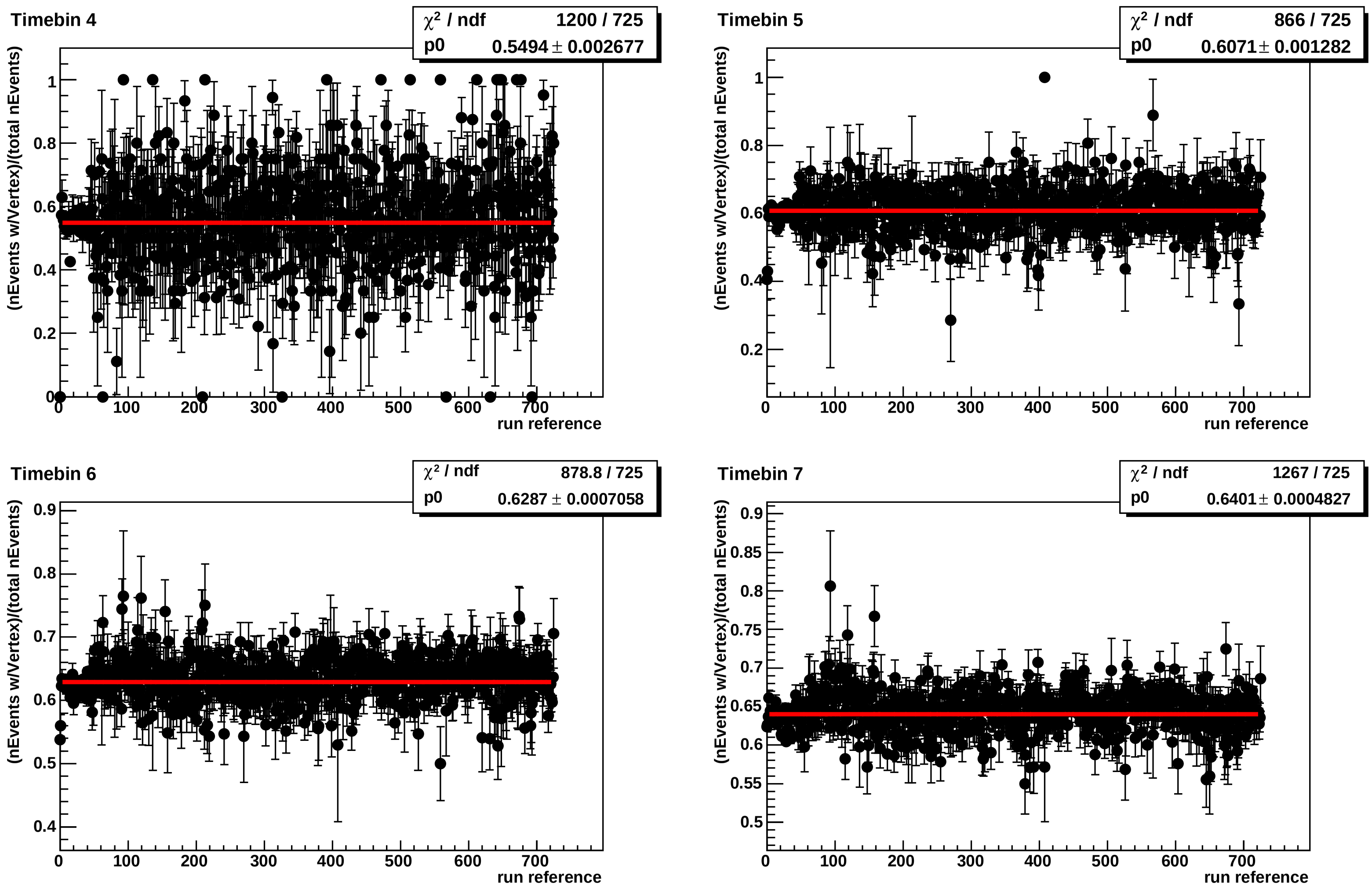

Figure B-6: Vertex Efficiency for the runs for time bins 4-7

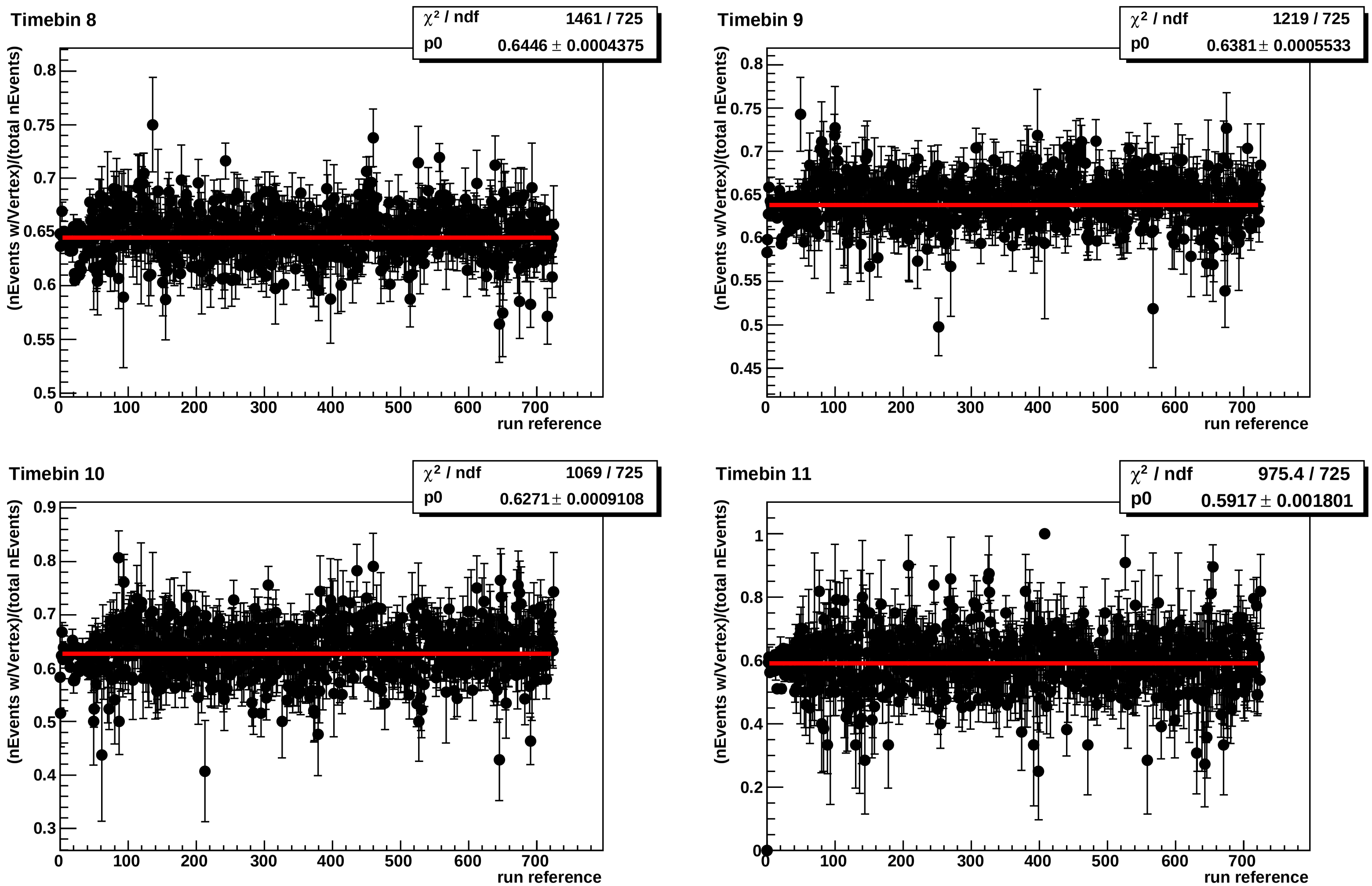

Figure B-7: Vertex Efficiency for the runs for time bins 8-11

B.4 Results

Table B.4 gives the numerical values of the 2005 inclusive jet cross-section.

Table B.1: The 2005 Inclusive Jet Cross-section Values

p_T range (GeV/c)	bht1 (pb/GeV)	bht2 (pb/GeV)	bjp1 (pb/GeV)	bjp2 (pb/GeV)
5.0 - 6.2	$(2.5 \pm 2.0) \times 10^6$	—	$(3.8 \pm 0.5) \times 10^7$	—
6.2 - 7.6	$(3.1 \pm 1.1) \times 10^6$	$(1.2 \pm 1.0) \times 10^7$	$(1.1 \pm 0.1) \times 10^6$	—
7.6 - 9.3	$(6.6 \pm 1.2) \times 10^6$	$(8.6 \pm 4.1) \times 10^6$	$(2.8 \pm 0.3) \times 10^5$	$(5.8 \pm 1.0) \times 10^6$
9.3 - 11.4	$(1.5 \pm 0.2) \times 10^5$	$(1.6 \pm 0.4) \times 10^5$	$(7.8 \pm 0.7) \times 10^5$	$(9.8 \pm 1.1) \times 10^5$
11.4 - 14.1	$(4.5 \pm 0.6) \times 10^5$	$(3.8 \pm 0.7) \times 10^5$	$(2.1 \pm 0.2) \times 10^4$	$(2.8 \pm 0.3) \times 10^4$
14.1 - 17.3	$(8.2 \pm 1.1) \times 10^4$	$(8.4 \pm 1.5) \times 10^4$	$(5.8 \pm 0.5) \times 10^4$	$(6.2 \pm 0.6) \times 10^4$
17.3 - 21.3	$(1.6 \pm 0.2) \times 10^3$	$(2.3 \pm 0.4) \times 10^3$	$(1.6 \pm 0.1) \times 10^3$	$(1.5 \pm 0.1) \times 10^3$
21.3 - 26.2	$(5.3 \pm 0.5) \times 10^3$	$(5.5 \pm 0.5) \times 10^3$	$(4.1 \pm 0.4) \times 10^3$	$(4.2 \pm 0.3) \times 10^3$
26.2 - 32.2	$(8.6 \pm 0.9) \times 10^2$	$(9.3 \pm 0.9) \times 10^2$	$(8.9 \pm 1.2) \times 10^2$	$(9.1 \pm 0.8) \times 10^2$
32.2 - 39.6	$(1.6 \pm 0.2) \times 10^1$	$(1.6 \pm 0.2) \times 10^1$	$(10.0 \pm 2.6) \times 10^1$	$(1.4 \pm 0.1) \times 10^1$
39.6 - 48.7	$(1.7 \pm 0.4) \times 10^0$	$(1.5 \pm 0.2) \times 10^0$	—	$(1.5 \pm 0.2) \times 10^0$
	minb (pb/GeV)			
5.0 - 6.2	$(7.0 \pm 0.6) \times 10^7$			
6.2 - 7.6	$(1.9 \pm 0.2) \times 10^6$			
7.6 - 9.3	$(4.1 \pm 0.5) \times 10^6$			
9.3 - 11.4	$(7.9 \pm 1.7) \times 10^5$			
11.4 - 14.1	$(6.6 \pm 3.9) \times 10^4$			

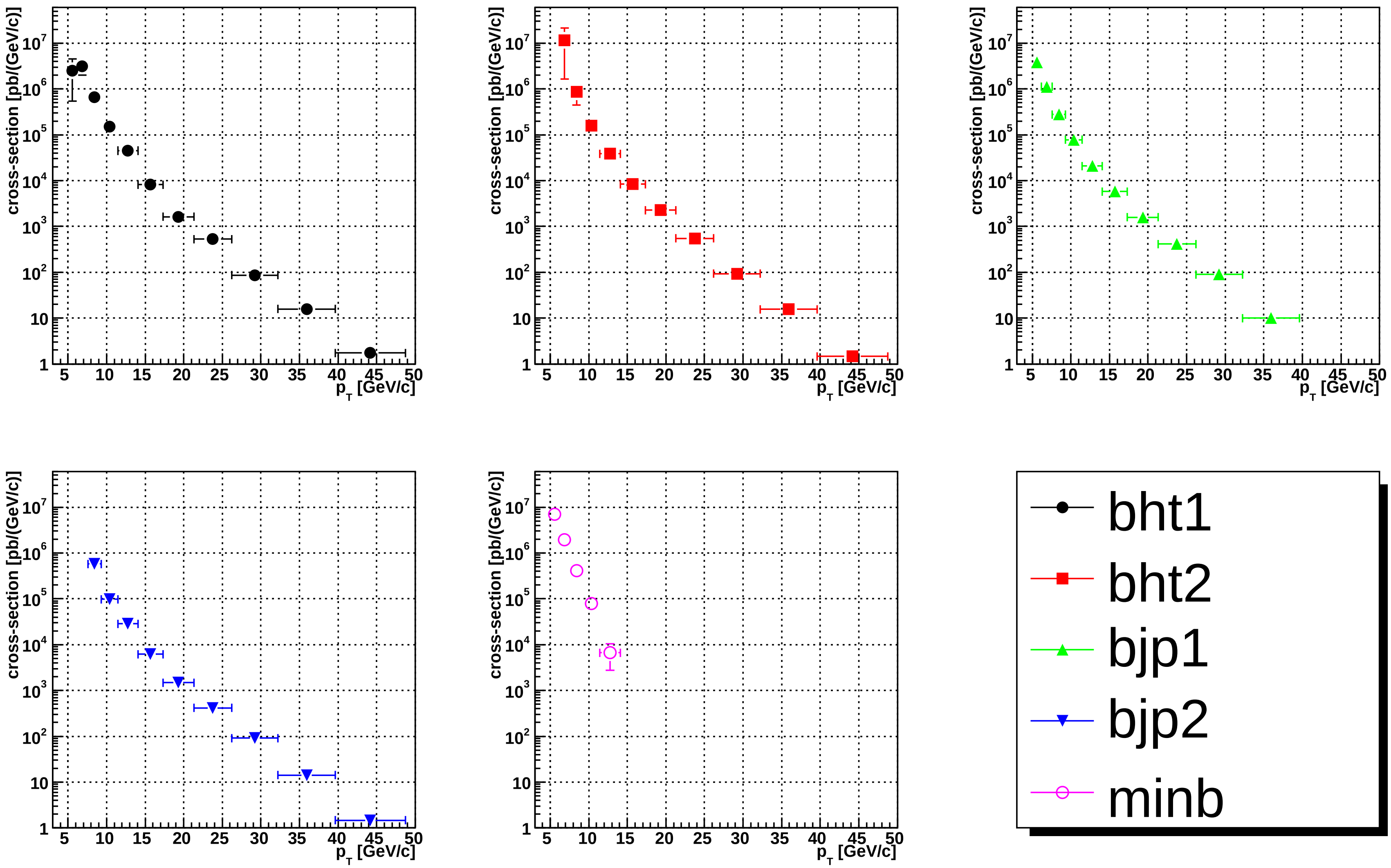

Figure B-8: 2005 Inclusive Jet Cross-section sorted by trigger

Appendix C

Additional Cross-Section Systematic Uncertainties Graphs

This chapter contains graphs used to determine the cross-section systematic uncertainties. The plots are sorted by trigger. Five triggers were used: MINB, BHT1, BHT2, BJP1 and BJP2. MINB was a minimum bias trigger that required particles to be incident on the BBC[1]. BHT1[2] (BHT2) required, in addition to the MINB trigger, that one of the BEMC towers measuring $\Delta\eta \times \Delta\phi = 0.05 \times 0.05$ had transverse energy $E_T >$ 2.9 GeV (3.7 GeV). The BJP1[3] (BJP2) trigger required, in addition to the MINB trigger, patches roughly the size of a jet ($\Delta\eta \times \Delta\phi = 1 \times 1$) had $E_T >$ 4.6 GeV (7.9 GeV).

C.1 Monte-Carlo/Data Comparison

The following graphs compare the data characteristics with the GEANT output. The GEANT point, shown as a brown hollow square, is what the Monte-Carlo simulation computed as what the data would show. The graphs were normalized to unity before comparison. Because the Monte-Carlo simulations were used to "correct" the cross-section calculation, it was important that they were reflecting what was happening

[1]The BBC is described in a previous chapter.
[2]Barrel High Tower 1
[3]Barrel Jet Patch 1

in the data.

Shown here are the comparisons for transverse momentum (p_T), jet pseudorapidity (η), azimuthal angle (ϕ), event vertex location (zver), neutral energy ratio (neuE), the number of BEMC towers in a jet (nBemcTowers), and the number of TPC tracks in a jet (nTpcTracks). The event vertex location is the distance of the collision from the center of the detector. The neutral energy ratio is the ratio of the jet energy from the BEMC to the total jet energy.

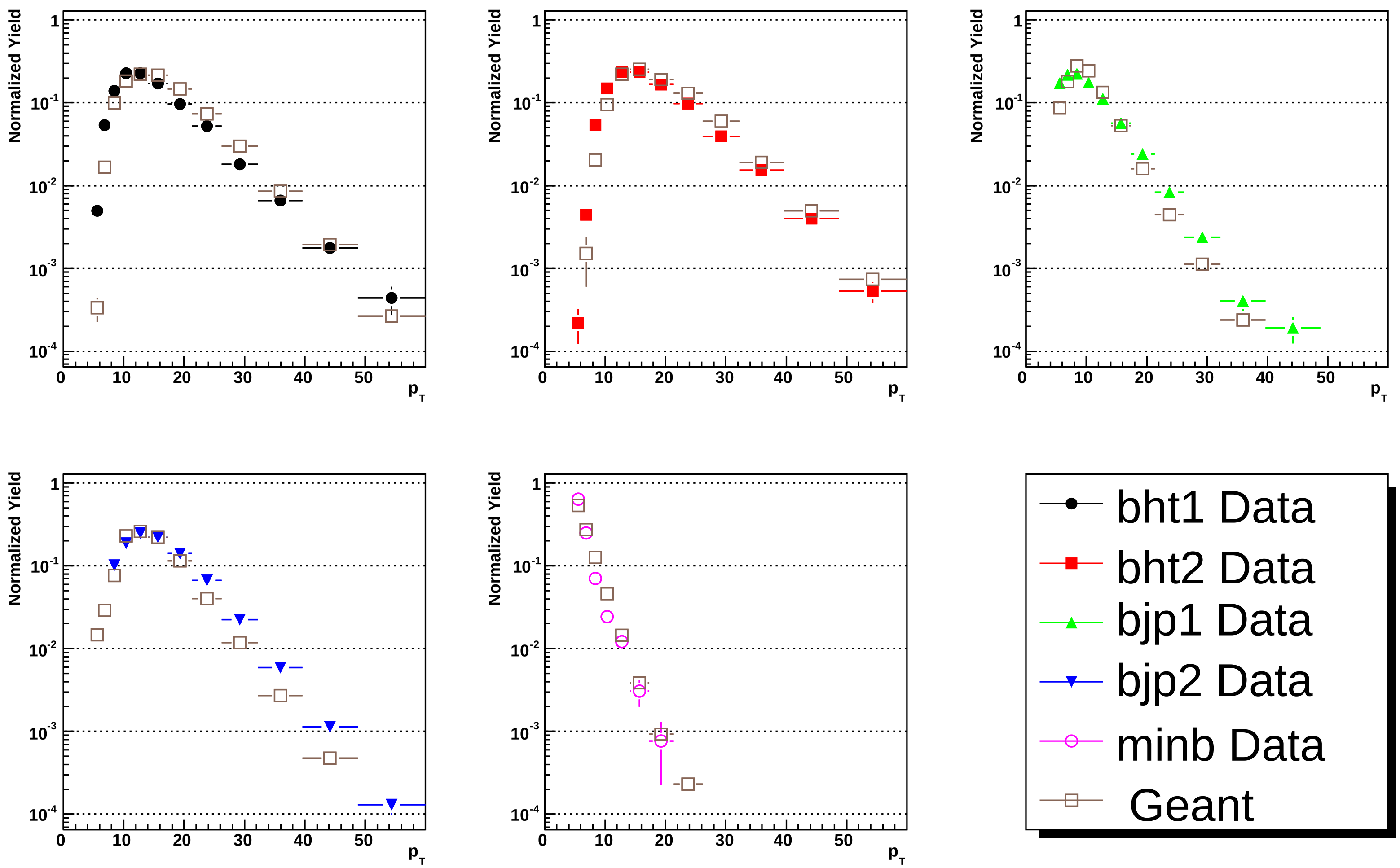

Figure C-1: Data-Monte Carlo transverse momentum comparison

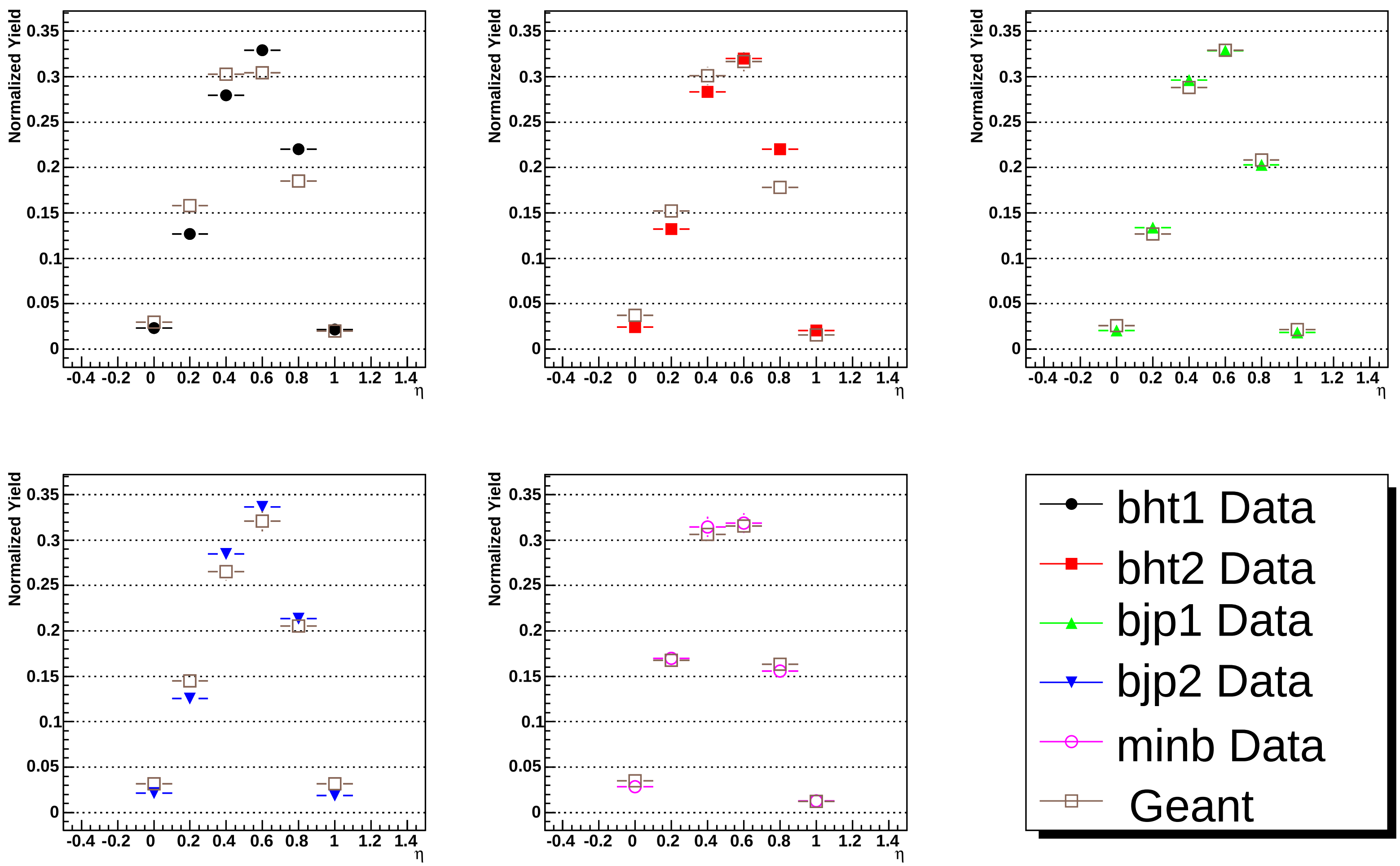

Figure C-2: Data-Monte Carlo jet pseudorapidity comparison

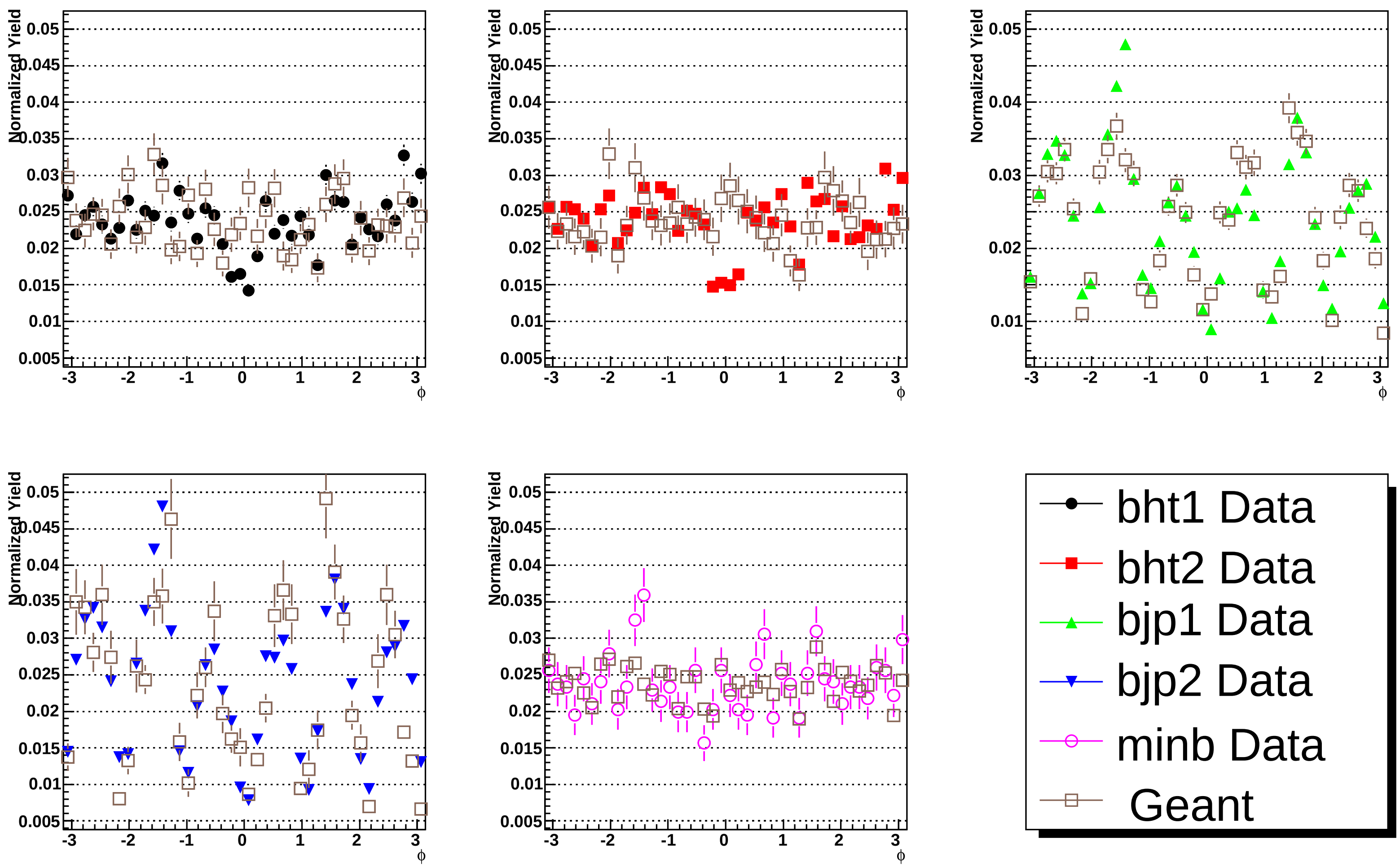

Figure C-3: Data-Monte Carlo azimuthal angle comparison

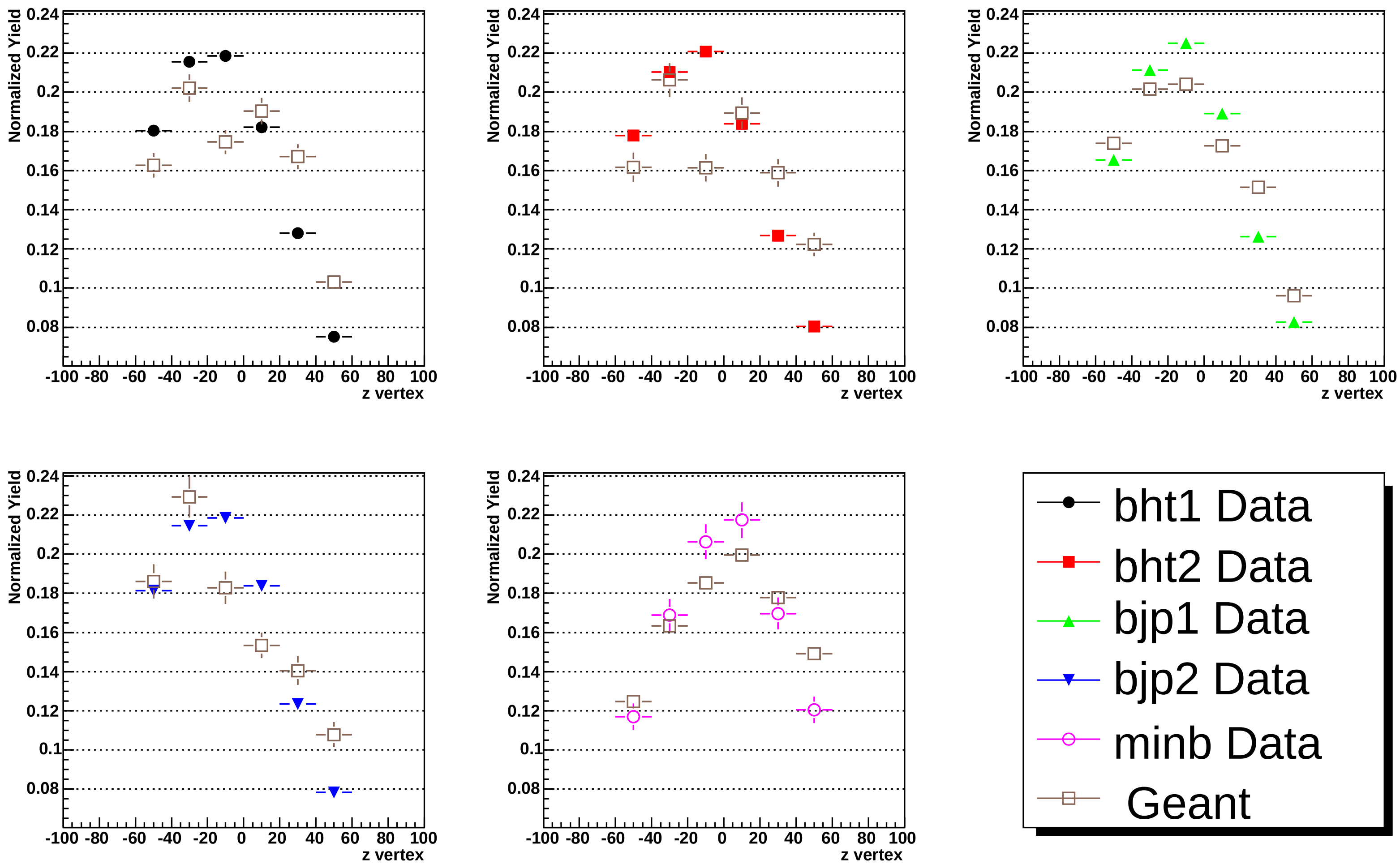

Figure C-4: Data-Monte Carlo z-vertex comparison

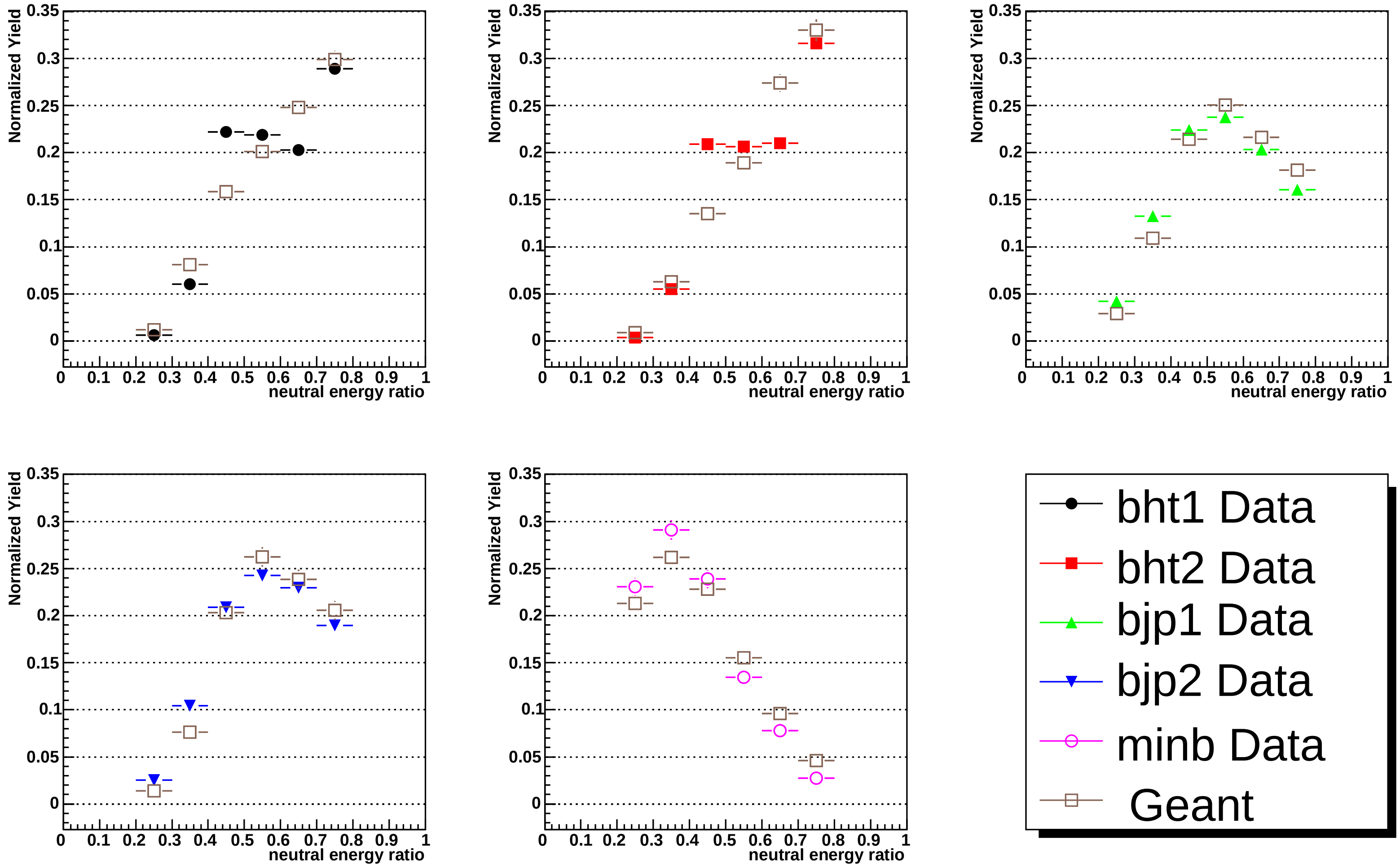

Figure C-5: Data-Monte Carlo neutral energy comparison

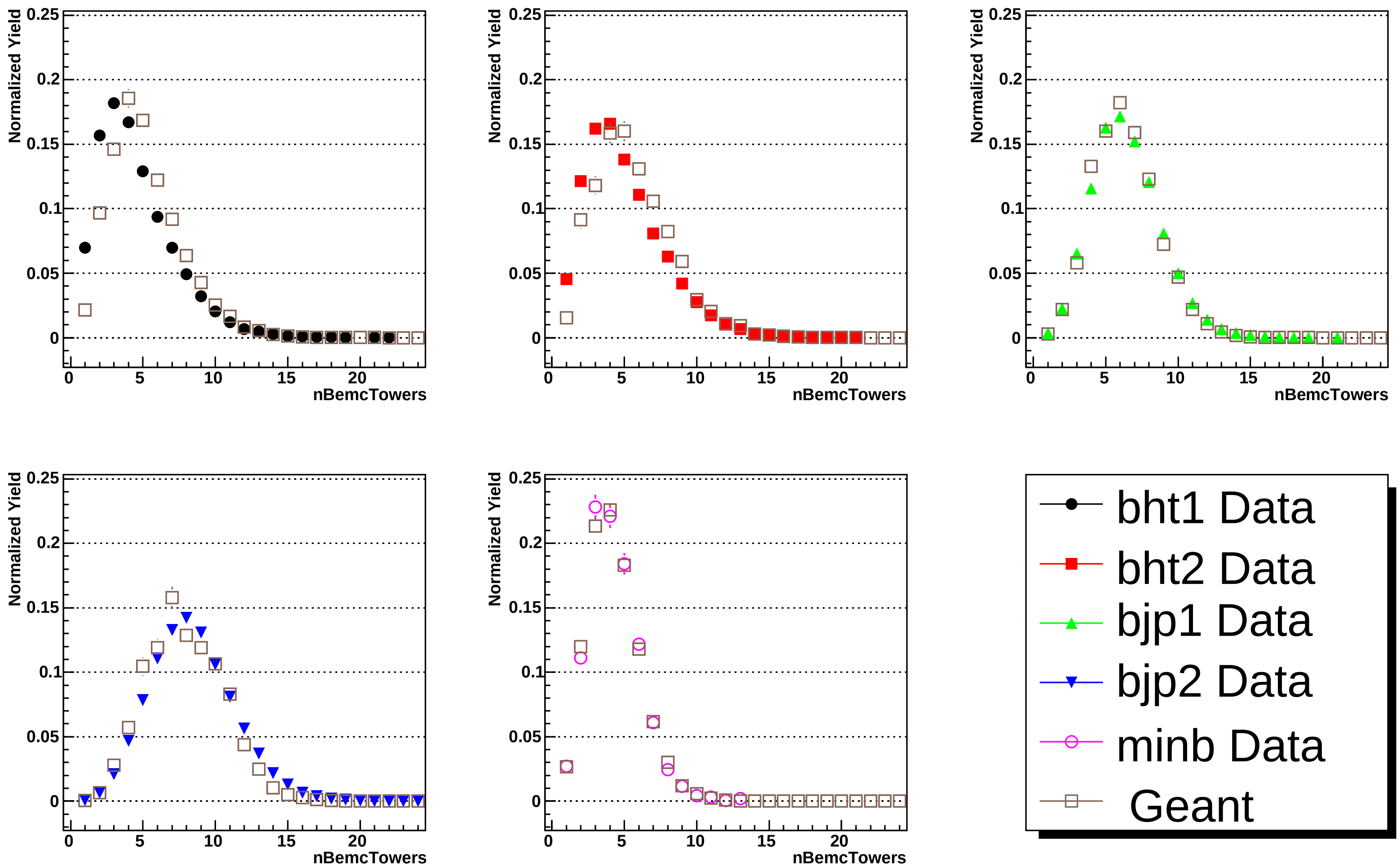

Figure C-6: Data-Monte Carlo number of BEMC towers in a jet comparison

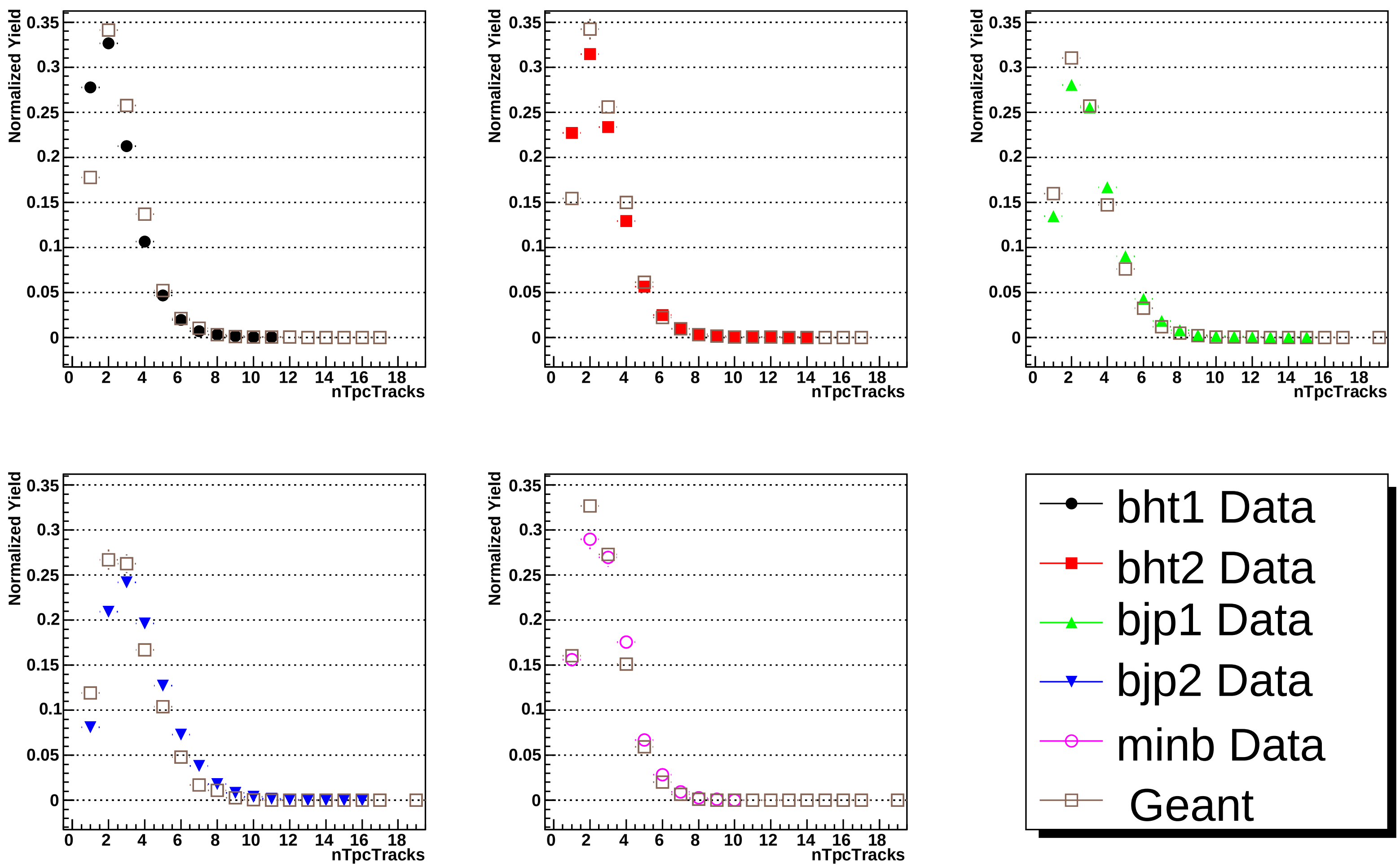

Figure C-7: Data-Monte Carlo number of charged tracks in a jet comparison

C.2 Jet Energy Scale

Uncertainties in the BEMC gains and TPC track momentum resulted in an uncertainty on the jet transverse energy and transverse momentum, and consequently an uncertainty in the cross-section. Figure C-8 shows the effect of varying the BEMC gains by 4.8%. Figure C-9 shows the effect of varying the TPC track momentum by 5%. In the following graphs, high[4] (low) refers to when the gain was increased (decreased). The exception to this is Fig. C-11 where high (low) refers to the amount the cross-section would increase (decrease).

[4] e.g. bht1 high

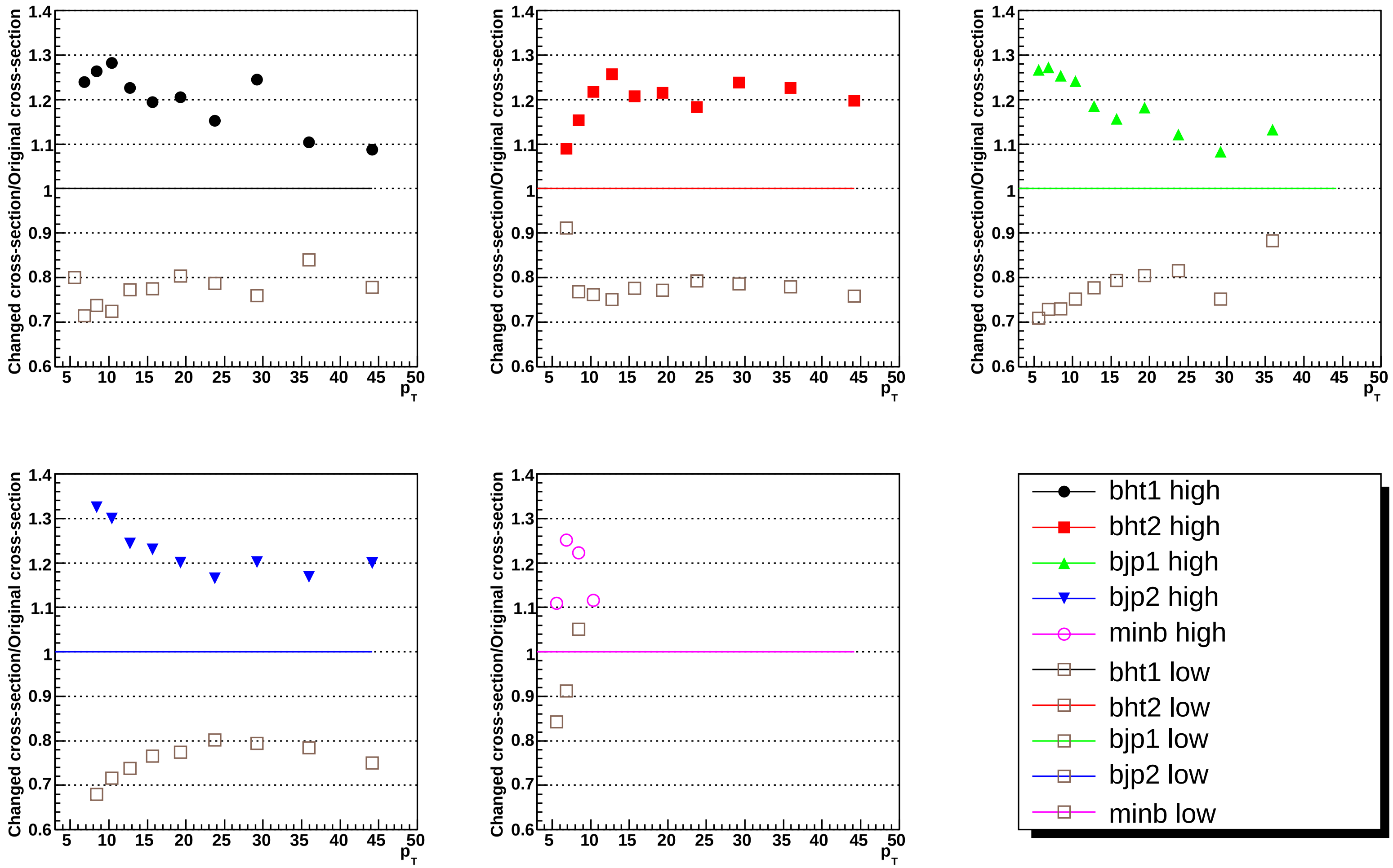

Figure C-8: Cross-section's fractional change due to BEMC gain variation.

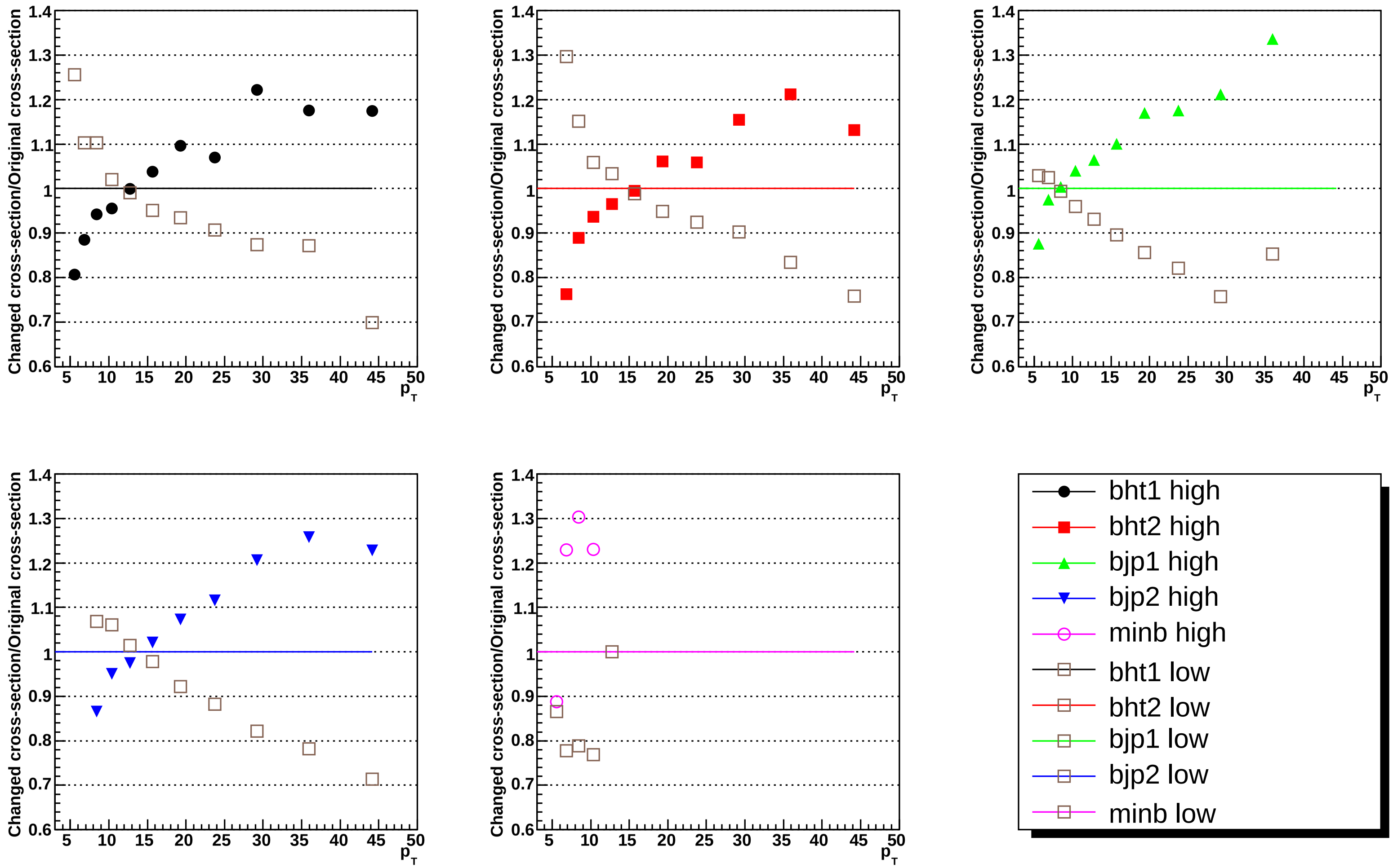

Figure C-9: Cross-section's fractional change due to Charged Track energy uncertainty

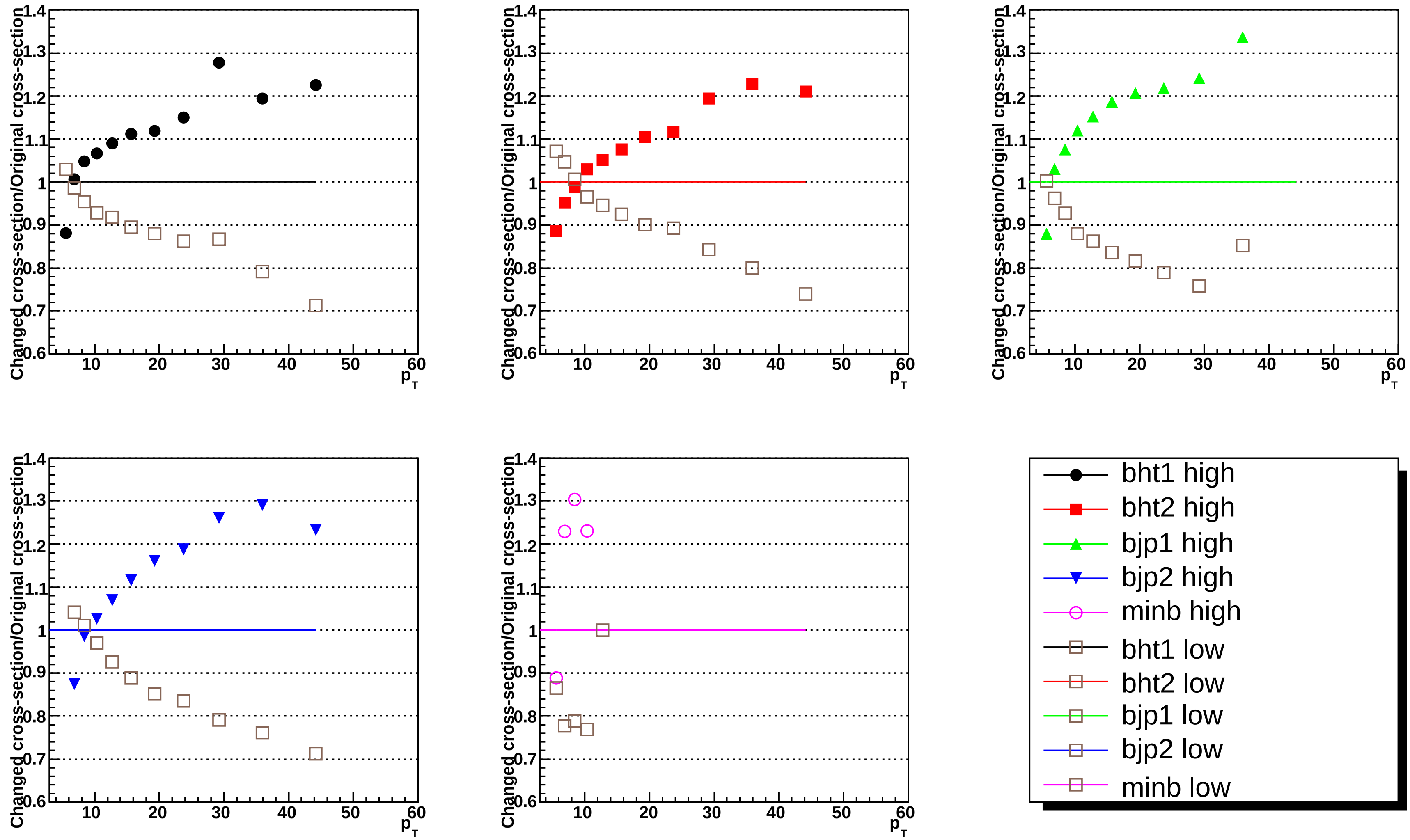

Figure C-10: Cross-section's fractional change due to Charged Track energy uncertainty with no transverse energy cut on the trigger tower (patch)

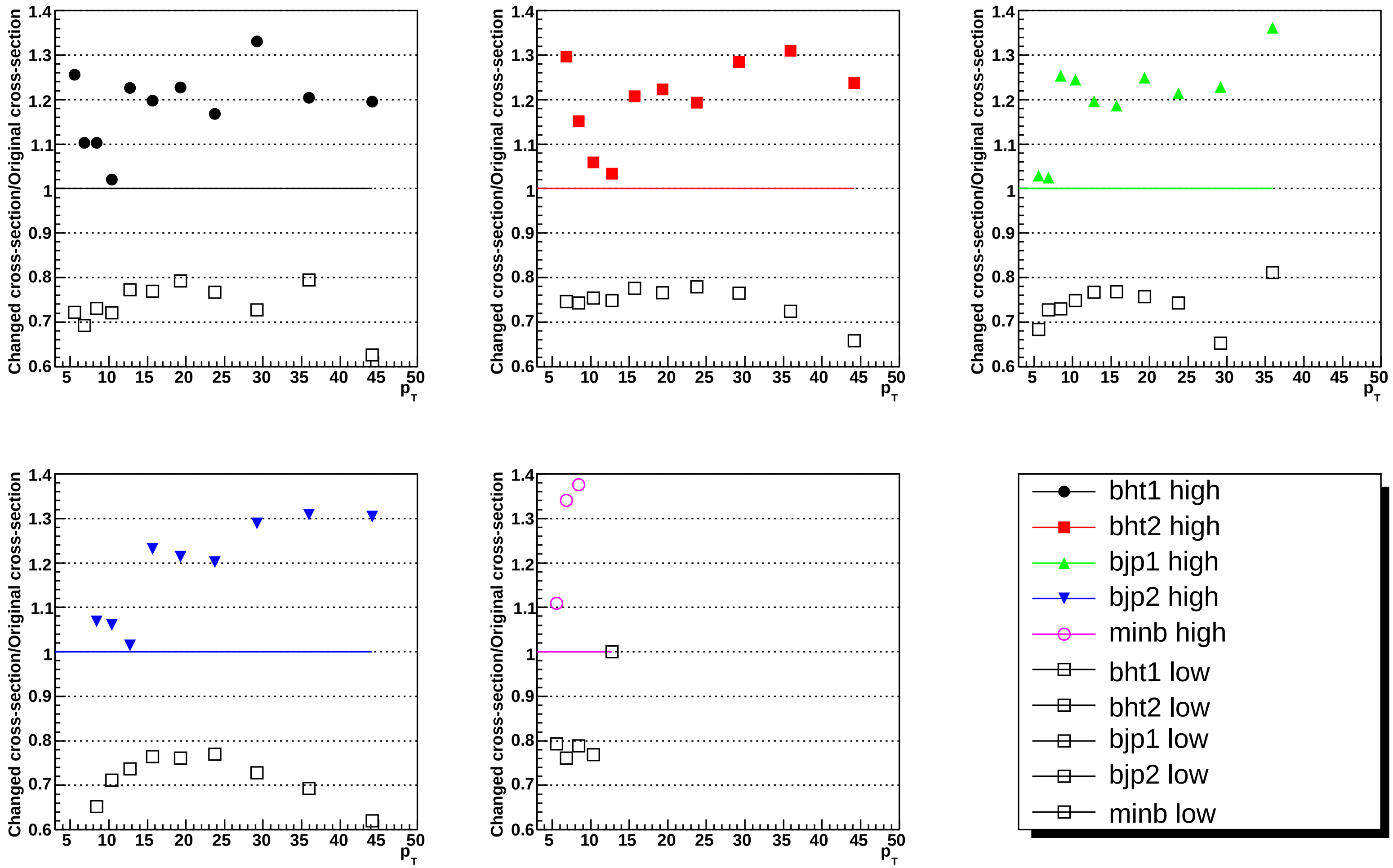

Figure C-11: Cross-section's fractional change due to Jet Energy Scale.

C.3 Z-vertex

The distance of the event location from the detector center varied from -200 cm to 200 cm. A cut was made on the jets that their event location was within 60 cm of the detector's center. However, if the Monte-Carlo simulations were correctly taking into account the variation of the events from the detector's center the cross-section would have been independent of the event location with respect to the detector's center. A more detailed description is in previous chapters. Each page is for a different trigger. In addition, the results are sorted by transverse momentum.

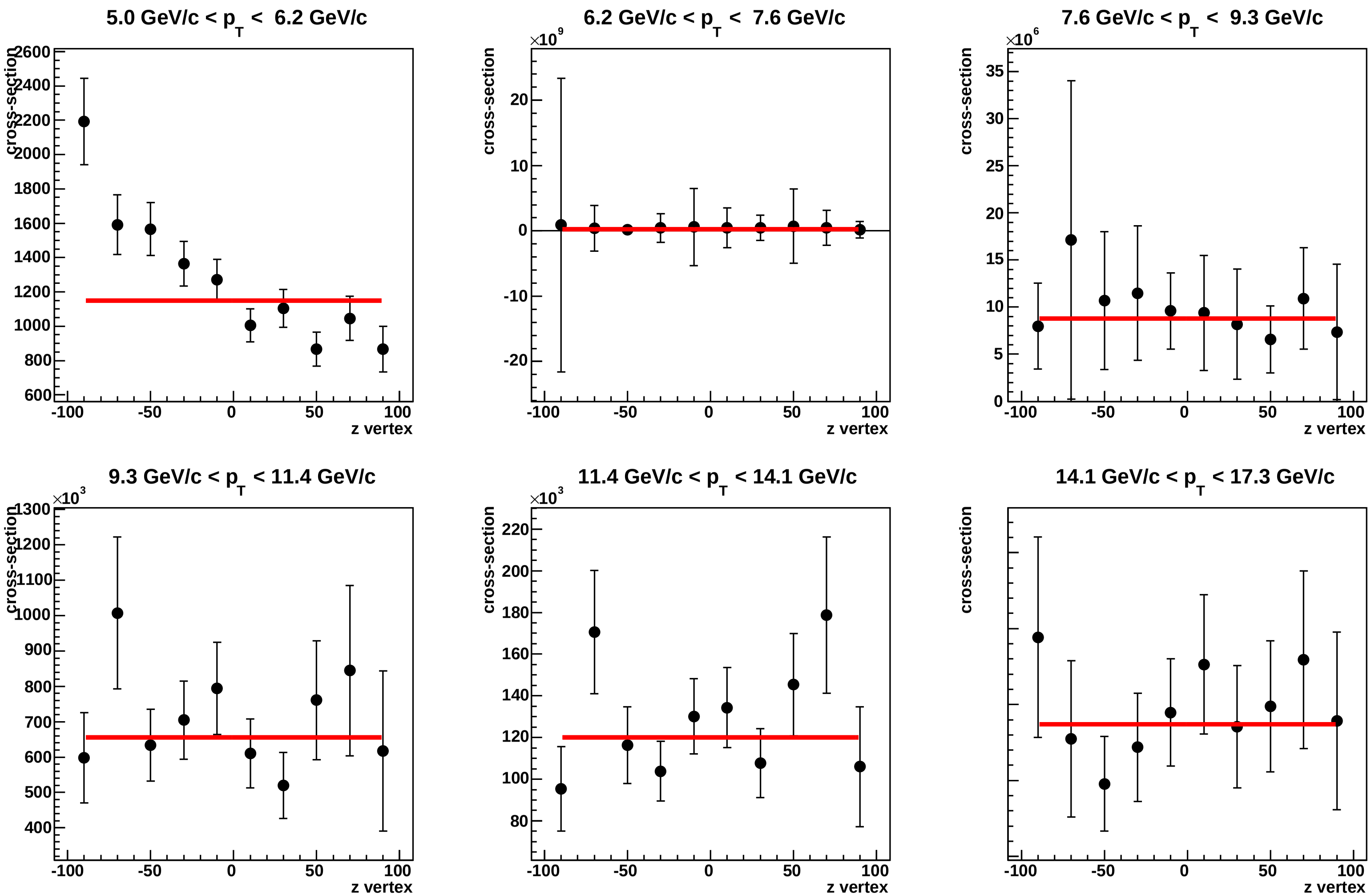

Figure C-12: Cross-section Comparison of different z-vertices for bht1 trigger for low p_T

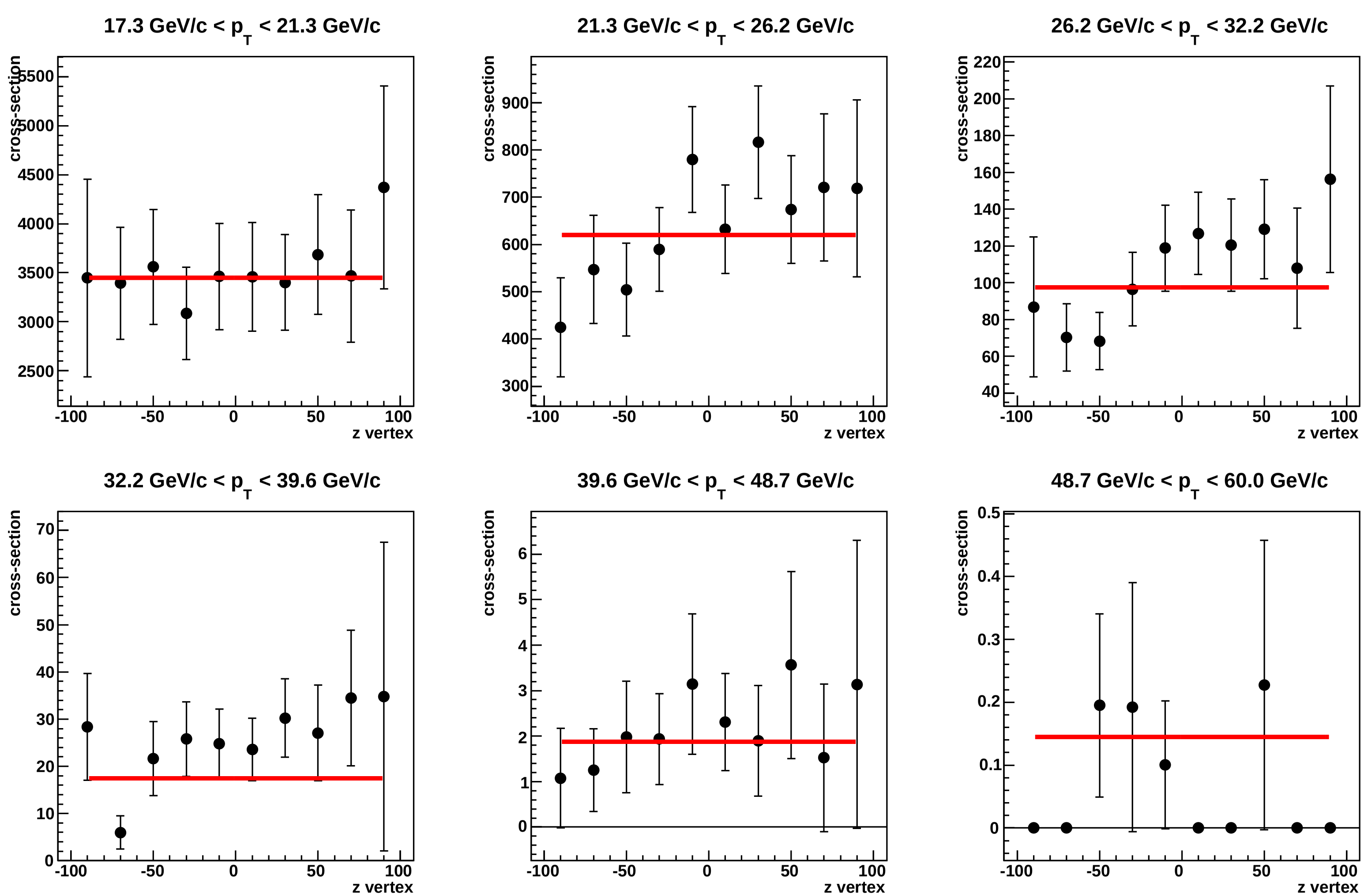

Figure C-13: Cross-section Comparison of different z-vertices for bht1 trigger for high p_T

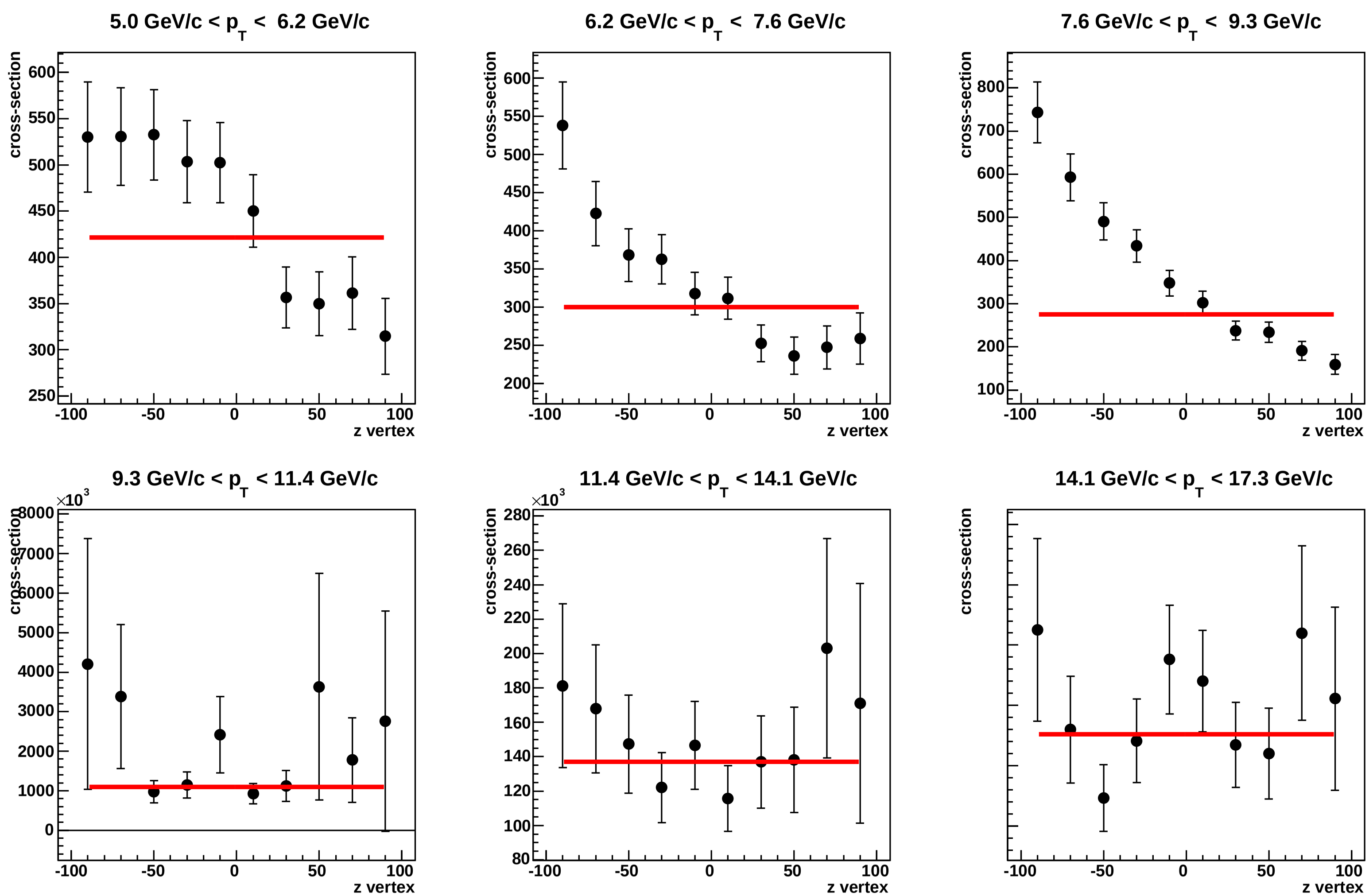

Figure C-14: Cross-section Comparison of different z-vertices for bht2 trigger for low p_T

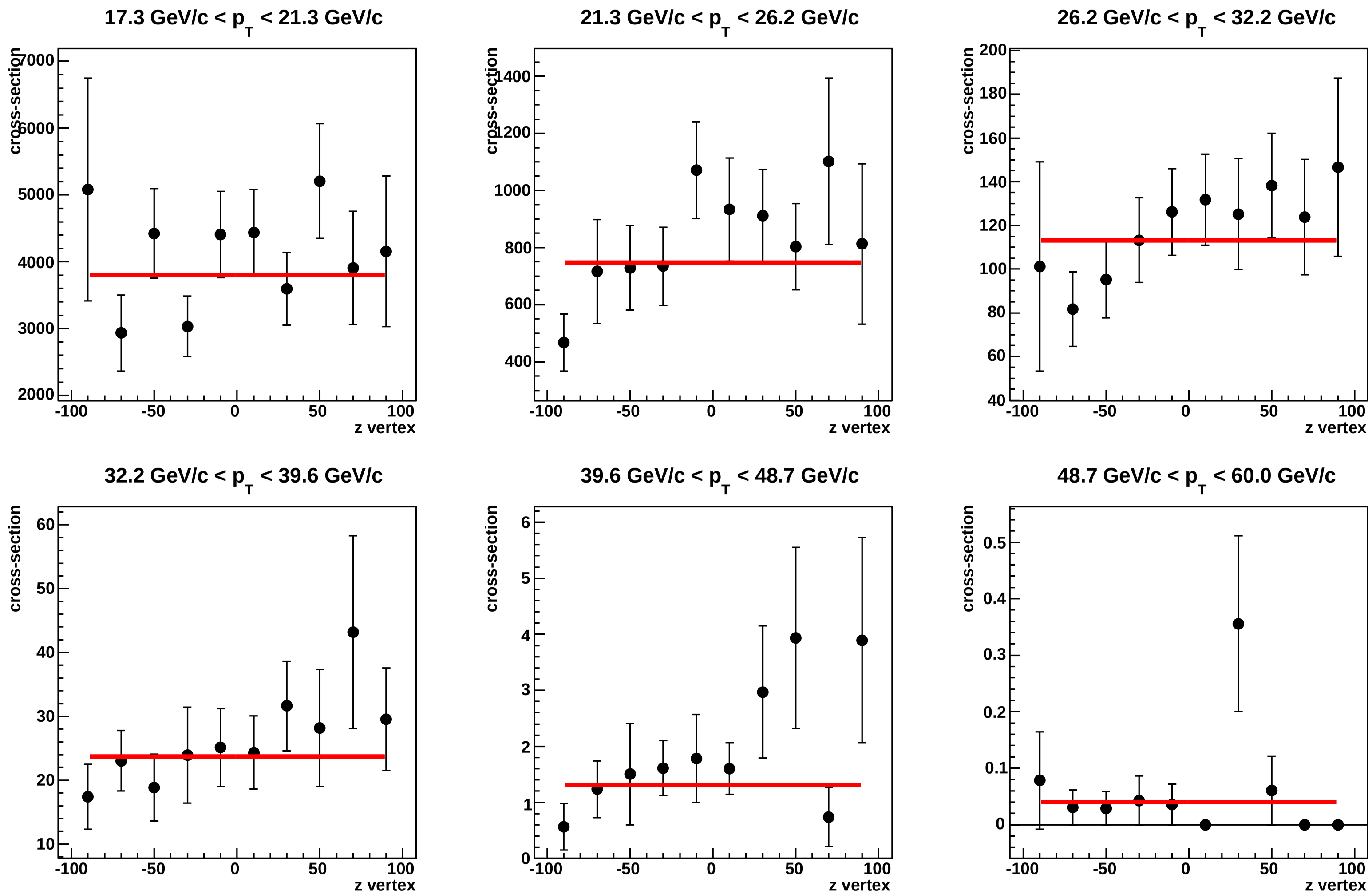

Figure C-15: Cross-section Comparison of different z-vertices for bht2 trigger for high p_T

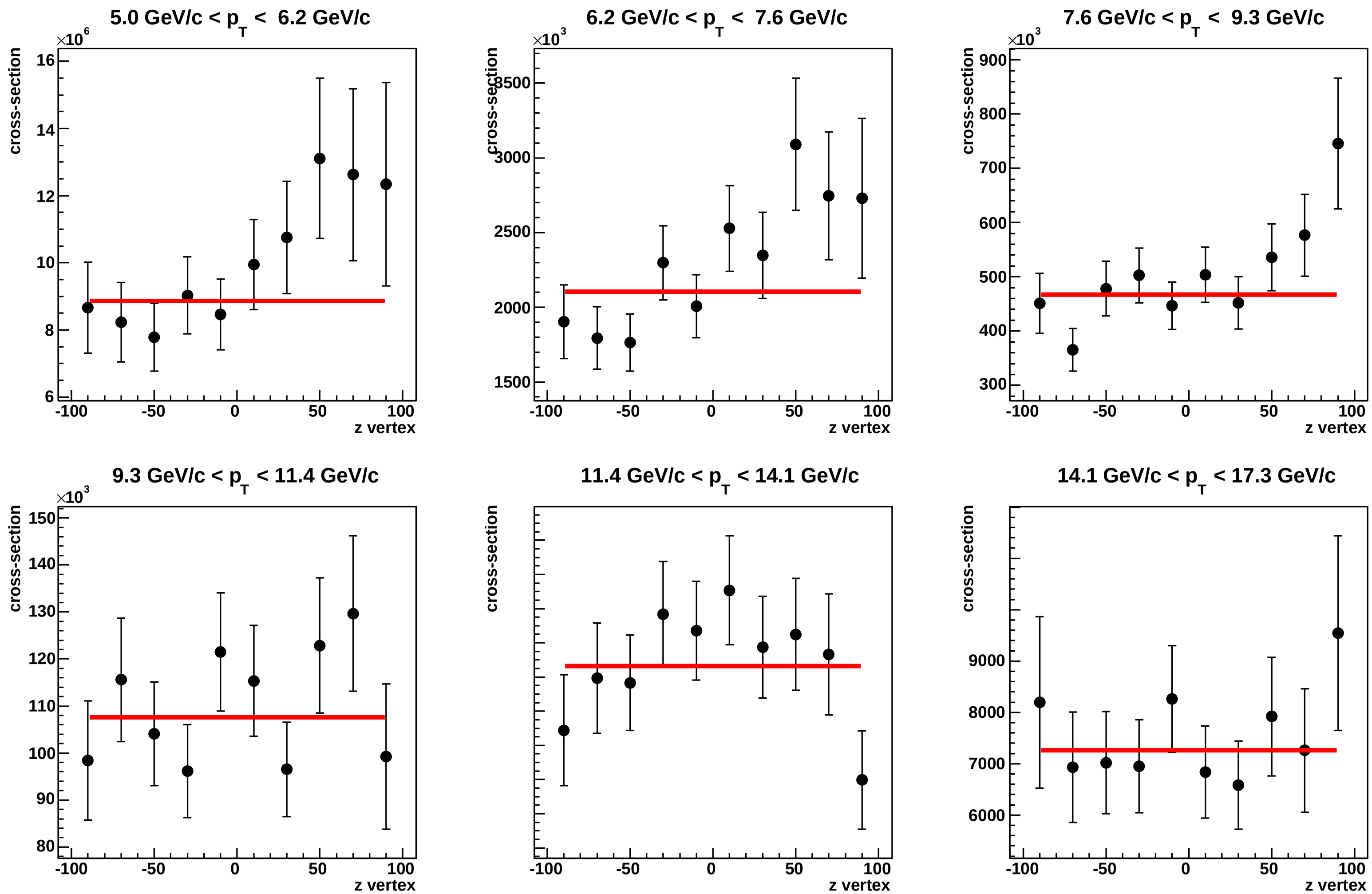

Figure C-16: Cross-section Comparison of different z-vertices for bjp1 trigger for low p_T

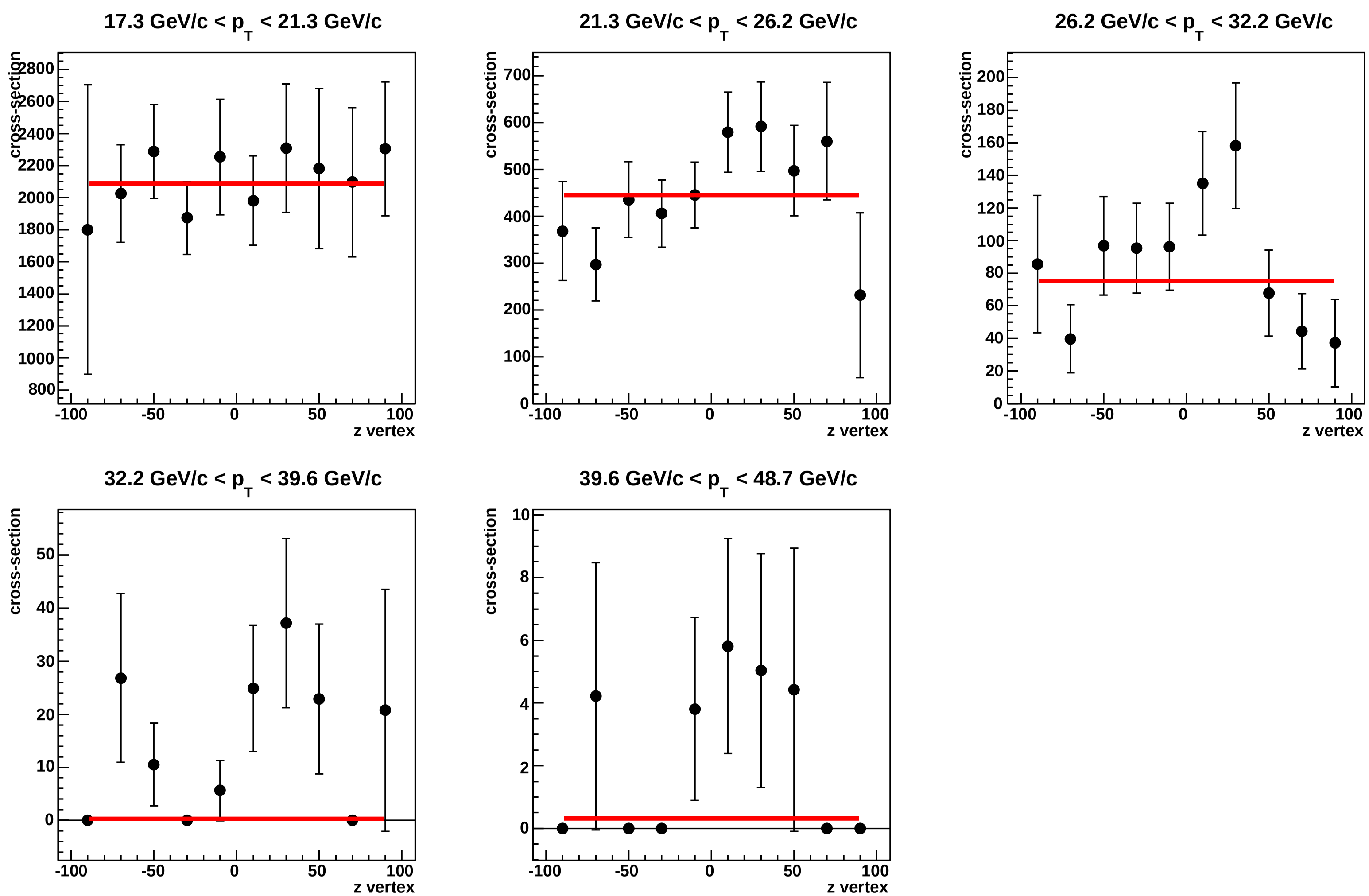

Figure C-17: Cross-section Comparison of different z-vertices for bjp1 trigger for high p_T

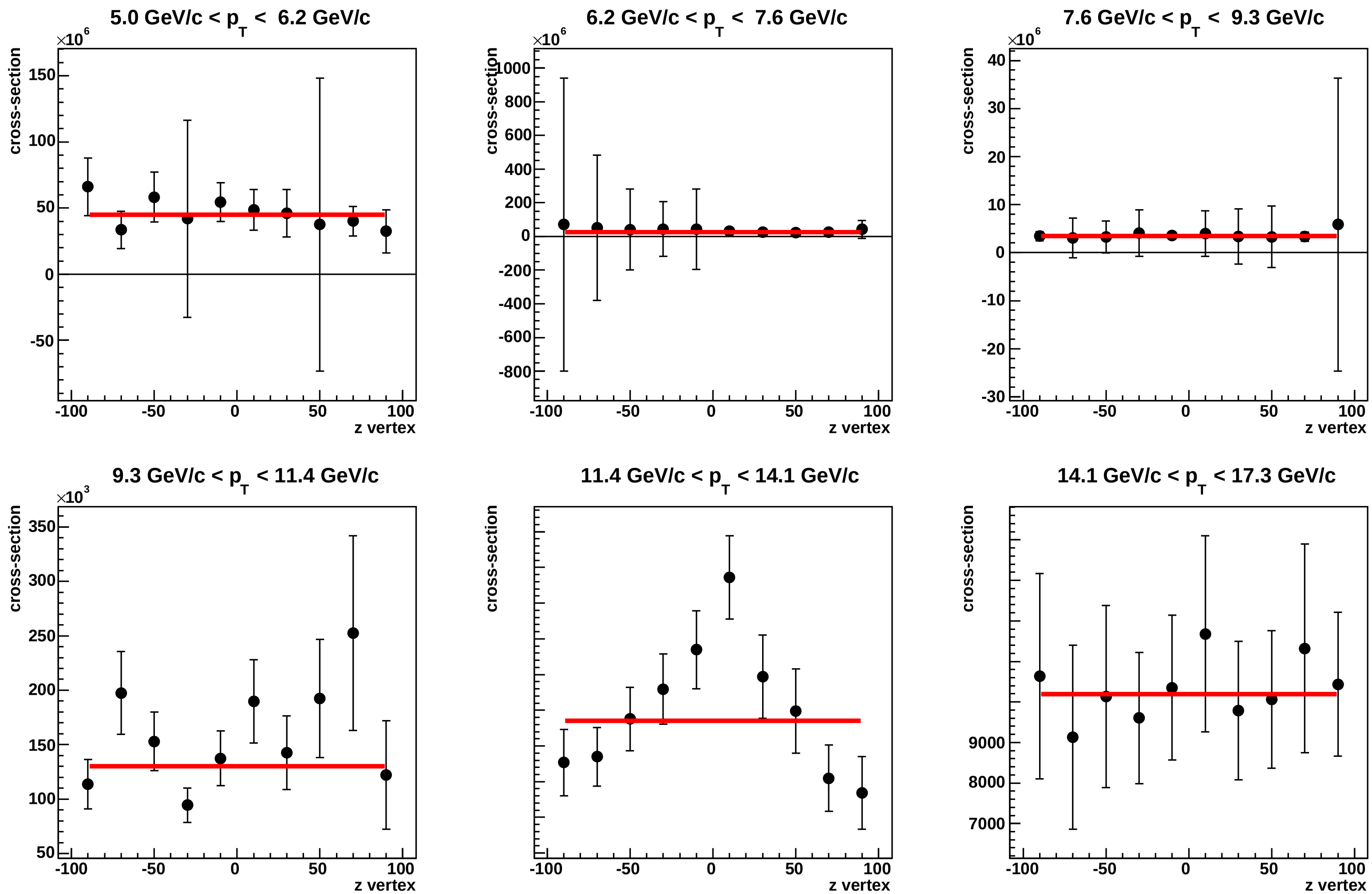

Figure C-18: Cross-section Comparison of different z-vertices for bjp2 trigger for low p_T

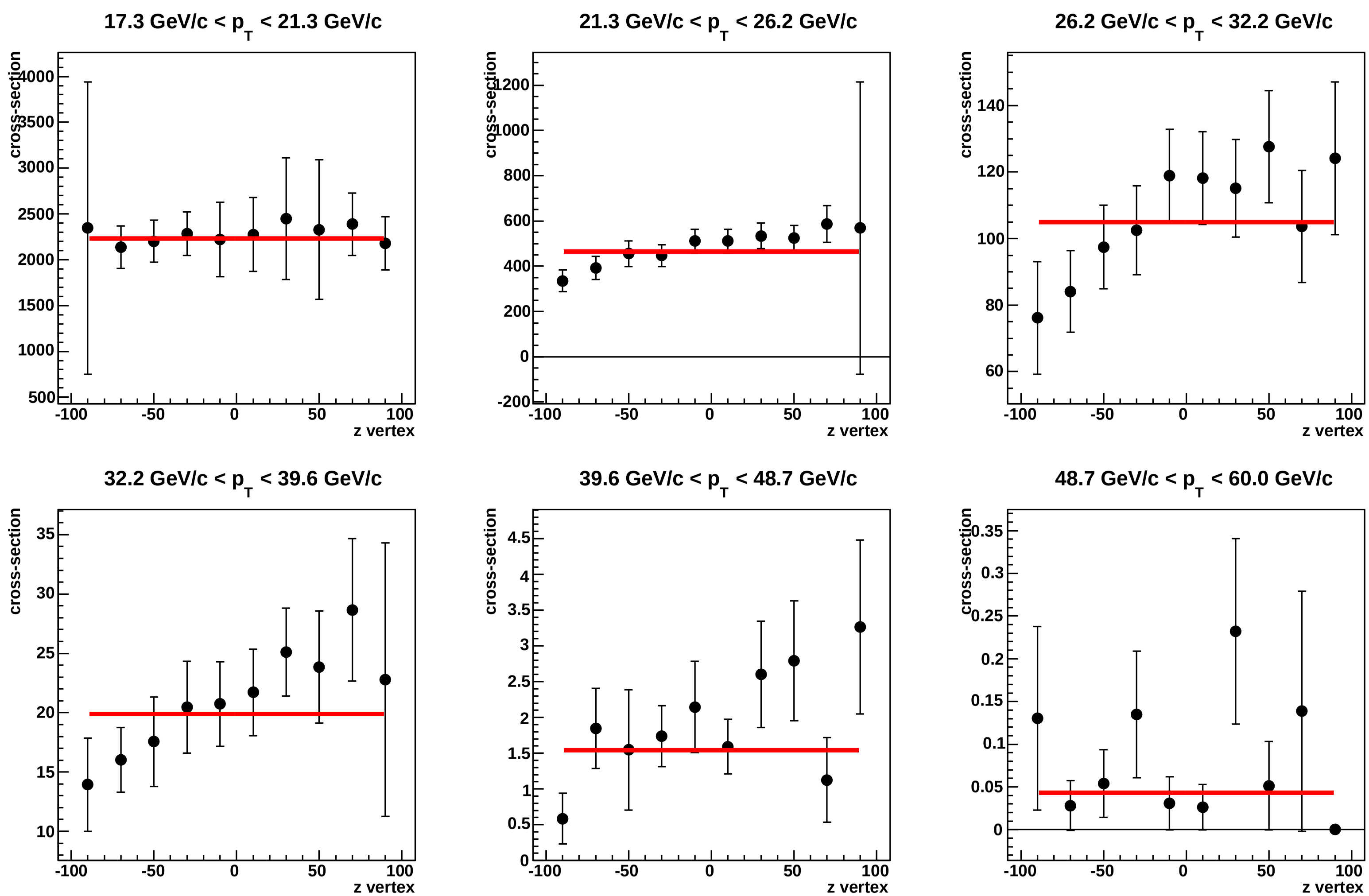

Figure C-19: Cross-section Comparison of different z-vertices for bjp2 trigger for high p_T

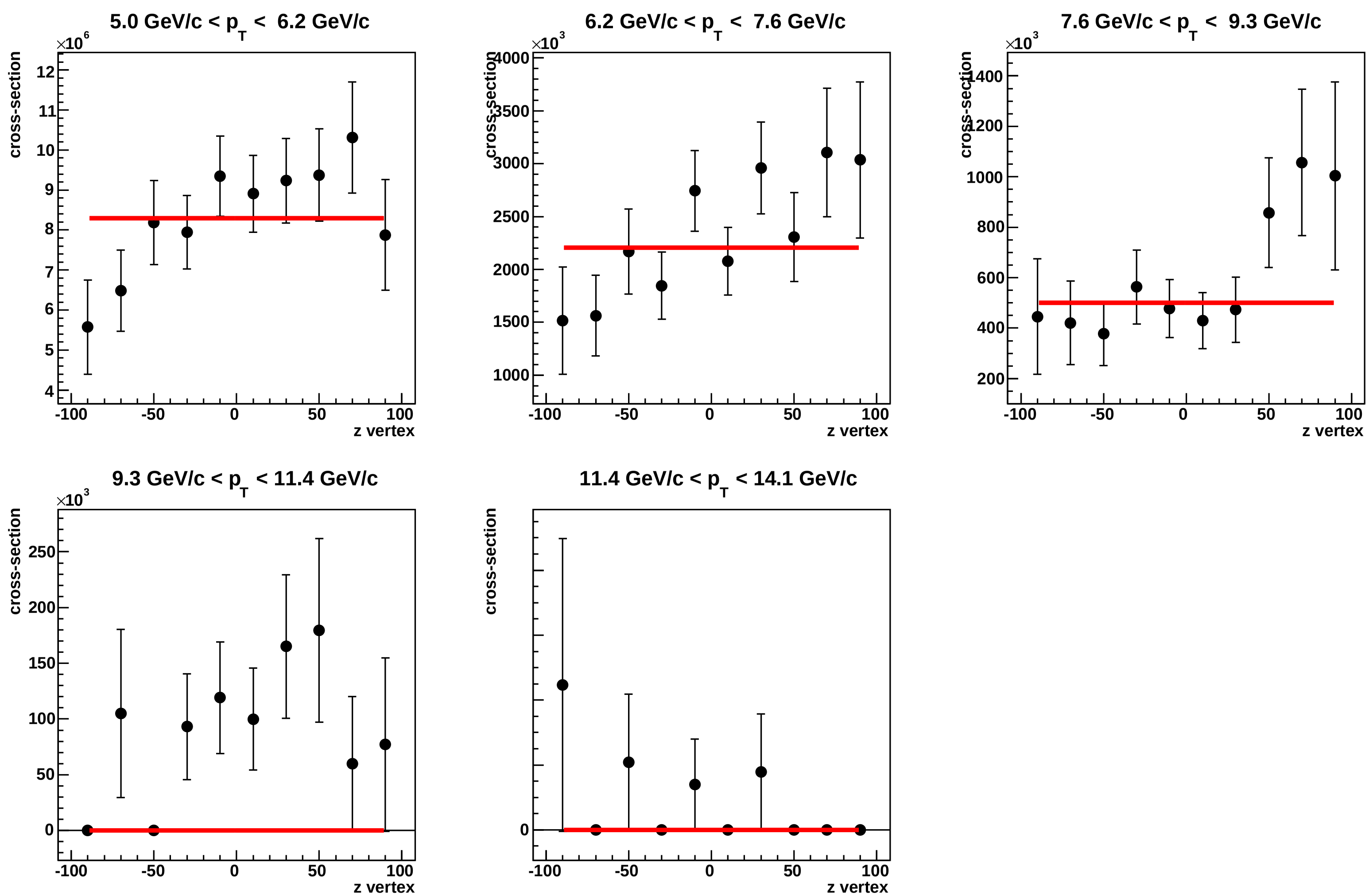

Figure C-20: Cross-section Comparison of different z-vertices for minb trigger for low p_T

C.4 Azimuthal Angle

The cross-section was calculated for $-\pi < \phi < 0$ and $0 < \phi < \pi$. From symmetry it was expected that the cross-sections would be the same. They were calculated for each trigger and compared. There was no systematic difference in azimuthal region found.

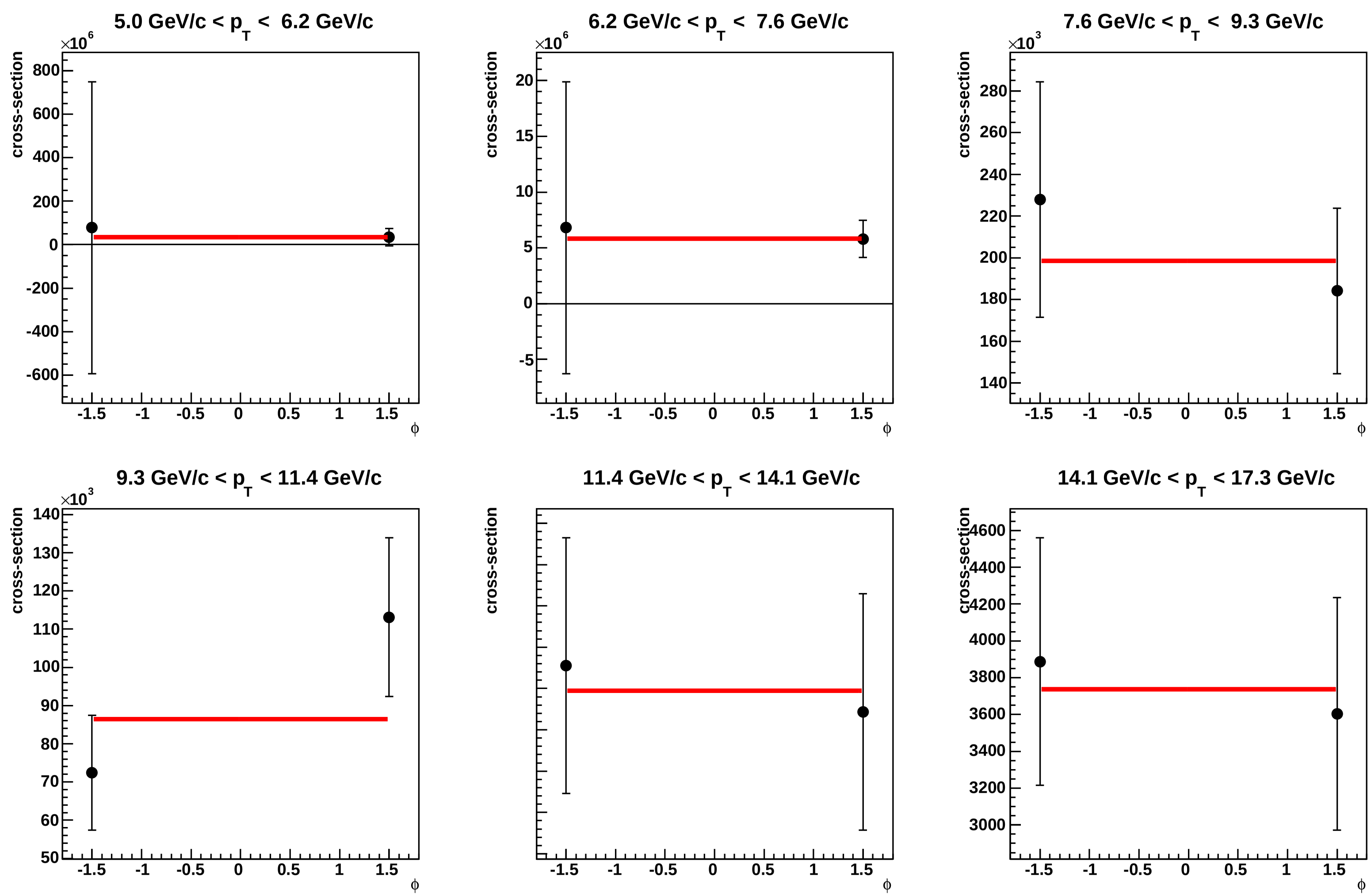

Figure C-21: Cross-section Comparison for negative phi and positive phi for bht1 trigger sorted by p_T

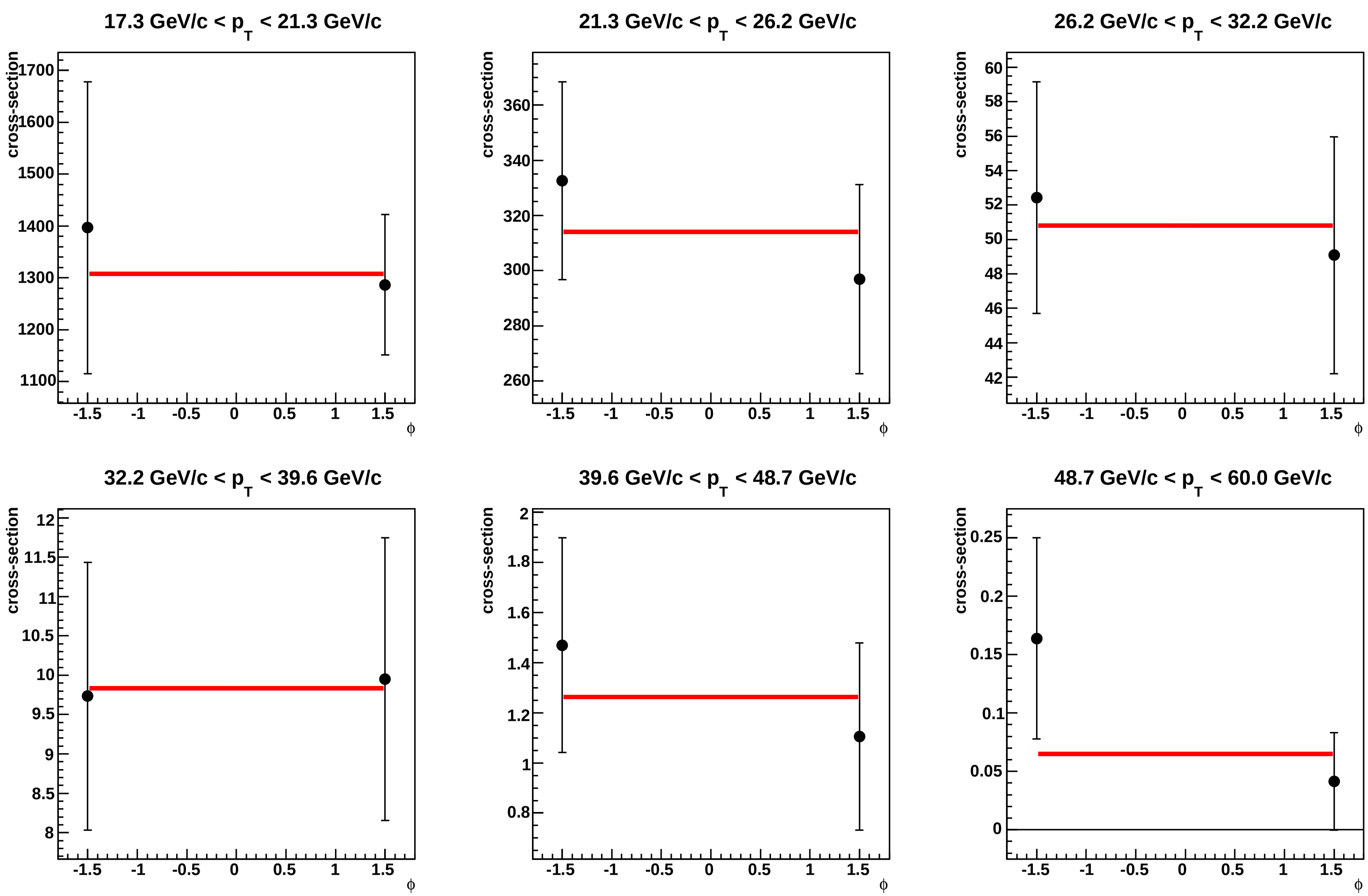

Figure C-22: Cross-section Comparison for negative phi and positive phi for bht1 trigger sorted by p_T

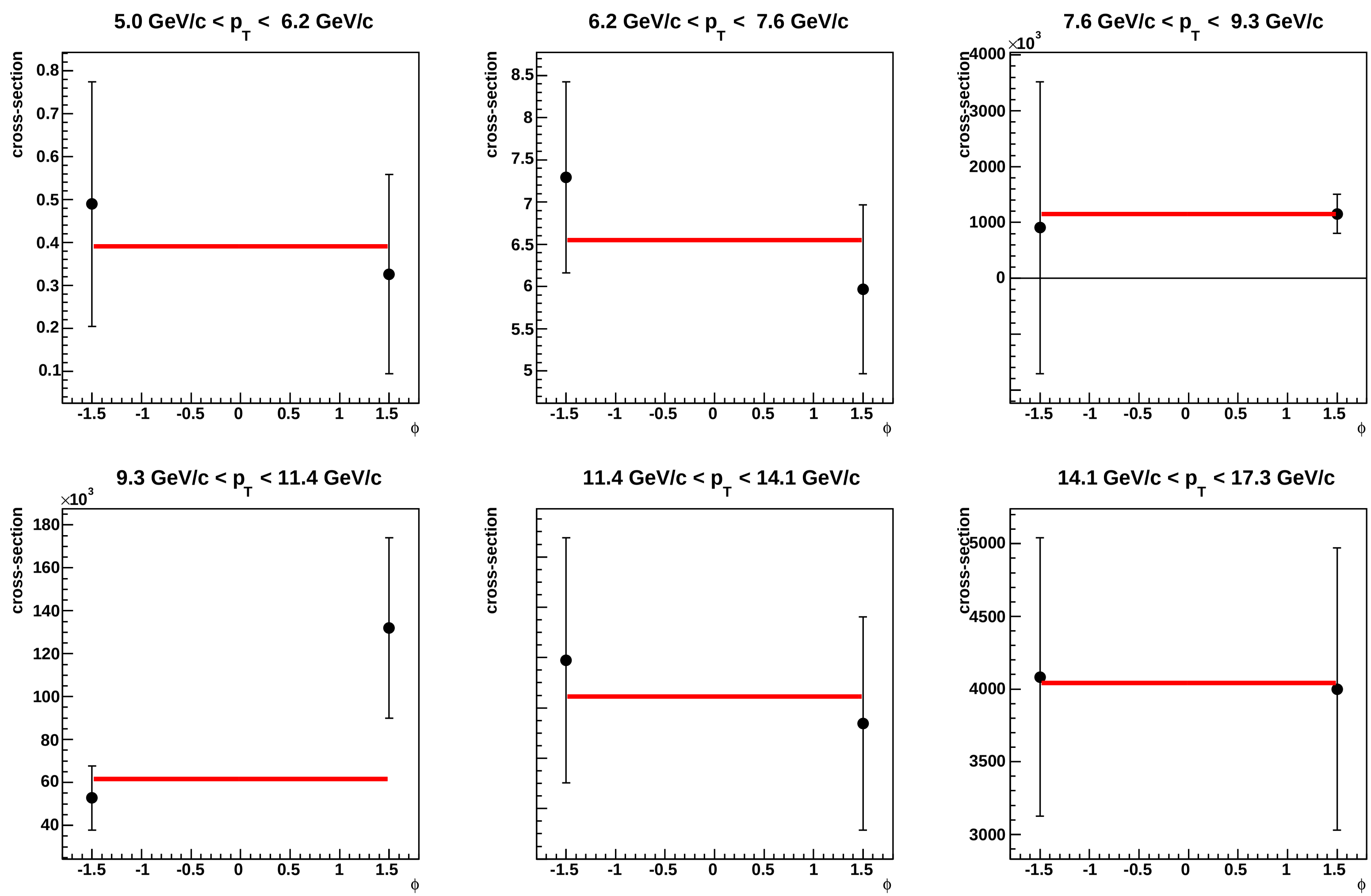

Figure C-23: Cross-section Comparison for negative phi and positive phi for bht2 trigger sorted by p_T

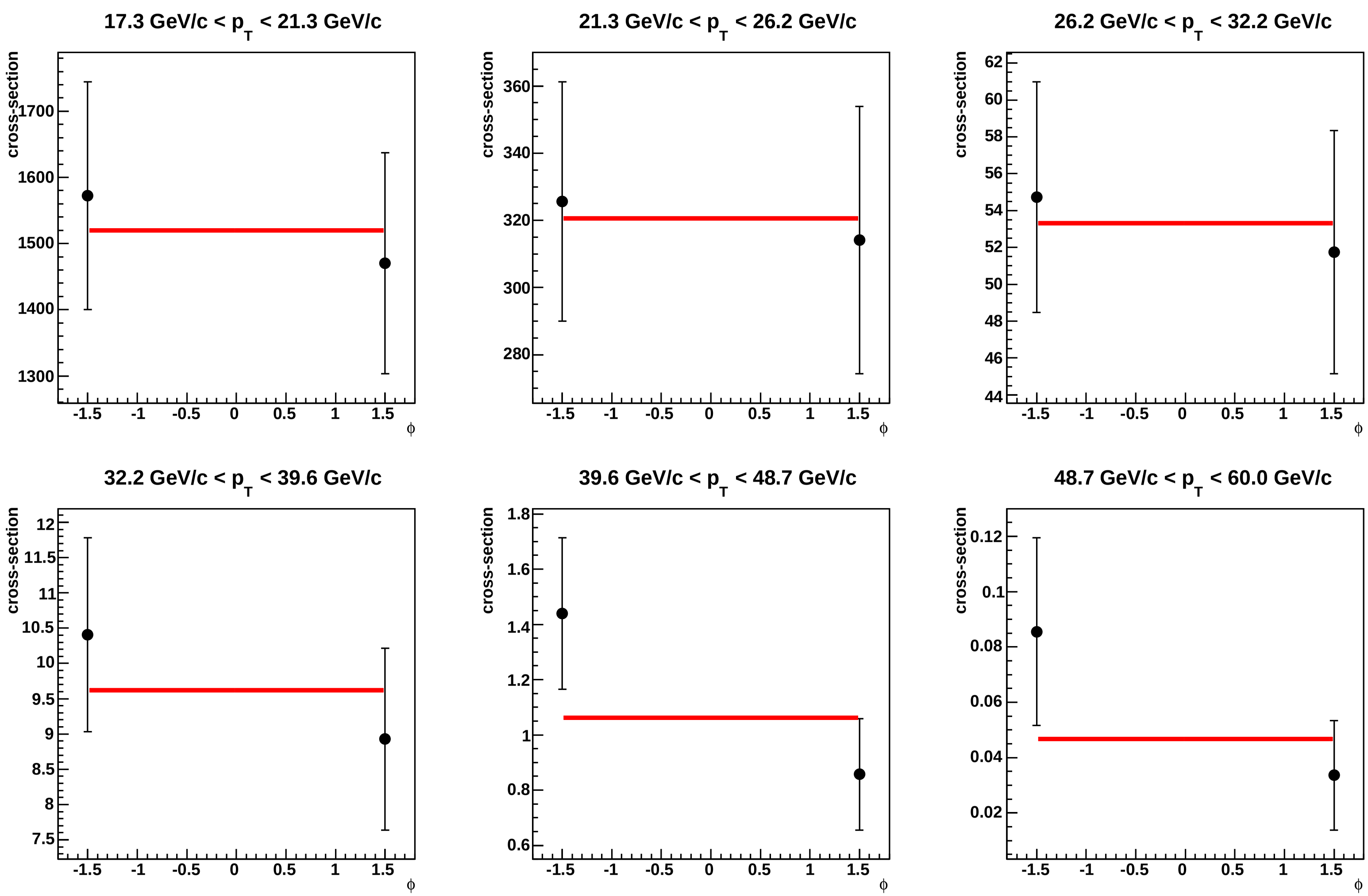

Figure C-24: Cross-section Comparison for negative phi and positive phi for bht2 trigger sorted by p_T

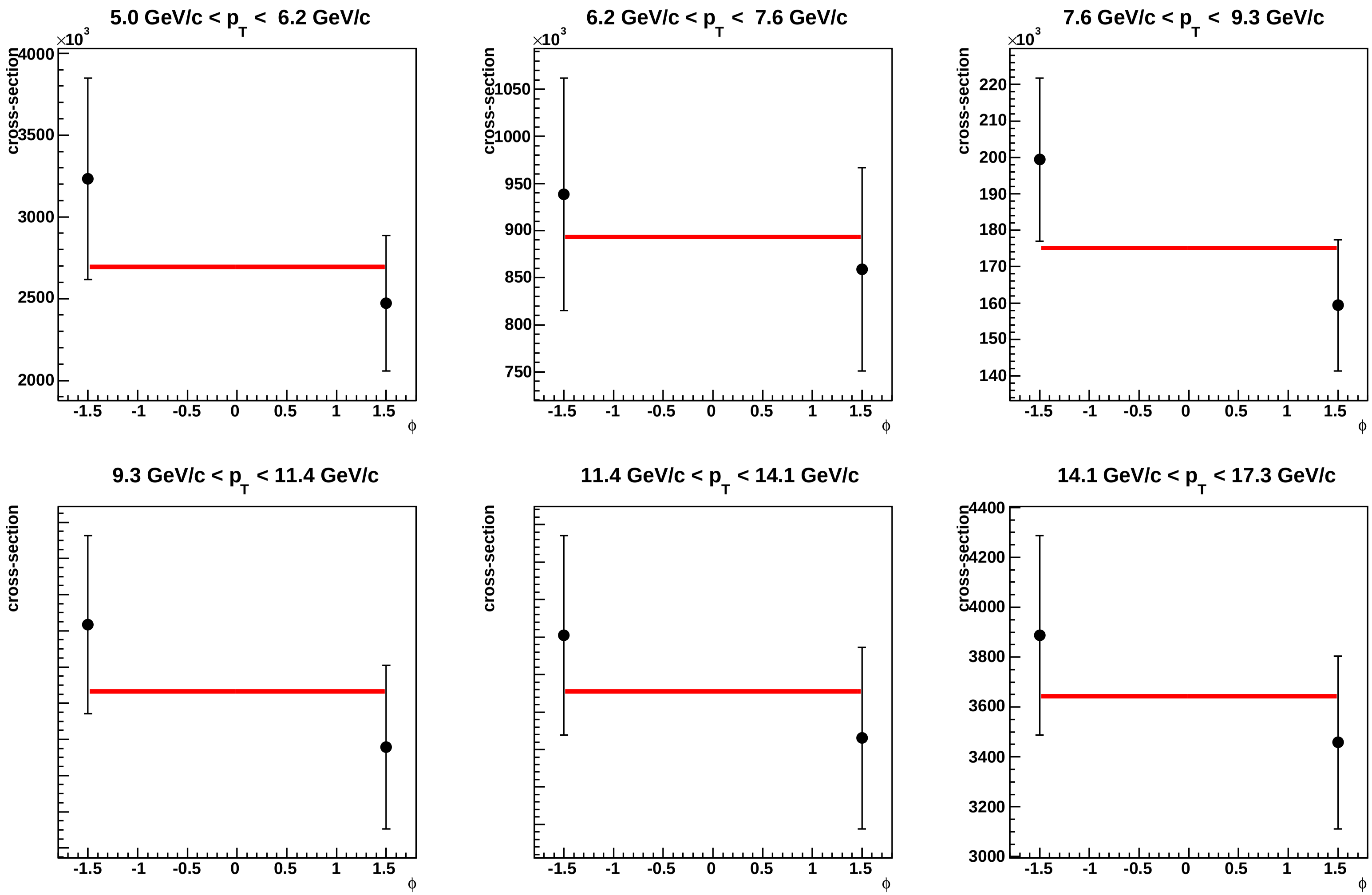

Figure C-25: Cross-section Comparison for negative phi and positive phi for bjp1 trigger sorted by p_T

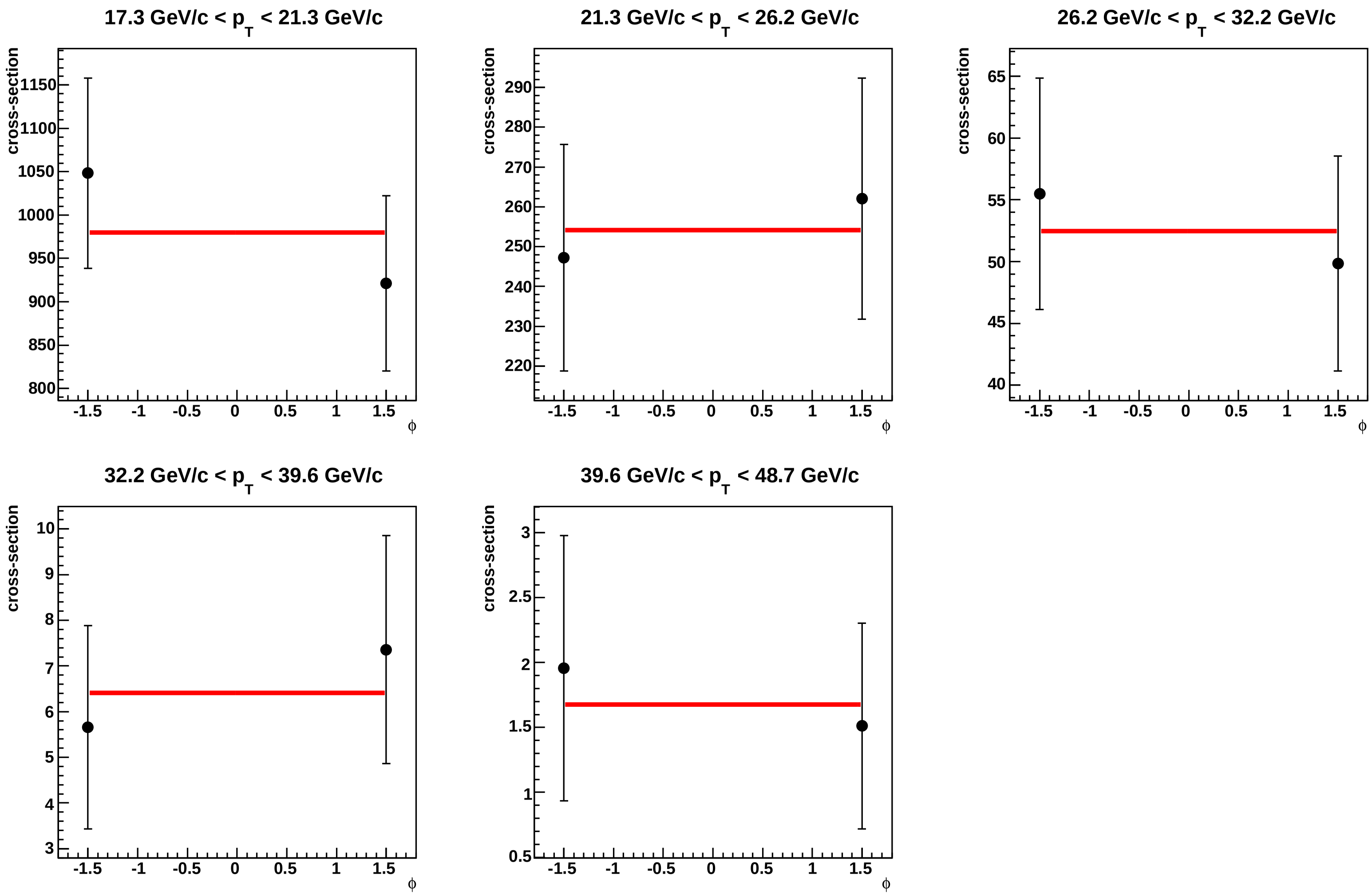

Figure C-26: Cross-section Comparison for negative phi and positive phi for bjp1 trigger sorted by p_T

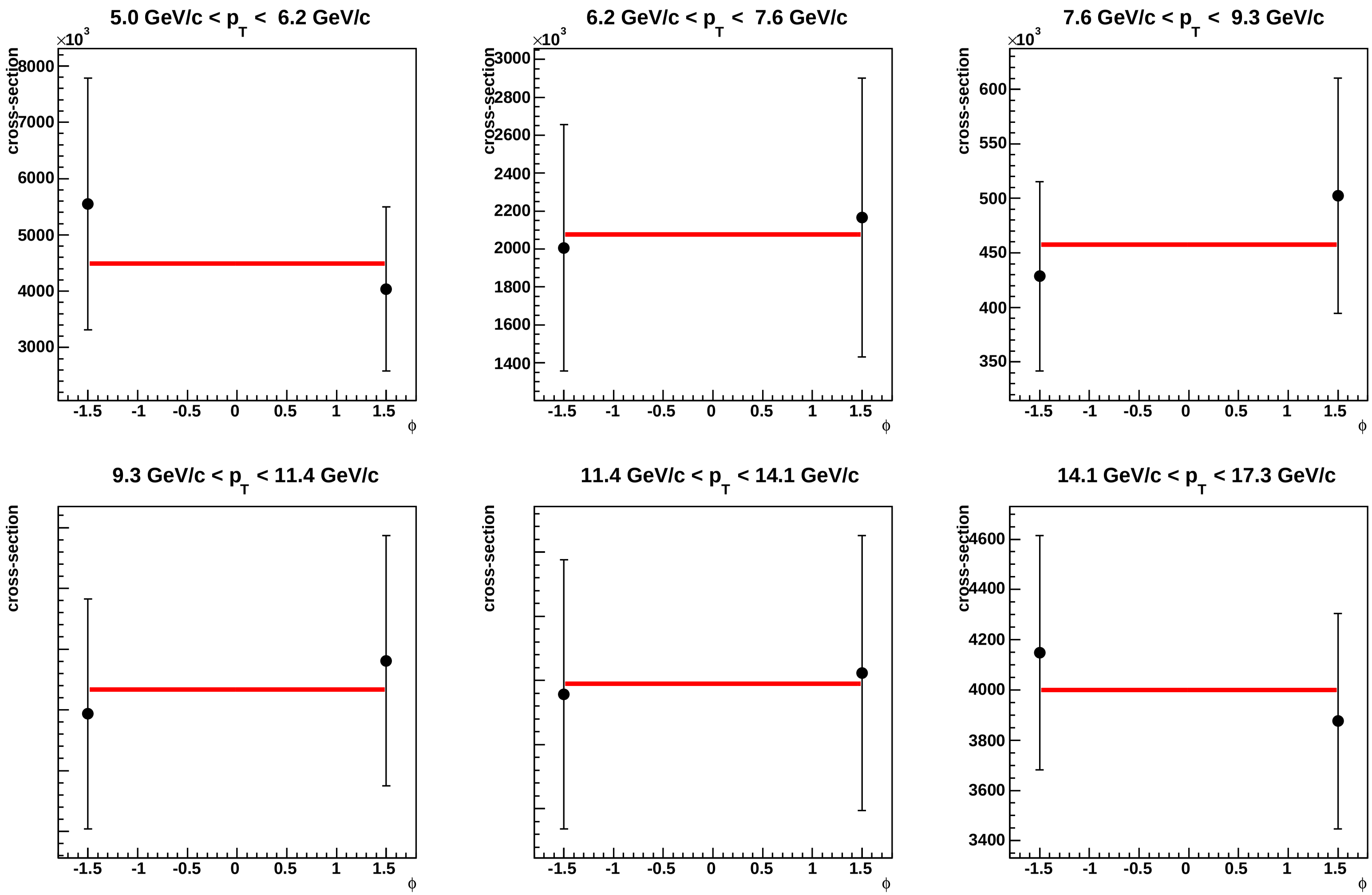

Figure C-27: Cross-section Comparison for negative phi and positive phi for bjp2 trigger sorted by p_T

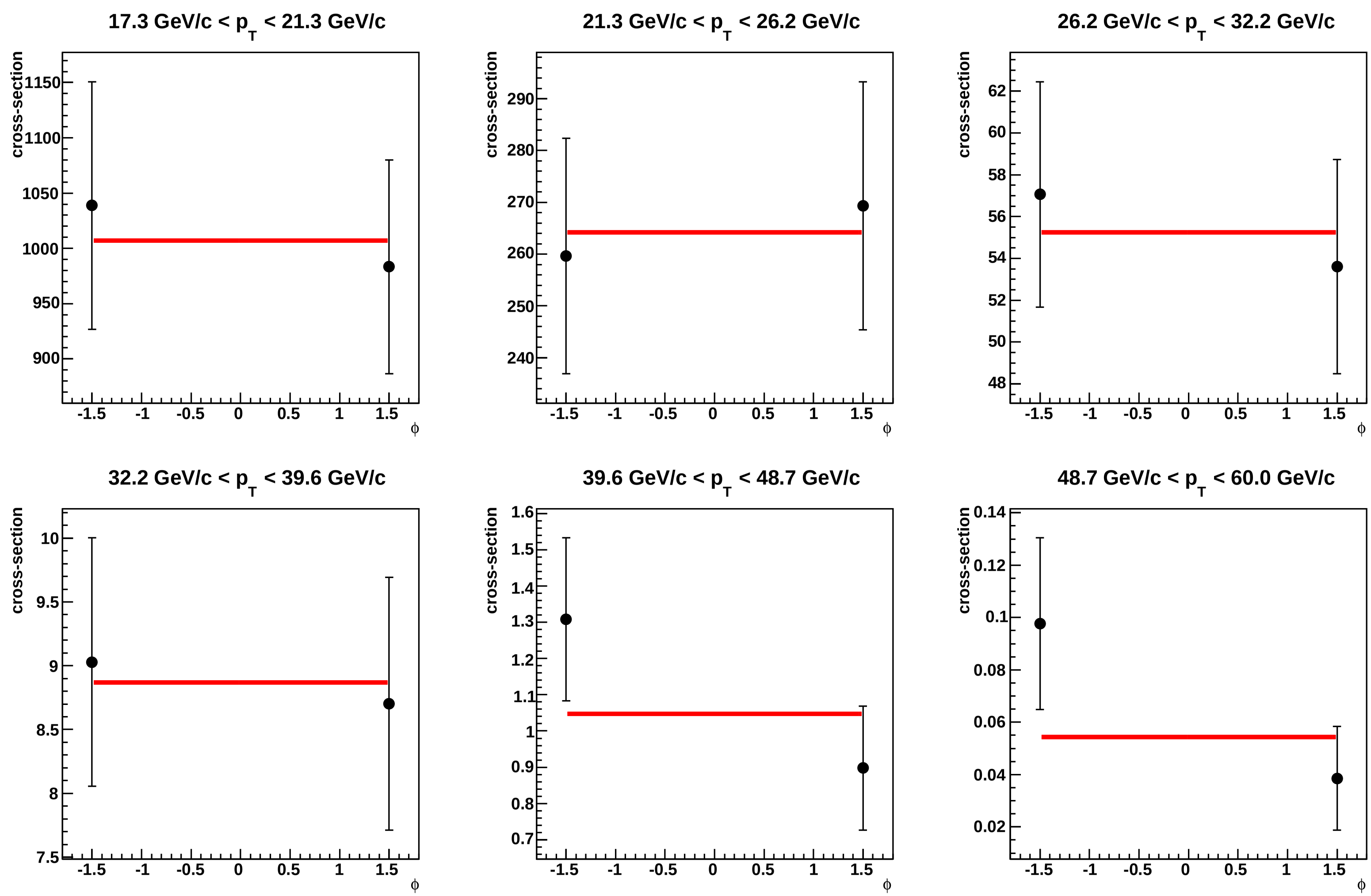

Figure C-28: Cross-section Comparison for negative phi and positive phi for bjp2 trigger sorted by p_T

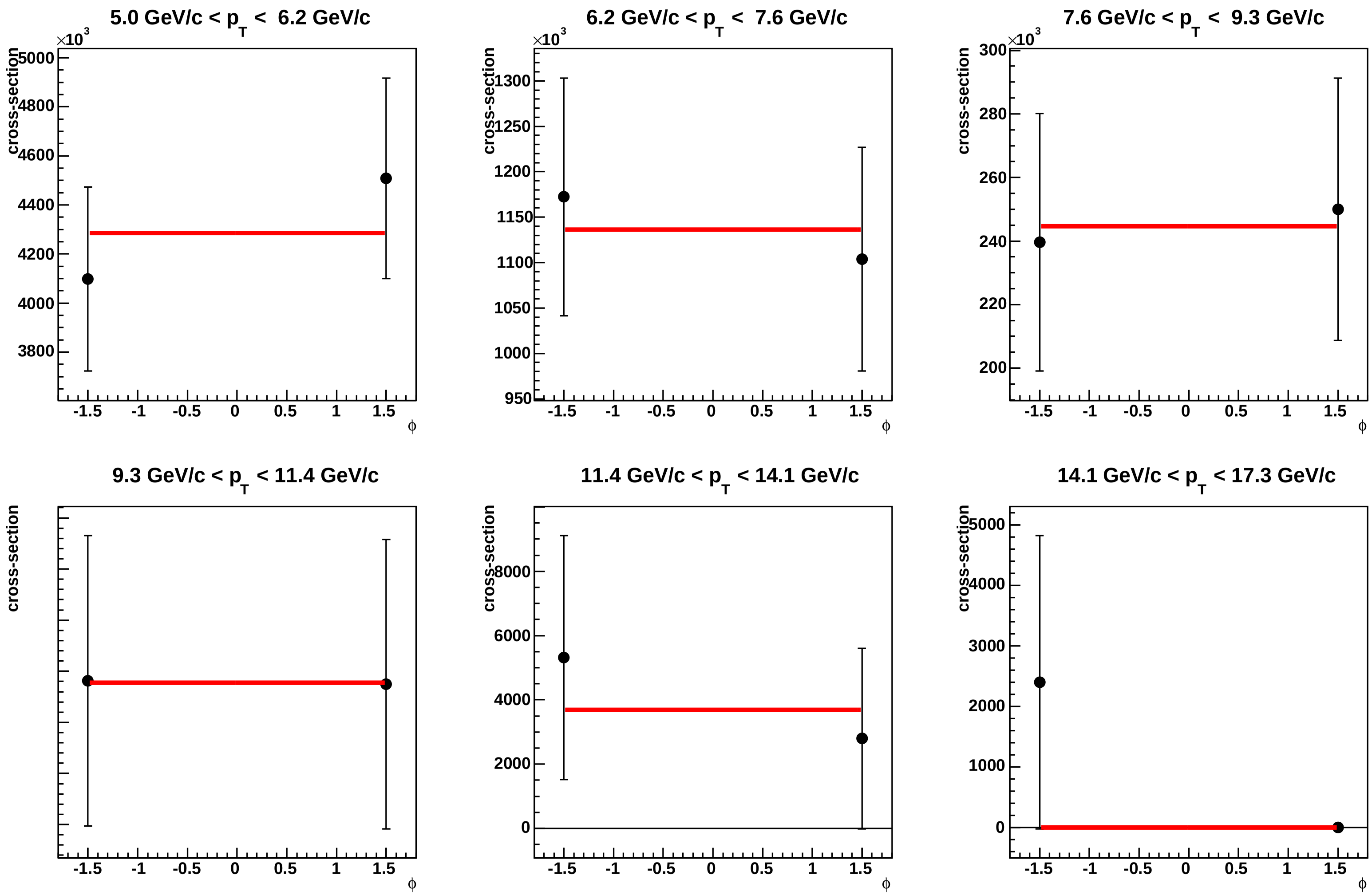

Figure C-29: Cross-section Comparison for negative phi and positive phi for minb trigger sorted by p_T

C.5 Proton Helicity

When protons collided at STAR they either had helicity equal to +1 or to -1. Since there were two beams, there were four possible configurations of the collisions. At STAR these were labeled UU, UD, DU and DD.[5] A check that the four possible combinations gave the same cross-section was made. For the following plots, spin=-0.5 corresponds to UU, spin=0.5 corresponds to UD, spin=1.5 corresponds to DU, and spin=2.5 corresponds to DD.

[5] U (D): spin upwards (downwards) while circulating at RHIC.

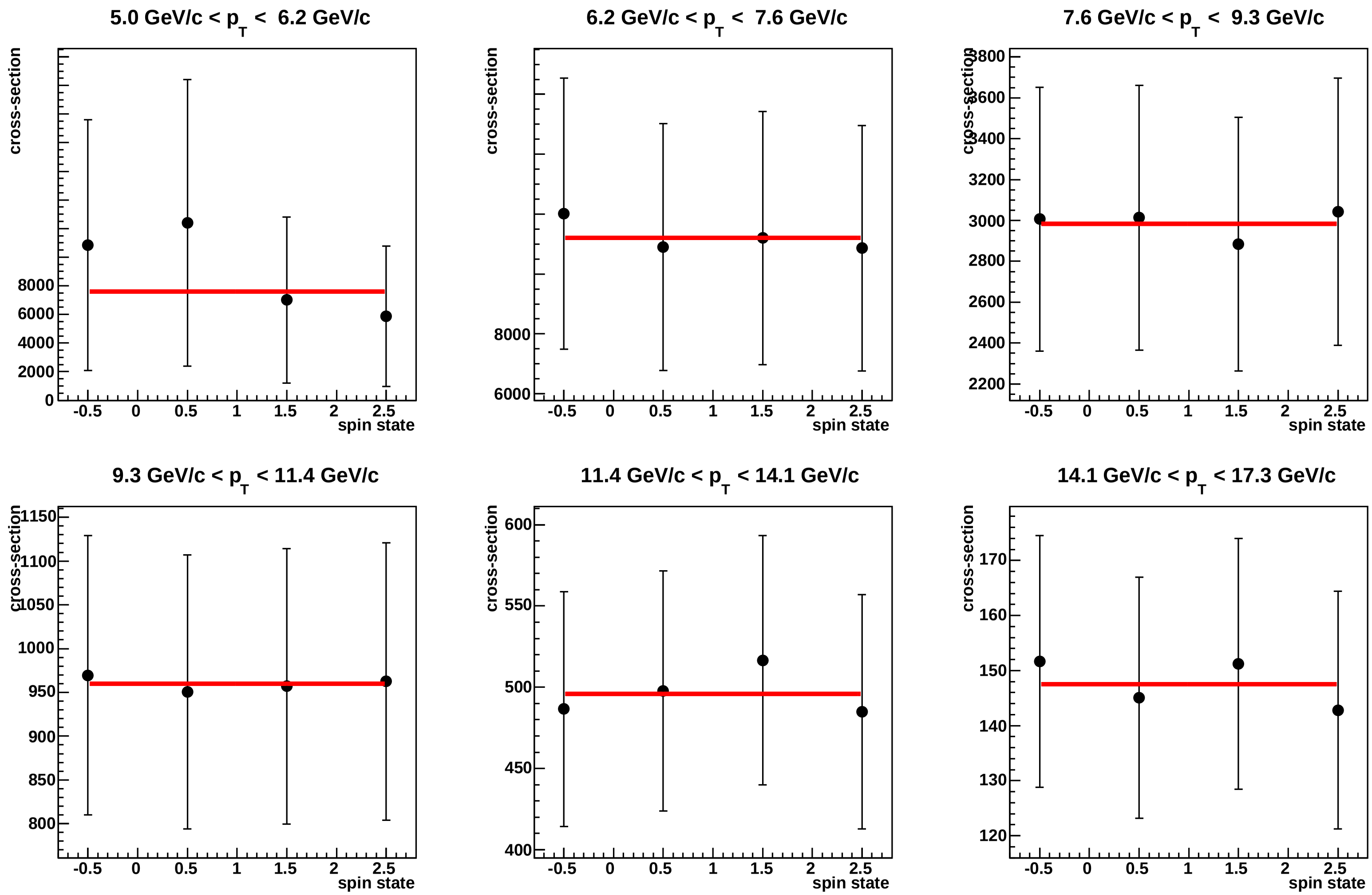

Figure C-30: Spin State Cross-section Comparison for BHT1 trigger sorted by p_T

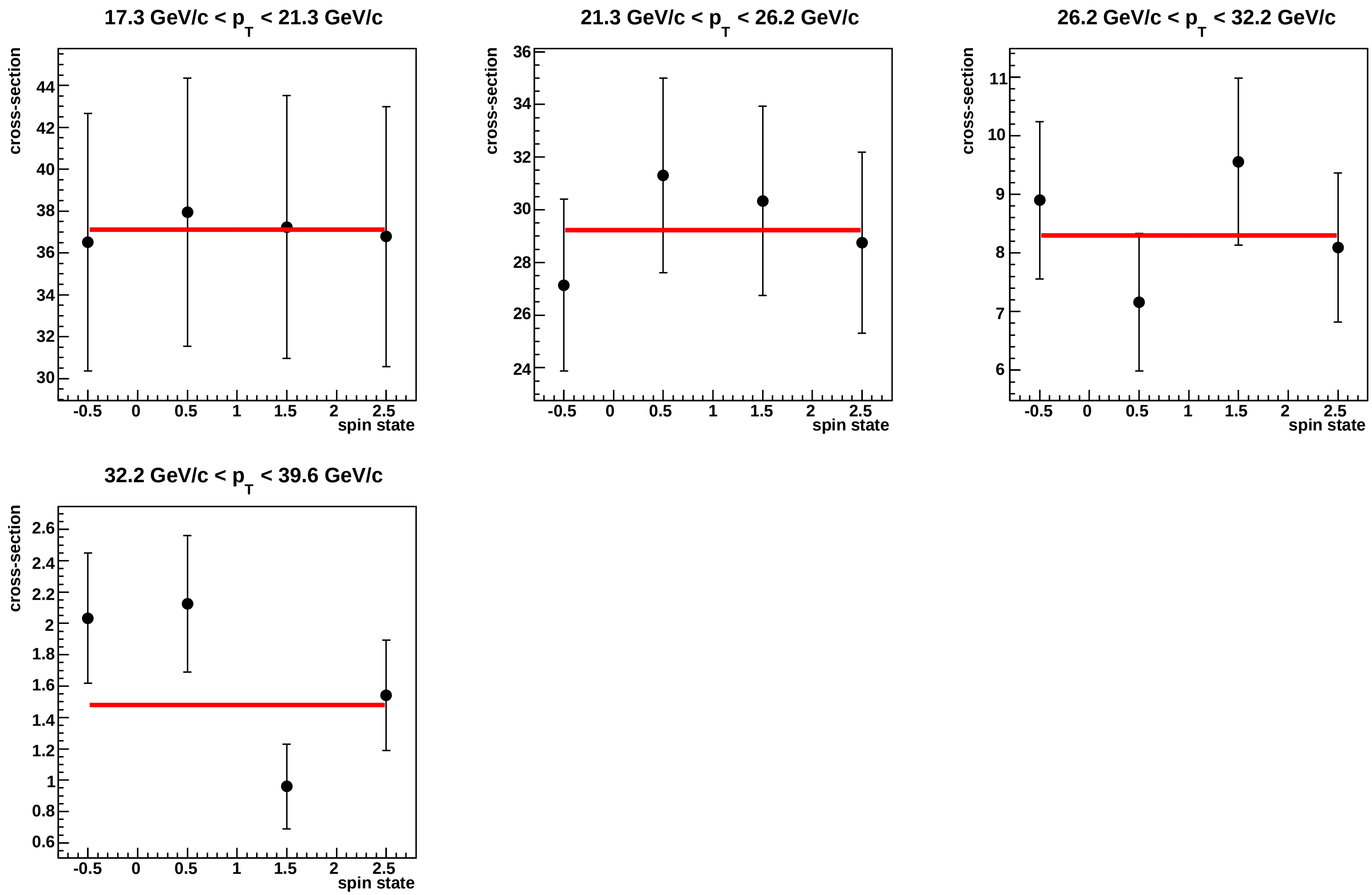

Figure C-31: Spin State Cross-section Comparison for BHT1 trigger sorted by p_T

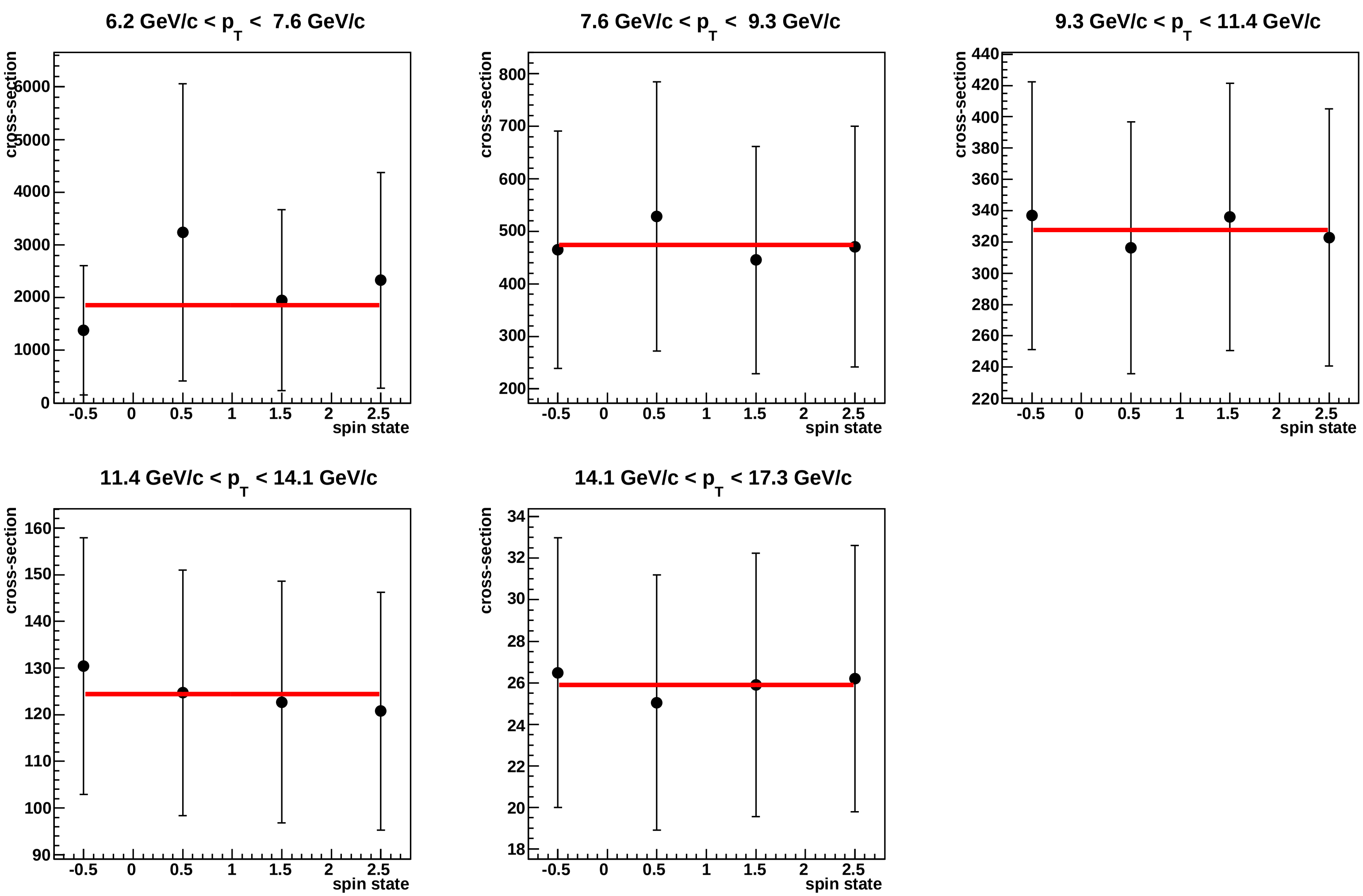

Figure C-32: Spin State Cross-section Comparison for BHT2 trigger sorted by p_T

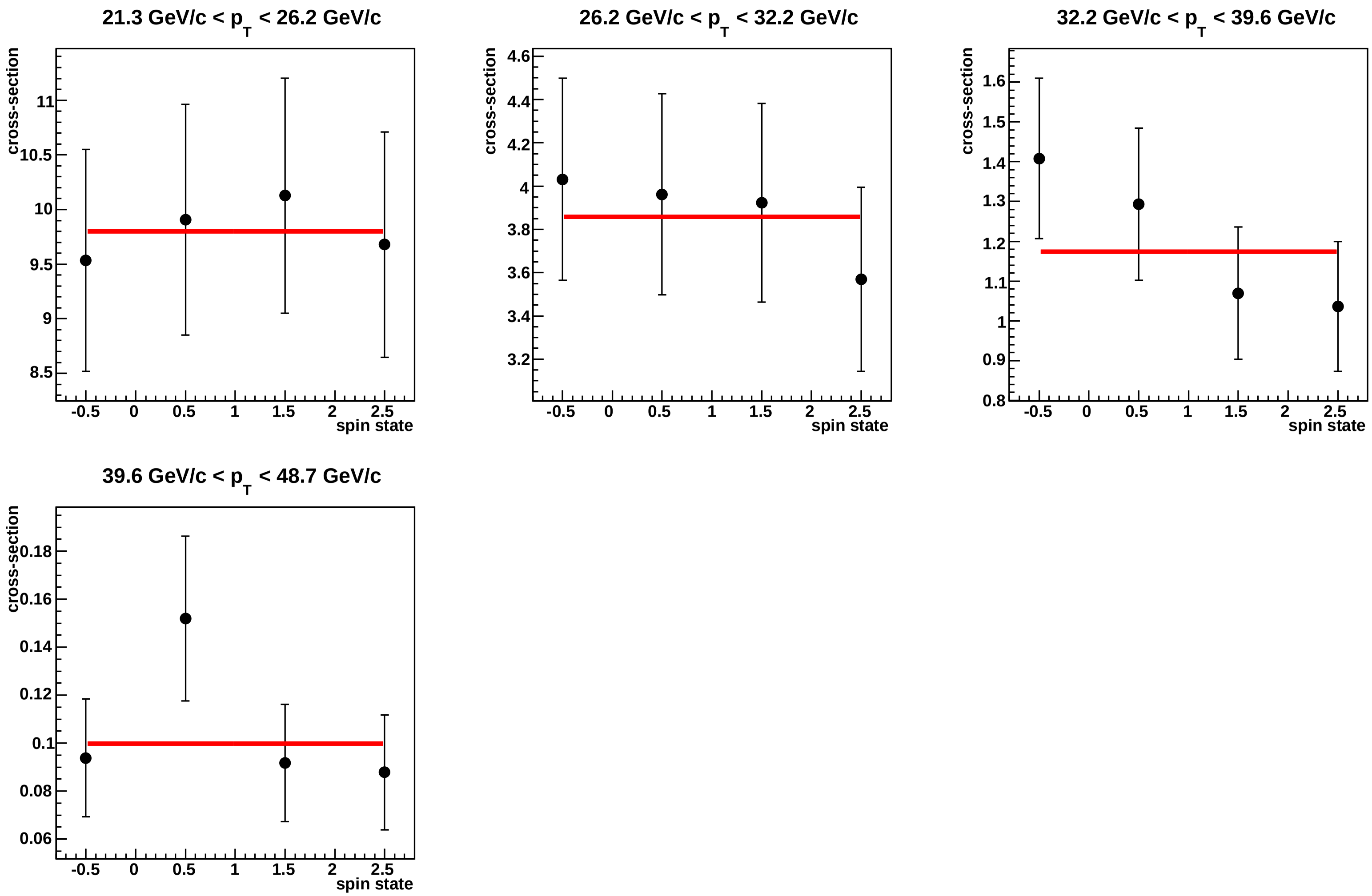

Figure C-33: Spin State Cross-section Comparison for BHT2 trigger sorted by p_T

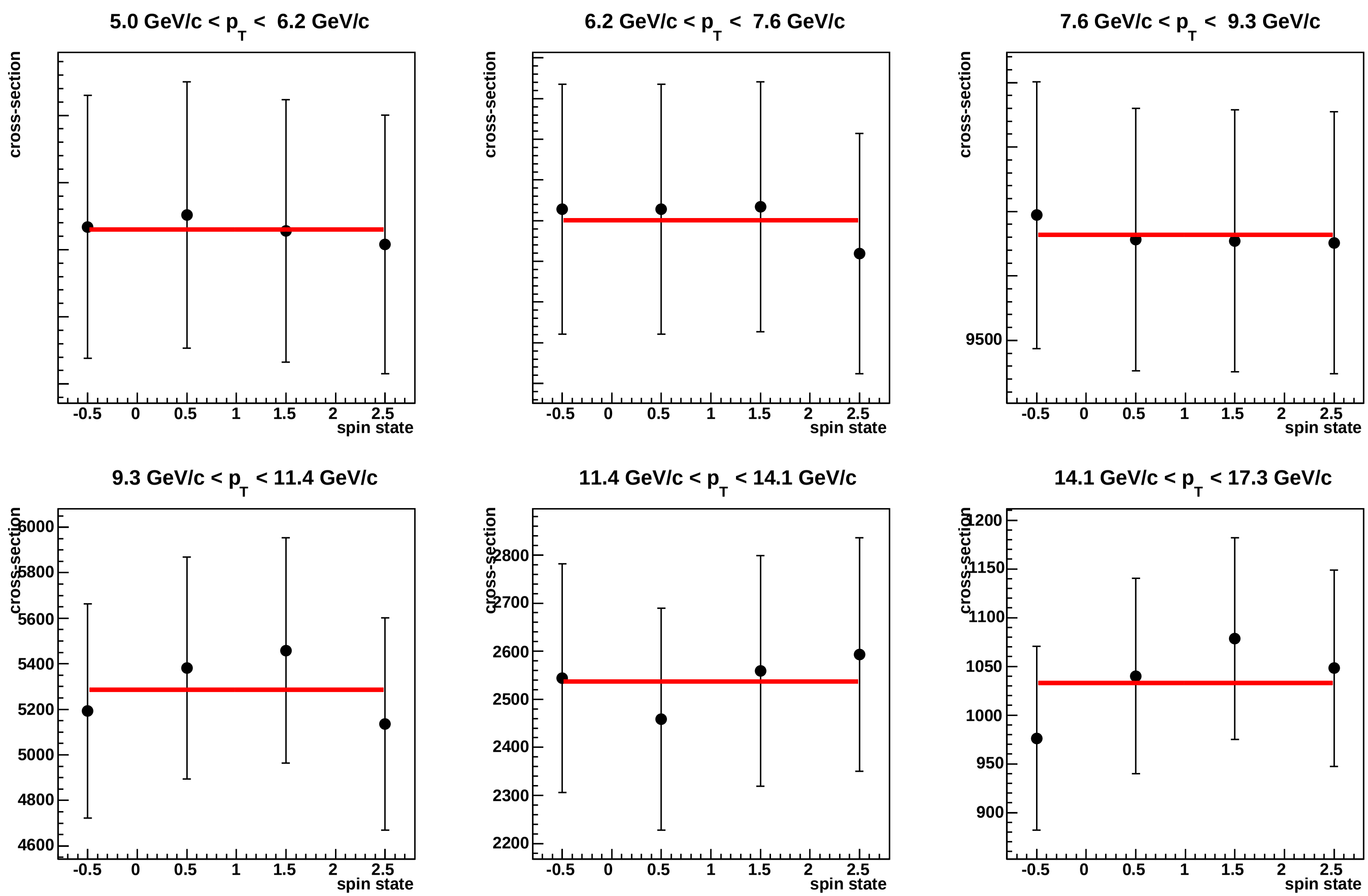

Figure C-34: Spin State Cross-section Comparison for BJP1 trigger sorted by p_T

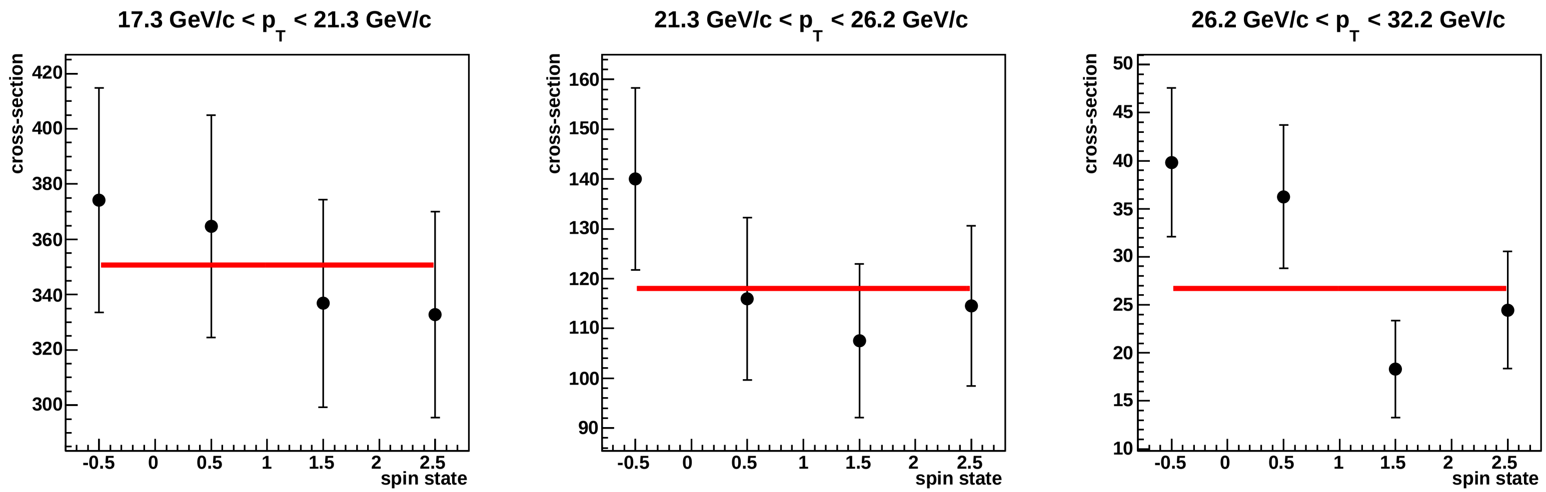

Figure C-35: Spin State Cross-section Comparison for BJP1 trigger sorted by p_T

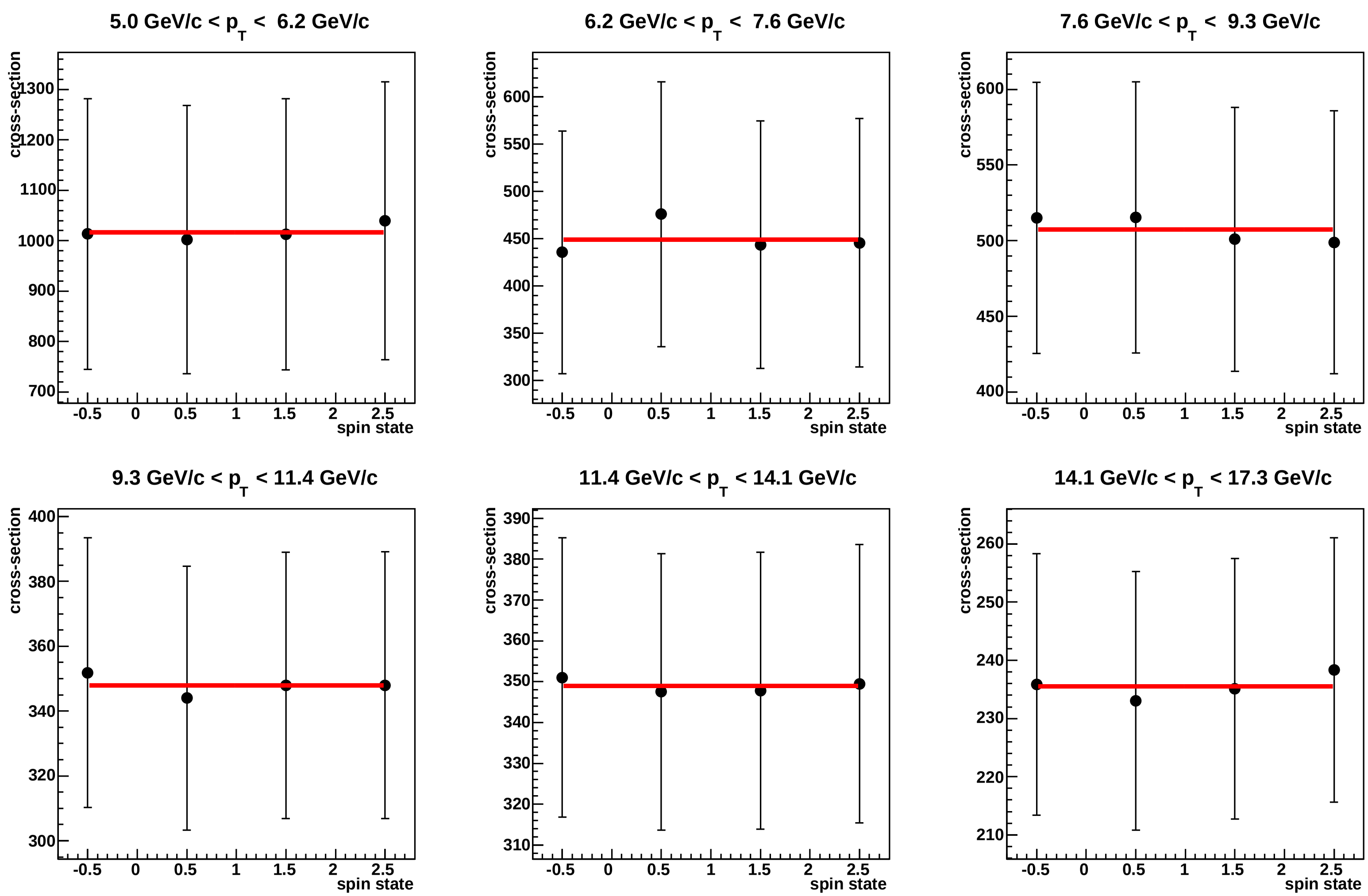

Figure C-36: Spin State Cross-section Comparison for BJP2 trigger sorted by p_T

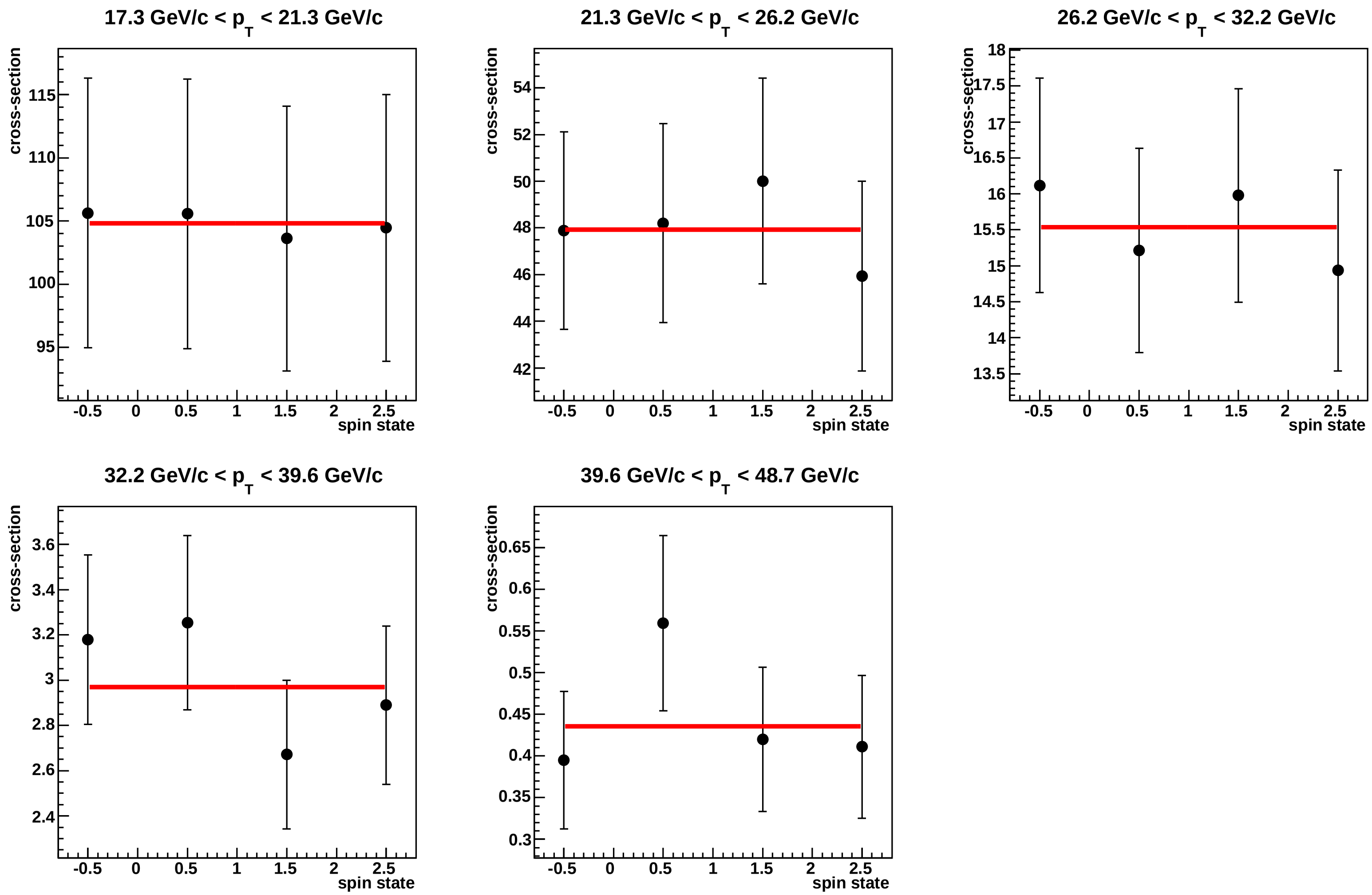

Figure C-37: Spin State Cross-section Comparison for BJP2 trigger sorted by p_T

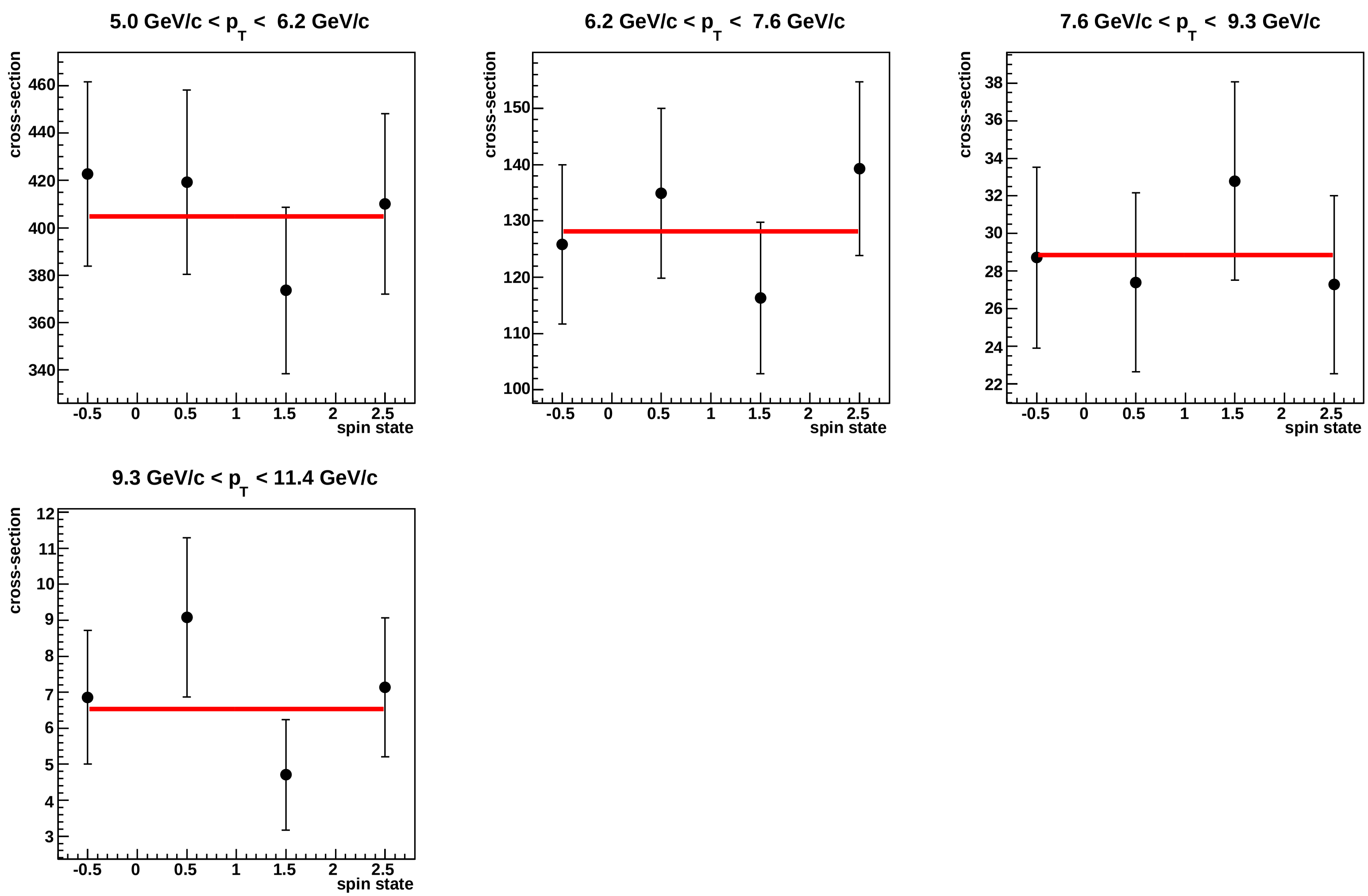

Figure C-38: Spin State Cross-section Comparison for MINB trigger sorted by p_T

Appendix D

Additional Cross-section Comparison Graphs and Tables

This chapter contains graphs and tables used to compare the 2005 cross-section to theory predictions and previous results. The NLO pQCD theory prediction curve[30] was calculated using CTEQ6M[37] parton distributions.

The plots are sorted by trigger. Five triggers were used: MINB, BHT1, BHT2, BJP1 and BJP2. MINB was a minimum bias trigger that required particles to be incident on the BBC[1]. BHT1[2] (BHT2) required, in addition to the MINB trigger, that one of the BEMC towers measuring $\Delta\eta \times \Delta\phi = 0.05 \times 0.05$ had transverse energy $E_T > 2.9$ GeV (3.7 GeV). The BJP1[3] (BJP2) trigger required, in addition to the MINB trigger, patches roughly the size of a jet ($\Delta\eta \times \Delta\phi = 1 \times 1$) had $E_T > 4.6$ GeV (7.9 GeV).

[1] The BBC is described in a previous chapter.
[2] Barrel High Tower 1
[3] Barrel Jet Patch 1

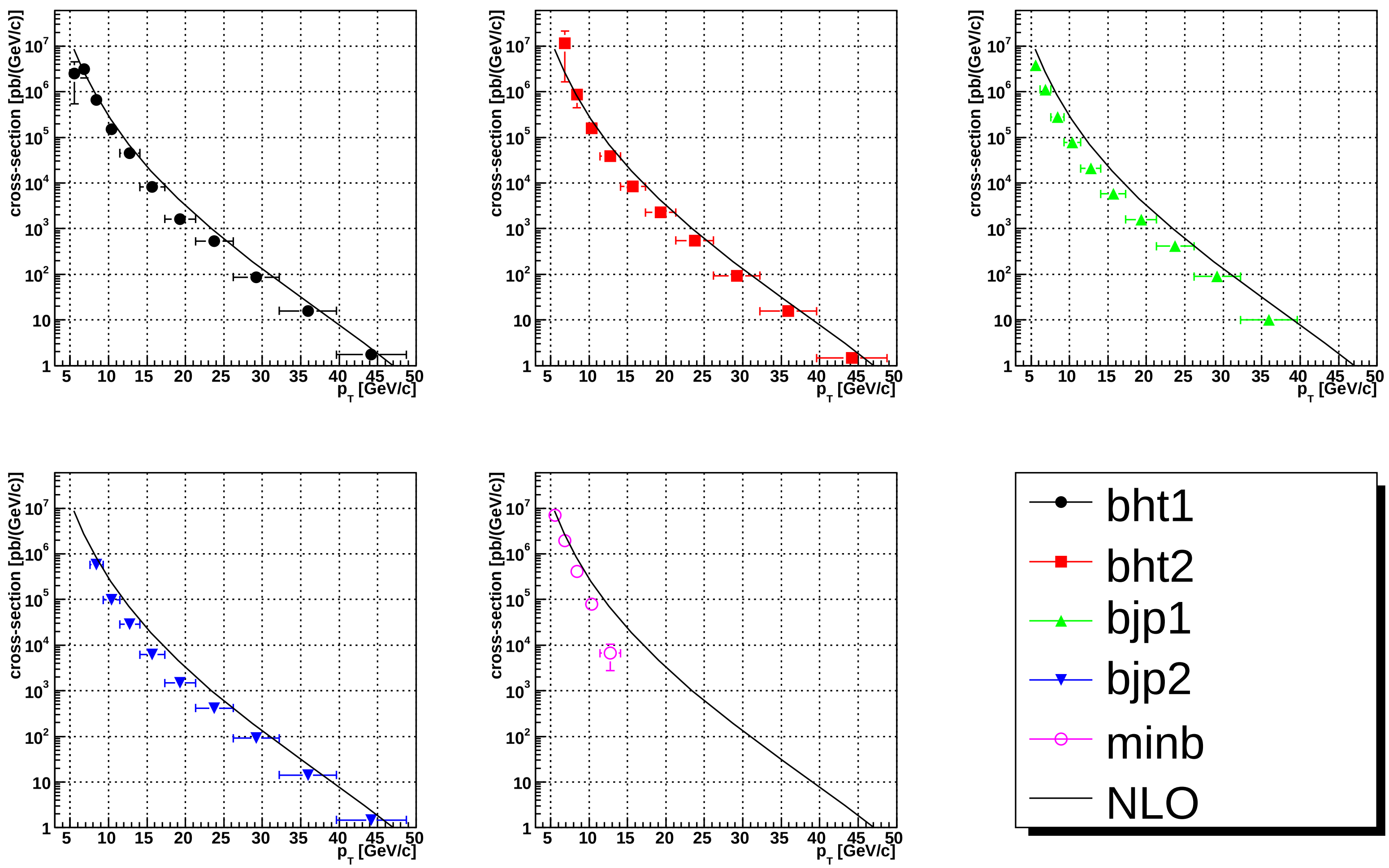

Figure D-1: 2005 Inclusive Jet Cross-section Sorted by Trigger

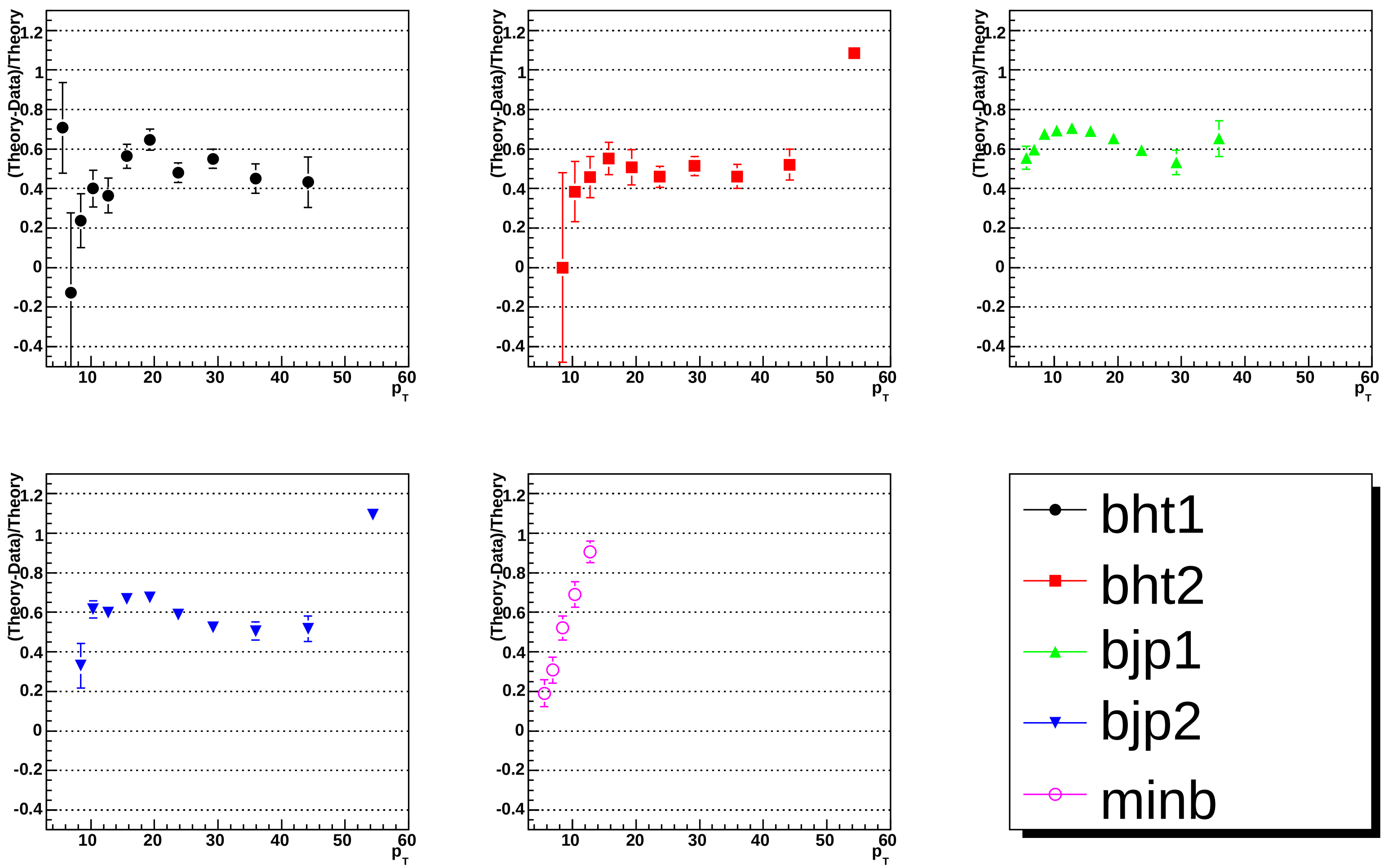

Figure D-2: 2005 Inclusive Jet Cross-section NLO pQCD cross-section Difference

THIS PAGE INTENTIONALLY LEFT BLANK

Appendix E

Symbols

ADC Analog to Digital conversion.

AGS Alternating Gradient Synchrotron. A synchrotron at BNL used for accelerating protons.

BBC Beam-Beam Counter. A detector element of STAR.

BEMC Barrel Electro-magnetic Calorimeter: A part of the STAR detector.

BNL Brookhaven National Laboratory

BRAHMS Broad Range Hadron Magnetic Spectrometers Experiment at RHIC

CBT Central Barrel Trigger. A STAR detector component

CERN European Organization for Nuclear Research

CTB Central Trigger Board: Part of the STAR detector.

DAQ Data acquisition system. Part of the STAR detector readout.

DESY Deutsches Elektronen-Synchrotron

DIS Deep inelastic scattering: Scattering of a particle off a parton inside the nucleon. This process probes distances small compared to the nucleon size and additional particles are created.

EMC European Muon Collaboration

E_T Transverse energy

HT High tower. A type of trigger.

JP Jet Patch. A type of trigger.

LINAC Linear Accelerator. Accelerates protons prior to their being injected into the AGS.

MB Minimum bias. The most basic trigger.

MWPC Multi-Wire Proportional Chamber: part of the readout system of the TPC

PHENIX Pioneering High Energy Nuclear Experiment. Experiment at BNL.

PHOBOS Experiment at BNL. Named for one of the Mars moons. (Modular Array for RHIC Spectroscopy).

PMT Photomultiplier Tube

pp2pp Experiment at RHIC BNL

pQCD Perturbative QCD

QCD Quantum Chromodynamics: Physics theory which describes the interactions of the strong force

QGP Quark Gluon Plasma

RHIC Relativistic Heavy Ion Collider:

SLAC Stanford Linear Accelerator Center

STAR Solenoidal Tracker at RHIC: The Collaboration under which this experiment was done.

SVT Silicon Vertex Tracker. A STAR detector component.

TOF Time of Flight. A STAR detector component.

TPC Time Projection Chamber: One of the elements of the STAR detector.

ZDC Zero-Degree Calorimeter. One of the elements of the STAR detector.

η pseudorapidity

ϕ azimuthal angle

Bibliography

[1] B. Adeva et al. Next-to-leading order QCD analysis of the spin structure function g_1. *Phys. Rev. D*, 58(11):112002, Oct 1998.

[2] M. Gluck, E. Reya, M. Stratmann, and W. Vogelsang. Models for the polarized parton distributions of the nucleon. *Phys. Rev.*, D63:094005, 2001.

[3] Elliot Leader. *Spin in Particle Physics*, section 12.2. Cambridge University Press, Cambridge, UK, 2005.

[4] J. Ashman et al. An investigation of the spin structure of the proton in deep inelastic scattering of polarized muons on polarized protons. *Nucl. Phys.*, B328:1, 1989.

[5] John Ellis and Robert Jaffe. Sum rule for deep-inelastic electroproduction from polarized protons. *Phys. Rev. D*, 9(5):1444–1446, Mar 1974.

[6] Marco Stratmann and Werner Vogelsang. Exploring the polarization of gluons in the nucleon. 2007.

[7] B. Jager, M. Stratmann, and W. Vogelsang. Single-inclusive jet production in polarized p p collisions at o(alpha(s)**3). *Phys. Rev.*, D70:034010, 2004.

[8] T. Gehrmann and W. James Stirling. Polarized Parton Distributions in the Nucleon. *Phys. Rev.*, D53:6100–6109, 1996.

[9] H. Hahn et al. The RHIC design overview. *Nucl. Instrum. Meth.*, 499:245+, 2003.

[10] B.B. Back et al. The PHOBOS detector. *Nucl. Instrum. Meth.*, 499:603+, March 2003.

[11] M. Adamczyk et al. The BRAHMS detector. *Nucl. Instrum. Meth.*, 499:437+, March 2003.

[12] K. Adcox et al. The PHENIX detector. *Nucl. Instrum. Meth.*, 499:469+, March 2003.

[13] S. Bultmann et al. The PP2PP experiment at RHIC: silicon detectors installed in roman pots for forward proton detection close to the beam. *Nucl. Instrum. Meth.*, 535:415+, March 2004.

[14] K.H. Ackermann et al. STAR detector overview. *Nucl. Instrum. Meth.*, 499:624+, March 2003.

[15] I. Alekseev et al. Polarized proton collider at RHIC. *Nucl. Instrum. Meth.*, 499:392+, March 2003.

[16] S. R. Mane, Yu. M. Shatunov, and K. Yokoya. Siberian snakes in high-energy accelerators. *J. Phys.*, G31:R151–R209, 2005.

[17] O. et al Jinnouchi. Measurement of the analyzing power of proton-carbon elastic-scattering. 2004.

[18] H. Okada et al. Measurement of the analyzing power A(N) in p p elastic scattering in the CNI region with a polarized atomic hydrogen gas jet target. 2006.

[19] F. Bergsma et al. The STAR detector magnet subsystem. *Nucl. Instrum. Meth.*, 499:633+, March 2003.

[20] M. Beddo et al. The STAR barrel electromagnetic calorimeter. *Nucl. Instrum. Meth.*, 499:725+, March 2003.

[21] R. Bellwied et al. The STAR silicon vertex tracker: A large area silicon drift detector. *Nucl. Instrum. Meth.*, 499:640+, March 2003.

[22] F.S. Bieser et al. The STAR trigger. *Nucl. Instrum. Meth.*, 499:766+, March 2003.

[23] W.J. Llope et al. The TOFp/pVPD time-of-flight system for STAR. *Nucl. Instrum. Meth.*, 522:252+, 2003.

[24] M. Anderson et al. The STAR time projection chamber: A unique tool for studying high multiplicity events at rhic. *Nucl. Instrum. Meth.*, 499:659+, March 2003.

[25] J.M. Landgraf et al. An overview of the STAR DAQ system. *Nucl. Instrum. Meth.*, 499:762+, March 2003.

[26] J. Kiryluk. Local polarimetry for proton beams with the star beam beam counters. Talk at SPIN2004, October 2004.

[27] C. Adler et al. The RHIC zero degree calorimeters. 470:488+, 2001.

[28] Gerald C. Blazey et al. Run II jet physics. In *Batavia 1999, QCD and weak boson physics in Run II*, pages 47–77, 2000.

[29] John Adams et al. Transverse momentum and collision energy dependence of high p(t) hadron suppression in au + au collisions at ultrarelativistic energies. *Phys. Rev. Lett.*, 91:172302, 2003.

[30] M. Stratmann and W. Vogelsang. private communication. 2006.

[31] Torbjorn Sjostrand, Leif Lonnblad, and Stephen Mrenna. PYTHIA 6.2: Physics and manual. 2001.

[32] Rick Field and R. Craig Group. PYTHIA Tune A, HERWIG, and JIMMY in Run 2 at CDF. 2005.

[33] Geant 3.21. *CERN Program Library.*

[34] John Adams et al. Measurements of transverse energy distributions in Au + Au collisions at s(NN)**(1/2) = 200-GeV. *Phys. Rev.*, C70:054907, 2004.

[35] B. I. Abelev et al. Longitudinal double-spin asymmetry and cross section for inclusive jet production in polarized proton collisions at s**(1/2) = 200-GeV. *Phys. Rev. Lett.*, 97:252001, 2006.

[36] G. D. Lafferty and T. R. Wyatt. Where to stick your data points: The treatment of measurements within wide bins. *Nucl. Instrum. Meth.*, A355:541–547, 1995.

[37] J. Pumplin et al. New generation of parton distributions with uncertainties from global QCD analysis. *JHEP*, 07:012, 2002.

[38] M. Harrison et al. RHIC project overview. *Nucl. Instrum. Meth.*, 499:235+, 2003.